Dissertation

for The Degree of Doctor of Science

The Evolutionary Description of Molecular Cloud Mass Functions and Star Formation in the Multiphase Interstellar Medium

(多相星間媒質中における分子雲質量関数の発展と星形成の理論的考察)

Masato I.N. KOBAYASHI
(小林将人)

Nagoya University, Graduate School of Science, Department of Physics

February 8, 2018

Abstract

Galaxies are fundamental building blocks of the expanding Universe, which are essentially large agglomeration of stars, the interstellar medium, and dark matter. Revealing galaxy formation and their evolutions is one of the central issues in astrophysics to understand the history of the Universe. Among various processes, the life cycle of the interstellar medium and stars have largely impacts on galaxy evolutions. Giant molecular clouds (GMCs) are key objects to bridge the distribution of the interstellar medium and individual stars, in a sense that GMCs are believed to be the sites of producing stars out of the interstellar medium gas.

Recent radio observations towards nearby galaxies started to map the whole disk and to identify GMCs even in the regions between galactic spiral structures. These surveys show that GMC mass functions (GMCMFs) noticeably vary across galactic disks. The observed variation indicates that massive GMCs preferentially reside along galactic spiral structures whereas inter-arm regions have many small GMCs. Also, radio observations within the Milky Way indicate the importance of Cloud-Cloud Collisions (CCCs) for the formation of star clusters and massive stars. High-resolution magnetohydrodynamics simulations show that multiple episodes of compression are required for creating a molecular cloud in the magnetized interstellar medium (ISM). Because GMCs are believed to be the sites of star formation, connecting these GMC-scale physics in various galactic environment and their impacts on galactic scale GMC distribution is essential to understand subsequent star formation and galaxy evolution. However, the relevant GMC formation processes and the entire galactic disks have six or more orders of magnitude difference in physical scales, thus detailed high-resolution simulations are limited to somewhat local calculations.

Our goal is to provide a framework that covers all the relevant processes in the life cycle of the interstellar medium and stars, and connects them to galaxy evolution consistently. As a first step, we set our goal of the current thesis to extract the essences from previous studies both in observations and local simulations, and formulate a semi-analytical time evolution equation of GMC mass functions (GMCMFs) coarse-grained on 100 pc scales (where pc is parsec: 1 pc = 3.086×10^{18} cm). To formulate such an evolution equation, we aim at including the following five processes consistently to each other, and evaluating the relative important of these processes as a function of galactic environment: 1) the GMC formation and evolution based on phase transition dynamics driven by the multiple episodes of

compression, 2) the GMC self-dispersal due to stellar-feedback by massive stars born within those GMCs, 3) the CCCs, 4) the amount of dispersed gas that has to be consumed for regenerating GMCs once GMCs become dispersed, and 5) the importance of CCC-driven star formation onto the total star formation activity on galactic scales.

We first formulate a time evolution equation that includes GMC formation, evolution, dispersal, and cloud-cloud collisions. The integration of the time evolution equation gives GMCMF time evolution. Our results predict that GMC mass functions have a single power-law exponent in the mass range $< 10^{5.5}\mathrm{M}_{\odot}$ (where $\mathrm{M}_{\odot}$ represents the solar mass), which is well characterized by GMC self-growth and dispersal timescales. In addition, our results suggest that the CCC effect is limited only in the massive-end of the mass function, therefore CCC is sub-dominant process shaping the GMCMF evolution, except for very crowded regions like galactic centers where the GMC number density is higher than normal galactic disk regions.

Next, we identify a gas *resurrection* channel that allows the gas dispersed by massive stars to regenerate GMC populations or to accrete onto the pre-existing GMCs. To evaluate this, we introduce "gas resurrecting factor", which is a fraction of such resurrected gas out of total amount of dispersed gas. We explore, both in semi-analytically and numerically, what resurrecting factor has to be achieved to reproduce the observed profile of GMCMF. Our analysis indicates that almost all the dispersed gas in arm regions can be captured by pre-existing massive GMCs because of their large surface area, whereas nearly half of the dispersed gas in inter-arm regions is used for replenishing the minimum-mass GMC populations because inter-arm regions host less number of massive GMCs than arm regions. We find that there is a one-to-one relation between the gas resurrecting factor and power-law slope of GMCMFs. Therefore, measurements of the GMCMF slope provide a powerful method to constrain those GMC timescales and the gas resurrecting factor in various environment across galactic disks.

In addition, we introduce CCC-driven star formation terms in our time evolution equation. This allows us to compute star formation subsequently taking place in CCC clouds. Our results suggest that, although CCC events between smaller clouds outnumber the ones between massive GMCs, CCC-driven star formation is mostly driven by massive GMCs $\gtrsim 10^{5.5}\mathrm{M}_{\odot}$. The resultant cumulative CCC-driven star formation may amount to a few 10 per cent of the total star formation in the Milky Way and nearby galaxies. We also predict the observability for CCC sites and show that almost all of the CCC sites that observations possibly reach consist of less massive GMCs $\lesssim 10^{5.5}\mathrm{M}_{\odot}$, which have less impacts on the total CCC-driven star formation. Therefore, in addition to recent observational indication of CCCs between low-mass GMCs, CCC sites due to massive GMCs still have to be observed to quantitatively evaluate CCC-driven star formation in total.

Finally, to connect our semi-analytical GMCMF evolution to galaxy evolution studies, we aim at formulating an effective equation of state for the multiphase ISM. We perform hydrodynamics simulations of colliding HI flow and analyze the shock propagation speed. Our analysis indicate that multiphase turbulent ISM has

an effective equation of state similar to isothermal ideal gas (*i.e.*, an effective polytropic index close to unity). We also find that the shock propagation speed does not significantly change in one-dimensional and multi-dimensional modelling. Although further investigations are definitely required, our semi-analytical study in the current thesis coupled with such an effective equation of state marks a first step to study galaxy evolution in which the evolution of the multiphase ISM and star formation are consistently calculated.

Contents

List of Figures

List of Tables

Chapter 1

Overview and Basic Frameworks[1]

Though we are politically enemies, yet with regard to Science it is presumable we shall not dissent from the practice of civilized people in promoting it.
— John Hancock

The speaker of the Masssachusetts Houose of Representatives, John Hancock, sent this letter to British army. This was the year of 1780 when the American Revolutionary War was ongoing and the British army controlled the Penobscot Bay. The reverend Samule Williams of Harvard University needed a British permission to pass the bay for observing the total Solar Ecipese at an island off the coase of Massachusetts. John Hancock's letter in the end successfully enabled Williams' journey.

However, the word "Science" here is not necessarily restricted to natural sciences. This has to cover all fields from religions, arts, educations, economics, languages, and even politics, and to natural sciences. In this faith, I would like to cotribute to fostering human relationships by revealing the mechanisms that govern the Universe. This is, I belive, the way people locate themselves and realize who they are and what they can do.

There is only one corner of the universe you can be certain of improving, and that's your own self. — Aldous Leonard Huxley

In this chapter, we begin with an overview of the history of the Universe. We will then review latest studies on different scales in the hierarchical structure order of the Universe, all of which are connected to our studies presented in this thesis or our future reasearch plans. Finally as a summary of this chapter, we address an introduction and motivation to the core part of this thesis, in which we investigate molecular cloud evolution and star formation in the multiphase interstellar medium.

[1] *The contents of this chapter are partially based upon the articles Kobayashi et al. (2015), Kobayashi et al. (2017b), and Kobayashi et al. (2017a)*

1.1 General Introduction; History of the Universe and Why Galaxies?

Each one of us has their own history as a human being. Along their lives, from their birth to date, people had diverse experiences by interacting others. You keep growing up and cannot be alone. The Universe also has its birth, "evolved" into its current rich structure, and still keep evolving, almost an analogous to human being lives. Cosmology and Astrophysics is the research field to reveal such evolution of the Universe.

The Universe is believed to be born hot and dense out of quantum fluctuations. The subsequent Inflation stretched out the Universe to initiate its uniformity, isotropy, and flatness. Even after the Inflation ended, the Universe kept its expansion with different speed at different epochs. The temperature of the Universe decreased with the expansion of the Universe. About 38 million years after its birth, the Universe became cool enough so that protons and electrons became bond together, which is called recombination. The scattering between these particles and photons terminated so that photons started to travel freely, and the Universe became transparent. Such photons that travel from the recombination era are called Cosmic Microwave Background (CMB) photons. However, the lack of luminous objects, there was an age when the Universe looked dark, which is called the Dark Age[2]. Small fluctuations at the recombination era developed density fluctuations in the Universe. Once the density fluctuation became dense enough, hydrogen atoms are transformed into hydrogen molecules. This advances the cooling processes so that the resultant gas contraction is the onset of star and galaxy formation. Such star/galaxy formation and evolution continued on different scales at different epochs of the Universe. The current Universe thus consists of a hierarchical structure, which contains diverse objects: planets, stars, star clusters, galaxies, galaxy clusters, the large scale structure.

As outlined in the previous paragraph, the Universe is a large cradle in which galaxies form and evolve. Therefore, this cradle is filled with lights emitted from galaxies. We, human beings, emerged in one such starry galaxy – the Milky Way. This fact fascinates us to contemplate why and how we emerge in the Milky Way, which can be rephrased as how the galaxies evolve in the long history of the Universe. To tackle on this question, we are determined to reveal the interwinding evolution of interstellar medium and stars because they are the fundamental elements in galaxies that shape subsequent galaxy formation and evolution. Thus, we set our main focus in this thesis is to give the evolutionary theoretical description for the time evolution of molecular clouds, which are believed to be the seeds of stars, and its connection to galaxy evolution.

[2]It seemed that a great astrophysicist Francesco Palla joked that "The Dark Age ended here in Florence at 14th century".

1.2 Structure Formation

1.2.1 Geometry

Let us assume "Cosmological Principle" such that the Universe is uniform and isotropic. Under this assumption, the geometry of the Universe can be given by Friedmann– Lemaître–Robertson–Walker (FLRW) metric:

$$\mathrm{d}s^2 = -c^2\mathrm{d}t^2 + a(t)^2\left[\frac{\mathrm{d}r^2}{1-Kr^2} + r^2\mathrm{d}\theta^2 + r^2\sin^2\theta\mathrm{d}\phi^2\right], \tag{1.1}$$

in a spherical coordinate system of r, θ, and ϕ (Friedmann 1922; Lemaître 1927). Here, $\mathrm{d}s^2$ is called a space-time line metric, c stands for the speed of light, $a(t)$ represents the scale factor, and K denotes the curvature. $a(t)$ can be understood as a ruler for the *size* of the Universe, which depends on the age of the Universe t. In Cosmology, the relative variation of a in time represents the expansion of the Universe and the current value of $a(t)$ is commonly normalized to unity so that $a(t) < 1$ in the past.

The geometrical evolution of the Universe then can be derived from Einstein's Equation as:

$$\left(\frac{\dot{a}}{a}\right)^2 = \frac{8\pi G}{3}\rho - \frac{Kc^2}{a^2} + \frac{\Lambda c^2}{3}, \tag{1.2a}$$

$$\frac{\ddot{a}}{a} = -\frac{4\pi G}{3}\left(\rho + 3\frac{P}{c^2}\right) + \frac{\Lambda c^2}{3}, \tag{1.2b}$$

where $\dot{a} = \mathrm{d}a/\mathrm{d}t$, $\ddot{a} = \mathrm{d}^2a/\mathrm{d}t^2$, ρc^2 is the energy density, P is the pressure, and Λ is the cosmological constant, which drives the accelerated expansion of the Universe. Let us introduce the Hubble parameter H and four cosmological parameters Ω as:

$$H(t) = \frac{\dot{a}(t)}{a(t)}, \quad \Omega_\mathrm{m} = \frac{8\pi G\rho_\mathrm{m}}{3H^2}, \quad \Omega_\mathrm{r} = \frac{8\pi G\rho_\mathrm{r}}{3H^2}, \quad \Omega_\mathrm{K} = -\frac{Kc^2}{a^2H^2}, \quad \Omega_\Lambda = \frac{\Lambda c^2}{3H^2}, \tag{1.3}$$

where the subscripts represent matter (m), radiation (r), curvature (K), and the cosmological constant (Λ) respectively. Equation 1.2a now can be written as:

$$H^2(t) = H_0^2\left[\frac{\Omega_{\mathrm{m},0}}{a^3} + \frac{\Omega_{\mathrm{r},0}}{a^4} + \frac{\Omega_{\mathrm{K},0}}{a^2} + \Omega_{\Lambda,0}\right], \tag{1.4a}$$

$$1 = \Omega_\mathrm{m} + \Omega_\mathrm{r} + \Omega_\mathrm{K} + \Omega_\Lambda, \tag{1.4b}$$

where the present-day values are denoted with the subscript 0. As one can see here, the large-scale geometrical evolution of the Universe is governed by the relative budget of each component. Current observations (*e.g.*, *Planck*: Planck Collaboration et al. 2014a,b) suggest that $\Omega_{\Lambda,0} = 0.6825$ and $\Omega_{\mathrm{m},0} = 0.3175$ and over 80 percent of $\Omega_{\mathrm{m},0}$ is carried by dark matter, which is typically believed to have no direct interaction with electromagnetic fields.

1.2.2 Redshifts

Due to the finiteness of the speed of light, observing structures at large distance corresponds to observing the Universe in the corresponding past. Latest observations (*e.g.*, *Planck* satellite) suggest that the Universe has its age of 13.8 Giga year thus the distant objects are located significantly further away from us accordingly. It is confusing to describe such cosmological large distance by using normal length/time units that we use on our daily life. Therefore, it is convenient to introduce some simple metric of order of unity to measure distances. The scale factor a is used in this purpose, too. As well as the scale factor a, "redshift" z is also such a metric defined as:

$$\frac{a_0}{a(t)} = 1 + z\,, \tag{1.5}$$

where a_0 represents the scale factor today (*i.e.*, $a_0 = 1$). By this definition, $z = 0$ corresponds to today and z increases as we look back in time (*e.g.*, the recombination occurs at $z \simeq 1100$). Galaxies mostly form and evolve after the Dark Age $z \lesssim 10$ and thus their location is often referred in z. With the current concordance cosmological framework, which is called the lambda-cold dark matter (ΛCDM) Universe, $z \sim 0.79$ corresponds to the half of the Universe age.

1.2.3 Dark Matter Halos

Based on the framework of the (ΛCDM) Universe, structure formation in the Universe is driven by the dynamics of cold dark matter[3]. The collisionless gravitational collapse of dark matter overdensities and their subsequent virialization leads to the formation of dark matter halos with different masses and sizes. Ordinary matter falls into dark matter halos and results in galaxy formation and evolution within the halos. Therefore, the distribution of dark matter halos both in configuration space and in mass can be interpreted as the initial/boundary conditions for galaxy formation and evolution. Number density of objects as a function of their masses is called a mass function and is widely used for statistical analysis of populations (see Appendix A for different definitions of mass functions).

The Press-Schechter formalism (Press & Schechter 1974) is a model to predict the mass function of dark matter halos by extrapolating the linear density perturbation with the spherical collapse theory of the halos. The derived mass function has a form of

$$n_{\rm dm}(m) = -\sqrt{\frac{2}{\pi}}\frac{\overline{\rho}_{\rm m,0}}{m^2}\frac{{\rm d}\ln\sigma_m}{{\rm d}\ln m}\frac{\delta_{\rm c}}{\sigma_m}\exp\left(-\frac{\delta_{\rm c}^2}{2\sigma_m^2}\right)\,, \tag{1.6}$$

where $n_{\rm dm}(m)$ is the differential number density of dark matter halos with mass m, $\overline{\rho}_{\rm m,0}$ represents the mean density within the halos at the present-day Universe,

[3]The origin and the nature of dark matter itself still remains in a mystery, although its existence was proposed over 80 years ago (Zwicky 1937). Dark matter is believed as a matter that mostly likely interact only through gravity and neither emit nor absorb photon. The property of dark matter is an active topic (Ostriker & Steinhardt 2003), but we do not discuss it further in this thesis.

σ_m is the variance average on the mass scale of m, and δ_c is the critical density for forming collapsed objects (*e.g.*, $\delta_c = 1.69$ in the spherical collapse theory). Equation 1.6 is well reproduced by numerical simulations of the large-sale structure[4]. Although the mapping between this function and observed galaxy luminosity/mass functions in unlikely to be given by a single fixed factor(*e.g.*, Somerville & Primack 1999), The Press-Schechter formalism gives insights for galaxy-dark matter halo connections. We will briefly discuss this issue in the next section.

1.3 Galaxies in the Universe

Galaxies are large systems consisting of dark matter, stars, and gas, bright in various wavelengths unlike dark matter. Thus galaxies act as a lighthouse to deliver to us the information of the Universe in the past. Also, they are hosts of stars, planets, and lives. Therefore, galaxies are fundamental building blocks in the Universe and studying galaxies at different redshifts cultivate our insights how the Universe and its contents evolved.

Originally, there was debate that whether or not the nebulae discovered in the 18th and 19th centuries (mostly by William Herschel and his sister and son) are small substructures in the Milky Way galaxy or indications that there are external galaxies in the Universe like the Milky Way. Based on the variable star luminosity-period relation (Leavitt 1908; Leavitt & Pickering 1912), variable star observations by Edwin, P. Hubble in 1924 suggested that the M31 (Andromeda Nebula) is an external system that subsumes billions of stars like our Milky Way. This discovery broadened the horizon of what people recognized as the Universe.

1.3.1 Galaxy - Dark Matter Connection

As introduced in the previous section, massive galaxies are believed to be hosted by dark matter halos. Therefore, revealing relations between physical quantities originated in galaxies and their host halos is one of the essential issues in galaxy studies.

Stellar-to-Halo Mass Relation

Stellar-to-halo mass relation (SHMR) is a relation between total stellar mass that galaxies subsume and mass of dark matter halos that host those galaxies. This relation is extensively investigated both theoretically and observationally, and Figure 1.1 shows one of such studies based on abundance matching technique by Behroozi et al. (2010). Their study compiled with other previous studies by different analyses suggest that the relation can be approximated as $M_* \propto M_{\rm halo}^{2.3}$ for $M_{\rm halo} < 7 \times 10^{11} {\rm M}_\odot$ and $M_* \propto M_{\rm halo}^{0.29}$ for $M_{\rm halo} > 7 \times 10^{11} {\rm M}_\odot$, where M_*

[4]Extensions of this formalism are discussed in great details by many authors (*e.g.*, Bond et al. 1991; Lacey & Cole 1993; Sheth & Tormen 1999).

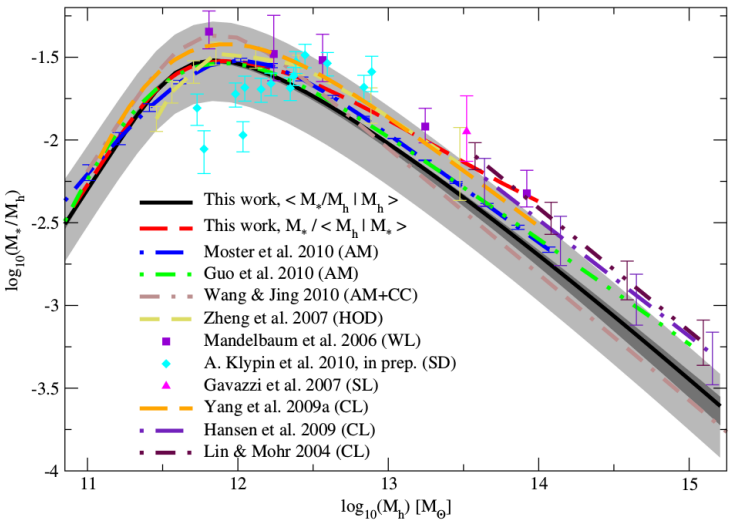

Figure 1.1: Stellar-to-halo mass relation. This figure show $M_*/M_{\rm halo}$ as a function of $M_{\rm halo}$ where M_* represents stellar mass of individual galaxies and $M_{\rm halo}$ denotes individual dark matter halo mass. Color schemes correspond to each study referred. The references followed by their probes are shown at the left bottom. The abbreviations of the probes are defined as; AM for abundance matching technique, CC for correlation function constraint, HOD for halo occupation distribution modeling, WL for weak lensing analysis, SD for satellite kinematics, SL for strong lensing analysis, CL for luminosity and mass analysis on cluster member galaxies. This relation indicate that dark matter halos with mass $\sim 7 \times 10^{11} {\rm M}_\odot$ have the most effective star formation activity among the mass range studied here. This figure is taken from Behroozi et al. (2010).

represents the total stellar mass in a galaxy and $M_{\rm halo}$ represents the mass of a dark matter halo. The star formation efficiency normalized by host dark matter halo mass has its peak at the halo mass of $\sim 7 \times 10^{11} {\rm M}_{\odot}$ in the present Universe, which likely corresponds to galaxies slightly smaller than the Milky Way galaxy by a factor few in stellar mass. Redshift evolution of this relation is continuously and intensively investigated (*e.g.*, Harikane et al. 2016) and is expected to highlight the coevolution of galaxies and dark matter halos in time.

Density Profile of Dark Matter Halos

A variety of large scale cold dark matter numerical simulations (*e.g.*, Dubinski & Carlberg 1991; Navarro et al. 1996b) have shown that the mass density distribution within halos is generally well described by a one parameter family, commonly referred to as the Navarro, Frenk, & White density profile (Navarro et al. 1997, hereafter NFW profile):

$$\rho(R_{3D}) = \frac{\delta_c \overline{\rho}_{\rm b}}{(R_{3D}/R_{\rm s})\,(1 + R_{3D}/R_{\rm s})^2}\,, \tag{1.7}$$

where $R_{\rm 3D}$ is the distance from the center of a given halo, $R_{\rm s}$ is the characteristic scale radius of the halo where the logarithmic slope of the density profile transitions from -1 to -3. If we define dark matter halos as a spherical overdensity in which the mean density is 200 times the mean background matter density, then the halo mas can be given as $M_{\rm 200b} = 4/3\pi R^3_{\rm 200b} 200 \overline{\rho}_{\rm b}$, where $\overline{\rho}_{\rm b}$ is the mean background density and $R_{\rm 200b}$ is the halo boundary. Then, the characteristic density δ_c appeared in Equation 1.7 can be given by

$$\delta_c = \frac{200}{3} \frac{c^3_{\rm 200b}}{\ln(1 + c_{\rm 200b}) - c_{\rm 200b}/(1 + c_{\rm 200b})}\,, \tag{1.8}$$

where the concentration parameter $c_{\rm 200b}$ is equal to the ratio $R_{\rm 200b}/R_{\rm s}$.

The power-law slope of the dark matter distribution on scales of a few kpc to a few tens of kpc can provide clues to the nature of dark matter (Flores & Primack 1994; Moore 1994; Weinberg et al. 2013). In particular, models with significant warm dark matter (*e.g.*, Macciò et al. 2012) or large self-interaction cross-sections (Spergel & Steinhardt 2000; Peter et al. 2013; Zavala et al. 2013) can result in a shallower density distribution in the core. Indeed, observations indicate such a shallower slope (*e.g.*, Tyson et al. 1998; de Blok et al. 2001). However, baryonic physics also can significantly alter the distribution of dark matter on small scales, either by feedback (Navarro et al. 1996a; Mashchenko et al. 2006; Zolotov et al. 2012; Arraki et al. 2014) or simply by gravitational effects (adiabatic contraction: Blumenthal et al. 1986; Gnedin et al. 2004; Sellwood & McGaugh 2005).

On radial scales below about one effective radius, the total mass profiles of galaxies transition from a dark matter dominated regime to a star-dominated regime. In addition, gas may represent a significant contribution in low mass galaxies. Disentangling the dark matter component from the stellar component on these scales

is challenging. There are significant systematic uncertainties in the determination of galaxy stellar masses from the integrated light coming out of stars. Variations in the IMF and the low mass cut-off for star formation result in a factor of two uncertainty in stellar mass estimates (e.g., Barnabè et al. 2013; Courteau et al. 2014). Moreover, the IMF may vary with galaxy type and cosmic time (van Dokkum 2008; Conroy et al. 2009; van Dokkum & Conroy 2010; Dutton et al. 2011; Conroy & van Dokkum 2012; Smith et al. 2012).

In Kobayashi et al. (2015), we analyze the data from the COSMOS program, which has imaged the largest contiguous area (1.64 degrees^2) with the *Hubble Space Telescope (HST)* using the *Advanced Camera for Surveys (ACS) Wide Field Channel (WFC)* (Scoville et al. 2007). Our analysis predicts future weak lensing experiments (*Euclid* and *WFIRST*) could detect weak lensing signal down to a few tens of kpc with high signal-to-noise ratio. Combined with stellar kinematics obtained in spectroscopic surveys, such small-scale weak lensing surveys would become a powerful tool to both probe the innermost density profile of dark matter halos at redshifts up to 0.94, and measure the stellar mass of central galaxies in those halos.

1.3.2 Cosmic Star Formation History

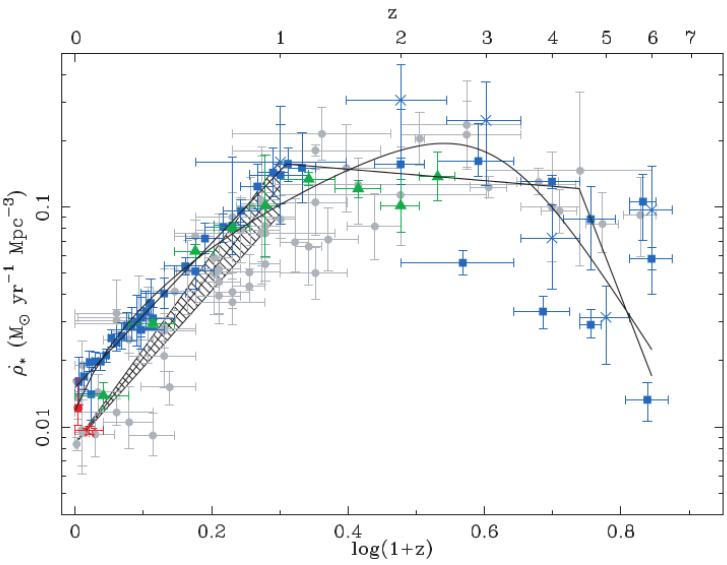

Figure 1.2: The time evolution of star formation rate density with redshift based on a compilation of multiple observations from radio, submillimeter, far infrared, optical, to ultra-violet lights. Here, average means averaged values per Mpc^3. This result indicates that overall star formation activity reached its maximum at redshift $z = 2 - 3$. This figure is taken from (Hopkins & Beacom 2006).

Star formation activity in galaxies is often evaluated by star formation rate,

which is defined as the stellar mass production rate in galaxies in the unit of $M_\odot$ per year. There are multiple indicators to derive the star formation rate from luminosity; ultra-violet photons from short-life massive stars (*e.g.*, OB stars), optical recombined photons (Hα line) reflects ionized regions around stars, far infrared represents dust that surround star-forming regions, X-ray emission occurs due to mass flow from a massive star to a companion compact object in high mass X-ray binary systems, and non-thermal radio emission from supernova remnants.

Recent deep observations reaching high-redshifts suggest that typical star formation activity is not constant with time but evolves over the history of the Universe. Figure 1.2 shows a compilation of observations in different wavelengths, indicating that the cosmic star formation rate density has its maximum at redshift $z = 2 - 3$. Therefore, main star-forming process may shift from one to another at this epoch, which could be attributed to galaxy merger rates, metallicity evolution, magnetic field enhancement *etc.*. Theoretical studies, such as our study in this thesis, are determined to identify the reason of this shift based on interstellar micro physics. This type of deep observations, too, is expected to proceed even further in the era of Thirty Meeter Telescope[5] and The Large Synoptic Survey Telescope[6].

1.3.3 Star Formation Main Sequence

One the one hand, the star formation rate represents current star formation activity. On the other hand, stellar mass embedded in galaxies reflects the star formation history that each galaxy has experienced, because the majority of stars contributing to stellar mass are expected to be low-mass long-lived stars.

Recent observations suggest that star-forming galaxies exhibit a tight correlation between these two properties. This is called star formation main sequence and Fig. 1.3 shows an example of such correlation, with only 0.3 dex root mean square scatter. This tightness indicates that current star formation activities are strongly regulated by integrated star formation history in the past. Ongoing observations at different redshifts indicate that this relation shifts to higher star formation rate up to $z \leq 2.6$, which leads to discussions whether galaxies have two star-forming modes (normal vs. star-burst) (*e.g.*, Daddi et al. 2007; Elbaz et al. 2007; Noeske et al. 2007; Zahid et al. 2012; Kashino et al. 2013; Rodighiero et al. 2014).

In addition to this average property, this relation is also compared between in field area and in galaxy cluster environment. Koyama et al. (2013) report that the difference is always small. Also Koyama et al. (2014) conduct detailed analysis in a galaxy cluster environment. Their results of star formation main sequence with the lack of low-mass blue galaxies indicate that the star formation activity is quickly quenched once they enter galaxy cluster environment, which is accompanied by an intense starburst in some short duration. Koyama et al. (2017) conduct radio observations towards star-forming galaxies that reside on star formation main sequence, and report that the molecular gas mass budget in those galaxies is simply

[5] http://www.tmt.org
[6] https://www.lsst.org

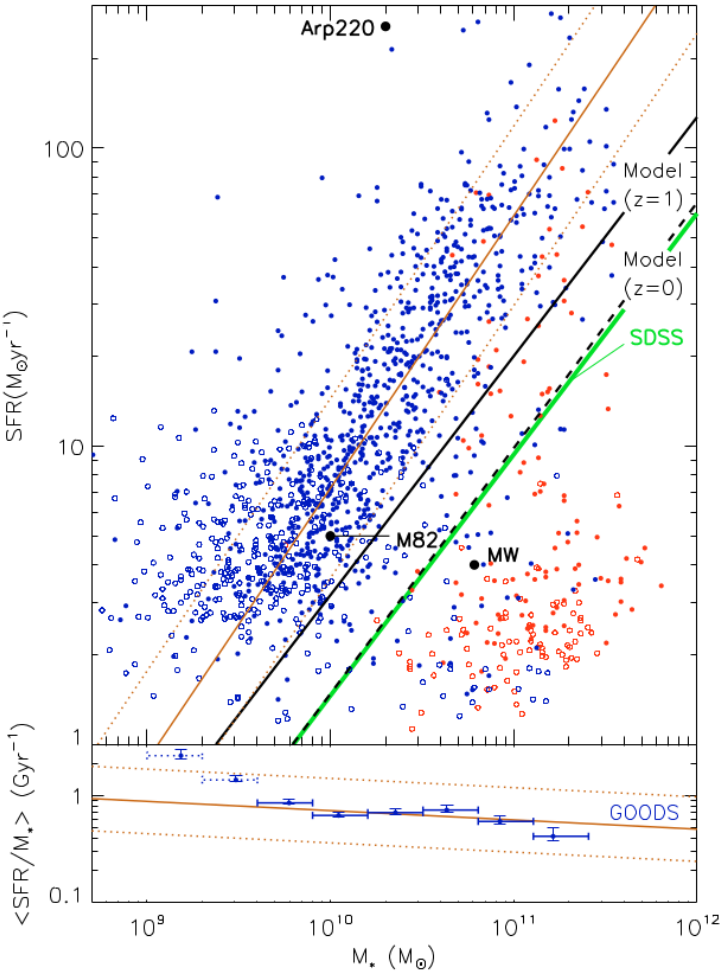

Figure 1.3: The relation between stellar mass and star formation rate. Upper panel: star formation main sequence. Filled circles represent galaxies whose star formation rate is estimated by a combination of ultra-violet and infrared observations, whereas open circles show galaxies whose star formation rate is estimated by ultra-violet observations alone. Colors correspond to galaxy colors. Blue galaxies from The Great Observatories Origins Deep Survey (GOODS) follow a mean relation of star formation rate $= 7.2 \times (M_*/10^{10}\mathrm{M}_\odot)^{0.9}$, where M_* is the stellar mass. This indicates that current star formation rate reflect past star formation history in each galaxy. Lower panel: The correlation between specific star formation, which is star formation rate divided by stellar mass, and stellar mass. This figure is taken from (Elbaz et al. 2007).

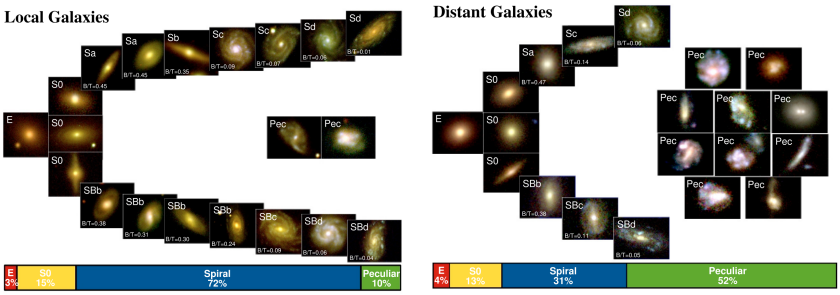

Figure 1.4: Comparison of Hubble diagram in the local Universe (left panel) and at redshift $z = 0.65$, which corresponds to 6 Giga year ago (righ panel). "E" denotes elliptical galaxies "S0" denotes lenticular galaxies, and others are spirals. The split of spiral galaxies are based on barred (SB) or non-barred structures. Local galaxies are selected from Sloan Digital Sky Survey and galaxies at $z = 0.65$ are chosen from GOODS(ACS) v2.0 images. The trend from the right to the left indicate that shape are more disordered in the past and spiral structures have been developed over the last 6 Giga year. This figure is taken from Delgado-Serrano et al. (2010).

proportional to two-thirds of star formation rate. This power-law proportionality looks very similar to Kennicutt-Schmidt's law we introduce in the next section. These results suggest the importance of galaxy evolution calculation consistently with interstellar medium evolution and subsequent star formation on parsec to sub-parsec scales, which we aim at as our future studies. This thesis is also meant as the first step for this purpose.

1.3.4 Morphologies

Galaxies have a large variety of morphologies and their diversities evolve with redshift. They are (empirically) classified into several sequences, one of which is Hubble "tuning fork" sequence presented in Hubble (1926). In the original scheme of Hubble (1926) based on optical images, the majority of galaxies are classified into spirals and ellipticals. As the name indicates, spiral galaxies have large spirals extended from central regions to outskirts seen as accumulation of stars and gas. Elliptical galaxies have less structured compared with spirals and have ellipse shapes. The rest 3 per cent of galaxies fall into irregulars. Spiral galaxies tend to be actively star-forming whereas most elliptical galaxies already exhausted their gas so that they do not form stars. Figure 1.7 shows an example of morphology diagram based on optical surveys. Much deeper surveys than shown in Figure 1.7 indicate that galaxies initially had less-ordered structures at redshift $z \gtrsim 2$ (*e.g.*, clumpy disks (Elmegreen et al. 2007; Förster Schreiber et al. 2009)) and developed their morphologies down to today (see Murata et al. (2014); *c.f.*, Genzel et al. 2008; *c.f.*environmental effects (Dressler 1980)).

Spiral arm is not ubiquitous but still very common features observed in 70 per

cent of nearby galaxies. With its importance of angular momentum transfer (not only in galactic disks but disks in general in the Universe), the origin of galactic spiral arms is continuously and intensively debated. Lin & Shu (1964) propose a model called Density Wave Theory, where spiral structures are created due to gravitational instability of disks. Spiral arms appear as a pattern of high-density regions and long-lived with a fixed global pattern speed. The background rotating gravitational field leads to gas accumulation in deep potentials and subsequent star formation there so that gas and stellar spiral structures could have some offsets. Several observations try to measure such in nearby galaxies (*e.g.*, Egusa et al. 2009, 2017), but this is still under debate and no definitive consensus has been obtained yet.

Gerola & Seiden (1978) introduce a model called Stochastic Self-Propagating Star Formation (SSPSF) model, where spiral arms consist of stars and gas, which look similar to trajectories of dropped ink on a differentially rotating disk. Based on this model, Seiden et al. (1979) explain the difference between spiral and elliptical galaxies based on competitions between the initial star formation rate and collapse rate of gas into a disk form, and Seiden & Gerola (1979) discuss that SSPSF model is likely to explain the observational features (*e.g.*, rotation curves and so on).

Also, pure gravitational effects are extensively investigated albeit their equations could have mathematically very complicated structures. For example, (Michikoshi & Kokubo 2016a,b) formulate swing amplification due to phase synchronization of stellar epicycle motion, and report that swing amplification successfully reproduce pitch angles in N-body simulations and that the number of spiral arms increase with the shear rate. Such spiral arms are transients because they become tightly wounded in time and keep their generations and disruptions, which is also observed often in galaxy simulations (*e.g.*, Baba et al. 2017) (see Pettitt et al. (2017) for tidally-driven spiral arms due to close encounter of satellite galaxies). However, observed prevalence of spiral arms in nearby galaxies, especially beautiful $m = 2$ mode, indicates that spiral structure is long-lived (*e.g.*, more than 10 rotations). We reserve this issue for our future investigations, but we may give further plausible explanation why star formation in spiral arms keeps ongoing and is sustain such long duration, by performing galactic scale simulations with our semi-analytical evolution model for molecular cloud and stars presented in this thesis.

1.4 Stars and Interstellar Medium in the Milky Way and Nearby Galaxies

Until the previous section, star formation in galaxies is assumed to take place in somewhat high density regions. In this and following sections, we review previous studies highlighting how the initial conditions for star formation are set.

1.4.1 Multiphase Interstellar Medium

The Interstellar Medium (ISM) is the medium filling the space between stars in galaxies, which is one of the main components of galaxies as well as stars and dark matter. The ISM mostly consists of hydrogen with some Helium and heavy elements. One of the cores in the ISM studies is how the ISM initiates star formation and how stars interact with surrounding ISM both in accelerating and preventing subsequent next generation of star formation.

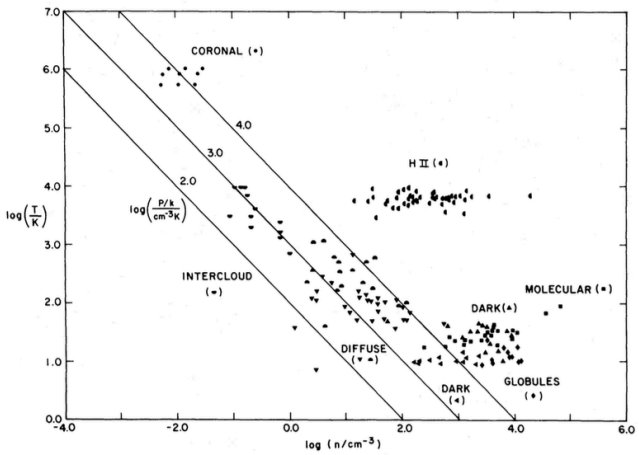

Figure 1.5: Phase diagram with observed properties of the multiphase ISM. The diagonal straight lines denote constant pressures. This indicates that WNM and CNM are in pressure equilibrium. This figure is taken from Myers (1978).

The ISM shapes its multiphase structures due to various heating and atomic/molecular line cooling processes. They are mostly classified as the following nomenclature (followed with hydrogen number density and temperature within each structure, respectively): i) Coronal gas of 10^{-2} cm^{-3} and 10^{6} Kelvin, ii) HII regions of 10^{1-3} cm^{-3} and 10^{4} Kelvin, iii) Warm Neutral Medium (WNM, or intercloud medium) of 10^{-2-0} cm^{-3} and 10^{3-4} Kelvin, iv) Cold Neutral Medium (CNM, or HI clouds) of 10^{0-2} cm^{-3} and 10^{1-3} Kelvin, and v) molecular clouds of $> 10^{2}$ cm^{-3} and 10 Kelvin. Figure 1.5 shows a compilation of observed properties of each phase. Coronal gas mostly consists of fully ionized hydrogen bright in X-rays, which is probably created by supernovae feedback. HII regions are partially ionized regions created by Ultra Violet lights from massive stars. WNM is warm phase of atomic hydrogen gas, which occupies most of the volume of galactic disks. CNM is cold phase of atomic hydrogen gas, which has a cloud-like structure. Molecular clouds are huge reservoir of hydrogen molecules out of which stars are born. Describing phase transition from WNM to CNM, and to molecular clouds is central of ISM and star formation studies. We will review phase transition theories in subsection 1.4.4.

1.4.2 Molecular Line Observations and Molecular Clouds

Molecular clouds are large and massive agglomeration of hydrogen molecules. In particular, giant molecular clouds (GMCs) are believed to the parental structure of hydrogen molecules (H_2) forming stars, which have a typical mass $\gtrsim 10^4 M_\odot$ and $\gtrsim 10$ parsec (*e.g.*, Williams et al. 2000; Kennicutt & Evans 2012). Therefore, it is necessary for understanding coevolution of the ISM and stars to identify the locations of GMCs in galaxies and establish a framework describing GMC formation, evolution, and dispersal on galactic scales.

Hydrogen molecule does not have any dipole moment and thus their emission is restricted to quadrapole or higher transitions[7]. Surveys of GMCs thus require other probes. Usually this probe is the second-abundant species in GMCs, which is monoxide carbon (CO) molecules. From 1970s, radio surveys started to map CO line emissions from the ISM, firstly from Orion Nebula (Wilson et al. 1970). Several groups have been conducting CO line surveys to date that covers a wide range of galactic disks from galactic centers to warps (*e.g.*, Burton et al. 1975; Scoville & Solomon 1975; Dame et al. 1987; Kawamura et al. 1998; Fukui et al. 1999; Dame et al. 2001; Fukui et al. 2001; Mizuno & Fukui 2004; Takeuchi et al. 2010; see Section 2.1.4 for the details.) Until now, over 1000 GMCs are identified in the Milky Way galaxy. Observations reveal that molecular clouds associated with CO line emissions are widely distributed in the Milky Way galactic thin disk, some of which are located even 100 parsec away elevated from the equatorial plane.

The relative fraction between different species and different rovibrational transition lines may vary within galaxies. Indeed, combined with HI observations, it is reveled that H_2-to-HI hydrogen fraction varies as a function of along galactocentric radii (Nakanishi & Sofue 2016). The molecular gas fraction increases towards the galactic center. On the other hand, ^{12}CO(2-1)/^{12}CO(1-0) ratio is found to be relatively constant across the disk of Galaxy M51(Koda 2013).

1.4.3 Magnetic Fields

Magnetic fields prevail across space and time. The first detection of magnetic fields was reported as polarized light of stellar emission (Hall 1949; Hiltner 1949). Since then, magnetic fields are observed in several methods: polarization, Chandra-Sekhar Fermi method, and quasar absorption lines (Beck 2001, 2007; Bernet et al. 2008; Fletcher et al. 2011; Jansson & Farrar 2012, *e.g.*,). The typical magnetic field strength of the ISM in disk regions is estimated about a few micro Gauss[8].

Observationally, it is probable that the energy density of magnetic fields is in equipartition with that of turbulence and cosmic rays (*e.g.*, Beck 2004, 2015) (and also that of radiation field and gas thermal energy as well if a scatter with one order

[7] WNM and CNM can be probed with hydrogen 21cm line, which is emitted by the spin-flip transition in atomic hydrogen whose corresponding photon wavelength and frequency are 20 mc and 1420 MHz, respectively.

[8] See Parker (1966) for a linear stability analysis of magnetic buoyancy in magnetized galactic disks and Mouschovias (1974) for final states of magnetically stratified disk structures.

of magnitude is allowed). We review previous studies to indicate that magnetic fields play an important role both for GMC formation and also molecular filament formation in Sections 2.2.2 and 1.5.3, respectively.

1.4.4 Phase Transition: Cloud Formation through Thermal Instability

As introduced in Subsection 1.4.1, the interstellar medium (ISM) constructs thermally bistable phases of atomic hydrogen due to the balance between radiative cooling and photoelectric heating (partially cosmic ray heating as well) (Field et al. 1969; Wolfire et al. 1995, 2003). One of the two phases is WNM and the other phase is CNM, which is a precursor of molecular clouds. The phase transition from WNM to CNM and molecular clouds is thus the key to understand star formation within galaxies.

Thermal Instability

Figure 1.6 from Inoue & Inutsuka (2012) summarizes the cooling and heating rates based on various processes and the resultant equilibrium in density-pressure diagram. The dominant heating process in the present-day ISM is photoelectric heating, which is driven by high-energy electrons ejected from dust particles (*e.g.*, Polycyclic Aromatic Hydrocarbon). Such ejection occurs when dust particles are exposed under Ultraviolet radiation from massive stars. The cooling can be operated by various processes. Most important coolants are Lyα photons, Oxygen atoms (OI), and singly-ionized carbon (CII).

One can obtain thermally equilibrium states by equating heating and cooling processes. The solid line in Figure 1.6 represents such equilibrium state in the present-day ISM. The left growing part corresponds to the WNM regime and the right growing part corresponds to CNM and molecular cloud regimes. At a given thermal pressure (typically $p/k_{\rm B} \simeq 4000$ in the ISM (Jenkins & Tripp 2011)), there is an intermediate regime in-between, which is thermally unstable characterized as the negative gradient of pressure with respect to volume number density. Any infinite small perturbation in pressure can grow either to WNM or CNM. If a fluid element obtains small negative pressure perturbation, it transfers to the heating-dominated regime so that it keeps being heated up until it reaches to the WNM equilibrium state, and vice versa for positive pressure perturbation.

Note that the temperatures of 10^4 Kelvin due to Lyα is not specific characteristic in the present-day ISM but universal (independent from metallicity), because this interaction between hydrogen and photons is simply determined by electroweak interaction, which presumably does not vary in the Universe.

The transition layer between WNM and CNM has a stability varying in different dimensions. At earlier stage of thermal instability studies, Yakov Borisovich Zel'dovich[9] and S.B. Pikelner (Zel'Dovich & Pikel'Ner 1969) investigate the one-

[9]His another famous pioneering study is the formalization of the Sunyaev-Zel'dovich effect on

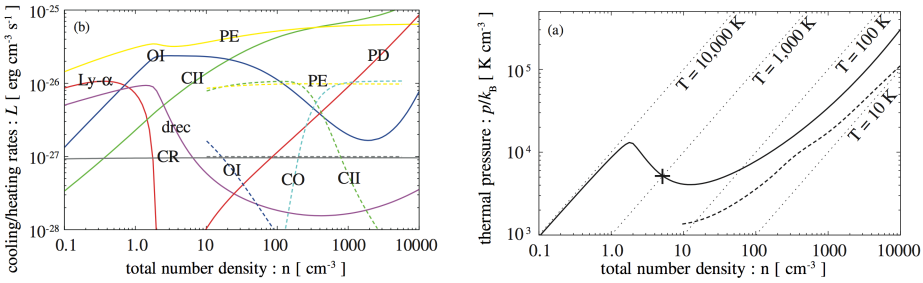

Figure 1.6: Heating and cooling rates and resultant bistable medium in the ISM. Left: the heating and cooling rates in the ISM as a function of volume density of the medium with an optically thin case (visual extinction $A_{\rm V} = 0$) in solid lines and an non-thin case (visual extinction $A_{\rm V} = 1$) in dashed lines. The dominant heating process is always photoelectric heating ("PE"). The cooling is operated by Lyman alpha photons ("Lyα") for diffuse and hot regime (*i.e.*, WNM of < 1 cm^{-3} and $\sim 10^4$ Kelvin, by Oxygen atoms ("OI") for intermediate regime ($1 - 10$ cm^{-3} and $100 - 10^4$ Kelvin), and by singly-ionized carbon ("CII") for dense regime (*i.e.*, CNM to molecular clouds of $\gtrsim 10$ cm^{-3} and $\lesssim 100$ Kelvin. In case with $A_{\rm V} = 1$, which is more realistic within molecular clouds, CO rovibrational lines become important coolant as shown by dotted lines. Note that horizontal gray line represents the heating rate by cosmic rays ("CR"). Cosmic rays is thus important for ionization but sub-dominant for heating. Right: Thermal pressure (divided by Boltzmann constant) as a function of volume density of the medium. The thick black solid line corresponds to the equilibrium state where heating and cooling balances out. The thin dotted guidelines represent the constant temperature with 10^4, 10^3, 10^2, and 10^1 Kelvin, respectively. The regime above the equilibrium line is cooling-dominated regime and the regime below is heating-dominated regime. The equilibrium denoted by a cross icon is in a thermally unstable state so that any pressure perturbation at this point grows toward either WNM or CNM. The dotted line corresponds to the $A_{\rm V} = 1$ case. This figure is taken from Inoue & Inutsuka (2012).

dimensional configuration given cosmic ray heating, radiation cooling, and thermal conduction, and propose that there is a static solution where both phases have an equal pressure $P_{\rm sat}$, named "Saturation Pressure". They estimate the translational motion of the transition layer between two phases whose initial pressure is different from $P_{\rm sat}$. They conclude that this motion is negligible compared with CNM clump size thus the configuration of bistable medium is determined by initial conditions. This motion can be fast if self-gravity of CNM clumps is included, and the motion terminates when all the CNM clumps coalesce where a static solution is achieved. However, in multidimensional cases, the transition layer is not static (Elphick et al. 1991) and has a complex structure due to its dependence on curvature (Nagashima et al. 2005, 2006, condensation and evaporation rates differ between different curvature). In reality (in three dimensional configuration space), individual CNM clumps can keep moving to achieve $P_{\rm sat}$ unless they evaporate. This develops turbulence in two phase medium whose velocity dispersion is subsonic from WNM point of view and supersonic from CNM point of view (see Subsection 2.2.2). This is one promising mechanism to sustain super-sonic turbulence in molecular clouds to the level that observations find in most of the clouds (see Subsection 1.4.5).

To override such equilibrium to form CNM out of WNM, WNM needs to be dynamically compressed and to become dense enough into the thermally unstable regime (*i.e.*, the cooling-dominated regime). This dynamically-driven phase transition is investigated by many simulations, which we cover in Section 2.2.2. In general, the thermally unstable condition can be described by Balbus condition:

$$\left[\frac{\partial}{\partial T}\left(\frac{\mathcal{L}}{T}\right)\right]_p < 0\,, \tag{1.9}$$

where $\mathcal{L}$ is the net heating and cooling rate per mass (Balbus (1995); see also Field (1965); Schwarz et al. (1972)).

Scales

We here introduce scales that are related to thermal instability.

The typical cooling timescale can be evaluated as

$$\tau_{\rm cool} = \frac{k_{\rm B}T}{n\Lambda} \tag{1.10}$$

where n is the volume number density of atomic hydrogen, $k_{\rm B}$ is the Boltzmann constant, and Λ is the cooling rate per volume. $\tau_{\rm cool}$ is about 10^{13} seconds for WNM and 10^{10} seconds for CNM. Therefore, in case of WNM colliding flow that we present in Chapter 7 for example, 1 Myr is a typical timescale required to develop thermally bistable medium.

There are three relevant spatial scales: Field Length, cooling length, and most unstable scale for thermal instability (see the linear stability analysis by Field

Cosmic Microwave Background (Zeldovich & Sunyaev 1969; Sunyaev & Zeldovich 1970).

(1965); Balbus (1988)). The typical spatial scale beyond which instability can grow is called Field Length:

$$l_{\rm F} \simeq \sqrt{\frac{\kappa T}{\rho \mathcal{L}}}\,, \tag{1.11}$$

where κ is thermal conductivity (*e.g.*, Parker 1953). Fluctuations below this scale can be smeared out by thermal conduction thus the thermal instability cannot grow. The typical spatial scale beyond which sound waves cannot propagate within $\tau_{\rm cool}$ is called cooling length:

$$l_{\rm a} = C_{\rm s}\tau_{\rm cool}\,. \tag{1.12}$$

Here $C_{\rm s}$ represents sound speed. Beyond this scale, the growth of thermal instability is suppressed because sound wave can propagate the information of thermal instability only up to the scales of $l_{\rm a}$ within the time duration of $\tau_{\rm cool}$. The typical spatial scale that has the maximum growth rate can be evaluated as:

$$l_{\rm TI} \simeq \sqrt{l_{\rm F} l_{\rm a}}\,. \tag{1.13}$$

As also already described by now, Equation 1.13 indicates that the most unstable mode is on a scale where sound wave can propagate within the cooling time but thermal conduction cannot so that thermal instability grows. The growth rate of this most unstable mode can be estimated as $\tau_{\rm cool}^{-1}$ in unmagnetized case (Field 1965; Koyama & Inutsuka 2000).

The typical Field Length is $l_{\rm F} \simeq 1$ parsec for WNM and $\lesssim 0.1$ parsec for CNM. Therefore, dynamically driven thermal instability is expected to generate mixture of WNM, CNM and molecular clouds on the scale of sub-parsec. Indeed, recent observations (HI line, OH recombination line, multiple CO line emissions, CO absorption in quasar line-of-sight *etc.*) indicate possible signature of such turbulent multiphase medium embedded even deep inside molecular clouds (*e.g.*, Bihr et al. 2015; Tachihara et al. 2012, Koda et al. 2017 in prep.).

1.4.5 Scaling Relations

Larson's Law

Observations indicate that there is a supersonic velocity dispersion prevailing in most of the GMCs in the Milky Way (Larson 1981; Fuller & Myers 1992; Heyer & Brunt 2004; *c.f.*, Nguyen-Luong et al. 2016). For example, CO line observations suggest a characteristic relation, which is summarized as

$$\delta v \propto l^{0.5}\,, \tag{1.14}$$

where δv is the velocity dispersion within GMCs and l is the size of GMCs. This is called Larson's Law. The most naive interpretation is that GMCs have a relatively constant column density. If there is a universal constant column density Σ independent of GMC mass, and individual GMCs with mass m have their radii of

l, then the mass of GMCs and their internal velocity-dispersion m can be evaluated (albeit order estimation) as

$$m = \pi l^2 \Sigma\,, \quad \delta v^2 = G\frac{m}{l}\,. \tag{1.15}$$

Therefore, this gives Larson's Law. This constancy in the column density matches with our assumption in this thesis (see Section 3.1.1).

Schmidt's Conjecture and Kennicutt-Schmidt Law

Schmidt (1959) originally proposed that the star formation rate (SFR) is probably proportional to gas column density as:

$$\mathrm{SFR} \propto (\Sigma_{\mathrm{gas}})^n\ , \tag{1.16}$$

This is called Schmidt law and can be intuitively understood that the level of star formation activity should have some dependence on the amount of available gas for star formation. He concluded $n \sim 2$ by combining the number count of white dwarfs, the abundance of helium in interstellar medium, the observed distribution of hydrogen over our galactic plane, and so on. Subsequent research implies $n \sim 1.4$ using SFR column density instead of just SFR, such as Kennicutt (1998):

$$\frac{\Sigma_{\mathrm{SFR}}}{\mathrm{M}_\odot/\mathrm{yr}^{-1}/\mathrm{kpc}^{-2}} = 2.5\times10^{-4}\left(\frac{\Sigma_{\mathrm{gas}}}{\mathrm{M}_\odot/\mathrm{pc}^{-2}}\right)^{1.4}\,. \tag{1.17}$$

This is called Kennicutt-Schmidt Law.

On the one hand, if it is $n = 1$, this likely suggests that individual star formation takes place in separate area of the ISM so that star formation is purely determined by the amount of the ISM. On the other hand, if it is $n = 2$, this likely suggests that gas cloud interaction (such as cloud-cloud collision) is important for triggering star formation. The observed values between $n = 1$ and 2 suggest that both individual isolated star formation and collision-induced star formation equally contribute to galactic star formation (see also Gao & Solomon 2004; Wu et al. 2005; Bigiel et al. 2008, 2011; *c.f.*, see also Roychowdhury et al. (2015) for the realtion in HI-dominated galaxies). Number of follow-up studies extensively investigate this relation and reveal following details in this relation.

First, this relation depends on the probe that are employed to evaluate gas mass. The original relation in Kennicutt (1998) is based on the sum of HI and H_2. In a series of studies (Lada et al. 2010, 2012), Charles Lada and his colleagues report that SFR is linearly correlated with gas mass if dense gas alone is employed. Here, dense gas is probed by HCN molecular-line emission (for the number density of 3×10^4 cm^{-3}). They also report that this linearity can be extrapolated and consistently connected to luminous and ultra-luminous infrared galaxies (LIRGs and ULIRGs) (see also Usero et al. (2015); Nguyen-Luong et al. (2016)). Gas depletion timescale can be derived by dividing the gas column density by SFR column density. Original

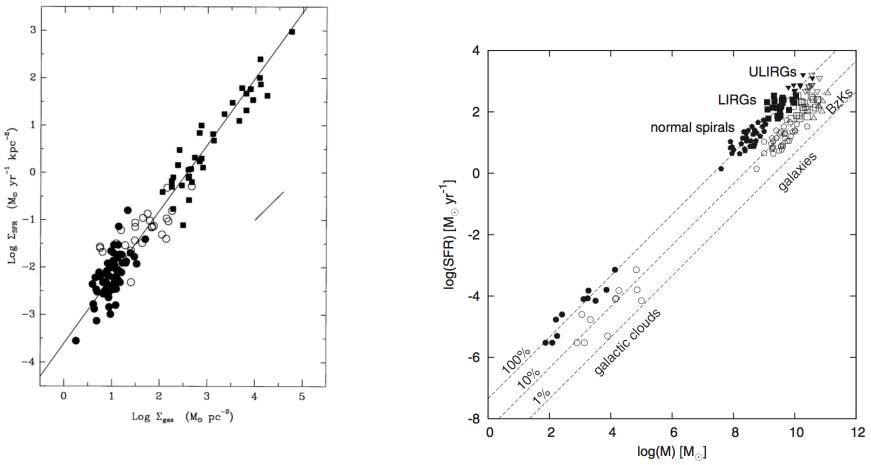

Figure 1.7: Observed Kennicutt-Schmidt Relations. Left: The relation produced by composition of normal disk galaxies (filled circle) and starburst galaxies (filled squares). The vertical axis shows the column density of star formation rate and the horizontal axis shows the column density of gas. Central regions of normal disk galaxies are also shown as open circles. The least-square fit shows as black solid line has a power of 1.4 as introduced in Equation 1.17. Right: The relation obtained from HCN molecular-line observations and CO molecular-line observations. The filled circles represent the samples based either on HCN line or extinction, and open circles correspond to samples based either on CO line or extinction. External galaxies on the top right corner are samples from Gao & Solomon (2004). Note that Lada et al. (2012) multiple a factor of 2.7 to SFR for external galaxy samples from Gao & Solomon (2004) to match with galactic clouds shown on the bottom left. The left panel is taken from Kennicutt (1998) and the right panel is taken from Lada et al. (2012).

value was 1 Gyr (*e.g.*, Kennicutt 1998), but can be down to 20 Myr if the dense gas mass is used (*e.g.*, Lada et al. 2010). Combined with the linearity, this timescale indicates that individual GMCs may disperse on a timescale about 20 Myr once star formation starts within them, but the typical timescale to completely consume all amount of gas turned into stars is about 1 Gyr averaged over the entire galactic disks. This can be explained by the timescale for individual GMC dispersal and star formation efficiency (see Section 3.1.2).

Recently, studies on local molecular clouds in our galaxy have reported that there is no such correlation *between* GMCs but does exist *within* GMCs given a certain extinction threshold (Lada et al. 2013; Evans et al. 2014). Observations towards nearby galaxies indicate this breakdown arises at scale of $\sim$ 300 pc(Komugi et al. 2005; Onodera et al. 2010). This breakdown is likely originated in the effects of two scales: timescale and physical scale. Once stars are born in GMCs, they

can leave their birthplace and migrate in the ISM. The typical azimuthal rotation speed of stars on the Milky Way galactic disk is about 200 km s^{-1}. Thus, in a significant case, stars can have a separation of 200 parsec from their parental GMC 1 Myr after their birth. Therefore, the observed breakdown in the Kennicutt-Schmidt relation can be attributed to this timescale. Alternatively, this can be due to spatial scales. Observations covering large area can sample GMCs at different stages so that they obtain mean relation. However, observations covering small area contain only specific stage of GMCs thus introduce large scatters in the Kennicutt-Schmidt relation. Conceptually speaking, such a sampling effect can be analogous to uncertainty principle in quantum physics (Kruijssen & Longmore 2014).

1.5 Star Formation

Stars form at densest parts of GMCs, which are called molecular cloud cores. In this section, we review recent progress both in theoretical and observational studies on structures hosting those cores and the properties of those cores.

1.5.1 Gravitational Collapse of Magnetized Clouds

To initiate star formation, GMCs have to gravitationally collapse (globally and/or locally). One can perform stability analysis of GMCs threaded by magnetic fields to estimate a critical mass of GMCs beyond which GMCs can collapse.

Let us consider a spherical cloud with mass M and radius R, then the total gravitational energy due to self-gravity $\mathcal{W}$ and the total magnetic field energy of this cloud can be written as:

$$\mathcal{W} = -\alpha \frac{GM^2}{R}\,, \quad \int_V \frac{|\mathbf{B}|^2}{8\pi} \mathrm{d}^3x + \oint \mathbf{x} \cdot \overleftrightarrow{T} \cdot \mathrm{d}A = \beta \frac{\Phi^2}{R}\,. \tag{1.18}$$

Here, "total" means total value integrated over the entire cloud. $\mathbf{B}$ is the magnetic field strength, $\int_V$ is the volume integration over the entire cloud, $\overleftrightarrow{T}$ is the Maxwell stress tensor[10], and Φ is the magnetic flux. α and β are coefficients, which typically have $\alpha = 3/5$ for a complete sphere and $\beta = 1/(6\pi^2)$ if the surface terms of magnetic field energy is negligible. Based on the virial theorem with magnetic fields, virialized clouds can have the following external pressure:

$$P_{\mathrm{ext}} = \frac{1}{4\pi}\left(-\alpha\frac{GM^2}{R^4} + \beta\frac{\Phi^2}{R^4} + 3\frac{a^2M}{R^3}\right)\,, \tag{1.19}$$

where a is the effective sound speed of this cloud (Shu 1992). If we define the critical mass $M_{\Phi,\mathrm{crit}}$ as the mass scale at which self-gravity and magnetic energy balances out:

$$M_{\Phi,\mathrm{crit}} = \sqrt{\frac{\beta}{\alpha G}}\Phi\,, \tag{1.20}$$

[10] *i.e.*, $T_{ik} = (B_iB_k/4\pi) - (|\mathbf{B}|^2/8\pi)\delta_{ik}$

then the external pressure can be written as:

$$P_{\rm ext} = \frac{1}{4\pi}\left[\frac{\alpha G}{R^4}(M_{\Phi,\rm crit}^2 - M^2) + 3\frac{a^2 M}{R^3}\right] . \tag{1.21}$$

If $M < M_{\Phi,\rm crit}$ (magnetically sub-critical), then $P_{\rm ext} > 0$ with $\mathrm{d}P_{\rm ext}/\mathrm{d}R < 0$ thus the external pressure cannot lead to any indefinite gravitational collapse as long as magnetic fields are frozen in gas. On the other hand, if $M > M_{\Phi,\rm crit}$ (magnetically critical), then self-gravity can overcome magnetic field pressure so that either sufficient external pressure or insufficient internal thermal pressure can lead to indefinite gravitational collapse (*c.f.*, Mouschovias 1976). By assuming the typical scale of clouds $R \simeq 1$ pc and the typical magnetic field strength $B \simeq 10\,\mu G$, one can estimate $M_{\Phi,\rm crit}$ with $\alpha = 3/5$ and $\beta = 1/(6\pi^2)$ as:

$$\begin{aligned} M_{\Phi,\rm crit} &= \sqrt{\frac{1}{6\pi^2 G}}\pi R^2 |B| \\ &= \sqrt{\frac{1}{6\pi^2 \times 6.673 \times 10^{-8}}} \cdot \pi (3.086 \times 10^{18})^2 \cdot 10^{-5}[\mathrm{g}] \\ &\simeq 10^2\,\mathrm{M}_\odot\,. \end{aligned} \tag{1.22}$$

Note that R has a dependence on the magnetic field strength and the number density as $R \propto B/n$ at the critical mass scale, thus $M_{\Phi,\rm crit} \propto B^3/\rho^2$. Therefore, Equation 1.22 corresponds to the case of $n = 300$ particles cm^{-3} and the combination of B and n may alter the value of $M_{\Phi,\rm crit}$ by one to two orders of magnitude.

Under the frozen-in condition, magnetically sub-critical GMCs cannot collapse to form stars unless magnetic fields dissipate to reduce the magnetic flux Φ. Such dissipation may take place through the ambipolar diffusion (*e.g.*, Nakamura & Li 2008; Kudoh & Basu 2011). The typical timescale for ambipolar diffusion on GMC scales can be estimated as

$$\tau_{\rm AD} = \frac{R}{v_{\rm d}} \simeq \frac{R}{v_{\rm A}^2}\gamma C R\sqrt{\rho} = \frac{4\pi\rho^{3/2}\gamma C R^2}{|\mathbf{B}|^2}\,, \tag{1.23}$$

where $v_{\rm d}$ is the drift velocity (*i.e.*, the relative velocity between ionized particles and neutral particles), $v_{\rm A}$ is the Alfven speed, γ is the drag coefficient $\gamma = 3.5 \times 10^{13}$ cm^3 g^{-1} s^{-1} (Draine 1983), and C is the mass-density coefficient that converts the mass density between ionized and neutral particles in an ionization steady state $C = 3 \times 10^{-16}$ cm$^{-3/2}$ g$^{1/2}$. Same parameters used in Equation 1.22 give

$$\tau_{\rm AD} \sim 10\mathrm{Myr}\,, \tag{1.24}$$

where we assume that hydrogen (including their ions) compose 91 per cent of molecular clouds and helium (including their ions) compose the rest 9 per cent, and thus employ 1.27 as the mean molecular weight for estimating ρ. This $\tau_{\rm AD}$ is comparable with typical mass-doubling timescale due to supersonic shocks as we

introduce in Section 2.2.3. Therefore, GMCs do not always collapse globally on the entire cloud scale but still substructures (*e.g.*, filaments; Section 1.5.3) within GMCs can collapse to form stars.

In most cases, column densities and line-of-sight magnetic field strengths are observables instead of mass densities or total magnetic field strengths. Therefore, it is more convenient to investigate a relation between column densities and line-of-sight magnetic field strengths. Provided that the column density N and the line-of-sight magnetic flux density B can be given as $N = M/\pi R^2/m_{\rm n}$ and $B_{\rm los} = \Phi/\pi R^2$ respectively, Equation 1.20 can be rewritten as

$$N_{\Phi,\rm crit} = \sqrt{\frac{\beta}{\alpha G}} \frac{B_{\rm los}}{m_{\rm n}} \,, \tag{1.25}$$

where $m_{\rm n} = 1.27 m_{\rm p}$ and $m_{\rm p} = 1.673 \times 10^{-24}$ gram if we employ 1.27 for the mean molecular weight in molecular clouds. Same parameters used in Equation 1.22 give

$$N_{\Phi,\rm crit} = 1.8 \times 10^{21} \left(\frac{B_{\rm los}}{10\,\mu{\rm Gauss}} \right) \ {\rm cm}^{-2} \,. \tag{1.26}$$

Figure 1.8 shows the observed relation between the column density and magnetic filed strength from the inter-cloud ISM scales ($N < 10^{21}$ cm^{-2}) down to molecular cloud core scales ($N > 10^{23}$ cm^{-2}) (see also Li et al. (2013)).

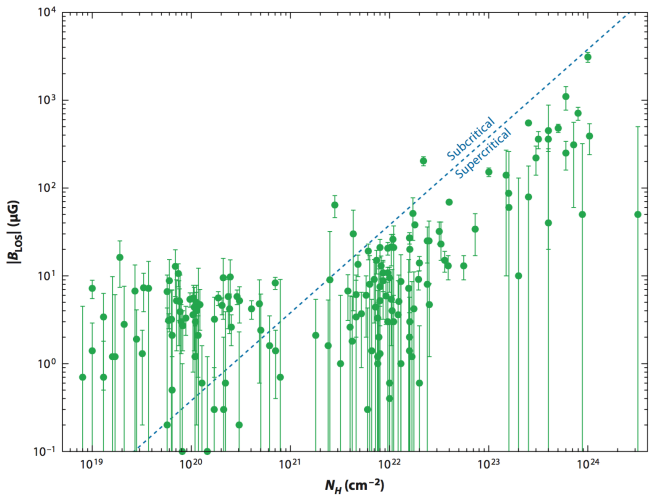

Figure 1.8: The relation between observed column density (horizontal axis) and line-of-sight magnetic field strength (vertical axis). The column density is the sum of HI and H_2 gas. The field strength is derived from HI, OH, and CN Zeeman measurements. The slanted dashed line corresponds to the critical line of $N_{\Phi,\rm crit} = 2.6 \times 10^{21}\,(B_{\rm los}/10\,\mu{\rm Gauss})\ {\rm cm}^{-2}$. This figure is taken from Crutcher (2012).

1.5.2 Initial Mass Function of Stars

Stellar initial mass function (hereafter IMF) is a mass spectrum for a coeval set of stars. The functional form of IMF reflects the star formation process and also alters the total stellar mass in individual galaxies. IMF $\phi(m)$ is defined as a relative frequency that a star of mass between m and $m+\delta m$ are born in a single population of stars and is described by:

$$\int_{m_{\rm min}}^{m_{\rm max}} m\phi(m){\rm d}m = 1{\rm M}_\odot\,. \tag{1.27}$$

Here, $m_{\rm min}$ and $m_{\rm max}$ represent minimum and maximum mass limits for stars respectively. Based on observations of stars in the Solar neighborhood, Salpeter (1955) suggests a power-law form of IMF as:

$$\phi(m){\rm d}m = m^{-2.35}{\rm d}m\,, \tag{1.28}$$

for the mass range of 0.3–14 $\rm M_\odot$. The functional form slightly differs between following theoretical investigations at the low-mass end (*e.g.*, Scalo 1986; Kroupa 2001; Chabrier 2003). Nevertheless, the IMF clearly suggests that low mass stars outnumber massive stars. Combined with the fact that low mass stars have longer life-time than massive stars, the IMF indicates that, in practice, the total stellar mass in galaxies are dominated by low mass stars. It is still under debate whether or not the IMF is universal (Bastian et al. 2010).

1.5.3 Filament Paradigm

Herschel satellite[11] is a space observatory that covers star formation in the Milky Way galaxy to galaxy evolution (Pilbratt et al. 2010). The Gould Belt Survey is one of its key projects (André & Saraceno 2005), which is a far-infrared and submillimeter photometric mapping survey of nearby molecular clouds by SPIRE (Griffin et al. 2010) and PACS (Poglitsch et al. 2010). They report that GMCs (ubiquitously) host filamentary structures within GMCs and prestellar cores preferentially reside in filamentary structures whose line mass is equal to or over the critical line mass of $17{\rm M}_\odot$ per parsec. Here, the critical line mass is the mass scale beyond which self-gravity overrides thermal pressure of filaments so that filaments can collapse indefinitely. The critical line mass can be evaluated as:

$$M_{\rm line,crit} = \frac{2c_{\rm s}^2}{G} \simeq 17{\rm M}_\odot{\rm pc}^{-1}\,, \tag{1.29}$$

where $c_{\rm s}$ is the sound speed of filaments and G is the gravitational constant. This value of $17{\rm M}_\odot$ per parsec is likely universal if GMCs' temperature is set by CO rovibrational lines ($\sim$ 10 Kelvin), whose corresponding sound speed is a few km

[11] *Herschel* Space Observatory (`http://www.cosmos.esa.int/web/herschel/home`), which is launched together with *Planck* satellite.

s^{-1} accordingly. The statement of prestellar core distribution is also clearly seen by comparison between Aquila cloud, where star formation is active, and Polaris cloud, where star formation is quiet so that there is almost no prestellar cores. Formation of such filamentary structures is investigated in various contexts (*e.g.*, Inoue & Fukui 2013) and is still an open question. In this thesis, we interpret that they are (end) products due to multiple supersonic compressions of magnetized WNM.

There are number of studies reporting interesting feature of the filamentary structures: for example, universal width of filaments, possible multiple sub-structures in individual filaments, and similarity between core mass functions and stellar initial mass functions.

Arzoumanian et al. (2011) report that filaments in IC 5146 have an almost constant width of 0.1 parsec. The critical line mass with this filament width of 0.1 parsec reproduces the observed peak of column density probability distribution, which is at visual extinction $A_{\rm V} \simeq 8$, or the column density of $\simeq 130 {\rm M}_{\odot}$ per parsec. This is similar to the value of critical column density threshold that previous studies propose for initiating star formation (*e.g.*, Lada et al. 2010; Heiderman et al. 2010). Therefore, filament structures with their universal width of 1 parsec may play an important role as a main star formation process, albeit observations of filament structures are still limited to less massive GMCs of $\sim 10^4 {\rm M}_{\odot}$. This universality of the filament width is intensively investigated both in theories and observations (see Shimajiri et al. (2017)).

Herschel team also reports that the mass function of cores in Gould Belt clouds resembles the stellar IMF (eg, André et al. 2010; Könyves et al. 2010; André et al. 2011; Roy et al. 2015). Here, the stellar IMF is the probability distribution of coeval set of stars and its differential form has a power-law distribution $\propto m^{-2.35}$, which is deduced from star populations in solar neighborhood (Salpeter 1955; see Section 1.5.2)[12]. The mapping from observed core mass functions to the stellar IMF is given by a factor of 0.3. This indicates that molecular cloud cores statistically end up with star formation efficiency of 30 per cent. The origin of core mass function is also intensively discussed, especially reproducing the power-law distribution of observed core mass functions. (Inutsuka 2001) propose that such power-law slope can be obtained by applying Press-Schechter formalism to 1-dimensional self-gravitational fragmentation. Here, they assume that an initial power spectrum is $P(k) \propto k^{-1.5}$ for the density perturbations of filaments, which seems in a good agreement with recently observed spectrum ($P(k) \propto k^{-1.6}$ (Roy et al. 2015)).

However, core formation and subsequent star formation may be altered if other supersonic shocks arrive. The typical timescale of shock arrival intervals can be about 1 Myr in the ISM of the Milky Way galaxy for example (McKee & Ostriker 1977). Therefore, although current studies on filaments focus more on filament formation and its connection to cores and protostars, future studies (both observations

[12]This universality is widely debated but the power-law slope is essentially the same between different formulations of the IMF (see Subsection 1.5.2)

and theories) also have to answer filament destruction due to repeated supersonic shock events (see Kirsanova et al. (2017) for some observational indications).

These progresses definitely indicate the importance of filamentary structures on star formation. It is further required to establish theoretical framework that connects filament paradigm to galactic star formation, especially if filaments prevail in all the star forming GMCs in the reality. This probably keeps being investigated and revealed by ongoing and future observations.

1.5.4 Multiplicity and Acceleration in Star Clusters

The formation of star clusters, especially along with cloud evolutions on galactic scales and subsequent galaxy evolution, is one of open questions (*c.f.*, Reina-Campos & Kruijssen 2017). There are previous studies based on Hertzsprung-Russel Diagram analysis (Rosenberg 1910; Russell 1914) suggesting a possible multiplicity of star formation epochs even in individual star clusters, both the ones in the Milky Way and in external galaxies (Magellanic Clouds) (*e.g.*, D'Antona et al. 1997; Beccari et al. 2017; D'Antona et al. 2017). Also some previous studies indicate that all the star clusters have accelerated its star formation activity to date (*e.g.*, Palla & Stahler 2000). Of course, it could have contamination from stars that happen to be on the line-of-sight and not-associated with concerned star clusters, or non-uniform distribution of gas within star clusters (Carretta et al. 2010).

These interpretations indicate that star formation is ongoing over long duration even in a single GMC. We aim at explaining such long-lasting star formation activity by the present thesis combined with future simulations we plan to perform. *Gaia* Satellite[13] is promising to proceed these studies further.

1.6 Aim and Structure of This Thesis

1.6.1 Aim of This Thesis

As introduced by now, GMCs are on the intermediate scale that connects galaxies and stars. Therefore, GMCs are essential to study star formation and subsequent galaxy evolution. In particular, GMC properties can play a pivotal role in governing star formation and eventually the evolution of galaxies; GMC distribution, density, mass function, *etc.* differ between galactic environment (*e.g.* bulge/arm/inter-arm regions, galactic star formation rates, galaxy morphologies, redshifts, *etc.*; see Colombo et al. 2014a; Utomo et al. 2015; Tosaki et al. 2016; *c.f.*Tacconi et al. 2010 for giant molecular clumps at a higher redshift). Thus, complete understanding of galaxy evolution requires a proper model of the GMC formation and subsequent star formation in different galactic environment. To investigate the life cycle of GMCs (*e.g.*, their formation process, lifetime, star formation within GMCs, *etc.*),

[13] http://sci.esa.int/gaia/

various physics need to be understood (*e.g.* self gravity, magnetic fields, cosmic rays, and so on).

Provided that star formation within GMCs is actively investigated (such as for the filament paradigm mentioned in Section 1.5.3), the GMC mass function (GMCMF) becomes the key to understand the star formation on galactic scales. This is because diversity of star formation rate across galactic disks may simply originate in the diversity of GMC populations on galactic scales if the star formation efficiency in individual GMCs is universal, as in the local star forming clouds (*c.f.*, Izumi et al. in prep). The GMCMF is actively studied in the solar neighborhood (*e.g.*, Yonekura et al. 1997; Williams & McKee 1997; Kramer et al. 1998; also see the review by Heyer & Dame 2015). On the other hand, such statistical study was difficult to conduct in external galaxies because of two reasons: the difficulties to identify individual GMCs in distant galaxies, and the enormous exposure time required to detect weak molecular line emissions from low mass GMCs $\lesssim 10^6 \mathrm{M}_\odot$.

Recently, however, large radio observations with exquisite resolution started to map the whole disks of nearby galaxies in detail and to shed lights on GMC's statistical properties on galactic scales (*e.g.* Engargiola et al. 2003; Rosolowsky et al. 2003, 2007; Koda et al. 2009, 2011, 2012; Schinnerer et al. 2013; Colombo et al. 2014a,b). In particular, the Plateau de Bure Interferometer(PdBI) Arcsecond Whirlpool Survey (PAWS) program (Schinnerer et al. 2013) demonstrates that the GMCMF varies on galactic scales. See Section 2.1 for the details and also see other observations (*e.g.*, in the Galaxy (Rice et al. 2016) and in M33 (Rosolowsky et al. 2003, 2007; Braine et al. 2018); *c.f.*the outer Galaxy (Heyer et al. 2001), LMC(Fukui et al. 2001), and M83 (Hirota et al. in prep.)). Presumably, this type of statistical GMC studies will proceed further down to both smaller mass scales $\lesssim 10^4 \mathrm{M}_\odot$ and smaller spatial scales thanks to ongoing latest observations (*e.g.*, in Atacama Large Millimeter/Submillimeter Array (ALMA); *c.f.*, Tosaki et al. 2016).

Meanwhile, recent radio observations have found increasing number of star cluster forming sites likely triggered by cloud-cloud collisions (CCCs; *e.g.*, Torii et al. 2011; Nakamura et al. 2012; Fukui et al. 2014; Torii et al. 2015; Fukui et al. 2016; Torii et al. 2017b,a; Nishimura et al. 2017a,b; Fukui et al. 2017a,b,c,d; Sano et al. 2017a; Ohama et al. 2017a,b; Kohno et al. 2017; Hayashi et al. 2017; Saigo et al. 2017; Tsutsumi et al. 2017; see also Furukawa et al. 2009; Ohama et al. 2010; Dobashi et al. 2014; Nakamura et al. 2014; Fukui et al. 2015b; Tsuboi et al. 2015; Dewangan et al. 2016; Dewangan 2017; Ohama et al. 2017c; Sano et al. 2017b; Torii et al. 2017c). This interpretation indicates the possible importance of CCC-driven star formation across the Milky Way galaxy from the solar circle to the Galactic Center (*c.f.*, Tan 2000).

On the theoretical side, supersonic shock compression is one of the key processes that forms molecular clouds as introduced in Section 1.4.4. This dynamically-driven phase transition is extensively investigated by multiphase ISM simulations in a context of shock wave propagation in WNM (*e.g.*, Walder & Folini 1998b,a; Koyama & Inutsuka 2002; Audit & Hennebelle 2005, 2008; Heitsch et al. 2005, 2006; Vázquez-Semadeni et al. 2006; Hennebelle & Audit 2007; Hennebelle et al.

2007). Due to the prevention by magnetic fields, successful molecular cloud formation is limited statistically only once in a few 10 times shocks (*c.f.*, Inoue & Inutsuka 2008; Inutsuka et al. 2015; see Section 2.2.2 for the details). This suggests that multiple episodes of supersonic WNM compression is essential for successful molecular cloud formation. Such phase transition dynamics appear on scales of sub-parsec scales (and even less than 0.1 parsec if individual molecular cloud core formation is also considered), thus it is still computationally expansive to perform detail simulations to directly connect individual cloud formation and subsequent star formation consistently along with galaxy evolution.

Cutting-edge simulations have been making a great progress in this connection by evaluating the effects of supernova feedbacks, photo dissociation and ionization feedback from massive stars, magnetic fields, galactic shear, *etc.*for star formation and galactic disk structures (Kim & Ostriker 2015a; Walch et al. 2015; Girichidis et al. 2016; Gatto et al. 2017; Peters et al. 2017; Seifried et al. 2017; Kim & Ostriker 2017). However, these are basically local calculations on a few 100 parsec to a few kilo parsec scales but not the entire galactic disk. Therefore, it is neither simple nor straightforward to interpret and extrapolate the results onto the entire galactic disks. It still has to be coupled with some semi-analytical analysis to extend their results to discuss galactic disks (*e.g.*, magnetized galactic disk structure Kim & Ostriker 2015b). Galactic scale simulations (*e.g.*, Tasker & Tan 2009; Wada et al. 2011; Dobbs & Pringle 2013; Fujimoto et al. 2014; Dobbs et al. 2015; Baba et al. 2017; Pettitt et al. 2017, and so on) have advantage to discuss statistical properties of molecular clouds and their connection to galactic structures such as bulges, stellar bars, and spiral arms. However, these require some assumed criteria to form/identify GMCs and stars. For example, one-phase medium is often assumed to fill the volume smaller than the spatial resolution of simulations by selecting one medium from theoretical models (*e.g.*, McKee & Ostriker 1977). It is, therefore, demanded to bridge the knowledge of multiphase medium on sub-parsec scales to galactic scales by extracting essence from these local and global/galactic calculations.

To connect individual GMC formation governed by multiple episodes of compression with the evolution of GMC populations over galactic disks, Inutsuka et al. (2015) propose a bubble scenario where the network of expanding shells due to expanding supernovae and HII regions create repeated supersonic shock propagations. Based on this paradigm, they formulate a time evolution equation of GMCMF due to the multiple episodes of compression and GMC self-dispersal. However, this formulation neglected the change of cloud mass function by CCCs. From 1970s, GMC evolution due to CCCs alone is extensively investigated by coagulation equation (*e.g.*, Kwan 1979; Scoville & Hersh 1979; Cowie 1980) and N-body simulations (*e.g.*, Levinson & Roberts 1981; Kwan & Valdes 1983; Tomisaka 1984, 1986). However, they do not consider rapid massive star formation in CCC clouds. Hydrodynamics simulations (and recent studies of magnetohydrodynamics simulations) of colliding binary GMCs (Habe & Ohta 1992; Anathpindika 2010; Haworth et al. 2015a,b; Wu et al. 2015; Inoue et al. 2017) indicate such possibility of rapid

massive star formation in shock-compressed layer. However, these studies focus on individual isolating clouds with relatively short simulation time and thus it is still not concluded that what would be the resultant mass spectrum of generated stars. Overall, the detailed formation/dispersal of clouds, CCC, and CCC-driven star formation were studied separately so far in previous studies.

To provide a framework that connects individual clouds and star formation consistently with galaxy evolution, we in this thesis aim at formulating a time evolution equation that includes all the processes: the formation and mass-growth of GMCs due to multiple episodes of compression, dispersal due to massive stars, mass-growth due to CCC, and CCC-driven star formation and subsequent feedback onto GMCs. Formulating such time evolution equation enables us to evaluate the relative importance of these processes shaping GMCMFs, and enables observations to put constraints on these processes that single snapshot of observation neither track in time nor spatially resolve. Based on this formulation, we also aim at evaluating the lifecycle of gas in the multiphase ISM and also the relative importance of CCC onto galactic-scale star formation activity.

1.6.2 Structure of This Thesis

The rest part of this thesis is organized as follows. In Chapter 2, we give a brief review of the history of observational and theoretical studies on giant molecular clouds (GMCs). We also introduce previous studies on cloud-cloud collisions (CCCs), highlighting formalism to solve this collisional process. At its end, we review a recent theoretical paradigm that Inutsuka et al. (2015) propose for GMC formation, evolution, and dispersal on galactic scales, which we are extensively based on throughout this thesis. Chapters 3, 4, and 5 form the core of this thesis. In Chapter 3, we present our basic formulation of the time evolution equation for GMCMF that includes giant molecular cloud formation, evolution, dispersal, and coagulation due to cloud-cloud collisions. In Chapter 4, we introduce the concept of "gas resurrection", which is replenishment of minimum-mass GMCs out of total amount of dispersed gas. Then, we define "resurrecting factor" and evaluate how much gas resurrection is required in different regions on a galactic disk, followed with discussions of how observations can deduce this value. In Chapter 5, we introduce a new formulation that includes CCC-driven star formation and discuss its impact onto total star formation activity in individual galaxies. At its end, we also evaluate the observability that can examine such CCC-driven star formation process. In Chapter 6, we list and discuss possible improvements expected in our formulation. To extend our semi-analytical formulation to indeed galactic-scale theory, we perform hydrodynamics simulations to establish an effective equation of state of the multiphase ISM in Chapter 7. Finally we summarize our studies in Chapter 8, followed with Appendices.

The abbreviation of units in this thesis are g for gram, cm for centi-meter, km for kilo-meter, s for second, and K for Kelvin. All the "Log" appeared in the figure labels are logarithm in the base of 10. Throughout this thesis, we assume that

GMCs are molecular agglomeration bright in ^{12}CO(1-0) line to be compared with observations.

Chapter 2

GMC Introduction: observations and theories[1]

In this section, we add further detailed reviews of previous GMC studies, which are directly relevant to this thesis.

2.1 Observational History: Observed GMC Mass Functions

We here summarize previous radio surveys identifying GMC distributions in nearby galaxies and the Milky Way galaxy.

2.1.1 CARMA and Nobeyama Telescopes

Koda et al. (2009) conducted observations on the Whirlpool Galaxy M51, by using the Combined Array for Research in Millimeter Astronomy (CARMA) to obtain high-fidelity imaging, and using Nobeyama Radio Observatory 45 m telescope with the 25-Beam Array Receiver System (BEARS) to obtain total power and short-spacing data. The angular resolution reaches $4''$ corresponding to a physical scale of 160 pc. They report that this combined observations identify significant number of small GMCs in inter-arm regions for the first time. They interpret this significant detection that small GMCs survive while they are crossing inter-arm regions from arm to arm. This leads to a rough estimation that the lifetime of GMCs with mass greater than $4 \times 10^5 \mathrm{M}_\odot$ is comparable with interarm-crossing time of 100 Myr. This type of lifetime estimation based on GMC number counts is also conducted with latest data by different groups (*e.g.*, Meidt et al. (2015)). Other studies (*e.g.*, Koda et al. 2016) estimate the lifetime based on an assumption that mass fraction in the ISM is conserved if conversion between HI and H_2 is steady.

[1] *The contents of this chapter are partially based upon the articles Kobayashi et al. (2017b) and Kobayashi et al. (2017a).*

This also leads to a very long lifetime for GMCs $\gtrsim$ 100 Myr. The lifetime of GMCs, too, has to be discussed being coupled with GMC evolution on galactic scales. See Subsection 5.3.2 for more detail discussion on GMC lifetime.

In the analysis by Koda et al. (2009), the identified GMCs amount to about 64 per cent of the total CO emission intensity. They thus expected that there are a large number of small GMCs in inter-arm regions that had have not been detected yet at its spatial resolution and sensitivity. Indeed, later observations resolve and identify such small GMC populations such as PAWS program, which is described in the following section.

2.1.2 PAWS Program

The Plateau de Bure Interferometer(PdBI) Arcsecond Whirlpool Survey (PAWS) program (PI: Eva Schinnerer) is one of the IRAM Large Programs[2], which was conducted by using PdBI and IRAM 30 m telescope and observed the inner disk of Galaxy M51(Schinnerer et al. 2013). This observation is in ^{12}CO(1-0) line over 200 hours integration (210 hours). Galaxy M51 is one of the close ($\sim$7.6 Mpc from the Earth (Ciardullo et al. 2002)) and nearly face-on (inclination of 22° (Colombo et al. 2014b)) galaxies, thus the survey reveals the cold gas kinematics with a high spatial resolution of $\sim$ 40pc ($1\farcs16 \times 0\farcs97$). They detect objects whose mass are $\geq 1.2 \times 10^5 \mathrm{M}_\odot$ at 5σ level (Pety et al. 2013), which results in 1507 GMC detections. The PAWS team subdivides M51 into seven regions to analyze the GMC properties in various galactic environment; the central regions(the nuclear bar (NB) region, the molecular ring (MR)), arm regions (inner density-wave spiral arms (DWI), outer density-wave spiral arms (DWO), material arms (MAT)), and inter-arm regions (downstream (DNS) regions, and upstream (UPS) regions) (see Figure 2 in Colombo et al. 2014a).

Thanks to this huge statistics of over 1000 GMCs, one of the highlighted results is the observed variation in GMC mass functions (GMCMFs) (Colombo et al. 2014a). When fitted with a power-law profile $n_{\mathrm{cl}}(m) \propto m^{-\alpha}$, where $n_{\mathrm{cl}}(m)$ represents the differential number density of GMC with mass m, the cumulative number density of GMCs with mass greater than m, $n(>m)$, can be given as $n(>m) = \int_m^\infty n_{\mathrm{cl}}(m)\mathrm{d}m$. Instead of deriving the differential number density, they fit the observed number counts of GMCs by a power-law profile with a truncation at the massive-end where the cumulative number of GMCs is described as

$$n(>m) = N_0 \left[\left(\frac{m}{m_0} \right)^{-\alpha+1} - 1 \right] . \tag{2.1}$$

Here, N_0 is the cumulative number of GMCs normalized at mass m_0. -1 introduces a cut-off at the massive end of $m \sim 2^{1/(1-\alpha)} m_0$ at which GMCMFs deviate from a single power-law profile. They find that bar and arm regions typically have

[2] http://www.iram-institute.org/EN/content-page-240-7-158-240-0-0.html

shallower slopes (*e.g.*, $-\alpha = -1.33$ in the "nuclear" bar region and $-\alpha = -1.75$ in the "density-wave spiral arm" region) whereas inter-arm regions (and an arm region at M51 outskirts) typically have steeper slopes (*e.g.*, $-\alpha = -2.55$ in the "downstream" region). This result indicates that massive GMCs preferentially reside along galactic spiral arms whereas the mass budget in inter-arm regions is dominated by less massive GMCs ($m < 10^{5.5}\mathrm{M}_{\odot}$) (see also Chapter A).

Note that, the high spatial resolution and high sensitivity in PAWS project decompose massive GMCs $\sim 10^{8}\mathrm{M}_{\odot}$ previously identified in Koda et al. (2009) into smaller GMCs. The fitted slope in GMCMFs may alter further due to decompositions in upcoming future surveys and such possibility is left for future investigations.

2.1.3 Galaxy M33

Rosolowsky et al. (2007) observed the ^{12}CO(1-0) line emission from Galaxy M33 using the NRO 45m telescope combined with the data from the BIMA interferometer and the FCRAO 14m telescope. The arm/inter-arm comparison shows limited differences in the GMCMF slopes (-1.9 and -2.2 respectively) with difficulties in defining arms. However, the innermost 2.1 kpc has a prominent cutoff at the massive end ($\gtrsim 4.5 \times 10^{5}\,\mathrm{M}_{\odot}$) whereas the outer regions up to 4.1 kpc do not.

A similar survey is conducted by Braine et al. (2018) in ^{12}CO(2-1) line with IRAM 30 m telescope. The derived GMCMFs indicate a trend that the GMCMF slope becomes stepper with galactocentric radii (from -1.36 in < 2.2 kpc, -1.68 in $(2.2-3.7)$ kpc, to -1.87 in > 3.7 kpc). Such galactocentoric radial variation is beyond our current scope in this thesis but needs to be investigated in future.

2.1.4 Milky Way Survey

In the Milky Way galaxy, there are number of radio surveys conducted to reveal the distribution of CO bright molecular gas. However, the geometry where we are located within the Galactic disk hinders them from covering the entire Galactic disk to perform systematic surveys (*e.g.*, limited sky coverage, large uncertainty in distance measurements). Dame et al. (1987, 2001) report ^{12}CO(1-0) mapping survey through the entire Galactic disk using difraction-limited Cassegrain systems with 1.2 m diameter parabolic primaries and 17.8 cm hyperbolic secondaries. Meanwhile, the group lead by Fukui in Nagoya University (Japan) operated NANTEN observatory in Chile to conduct similar mapping survey, which is extended to Large Magellanic Cloud (*e.g.*, Fukui et al. 1999, 2001). Recently, Rice et al. (2016) have compiled the Galactic plane survey data obtained with 1.2 m twin telescopes (one in Cambridge, Massachusetts, and the other in Cerro Tololo, Chile). Based on the Dendorogram scheme, they generate a catalog of 1064 massive molecular clouds in the Milky Way galactic plane, whose mass are greater than $3 \times 10^{3}\mathrm{M}_{\odot}$. The identified clouds within the solar circle show mass profiles with a power-law slope of $-\alpha = -1.6$ and a mass truncation at $m_0 = 1.0 \times 10^{7}\mathrm{M}_{\odot}$ whereas the

clouds beyond the solar circle exhibit a slope of $-\alpha = -2.2$ and a truncation at $m_0 = 1.5 \times 10^6 \mathrm{M}_\odot$. Again we reserve such variation as a function of galactocentric radii for future studies, but it needs to taking into account the gas fraction variation as well (*i.e.*, H_2 gas usually dominate the hydrogen mass budget in inner part of galaxies, whereas HI gas dominate the mass budget at outskirts; *e.g.*, Nakanishi & Sofue (2016) in the Milky Way galaxy).

2.1.5 Summary of Observational History

Besides these observations that we list here, there are large surveys expected to operate near future especially by ALMA (see Section 8.2). It is therefore demanded to construct a theoretical framework to connect GMC-scale physics onto their distribution on galactic scales before the era of such large surveys with high sensitivity and high spatial resolution. In this thesis, we aim to reproduce observed variation of GMCMFs based on GMC-scale physics, especially the one observed in PAWS survey.

2.2 Theoretical History

In this subsection, we explore the history of theoretical studies. First, we summarize previous statistical studies of coagulation process, and following studies of GMC mass-growth due to GMC coagulation. Second, we review high-resolution ISM simulations that investigate the formation of individual molecular clouds. Finally, we introduce Inutsuka et al. (2015), which propose a paradigm connecting individual GMC formation to GMC formation and evolution on galactic scales.

2.2.1 Coagulation Equation

Statistical study of time evolution in particle group through coagulation process has already had its history more than 100 years. In 1916, Marian Smoluchowski introduced an equation that solves time evolution of particle numbers through binary collision and resultant coagulation:

$$\frac{\mathrm{d}n_k}{\mathrm{d}t} = \frac{1}{2}\sum_{i+j=k} n_i n_k A_{ij} - n_k \sum_{i=1}^{\infty} n_i A_{ik}\,. \tag{2.2}$$

This is called "coagulation equation" (Smoluchowski 1916) and is valid when the number of particles is large. This form is simple in a sense that this is perfect inelastic collision where collision does not generate any fragment and thus the mass of individual particles grow monotonically. In spite of such simplicity, it is known that the analytical solution of this equation exists only in three cases, in which the kernel function A_{ij} has special forms. To summarize this classification Trubnikov (1971) introduce a generalized form of A_{ij} as

$$A_{ij} = \alpha + \beta(i+k) + \gamma ik\,. \tag{2.3}$$

With this formulation, Trubnikov (1971) show that the conditions for three possible analytic solution correspond to 1) constant kernel with $\alpha \neq 0$ and $\beta = \gamma = 0$, 2) additive kernel with $\beta \neq 0$ and $\alpha = \gamma = 0$, and 3) multiplicative kernel with $\gamma \neq 0$ and $\alpha = \beta = 0$. In the additive kernel case, the particle number spectrum exhibits an asymptotic power-law profile of $k^{-3/2}$ (see Trubnikov (1971)), which is the most relevant to GMC studies as we present in Section 3.1. See also Smoluchowski (1916) for the constant kernel case and Safronov (1972) for the multiplicative kernel case. To date, this type of coagulation equation is extensively investigated in the context of dust grain-growth in protoplanetary disk (*e.g.*, Malyshkin & Goodman 2001; Kobayashi et al. 2016; *c.f.*, Wetherill & Stewart 1989; Kokubo & Ida 1996; Kobayashi & Tanaka 2010).

From 1960s, GMCMF evolution due to CCC is largely investigated by solving time evolution equations based on the coagulation equation (*e.g.*, Field & Saslaw 1965; Kwan 1979; Scoville & Hersh 1979; Cowie 1980) and N-body simulations (*e.g.*, Levinson & Roberts 1981; Kwan & Valdes 1983; Tomisaka 1984, 1986). For example of Kwan (1979), they solve the following equation:

$$\begin{aligned}\frac{\partial N(m)}{\partial t} = & - N(m) \sum_{m'=m_0}^{\infty} N(m')\sigma(m,m')v(m,m') \\ & + \frac{1}{2} \sum_{m'=m_0}^{m-m_0} N(m')N(m-m')\sigma(m',m-m')v(m',m-m') \\ & - \frac{N(m)}{\tau} H(m-m_1) + \left[\sum_{m'=m_1}^{\infty} N(m')m' \right] \frac{1}{\tau} \frac{\delta(m,m_0)}{m_0} \,. \end{aligned} \tag{2.4}$$

Here, $N(m)$ represents the number of GMCs with mass m, m_0 is minimum mass in the concerned GMC population, σ corresponds to the effective cross section between GMCs with mass m and m', v is the relative velocity between GMCs, τ is the typical lifetime of GMCs whose mass are greater than m_1, and H is the Heaviside step function:

$$H(m-m_1) = \begin{cases} 0 & (\text{for } m < m_1) \\ 1 & (\text{for } m \geq m_1) \,, \end{cases} \tag{2.5}$$

and δ is the Kronecker delta. Therefore, on the right hand side, the first two terms correspond to coagulation process of binary GMCs, whereas the third term represents self-dispersal of GMCs, and the last term is replenishment of the minimum-mass GMC population with an assumption that disruption of GMCs with mass $m \geq m_1$ somehow always generate fragments whose mass are m_0.

They report that the choice of m_0 does not impact the GMCMF evolution in the mass range of $m > 10m_0$. The GMCMFs exhibit a power-law spectrum, which is approximately fitted as $N(m)/m_0 \propto m^{-1.5}$. The power varies with the dependence of σ and v on GMC masses. This dependence can be evaluated in a

steady sate case as $\epsilon = -(a+b+3)/2$ given that $N(m) \propto m^{\epsilon}, \sigma \propto m^{a}$, and $v \propto m^{b}$ (see also Cowie (1980)). We give ample description to derive this dependence in Subsection 5.3.4. In addition, it is reported that this CCC-driven mass-growth process is relatively slow[3] so that Kwan (1979) expect GMC longevity where the estimated lifetime of GMCs become 2×100 Myr.

Note that, as one can see from the Kronecker delta in Equation 2.4, this type of summation formulation inevitably includes discretization of GMC populations in mass, which presumably appears only in numerical calculations but not in reality. In Subsection 3.1, we introduce an integral form of coagulation equation for CCCs. This enables us to perform mass and number flux analysis easier and thus provides a clear view on GMC mass dependence throughout the analysis of collision frequency, gas resurrection, *etc.*as we show from now.

2.2.2 Simulations on Phase Transition Dynamics

As introduced in Section 1.4, the ISM comprises multiphase structures and the successful phase transition from WNM to CNM and molecular gas is central of determining the initial condition for star formation on galactic scales. In this Subsubsection, we briefly review multiphase ISM simulations to emphasize that multiple episodes of WNM compression due to supersonic shocks is essential for overriding pressure equilibrium to trigger successful phase transition.

There are previous studies investigating CNM formation in colliding HI flow. This is analogous to single shock propagation but does not have to follow the shock front propagation because two flows confine the shock-compressed layer at the center of simulation boxes. Multiphase medium is developed within the shock-compressed layer, and the contact surface between this medium and WNM flows become shock fronts. Because the flows are kept injecting, the mass in the shock-compressed layer increase and the shock front propagates slowly outwards to the upstream of WNM flows in the lab frame[4]. Hennebelle & Pérault (1999) perform a simulation of one-dimensional WNM colliding flow in a plane-parallel geometry. They show that dynamically-driven phase transition is indeed effective to form CNM from WNM (*c.f.*, see Burkert & Lin 2000 for the dependence on the amplitude of the initial perturbation.) Audit & Hennebelle (2005) conduct a two-dimensional simulation with 1000^2 grids, which corresponds to 0.02 pc spatial resolution. They report that thermally unstable gas with its temperature of ~ 5000 K and its volume number density of ~ 5 particles per cubic centimeter form filamentary structures in shock-compressed layer (see also Heitsch et al. (2005); *c.f.*,

[3]This is partially because their choice of the relative velocity $v \propto m^{-0.5}$ underestimates the CCC rates for massive GMCs. From observations within the Milky Way galaxy (*e.g.*, Stark & Brand (1989); Stark & Lee (2005, 2006) as we introduce in Subsubsection 6.1.4, the cloud-to-cloud velocity dispersion is approximately independent of GMC masses.

[4]Instead of colliding HI flow, Walder & Folini (1998b,a) perform two-dimensional simulations of colliding hot gas flow (mostly ionized and having temperatures of 10^8 and 10^6 K) albeit without thermal conduction, and find that knots and filaments-like structures are developed within one cooling time, which may appear in supernova remnants.

CNM dynamical disruption in turbulent medium (Heitsch et al. 2006)). Hennebelle & Audit (2007) and Hennebelle et al. (2007) extend their studies to perform further high spatial resolution simulation up to 10000^2 grids (see also Audit & Hennebelle (2008); *c.f.*, Kritsuk & Norman (2002)). They find that the differential number density of formed CNM cloud mass spectrum follows $n_{\rm cl} \propto m^{-1.7}$, which is within the range of GMCMFs observed in ^{12}CO line in nearby galaxies (*e.g.*, PAWS survey) and also molecular clouds in the Milky Way galaxy. Their results also indicate that the mass-size relation among CNM clouds show $m \propto l^{1.7}$ similar to characteristics observed in molecular clouds. Thus dynamically-driven thermal instability seems a promising process to create CNM as a precursor of molecular clouds. Vázquez-Semadeni et al. (2006, 2007) also perform similar colliding HI flow simulations by employing smoothed particle hydrodynamics (SPH) method. Their results indicate that long-lasting continuous injection of HI flow delay global collapse of CNM in the shock-compressed layer. These colliding flow simulations indicate that, once WNM become dense enough, then the cooling operates effectively so that WNM can become denser isobarically to form CNM within only 1-2 Myr.

Other previous studies track the propagation of one shock front, which is a more general case than specific conditions such as colliding HI flow. Koyama & Inutsuka (2000) perform one-dimensional calculation with detail heating, cooling, and chemical processes where they test a shock wave propagation into WNM and CNM (see Subsecion C.2 for the details of heating and cooling). They report that the shock injection into WNM creates a thin and dense H_2 layer in the shock-compressed layer. Their linear perturbation analysis also suggests that this H_2 layer can fragment into smaller cloudlets. Koyama & Inutsuka (2002) conduct hydrodynamics simulations to track a strong shock propagation whose Mach number is ~ 3. They employ 2048×512 Cartesian grid points, which corresponds to a spatial resolution of 0.0007 pc (~ 140 A.U.). They indeed identify small molecular cloudlets formed in the shock-compressed layer. Their results also indicate that, compared with radiative shocks, thermal energy can be partially transported to the kinetic energy of cloudlets' translational motion. WNM keep pushing CNM in the ISM thus the relative velocity between cloudlets is subsonic for WNM but supersonic for cloudlets. This motion is driven solely by WNM pressure so that this motion does not decay as quickly as radiation do. Therefore, interstellar supersonic turbulence may originate in such phase transition.

After these hydrodynamics investigations, effects of magnetic fields started to be extensively investigated. Magnetic field pressure presumably opposes the shock compression thus could alter the above discussions of dynamically-driven CNM formation and subsequent molecular cloud formation. Inoue & Inutsuka (2008) conduct a two-dimensional two-fluid magnetohydrodynamics simulations where two-fluid means neutral and ionized gas. They inject two WNM flows colliding at the center of their simulation box. The initial converging velocity is 20 $\mathrm{km\,s^{-1}}$ and magnetic field strength is 2.0 micro Gauss[5]. Although the typical ionization frac-

[5] 20 $\mathrm{km\,s^{-1}}$ corresponds to the Mach number of 2.1 for unperturbed magnetized WNM and 2.4

tion is low $\sim 10^{-4}$ in WNM and even lower in molecular clouds $\sim 10^{-7}$ (due to cosmic rays), neutral gas "feel" (*i.e.*, is affected by) magnetic fields because of the collisional coupling with ionized gas. Therefore, isobaric rapid contraction is soon terminated once magnetic field pressure starts to sustain the ram pressure of colliding flow. Then gas starts isochoric cooling without density enhancement. When the gas reaches an equilibrium of heating and cooling, they finally degenerate into WNM or CNM. Thus dense molecular cloud cannot form only by a single supersonic shock[6]. In their calculations, ambiploar diffusion is automatically included by calculating two-fluid equations. However, in two or more dimensional cases, the most unstable mode of thermal instability grows along magnetic field lines thus ambiploar diffusion effect is anyway less important. The prevention of molecular cloud formation may depend on the angle between the magnetic field orientation and the direction of supersonic WNM flows; the completely transverse geometry studied in Inoue & Inutsuka (2008) is probably the most severe case where magnetic field pressure plays its maximum role against colliding flow. Indeed, through a series of simulations including three-dimensional calculations (Inoue & Inutsuka 2009, 2012), they demonstrate that the successful molecular gas formation requires the angle typically less than 15 degree (*i.e.*, 0.26 radian). Inoue & Inutsuka (2009) show that this critical angle has some dependence on the speed of converging flow as:

$$v > v_{\rm crit} = \frac{r-1}{r}\frac{B\cos\theta}{\sqrt{4\pi\rho_0}}\,. \tag{2.6}$$

Here, r is the density ratio between in front of and back of the shock front ($r = \rho_1/\rho_0$), B is the magnetic field strength, and θ is the angle between converging flows and mean magnetic fields in the pre-shock region. Even in one-dimensional simulations, similar angle $\sim$ 20 is reported (*e.g.*, Hennebelle & Pérault 2000) and is the most stringent when the kinetic and magnetic energies are comparable. Other magnetohydrodynamics simulations from different groups (*e.g.*, Heitsch et al. 2009; Körtgen & Banerjee 2015; Valdivia et al. 2016) obtain essentially same results and claim that such prevention of molecular gas formation occurs unless supersonic shock propagates along the magnetic fields (*c.f.*, magnetohydrodynamics simulation for super shells Ntormousi et al. 2017; *c.f.*, Arata et al. (2017) in the context of galaxy mergers).

The above discussions focus on individual molecular cloud formation on the scales of pc to sub-pc. From the viewpoint of such a limited volume in the ISM, supersonic HI flows originated from massive stars (OB stars) and supernova remnants can, in principle, come from any direction. Most of the shock arrivals is likely misaligned with local magnetic field directions. Therefore, it is expected that successful molecular cloud formation takes place when the most recent shock propagates along the magnetic filed lines with an angle less than 15 degree, which

for unperturbed unmagnetized WNM.

[6]During the shock compression, magnetic fields are enhanced. Inoue & Inutsuka (2008) report the enhanced field strength is up to 11.7 micro Gauss. Therefore, even with only a few micro Gauss initial magnetic fields, gas anyway cannot be compressed enough to directly form molecular clouds.

occurs in the ISM on average once out of a few 10 times misaligned shocks. This suggests that multiple episodes of supersonic WNM compression is essential for successful molecular cloud formation.

2.2.3 Expanding Bubble Paradigm

Based on interpretations from multiphase magnetohydrodynamics simulations introduced in the previous section, Inutsuka et al. (2015) propose a new scenario of GMC formation and evolution on galactic scales (hereafter, SI15 scenario), which is driven by the network of expanding shells. In SI15 scenario, the expanding *bubbles* correspond to expanding HII regions and the late phase of supernova remnants. While they expand, dense HI shell forms on the surface of expanding shells, and supersonic shocks propagate into the ISM. Molecular clouds are created in some limited volume of the ISM where the ISM already experienced multiple episodes of supersonic shocks (*i.e.*, swept up multiple times by different expanding shells) or where neighboring expanding shells are colliding with each other by chance.

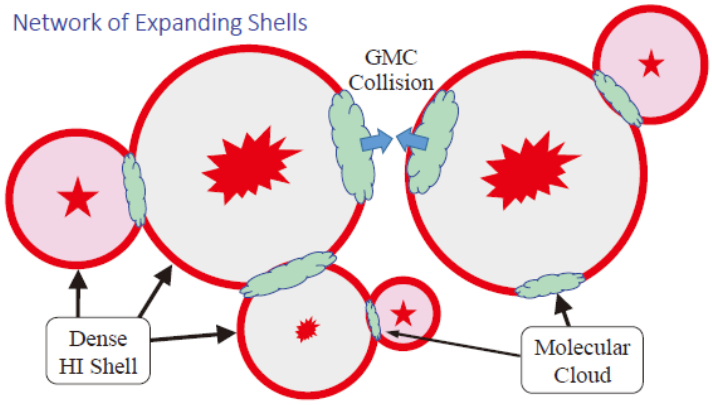

Figure 2.1: A schematic view of expanding bubble paradigm proposed in Inutsuka et al. (2015). The red flashing icons represent massive stars or supernovae and the surrounding red thick circles correspond to expanding HII regions and supernova remnants. While they are expanding, dense HI shells form on their surfaces. Molecular clouds are drawn as green clouds. Such successful molecular cloud formation takes place only in some limited volume of the ISM thus not all the 4π steradian of the shells are surrounded by molecular clouds. GMC collisions can be understood as a collision of clouds on neighboring shells. This figure is taken from Inutsuka et al. (2015).

Such repeating shock passages, especially due to supernovae, can be deduced even on Earth. ^{60}Fe is a radio isotope with its half-lifetime with about 2.6 Myr.

As well as ^{26}Al[7], ^{60}Fe is produced during supernovae thus informs us of recent history of supernova events nearby the Solar System (*i.e.*, looking back in time over a few Myr). Compared with other short-lived radionuclei whose half-lifetimes are less than 100 Myr, ^{60} is only produced efficiently by stellar nucleosynthesis and primordial ^{60}Fe already decayed since the formation of the Solar System. Thus ^{60}Fe is the most suitable radionuclide to examine the ISM environments. The deposition of radio isotope ^{60}Fe in Ferro Manganese (FeMn) crusts and FeMn nodules in the Indian, Pacific, and Atlantic oceans indicate that there were at least two supernova events during the last 10 Myr within the vicinity ~ 100 pc of the Sun (*e.g.* Wallner et al. 2016; Breitschwerdt et al. 2016). Model calculations of ^{60}Fe propagation (*e.g.*, Gounelle et al. 2009) indicate that ^{60}Fe in the early solar system can be explained by ^{60}Fe inherited in parental molecular cloud of the solar system due to multiple supernova events in some previous episodes of star formation[8].

Note that supernova remnants can be bright (*e.g.*, in X-ray wavelengths) typically about 1 Myr. On the other hand, molecular cloud formation has a timescale with the order of a few 10 Myr as we introduce in the last paragraph of this chapter. Therefore, bubble paradigm does not necessarily claim that observations reveal many bright supernova remnants associated with dense HI shells everywhere in galactic disks. Nevertheless, observations indicate such possible molecular cloud formation and subsequent triggered star formation due to supersonic shock compressions (*e.g.*, Walborn & Parker 1992; Thompson et al. 2012; Battersby et al. 2014; Palmeirim et al. 2017; *c.f.*, correlation between HI shells and molecular clumps obserevd in CO lines (Ehlerová & Palouš 2016); semi-analytical estimation of HI hole size function (Oey & Clarke 1997), observed luminosity function of HII regions (Kennicutt et al. 1989); Nobeyama 45 m telescope Legacy Survey FUGIN in CO multiline (Umemoto et al. 2017), *c.f.*Oey & Smedley 1998; Oey et al. 2005; Dawson et al. 2011b,a, 2013).

Based on this bubble scenario, Inutsuka et al. (2015) formulate a continuity equation that gives the time evolution of the GMCMF. Their formulation is twofolds: GMC formation and self-growth due to multiple episodes of compression and GMC self-dispersal due to star formation within those GMCs. Their results suggest that the ratio of typical timescales for formation and dispersal processes determines the slope of the GMCMF (see Section 3.2.2 for the further explanation).

They estimate the formation timescale in the following manner. The successful molecular cloud formation is limited when a supersonic shock propagates in an angle less than 0.26 radian with respect to the magnetic field. Given that the supersonic shock arrives isotropically, the success rate is about $2 \times 0.26^2\pi/(4\pi) \sim 0.03$ per shock. Gas in the ISM typically experiences supersonic shocks due to supernovae every 1 Myr (*e.g.*, McKee & Ostriker 1977)[9]. Combined with the fact that

[7] ^{26}Al is another metal element observed in the ISM with its 0.71 Myr half-lifetime

[8] Note that chemical abundance pattern may be altered by acrretion of planets and ISM gas. Even in the vicinity of the Earth, neutral elements are observed, which are probably originated in the ISM and penetrate through the Heliosphere of the Sun (Möbius et al. 2009).

[9] Even a simple order-of-magnitude estimation can derive this 1 Myr. For example, given that

HII regions can also create such shocks, the expected time interval between consecutive shocks $T_{\rm exp}$ is somewhat smaller than 1 Myr. Overall, the typical timescale required to produce molecular clouds from WNM is given as $T_{\rm exp}/0.03 \sim 10$ Myr, which we opt to use our fiducial formation timescale in this thesis (see Section 3.1.1).

supernovae occur at least one per century per galaxy (Adams et al. 2013), and the typical expansion radius of individual supernovae is about 100 pc over 1 Myr, then the total volume that can be swept up by supernovae within 1 Myr is 10^6 pc^3 $\times 10$ Myr $/100$ yr $= 10^{10}$ pc^3. This is comparable with the volume of the Milky Way thin disk with its area of 100 kpc^2 and its depth of 100 pc. Therefore statistically, any volume of galactic thin disk experience supersonic shock originated in supernovae typically once per 1 Myr.

Chapter 3

Basic Time Evolution Equation for GMC Mass Functions[1]

In this chapter, we introduce our basic time evolution equation for GMC mass functions, which is a semi-analytical formulation coarse-graininig the formation, evolution, and dispersal processes of indivudial GMCs onto galacitc scales.

3.1 Basic Time Evolution Equation for GMC Mass Function

As defined in Section 2.1, we denote the cumulative number density of GMCs with mass greater than m as $n(>m)$ throughout this thesis, thus the cumulative number density of GMCs with mass greater than m is given as $n(>m) = \int_m^\infty n_{\rm cl}(m){\rm d}m$. Based on SI15 scenario described in Subsubsection 2.2.3, we now introduce our formulation including the CCC terms to compute the time evolution of the GMCMF. The evolution of differential number density of GMCs with mass m, $n_{\rm cl}$, is given as:

$$\begin{aligned}
&\frac{\partial n_{\rm cl}}{\partial t} + \frac{\partial}{\partial m}\left(n_{\rm cl}\left(\frac{{\rm d}m}{{\rm d}t}\right)_{\rm self}\right) \\
&\quad = -\frac{n_{\rm cl}}{T_{\rm d}} \\
&\qquad + \frac{1}{2}\int_0^\infty \int_0^\infty K(m_1, m_2) n_{{\rm cl},1} n_{{\rm cl},2} \\
&\qquad\qquad \times \delta(m - m_1 - m_2){\rm d}m_1{\rm d}m_2 \\
&\qquad - \int_0^\infty K(m, m_2) n_{\rm cl} n_{{\rm cl},2}{\rm d}m_2 \,,
\end{aligned} \tag{3.1}$$

where $({\rm d}m/{\rm d}t)_{\rm self}$ is the mass gain rate of GMCs due to their self-growth, $T_{\rm d}$ is the timescale of GMC self-dispersal, $n_{{\rm cl},1}$ and $n_{{\rm cl},2}$ are the differential number

[1] *The contents of this chapter are partially based upon the articles Kobayashi et al. (2017b) and Kobayashi et al. (2017a).*

densities of GMCs with mass m_1 and m_2 respectively, $K(m_1, m_2)$ is the kernel function on the collision between GMCs with m_1 and m_2, and δ is the Dirac delta function.

In the following subsections, we give ample description for each term in Equation (3.1). The first three terms are essentially the same formulation that Inutsuka et al. (2015) originally propose, but we clarify the difference from the original formulation. We also discuss the detailed variation from this fiducial formulation in Chapter 6. Hereafter, we opt to employ 100 pc as the disk scale height where GMCs populate, which is observed in the Milky Way galaxy (*e.g.*, Dame et al. 1987). The scale height observationally indicated has a variation by a factor two to three (*e.g.*, 35 pc (Stark & Lee 2005), half-luminosity height $\lesssim$ 60 pc (Bronfman et al. 2000)), thus CCC rate may increase by at most a factor two to three because a smaller thickness of the galactic disk means a larger number density of molecular clouds in the disk.

3.1.1 Self-Growth Term

The second term on the left hand side of Equation (3.1) represents the GMC self-growth (*i.e.*, mass-gain rate from the ambient ISM). This term is a flux term in the conservation law. The ordinary continuity equation in fluid mechanics is a simple example of an analogous conservation law, which considers the mass conservation in configuration space. On the other hand, we here consider GMC number conservation in GMC mass space because the number should be the conserved quantity unless GMCs experience an abrupt change (*e.g.*, dispersal or CCCs). This term, therefore, calculates the GMC number flux in GMC mass space, which corresponds to GMC mass-growth in configuration space.

We consider that $(\mathrm{d}m/\mathrm{d}t)_{\mathrm{self}}$, the GMC self-growth speed, is determined by the multiple HI cloud compression due to supersonic shocks, which depends on the shape of GMCs. Observations suggest that the GMC column density does not vary much between GMCs (*e.g.*, typically a few times $10^{22}\,\mathrm{cm}^{-2}$ (Onishi et al. 1999; Tachihara et al. 2000); See also Section 1.4.5 about the similar indication of constancy by Larson's Law). Therefore, we can assume that GMCs have rather pancake shape than perfect spherical structure, which suggests that the GMCs' surface area is roughly proportional to their mass. In addition, the amount of HI cloud accumulated onto pre-existing GMCs through the multiple episodes of compression is presumably proportional to the GMC's surface area. Altogether, $(\mathrm{d}m/\mathrm{d}t)_{\mathrm{self}}$ should be proportional to GMC mass divided by a typical self-growth timescale that is independent of mass:

$$\left(\frac{\mathrm{d}m}{\mathrm{d}t}\right)_{\mathrm{self}} = \frac{m}{T_{\mathrm{sg}}}\,. \tag{3.2}$$

where T_{sg} is a typical timescale for the GMC self-growth.

In SI15 scenario, GMCs are formed via multi-compressional processes, which also cause the self-growth of GMCs. Here, repeated supersonic shocks can initiate

phase transition due to the thermal instability on the surface of pre-existing GMCs, which is similar to the molecular cloud formation. Thus the created molecular gas can accrete onto such pre-existing GMCs by the shocks and aid their mass-growth. Therefore, in our calculation, we adopt that $T_{\rm sg}$ is comparable to the typical GMC formation timescale, $T_{\rm f}$, which is estimated as a few 10 Myrs as discussed in Section 2.2.3 (*c.f.* Inoue & Inutsuka 2012; Inutsuka et al. 2015). The resultant $({\rm d}m/{\rm d}t)_{\rm self}$ becomes:

$$\left(\frac{{\rm d}m}{{\rm d}t}\right)_{\rm self} = \frac{m}{T_{\rm f}}\,. \tag{3.3}$$

Indeed, as introduced in Section 1.5, star-forming filaments observed nearby the Solar System may be formed through multiple episodes of supersonic shock compressions, which can also trigger the mass-growth of the parental GMCs as we suggest in this section.

Equation (3.3) with a constant $T_{\rm f} = 10$ Myr indicates that GMCs grow exponentially in mass. Given the minimum mass for GMCs ($m_{\rm min}$) are $\sim 10^4{\rm M}_\odot$, GMCs require at least 100 Myr for the exponential growth up to $10^{6.5}{\rm M}_\odot$ (see also Section 6.2). With additional 14 Myr required for destroying GMCs due to star formation (see Section 3.1.2), we expect that observed massive GMCs $\sim 10^{6.5}{\rm M}_\odot$ typically have their ages $\gtrsim$ 114 Myr. 114 Myr is almost comparable or larger than a typical timescale for the half galactic rotation $\sim$ 100 Myr. Therefore, this 114 Myr indicates that massive GMCs $\sim 10^{6.5}{\rm M}_\odot$ in inter-arm regions are not directly formed "in-situ" in inter-arm environment; they may be remnants that were originally born in arm environment and survived the destructing processes (*e.g.*, by stellar feedback and galactic shear). Modeling such transition from arm environment into inter-arm environment has to be investigated further to study the observed spur features extended from spiral arms (*e.g.*, Corder et al. 2008; Schinnerer et al. 2017) and flocculent spiral arms (*e.g.*, in Galaxy M33). However, we leave this for future studies and only present our plans in Chapter 7. Therefore in this thesis, we focus on the GMCMF variation purely due to the environmental differences. Note that 114 Myr is the "age" of large GMCs $\sim 10^{6.5}{\rm M}_\odot$ but not the typical GMC "lifetime"(see Sections 3.1.2 and 5.3.2).

We should note here that Inutsuka et al. (2015) originally assume that $T_{\rm f}$ is constant and independent of GMC mass. However, as seen in the previous paragraph, constant $T_{\rm f}$, in principle, produces infinitely massive GMCs as a consequence of the exponential growth. This indicates that constant $T_{\rm f}$ over-estimates the growth rate of very massive GMC whose mass is comparable to the mass of a shell swept up by an expanding bubble. Once the GMC mass is comparable to or larger than the typical mass of a swept-up shell, the growth in mass should saturates, because the dense gas that can be used to form a cloud is limited by the amount of total mass in the expanding shell. Therefore, our bubble paradigm is less likely to create large GMCs beyond that mass. Indeed, observations have revealed that GMCs exist only up to $\sim 10^8{\rm M}_\odot$ (*e.g.*, Rosolowsky et al. 2007; Colombo et al. 2014a). As long as we are based on SI15 scenario, we need to implement such saturation. For

modeling this, we modify $T_{\rm f}$ by applying a growing factor with a truncation mass $m_{\rm trunc}$ as:

$$T_{\rm f}(m) = T_{\rm f,fid}\left(1+\frac{m}{m_{\rm trunc}}\right)^{\gamma}. \tag{3.4}$$

Here the subscript fid stands for the fiducial constant value (*i.e.*, $T_{\rm f,fid} = 10$ Myr) and the exponent γ determines the gas-deficient efficiency. The Taylor series expansion of Equation (3.4) gives $T_{\rm f}(m) \simeq T_{\rm f,fid}(1+\gamma m/m_{\rm trunc})$. Therefore, when GMCs grow up to $m_{\rm crit} \sim m_{\rm trunc}/\gamma$, $T_{\rm f}$ deviates longer than $T_{\rm f,fid}$ so that the choice of $m_{\rm trunc}$ and γ modify the massive end of the GMCMF. Essentially, $m_{\rm crit}$ represents the typical maximum GMC mass that can be created in SI15 scenario. In this scenario, GMCs are created from interstellar medium swept up by supersonic shock compression, thus it is less likely to form GMCs more massive than the total mass that a single supernova remnant can sweep. The total mass initially contained within a sphere of 100 pc radius with HI density $10\,{\rm cm}^{-3}$ is about $7.7\times10^5{\rm M}_\odot$. Thus $m_{\rm crit} = 7.7\times10^5{\rm M}_\odot$ and this gives $m_{\rm trunc} = 7.7\times10^6{\rm M}_\odot$, given that we opt to use $\gamma = 10$ by assuming that this gas shortage becomes appreciable once the GMC mass exceeds 10 per cent of $m_{\rm trunc}$. Indeed, this truncation mass scale is comparable with observed values (*e.g.*, $m_0 = 1.5$–$10.0\times10^6{\rm M}_\odot$ in the Milky Way galaxy (Rice et al. 2016), $m_0 = 5.2$–$158.6\times10^6{\rm M}_\odot$ in Galaxy M51 (Colombo et al. 2014a)).

The detailed modeling of $m_{\rm trunc}$ and γ change the relative importance of GMC self-growth/dispersal and CCC. For example, one can consider that the initial medium can be more diffuse (*e.g.*, WNM with $1\,{\rm cm}^{-3}$) and also only a portion of the sphere rather than the entire sphere becomes a single GMC. However, these details would not largely impact if we focus on the GMCMF slope (see Section 3.2.1). Therefore, we will reserve the detailed investigation for future works.

Note that, in principle, $T_{\rm f}$ is the ensemble averaged timescale over different GMC mass-growth processes, for which we here consider the multiple episodes of supersonic compressions is the most important under the magnetic fields. The relative importance of different mass-growth processes depending on galactic environment needs to be further investigated in the future. Also note that the second term on the left hand side of Equation (3.1) has its boundary condition at $m = m_{\rm min} = 10^4{\rm M}_\odot$. The flux at this boundary in our formulation corresponds to the minimum-mass GMC production rate. In later sections, we will explain that this rate differs between setups (see the first paragraph in Section 3.2 and the second paragraph in Section 4.2).

3.1.2 Dispersal Term

The first term on the right hand side gives the GMC self-dispersal rate. Here, self-dispersal means that massive stars born within GMCs destroy their parental GMCs by any means (ionization, dissociation, heating, blowing-out, etc.). The

characteristic self-dispersal timescale, $T_{\rm d}$, is given as:

$$T_{\rm d} = T_* + T_{\rm dest}\ , \tag{3.5}$$

Here, T_* is the typical total duration since GMC birth until protostars evolve into main-sequence stars. $T_{\rm dest}$ is the typical timescale for the complete GMC destruction once stars become main-sequence stars. According to recent theories and observations within the Milky Way galaxy, the filamentary structure in densest parts of GMCs may host most of star formation in GMCs (*e.g.*, Inutsuka 2001; André et al. 2010, 2011; Roy et al. 2015), and such filaments too can form through multiple supersonic shocks (*c.f.*, Inoue & Inutsuka 2012; Inutsuka et al. 2015). Therefore, we assume that T_* would have a similar timescale as $T_{\rm f}$ so that we employ $T_* \sim 10$ Myr. $T_{\rm dest}$ can be estimated by line-radiation magnetohydrodynamics simulations. Inutsuka et al. (2015) reported one of such simulation results, which updated the work in Hosokawa & Inutsuka (2006a) by including magnetic fields. Their results indicate that, once a massive star with mass $> 30{\rm M}_\odot$ is formed in a GMC, the star destroys more than $10^5{\rm M}_\odot$ surrounding molecular hydrogen within 4 Myr. Therefore, typical $T_{\rm d}$ is $10 + 4 = 14$ Myr. This essentially measures the time-scale for CO dissociation over which GMCs are no longer identified in CO line observations. Thus this formulation implicitly allows the formation of CO-dark molecular gas (hereafter CO-dark gas) whose population is left to be studied in the future.

$T_{\rm d}$ can be understood as the typical GMC "lifetime" averaged over all the populations because $T_{\rm d}$ is the typical timescale within which GMCs disperse in the system. This is consistent with the short lifetime indicated by observations (*e.g.*, in LMC (Kawamura et al. 2009) and in M51 (Meidt et al. 2015)) (see Section 5.3.2 for detailed discussions).

$T_{\rm dest}$ is basically independent of GMC mass because, for example, 10 times massive GMCs generate 10 times more $> 30{\rm M}_\odot$ stars, which in turn results in destroying 10 times more molecular gas (see Inutsuka et al. 2015). Therefore, if T_* is irrespective of GMC mass, $T_{\rm d}$ does not depend on GMC mass. Thus, we opt to use $T_{\rm d} = 14$ Myr throughout the current thesis. Note that this argument of mass independence is valid only if parental GMCs are $> 10^5{\rm M}_\odot$ because this is the minimum mass required to generate stars $> 30{\rm M}_\odot$ if we adopt Salpeter initial stellar mass function (Salpeter 1955). In case of GMCs $< 10^5{\rm M}_\odot$, the self-dispersal may be less effective (see Inutsuka et al. 2015) and more careful treatment is desired. In addition, T_* can be one order of magnitude shorter if CCC triggers rapid formation of massive stars (*c.f.* Fukui et al. 2016) (see also Section 3.2.4 and Chapter 5). For simplicity, however, we do not consider any T_* and $T_{\rm dest}$ variation in the current article (see also Section 3.2.4).

Here, we assume at least single $> 30{\rm M}_\odot$ star can be born in a $10^5{\rm M}_\odot$ GMC, given the Salpeter initial mass function for stars. This corresponds to a star formation efficiency in individual GMCs of 1 per cent. Thus, the typical gas depletion timescale averaged out over the entire galactic disks can be estimated by dividing

$T_{\rm d}$ by this efficiency. This gives $T_{\rm d}/0.01 \simeq 1.4$ Gyr. The consistency with the deduced value of 1 Gyr from Kennicutt-Schmidt relation (see Section 1.4.5) endorse our choice of parameters here.

Note that $T_{\rm d}$ does not always guarantee complete blow-out of GMCs physically. Meanwhile, several detailed semi-analytical studies (*e.g.*, Kim et al. 2016; Rahner et al. 2017) report that, in some range of initial conditions of hydrogen number density in GMCs, GMC mass, and star cluster mass, stellar feedback from a single star cluster (both wind and radiation) cannot completely blow out GMCs because of the gravity between the swept-up shell and the star cluster. This complete blow-out process as well as CO-dark gas population also need to be investigated in the future.

Note that, similarly to $T_{\rm f}$, $T_{\rm d}$ is in principle the ensemble averaged timescale over different GMC destructive processes. Therefore, other processes may play an important role as well in different galactic environment. For example, galactic shear (*c.f.*, Koda et al. 2009) can dominate in much inner regions in galactic disks but may be sub-dominant in the disk regions of typically > 5 kpc (*c.f.*, Dobbs & Pringle 2013). The relative importance of different destructive processes needs to be further studied in the future (*c.f.*, Jeffreson 2017 in prep.) For simplicity, we assume that the inclusion of these processes would not vary $T_{\rm d}$ significantly. In addition, rapid star formation triggered by CCC also needs to be properly modeled in $T_{\rm d}$ if CCC becomes effective. We explore formulations for such CCC-driven star formation in Chapter 5.

3.1.3 Cloud-Cloud Collision Terms

The second and third integration terms on the right hand side represent the collisional coagulation between GMCs (*i.e.*the CCC process). This formulation is essentially the same as the evolution of a system through two body coalescence; for example, colliding dust particles in protoplanetary disks (*e.g.*, Trubnikov 1971; Malyshkin & Goodman 2001). The second term on the right hand side produces a GMC with mass $m(= m_1 + m_2)$ through CCC between GMCs with their mass m_1 and m_2. Similarly, the last term on the right hand side creates a GMC with mass $m + m_2$ through CCC between GMCs with their mass m and m_2, so that the negative sign indicates that this collision decreases the number density of GMCs with mass m. $K(m_1, m_2)$ is the product of the total GMC collisional cross section between GMCs with mass m_1 and m_2, $\sigma_{{\rm col}\,1,2}$, and the relative velocity between GMCs, $V_{\rm rel}$:

$$K(m_1, m_2) = \sigma_{{\rm col}\,1,2}\, V_{\rm rel} = c_{\rm col} \frac{m_1 + m_2}{\Sigma_{\rm mol}} V_{\rm rel,0}\,. \tag{3.6}$$

Here, $c_{\rm col}$ is a correction parameter, $\Sigma_{\rm mol}$ is a GMC column density, and $V_{\rm rel,0}$ is the fiducial relative velocity between GMCs. $c_{\rm col}$ reflects various effects (*e.g.*, geometrical structure, gravitational focusing, relative velocity variation) and is expected to be on the order of unity (see discussions in Chapter 6).

The total collisional cross section can be essentially evaluated as the total geometrical cross section of two colliding GMCs. The GMC geometrical surface area can be estimated as their mass divided by a characteristic column density $m/\Sigma_{\rm mol}$, given the observational fact that the majority of GMCs have a constant column density of a few times $10^{22}\,{\rm cm}^{-2}$ if averaged over the entire cloud scale (*e.g.*, Onishi et al. 1999; Tachihara et al. 2000; see also subsection 6.1.3 for its variation). We opt to employ an observed value $\Sigma_{\rm mol} = 2 \times 10^{22} \mu m_{\rm H} {\rm cm}^{-2}$, where μ is the mean molecular weight and $m_{\rm H}$ is the atomic hydrogen weight. Observationally, the cloud-to-cloud velocity dispersion is measured as $8-10\,{\rm km\,s}^{-1}$ (Stark & Brand 1989; Stark & Lee 2005, 2006). The bubble paradigm predicts that GMCs are repeatedly pushed by supersonic shocks due to expanding shells and thus the sound speed of the medium within those expanding shells (*i.e.*, a typical expanding speed of ionization-dissociation front) set the GMC velocity dispersion, which is about $10\,{\rm km\,s}^{-1}$. Therefore, observed velocity dispersion is consistent with our bubble paradigm and we opt to set $V_{\rm rel,0} = 10\,{\rm km\,s}^{-1}$ (see Appendix 6.1.4). Note that we turn off CCC calculations that involve GMCs whose cumulative number is less than 1, because such GMC populations are less likely to exist in the real Universe.

Several variations (*e.g.*, gravitational focusing effect, angle variation at which GMCs collide with each other) may make the total collisional cross section differ from the total geometrical cross section. A factor of few differences due to these variations may impact the GMCMF massive-end evolution (and the total SFR on the entire galactic disks computed in Chapter 5), but do not on the power-law slope as shown in Section 3.2. Thus, for simplicity, we opt to choose $c_{\rm col} = 1$ throughout this thesis (see also subsection 6.1 for other details involved in $c_{\rm col}$).

In Equations 3.1 and 3.6, we restrict ourselves only to a perfect inelastic collision case (*i.e.*, coagulation) for simplicity and ignores fragmentation at all. This assumption is based on the observational fact that cloud-to-cloud velocity dispersion ($\sim 10\,{\rm km\,s}^{-1}$: *e.g.*, Stark & Lee 2005) does not largely exceed the sound velocity ($\sim 10\,{\rm km\,s}^{-1}$) of inter-cloud medium (*i.e.*, WNM). However, the fragmentation may have a severe impact under the CCC-dominated phase (*i.e.*, the GMC number density is high) such as in the Galactic Center (Tsuboi et al. 2015). This is beyond our current scope and left for future studies.

3.2 Results: Slope of Giant Molecular Cloud Mass Function

We perform the time integration of Equation (3.1) to determine what controls the observed GMCMF. Table 3.1 lists the parameters we use; especially Cases 1 to 4 correspond to the analysis in this section. Throughout this section, we assume that minimum-mass GMCs are always continuously created so that the rate producing new-born minimum-mass GMCs compensates the decrease in the population of minimum-mass GMCs due to self-growth, self-dispersal, and CCC. This treatment makes the number density of minimum-mass GMCs always constant. Observation-

Table 3.1: Studied setups for the time evolution of GMC mass functions

Cases	Parameters				
	$T_{\rm f,fid}$ (Myr)	$T_{\rm d}$ (Myr)	Cloud-Cloud Collisions	$\varepsilon_{\rm res}$	Figures
1	10	14	yes	support	Fig. 3.1
2	10	14	no	support	Fig. 3.2
3	4.2	14	yes	support	Fig. 3.4
4	22.4	14	yes	support	Fig. 3.5
5	10	14	yes	1	Fig. 4.1
6	10	14	yes	0.09	Fig. 4.2
7	4.2	14	yes	0.0123	Fig. 4.4
8	22.4	14	yes	0.45	Fig. 4.6

Note. 8 cases that we study in this thesis, including the setups employed in the next chapter. Individual parameters are described in Sections 3.1 and 4.1. Each column represents as follows; $T_{\rm f,fid}$ shows the formation timescale. $T_{\rm d}$ gives the dispersal timescale. Cloud-Cloud Collisions indicate whether we include the CCC terms (yes) or not (no). $\varepsilon_{\rm res}$ represents the resurrecting factor introduced in Section 4.1 (*i.e.*the fractional mass out of total dispersed gas that is consumed to form newer generation of GMCs), where "support" means that we artificially keep the population of minimum-mass GMCs fixed. Figures indicate the corresponding figures in this thesis.

ally, star formation rate density in the Universe has its peak at redshift $z \sim 2-3$ and is relatively constant at present (Madau & Dickinson 2014). Therefore, our treatment of steadiness in the minimum-mass GMC population is based on our assumption that GMCs, as a precursor of stars, also have its steady state to constantly produce stars in nearby galaxies compared with the long history of the Universe. Without any sufficient creation, minimum-mass GMCs are exhausted due to self-growth, self-dispersal, and CCC, thus the observed GMCMF cannot be reproduced. In Section 4.2, we will discuss possible variation in the rate of producing new-born minimum-mass GMCs by dispersed gas "resurrection" (*i.e.*, regeneration of GMC populations from dispersed gas produced by massive stars).

We set the timestep width as 0.1% of the shortest timescale in each time step. We use the logarithmically spaced mass grid where the $i+1$-th mass is larger by a factor 1.0125 than the i-th mass. The initial GMCMF has a delta-function like mass distribution where only minimum-mass GMCs exist, by which we can highlight how fast the GMCMF evolves. All the figures presented here show the GMCMF up to the mass where the cumulative number of GMCs > 1, except that the GMCMFs in Figs. 3.1 and 3.2 are shown beyond that mass to show the CCC effect clearly. Note that we turn off the CCC calculation between certain GMC pairs when at least one of GMCs in the pair has its cumulative number, $n_{\rm cl}(>m)$, less than 1 because such GMCs are less likely to exist in real galaxies so that this type of CCC is also expected to be rare. The spikes and kinks that appear in the massive end (especially in Figs. 3.1 and 3.5) are due to the numerical effect by this CCC turn-off procedure so that actual GMCMFs in the Universe would be smoother. The results of PAWS survey (*c.f.*, Colombo et al. 2014a) are used in the plots for comparing the GMCMF slopes between our calculation and observations. We first investigate how the relative importance between self-growth/dispersal and CCC varies as a function of GMC mass. Then we identify which process controls the GMCMF slope and explore an analytical evaluation for this slope.

3.2.1 CCC Contribution to the GMCMF Slopes and Massive Ends

Figures 3.1 and 3.2 show our fiducial calculations (*i.e.*, $T_{\rm f,fid} = 10$ Myr, $T_{\rm d} = 14$ Myr), which correspond to Case1 and Case2 respectively. The only difference between these two cases is whether the calculation includes the CCC terms (Figure 3.1) or not (Figure 3.2). Both computed GMCMFs demonstrate almost the same slope $-\alpha \sim -1.7$ (where $n_{\rm cl} \propto m^{-\alpha}$), which successfully fits into the middle of the observed range. This similarity in two slopes indicates that CCC does not impact the GMCMF slope significantly whereas the shape of the massive end is modified by the relative importance between self-growth/dispersal and CCC.

To examine the relative contribution of CCC, we compute the collision timescale, $T_{\rm col}$, as:

$$T_{\rm col} = \frac{n_{\rm cl}(m)}{(\partial n_{\rm cl}/\partial t)_{\rm CCC}}, \tag{3.7}$$

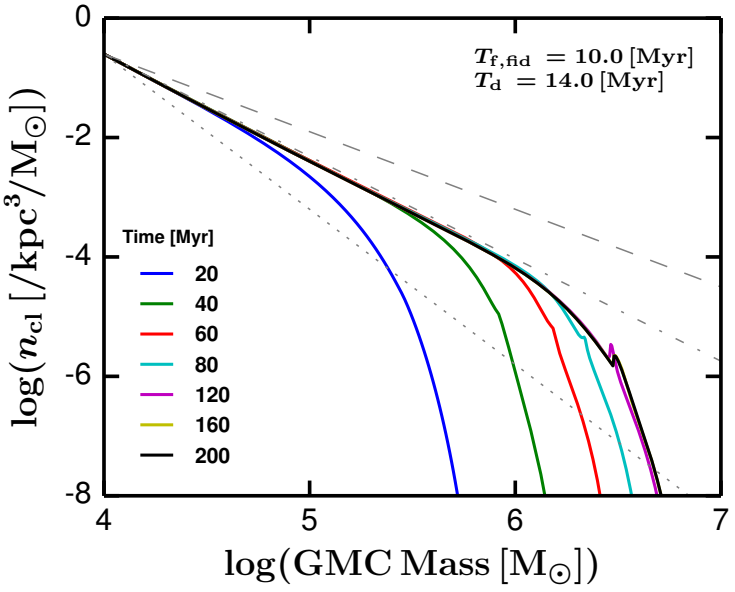

Figure 3.1: Case 1: Differential number density $n_{\rm cl}$ as a function of GMC mass, based on the fiducial calculation with CCC. The color corresponds to the time evolution. Note that the yellow line corresponds to 160 Myr is almost fully overlapped by the black line for 200 Myr, thus it is not visible on this plot. As a reference, we plot three gray straight lines; dot-dashed line fits the computed GMCMF slope (~ -1.7), dashed line corresponds to the observed shallow slope whereas the dotted line shows the observed steep slope. The calculated GMCMF fits into the middle of the observed slope range.

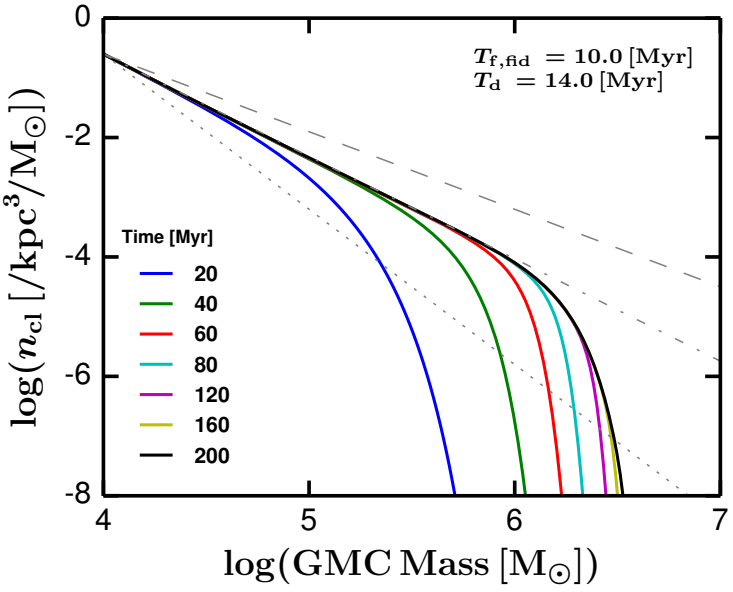

Figure 3.2: Case 2: Differential number density $n_{\rm cl}$ as a function of GMC mass, based on the fiducial calculation without CCC. The color corresponds to the time evolution. As a reference, we plot three gray straight lines; dot-dashed line fits the computed GMCMF slope (~ -1.7), dashed line corresponds to the observed shallow slope whereas the dotted line shows the observed steep slope. The calculated GMCMF fits into the middle of the observed slope range. The similarity with Figure 3.1 indicates that CCC does not impact on the GMCMF slope significantly but modify the massive end.

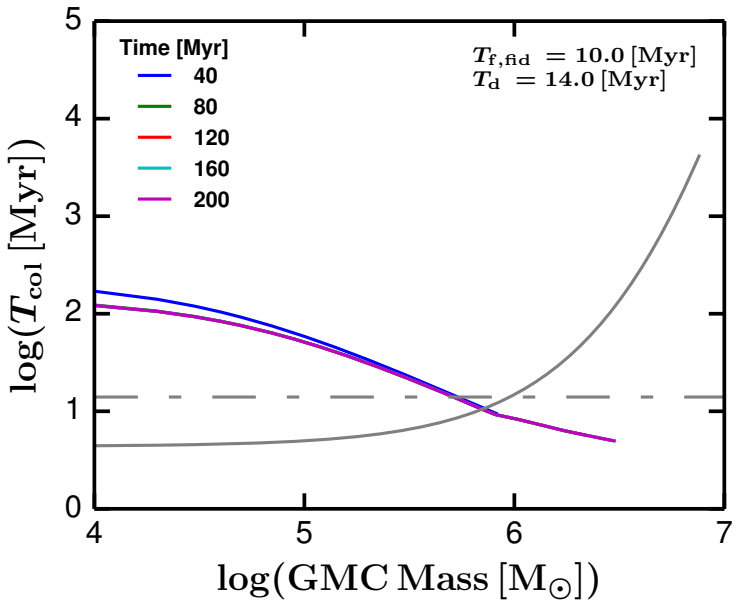

Figure 3.3: The three timescales as a function of GMC mass in Case 1. The gray solid line represents $T_{\rm f}$, the gray horizontal dot-dashed line corresponds to $T_{\rm d}$, and the colored lines show the time evolution of $T_{\rm col}$. Note that the three colored lines (*i.e.*, the green line for 80 Myr, the red line for 120 Myr, and the cyan line for 160 Myr) are overlapped by the purple line for 200 Myr so that they are not visible on this plot. The figure indicates that GMC self-growth dominates in low-mass regime, but CCC deforms the GMCMF at its high-mass end where $T_{\rm col}$ is one order of magnitude smaller than self-growth timescale. Note that the gray line of $T_{\rm f}$ shown here has a factor difference from original $T_{\rm f}$ defined as Equation (3.4) (see Equation 3.9 for the reason).

Here, the denominator is the time evolution due to CCC (see Equation (3.1)):

$$\begin{aligned}\left(\frac{\partial n_{\rm cl}}{\partial t}\right)_{\rm CCC} =& \frac{1}{2}\int_0^\infty \int_0^\infty K(m_1, m_2) n_{{\rm cl},1} n_{{\rm cl},2} \\ & \times \delta(m - m_1 - m_2) {\rm d}m_1 {\rm d}m_2 \\ & - \int_0^\infty K(m, m_2) n_{\rm cl} n_{{\rm cl},2} {\rm d}m_2 \,.\end{aligned} \tag{3.8}$$

Figure 3.3 shows the time evolution of computed $T_{\rm col}$, with $T_{\rm f}$ and $T_{\rm d}$ overplotted together. The figure indicates that the GMC mass growth is determined by GMC self-growth in low-mass regime where $T_{\rm f}$ ($\sim \mathcal{O}(1)$ Myr) is one order of magnitude shorter than $T_{\rm col}$ ($\sim \mathcal{O}(2)$ Myr), and is determined by CCC at the high-mass end where $T_{\rm col}$ ($\sim \mathcal{O}(1)$ Myr) becomes one order of magnitude smaller than $T_{\rm f}$ ($\sim \mathcal{O}(2)$ Myr). This indicates that the GMCMF slope in $m \lesssim 10^{5.5}{\rm M}_\odot$ is well characterized by the combination of the GMC self-growth and dispersal. In the next section, we are going to focus only on the GMCMF slopes and will discuss the massive-end behavior in Section 3.2.4.

$T_{\rm f}$ defined in Equation (3.1) are the timescales for the *number* flow. However $T_{\rm col}$ defined in Equation (3.7) is the timescale for the *mass* flow. To compare these two timescales, we need to convert $T_{\rm f}$ to the mass flow timescale, which can be evaluated as:

$$\begin{aligned}T_{\rm f,\,mass\,flow} &= m n_{\rm cl} \Bigg/ \frac{\partial}{\partial m}\left(\frac{m^2 n_{\rm cl}}{T_{\rm f}(m)} - \int_{m_{\rm min}}^{m} \frac{m n_{\rm cl} {\rm d}m}{T_{\rm f}(m)}\right) \\ &= m n_{\rm cl} \Bigg/ \left(\frac{\partial}{\partial m}\left(\frac{m^2 n_{\rm cl}}{T_{\rm f}(m)}\right) - \frac{m n_{\rm cl}}{T_{\rm f}(m)}\right) \,,\end{aligned} \tag{3.9}$$

(see Equation (4.4)). The gray line in Figure (3.3) shows this $T_{\rm f,\,mass\,flow}$ instead of $T_{\rm f}$.

Note that Equation 3.8 considers the net change in the differential number density of GMC populations with mass m, which is based on the Eulerian framework in the fixed GMC mass coordinate. Later in Section 5.2.3, we will investigate the mass-growth of individual GMCs in the Lagrange framework.

3.2.2 Characteristic Slope of the GMCMF

As shown in Section 3.2.1, CCC does not modify the GMCMF evolution significantly. Especially in lower mass range (*e.g.*, $m < 10^{5.5}{\rm M}_\odot$) CCC does not affect the mass function, and hence our formulation can be rewritten without the CCC terms. Therefore, the evolution of differential number density of GMCs with mass m, $n_{\rm cl}$, is now simply given as:

$$\frac{\partial n_{\rm cl}}{\partial t} + \frac{\partial}{\partial m}\left(n_{\rm cl}\frac{m}{T_{\rm f}}\right) = -\frac{n_{\rm cl}}{T_{\rm d}} \,. \tag{3.10}$$

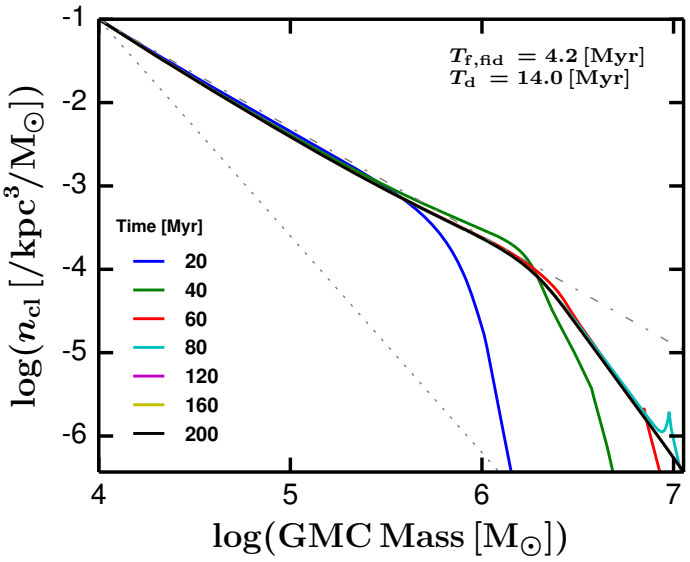

Figure 3.4: Case 3: Differential number density $n_{\rm cl}$ as a function of GMC mass, based on the calculation with $T_{\rm f,fid} = 4.2$ Myr including CCC. The color corresponds to the time evolution. Note that the two colored lines (*i.e.*, the purple line for 120 Myr and the yellow line for 160 Myr) are overlapped by the black line for 200 Myr so that they are not visible on this plot. As a reference, we plot two gray straight lines; dot-dashed line corresponds to the observed GMCMF slope (~ -1.3) in the arm regions, whereas the dotted line shows the observed steep slope in inter-arm regions. The agreement between the observed slope and the computed slope suggests that the arm regions typically have a shorter self-growth timescale, $T_{\rm f} \sim 4$ Myr. This is well characterized by the steady state solution without CCC shown in Equation (3.11). Again, the CCC effect is limited but modifies the GMCMF massive-end.

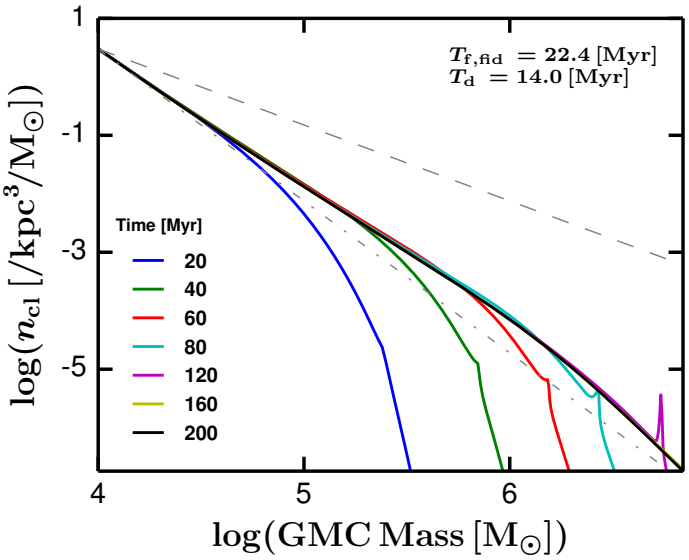

Figure 3.5: Case 4: Differential number density $n_{\rm cl}$ as a function of GMC mass, based on the calculation with $T_{\rm f,fid} = 22.4$ Myr including CCC. The color corresponds to the time evolution. Note that the yellow line for 160 Myr is overlapped by the black line for 200 Myr, thus it is not visible on this plot. As a reference, we plot two gray straight lines; the dot-dashed line represents the observed steep slope (~ -2.6) in the inter-arm regions, whereas the dashed line shows the observed shallow slope in the arm regions. Although the GMCMF shows the slope ~ -2.2 relatively shallower than the observed one ~ -2.6 due to the coagulation by CCC, the basic correspondence suggests that the inter-arm regions typically have a longer self-growth timescale $T_{\rm f} \sim 22$ Myr. This is well characterized by the steady state solution without CCC shown in Equation (3.11).

This formulation has been already (and originally) proposed by Inutsuka et al. (2015) because they consider only self-growth/dispersal alone in their time evolution equation, albeit their $T_{\rm f}$ is independent of GMC mass and constant. One can obtain the steady state solution of this differential equation for $m \lesssim m_{\rm crit}$ with a constant $T_{\rm f}$ as:

$$n_{\rm cl}(m) = n_0 \left(\frac{m}{\rm M_\odot} \right)^{-1-\frac{T_{\rm f}}{T_{\rm d}}} , \tag{3.11}$$

where n_0 is the differential number density normalized at $m = 1{\rm M_\odot}$. This predicts that GMCMFs have slopes with a single power-law exponent, which is well characterized by $-1 - T_{\rm f}/T_{\rm d}$. Indeed, the computed GMCMF shows the slope consistent with this exponent $-1-T_{\rm f}/T_{\rm d}$ without CCC (see Figure 3.2), and in the lower mass ($m < 10^{5.5}{\rm M_\odot}$) part even in the case with CCC (see Figure 3.1).

To examine the validity of the $-1 - T_{\rm f}/T_{\rm d}$ prediction, we conduct the calculation again by employing various $T_{\rm f}$. Figures 3.4 and 3.5 are the two representative results and both cases exhibit the slope well characterized by $-1 - T_{\rm f}/T_{\rm d}$. Figure 3.4 employs a shorter formation timescale, $T_{\rm f,fid} = 4.2$ Myr, and reproduces the observed shallow slope in arm regions. Similarly, Figure 3.5 shows the result with $T_{\rm f,fid} = 22.4$ Myr, which reproduces the observed steep slope in inter-arm regions. Therefore, the arm regions are likely to have a larger number of massive stars forming HII regions and supernova remnants thus experience the recurrent supersonic compression twice more frequently than the fiducial case, and the inter-arm regions typically have a smaller number of massive stars thus experience less frequent supersonic compression, which results in about factor two longer formation timescale than the fiducial case. This may also explain the observed steep slope at outskirts of galaxies (*e.g.*, the observed steep slope in the CO luminosity function in Galaxy M33; see Gratier et al. 2012) where star formation is less active compared with normal disk regions. Note that the above argument might be modified, if the effect of large-scale dynamics (*e.g.*, interaction with shock waves or strong shear flows) may play an important role in the destruction of GMCs than the stellar feedback, especially in the outskirts of galaxies with prominent spiral structures.

Note that we here assume that the $T_{\rm d}$ variation between different regions is limited compared with the $T_{\rm f}$ variation. This is because $T_{\rm d}$ is basically independent of GMC mass as explained in Section 3.1.2 and also because observations suggest that the star formation efficiency is almost the same throughout the galactic disks in nearby galaxies (*e.g.*, Schruba et al. 2011) and in the Galaxy (Izumi et al. in prep.). However, $T_{\rm d}$ might be longer in inter-arm regions compared with arm regions due to its less star forming activity where $T_{\rm d}$ can be up to ~ 30 Myr (the upper limit measured in M51 by Meidt et al. 2015), or might be a factor longer in smaller clouds $\lesssim 10^5{\rm M_\odot}$ where it is invalid to apply our mass-independent assumption on the cloud destruction rate due to massive stars. The significance of $T_{\rm d}$ variation should be investigated more and we will leave this for future work.

Our results suggest that the variation of the GMCMF slopes are governed by

$T_{\rm f}/T_{\rm d}$ diversity in different environment on galactic scales. We predict that future large radio surveys with higher spatial resolution and higher sensitivity may uniquely constrain the timescale ratio $T_{\rm f}/T_{\rm d}$ with its dependence on different environment on galactic disks, by identifying smaller GMCs and measuring the power-law slope in GMCMF[2].

Equation (3.11) indicates that $T_{\rm f}$ can vary from 4 to 22 Myr to reproduce observed variation in GMCMF slope given that $T_{\rm d}$ is presumably determined more by stellar evolution but not by galactic environment (*e.g.*, arm or inter-arm; see Kobayashi et al. (2017b)). Indeed for example, based on PAWS data on Galaxy M51, Leroy et al. (2017) report that the depletion timescale due to star formation is almost constant with the total molecular column density in CO(1-0) line averaged on 40pc scale where the depletion timescale is defined as the total amount of molecular gas divided by SFR. Their derived depletion timescale ~ 2 Gyr and star formation efficiency ~ 0.3 per cent gives ~ 6 Myr as individual GMC dispersal timescale, which is a factor shorter than our fiducial dispersal timescale $T_{\rm d} = 14$ Myr. This factor difference ($14/6 = 2.3$) may arise from shorter $T_{\rm d}$ in GMCs undergoing CCC (see subsection 5.1.2) but needs to be further investigated.

3.2.3 Possible Range of Formation/Self-Growth Timescale

The possible range of $T_{\rm f}$ variation can be analytically evaluated (albeit order-of-magnitude estimation) given an SFR density. Let us assume that the mass spectrum of a coeval set of stars follows the Salpeter IMF (Salpeter (1955); see also section 1.5.2). The mass density of stars whose mass are between m_1 and m_2, $\rho(m_1 - m_2)$, can be given as:

$$\begin{aligned}\rho(m_1 - m_2) &= \int_{m_1}^{m_2} A\,\phi(m)\,m{\rm d}m \\ &= \frac{A}{0.35}\left(m_1^{-0.35} - m_2^{-0.35}\right)\,.\end{aligned} \tag{3.12}$$

The mass fraction of supernova progenitors out of the total stars in this stellar system is given as:

$$\frac{\rho(8{\rm M}_\odot - 30{\rm M}_\odot)}{\rho(0.08{\rm M}_\odot - 30{\rm M}_\odot)} \simeq 0.085\,. \tag{3.13}$$

Here we consider the mass range for the supernova progenitors as $8{\rm M}_\odot - 30{\rm M}_\odot$ (*c.f.*, Jennings et al. 2014) and the most massive stars in this stellar system as $30{\rm M}_\odot$. The typical mass of supernova progenitors can be also estimated as:

$$\frac{\rho(8{\rm M}_\odot - 30{\rm M}_\odot)}{\int_{8{\rm M}_\odot}^{30{\rm M}_\odot} A\phi(m){\rm d}m} \simeq 13.7{\rm M}_\odot\,. \tag{3.14}$$

[2]In a crowded region such as galactic centers, the number density of GMCs is higher than in disk regions. CCC may be a faster process than mass-growth or self-dispersal. In such cases, the power-law slope varies with the dependence of the kernel function K on GMC masses. See for this analysis in, for example, equation (A4) in Kwan (1979) and equation (31) in Kobayashi et al. (2017b).

Therefore, in a given location of the ISM that has the SFR density as $\rho_{\rm SFR}[{\rm M}_\odot\ {\rm yr}^{-1}\ {\rm pc}^{-3}]$, the typical timescale, $\tau_{\rm sweep}(\rho_{\rm SFR})$, over which a unit volume of the ISM (1 pc^3) can be swept up by a supersonic shock originated in supernovae is

$$\tau_{\rm sweep}(\rho_{\rm SFR}) = \frac{1\,{\rm pc}^3}{(100\,{\rm pc})^3\,\rho_{\rm SFR}\,0.085\,(1/13.7{\rm M}_\odot)} \tag{3.15}$$

The typical SFR in the Milky Way and Galaxy M51 is about 2 $\mathrm{M}_\odot\ \mathrm{yr}^{-1}\ \mathrm{galaxy}^{-1}$ (Kennicutt & Evans 2012; Eufrasio et al. 2017), which corresponds to $\rho_{\rm SFR} \simeq 2\times10^{-10}\ \mathrm{M}_\odot\ \mathrm{yr}^{-1}\ \mathrm{pc}^{-3}$. Thus the typical $\tau_{\rm sweep}$ can be estimated as $\tau_{\rm sweep} \simeq 0.8\,{\rm Myr}$. This is consistent with the time interval of 1 Myr between repeated shocks that we assume to estimate the typical $T_{\rm f}$ in our model (see section 2.2.3). Multi-line observations and their following analysis indicate that arm (inter-arm) regions in Galaxy M51 would have $\rho_{\rm SFR} \simeq 3-5(0-1)\times10^{-10}\ \mathrm{M}_\odot\ \mathrm{yr}^{-1}\ \mathrm{pc}^{-3}$ with the assumed galactic-disk thickness of 100 pc in Galaxy M51. The expected $\tau_{\rm sweep}$ in arm (inter-arm) regions is $0.3-0.5(1.6)$ Myr thus corresponding $T_{\rm f}$ is about $3-5(16)$ Myr.

3.2.4 Possible Modification in the Massive-end.

The shape of the GMCMF massive-end, typically $>10^6{\rm M}_\odot$, is determined by the relative importance of GMC self-growth and CCC as shown in previous sections. The quantitative discussion involves many uncertainties from our modeling; for example, more detailed prescription for γ is necessary for GMC self-growth (*i.e.*, $T_{\rm f}$), and it is also required to model T_* variation due to the drastic star formation invoked by CCC, which is inferred by observations in the Galaxy (*c.f.*, Fukui et al. (2014); also see Section 5.1). It is challenging to study to what extent this type of drastic star formation affects (*i.e.*destructs) surrounding GMCs on cloud scales, but this needs to be investigated by massive hydrodynamics simulations. Instead of detailed simulations, we will explore a semi-analytical formulation of CCC-driven star formation in Chapter 5.

Despite these limitation, our results indicate that, if CCC becomes effective, another structure may appear in the massive-end. This possibly explains the extra power-law feature observed in some regions (*e.g.*, Material Arms) from PAWS survey (Colombo et al. 2014a).

Chapter 4

Gas Resurrection[1]

In this chapter, we explore the fate of dispersed gas by modeling "gas resurrecting" process and emphasize that, as future studies, detailed investigations are needed to identify what phase of gas is important for driving the gas recycling in the ISM

4.1 Gas Resurrecting Factor

For all the time evolutions of the GMCMF we have shown by the previous chapter, we assume that minimum-mass molecular clouds are continuously provided. Numerically, this treatment corresponds to employment of steady fixed minimum-mass GMC population. In addition, we assume that the dispersed gas removed from the system is never restored into the system. Thus, the dispersal term in equation (3.1) produces dispersed gas with the rate of $n_{\rm cl}(m)/T_{\rm d}$ but this term alone does not restore dispersed gas back into GMC populations.

However in reality, when GMCs disperse, they turn into ambient ISM in several phases: ionized, atomic, CO-dark, optically thick HI etc. Irrespective of phases, those dispersed gas may experience another supersonic shocks due to massive stars or supernovae while floating around in the ISM. Therefore, the dispersed gas can become either seeds of newer generation of molecular clouds or mass accreting onto the pre-existing GMCs to aid their mass-growth. Hereafter, we call this process as "gas resurrection" following the nomenclature that we proposed in Kobayashi et al. (2017b). To establish a complete picture of gas resurrecting processes in the ISM, we need to evaluate the fate of such dispersed gas. This aspiration requires detailed numerical simulations, ideally, three dimensional radiation magnetohydrodynamics simulations, which are however computationally too expensive to conduct.

Instead in this thesis, we quantify the amount of dispersed gas by introducing the "resurrecting factor", $\varepsilon_{\rm res}$, which is the mass fraction out of the total dispersed

[1] *The contents of this chapter are partially based upon the articles Kobayashi et al. (2017b) and Kobayashi et al. (2017a).*

gas that are transformed to newer generation of minimum-mass GMCs. In Section 3.2, we artificially set the production rate of minimum-mass GMCs to keep its number density constant. Here instead, we evaluate this production rate due to gas resurrection as:

$$\left.\frac{\partial\left(n_{\rm cl}m\right)}{\partial t}\right|_{\rm res} = \varepsilon_{\rm res}\,\dot{\rho}_{\rm total,disp}\,\delta(m-m_{\rm min})\,. \tag{4.1}$$

Here, $\dot{\rho}_{\rm total,disp}$ is the total amount of dispersed gas produced from the system per unit time per unit volume defined as:

$$\dot{\rho}_{\rm total,disp} = \int_0^\infty \frac{mn_{\rm cl}}{T_{\rm d}}{\rm d}m\,, \tag{4.2}$$

$m_{\rm min}$ is the minimum-mass of GMCs (*i.e.*, $10^4{\rm M}_\odot$ in this study), and δ is the Dirac delta function. Therefore, this equation evaluates the replenishment rate of the minimum-mass GMC due to the $\varepsilon_{\rm res}$ fraction of total amount of disperse gas produced in the system per unit time, $\dot{\rho}_{\rm total,disp}$. By this definition, $\varepsilon_{\rm res}$ can be considered as the probability that dispersed gas becomes minimum-mass GMCs before they accrete onto the pre-existing GMCs. Therefore, in a steady state case, the $1-\varepsilon_{\rm res}$ fraction of dispersed gas are consumed for the self-growth of pre-existing intermediate-mass GMCs, whose rate is given by the flux term $m/T_{\rm f}$ in Equation 3.1.

By solving Equation 4.1 coupled with Equation 3.1, one can obtain GMCMF evolution along with gas resurrection consistently. The combination of Equations 3.1 and 4.1 gives the following new time evolution equation that we are going to solve:

$$\begin{aligned}
\frac{\partial n_{\rm cl}}{\partial t} &+ \frac{\partial}{\partial m}\left(n_{\rm cl}\left(\frac{{\rm d}m}{{\rm d}t}\right)_{\rm self}\right) \\
&= -\frac{n_{\rm cl}}{T_{\rm d}} \\
&+ \frac{1}{2}\int_0^\infty\int_0^\infty K(m_1,m_2)n_{{\rm cl},1}n_{{\rm cl},2} \\
&\qquad\qquad \times\delta(m-m_1-m_2){\rm d}m_1{\rm d}m_2 \\
&- \int_0^\infty K(m,m_2)n_{\rm cl}n_{{\rm cl},2}{\rm d}m_2 + \frac{1}{m}\left.\frac{\partial\left(n_{\rm cl}m\right)}{\partial t}\right|_{\rm res}\,.
\end{aligned} \tag{4.3}$$

The last term corresponds to the gas resurrection, where we need $1/m$ factor because Equation 4.3 evaluates the differential number density whereas Equation 4.1 evaluates the differential mass density.

From now, we are going to focus only on steady state GMCMFs for simplicity. We may assume that the GMCMFs are quasi-steady in the Galaxy and nearby massive spiral galaxies because, as already discussed in Chapter 3, they probably have already undergone active star formation phase at redshift ~ 2 and have relatively constant star formation activity at the present day (*e.g.* Madau & Dickinson 2014).

Note that, although we have already proved that the CCC effect is limited, we fully solve Equation (4.3) including the CCC terms to compute the time evolution in all the following results. We mainly analyze Cases 5 to 8 in Table 3.1. The spikes and kinks that appear in the massive end (especially in Figs. 4.1, 4.4, and 4.6) are due to the numerical effect by the CCC turn-off procedure as explained in the second paragraph in Section 3.2. Note that, similar to Chapter 3, we show the GMCMFs up to the mass where the cumulative number of GMCs > 1, except that it is only up to $10^7 \mathrm{M}_\odot$ in Fig. 4.1 because GMCs more massive than the observed ones are created due to our rather artificial choice of an excessively CCC-dominated condition and we would like to focus on the slopes in the observed mass range.

4.2 Results: Fate of Dispersed Gas

4.2.1 Not All the Dispersed Gas are Consumed for Minimum-Mass GMC Creation

Here, we examine the fiducial timescales $T_{\rm f,fid} = 10$ Myr and $T_{\rm d} = 14$ Myr. First, we employ an extreme case where $\varepsilon_{\rm res} = 1$; all the dispersed gas is consumed to form minimum-mass GMCs (Case 6) and Figure 4.1 shows the result. Initially the GMCMF exhibits slopes slightly steeper than -1.7 predicted by Equation (3.11). However the slope becomes more steepened in the low-mass regime and the total mass in the system keeps increasing so that the GMCMF does not show any steady state (see Figure 4.3). Therefore, the slopes are provisional and transitional. Indeed, the CCC becomes significantly effective after 60 Myr so that GMCs more massive than observed ones are instantly created after 60 Myr, which do not reproduce the observed GMCMFs.

The steepened slope observed in the low-mass end in Figure 4.1 appears due to overloading $\varepsilon_{\rm res}$, because pre-existing GMCs cannot acquire the excessive amount of resurrecting gas faster than a given self-growth timescale (in this case 10Myr). To achieve a steady state with a shallower slope, we need to reduce $\varepsilon_{\rm res}$. Figure 4.2 shows a result with $\varepsilon_{\rm res} = 0.09$ where we successfully reproduce a slope $-\alpha = -1.7$ throughout all the mass range and achieve a steady state GMCMF. To check the steadiness, we compute the total mass in the system as a function of time with various $\varepsilon_{\rm res}$ and Figure 4.3 shows the result. $\varepsilon_{\rm res} = 0.09$ indicates that the GMCMF settle down on the steady state with a slight decrement in its total mass before the calculation ends at 200 Myr. Contrarily, excessive input $\varepsilon_{\rm res} \gg 0.09$ leads to growth of the total mass and do not become steady by 200Myr as, for example, already seen in Figure 4.1. Less input $\varepsilon_{\rm res} \ll 0.09$ leads to too much gas dispersal into the ISM and eventually decreases the total mass in the GMC phase, which would not reach any steady state before 200Myr. In Section 4.2.4, we will investigate an analytical justification why $\varepsilon_{\rm res} \sim 0.09$ reaches a steady state and present the possible range of $\varepsilon_{\rm res}$ that provides a steady GMCMF.

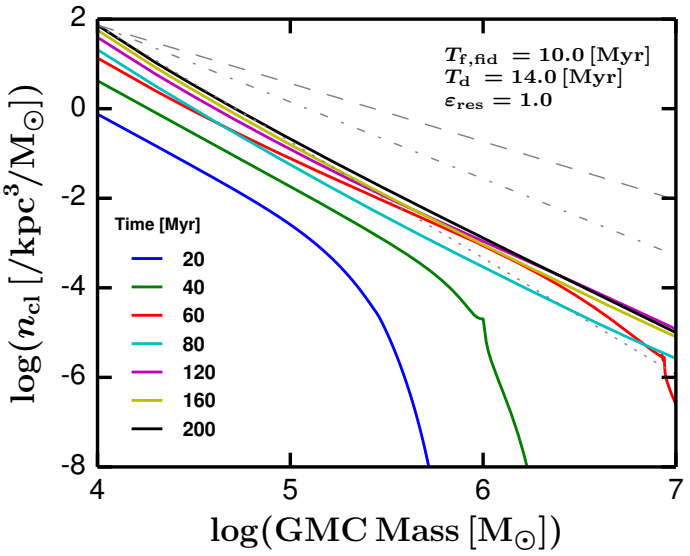

Figure 4.1: Case 5: Differential number density $n_{\rm cl}$ as a function of GMC mass including CCC with the fiducial timescales ($T_{\rm f,fid} = 10$Myr and $T_{\rm d} = 14$Myr) and with $\varepsilon_{\rm res} = 1$. The color corresponds to the time evolution. As a reference, we plot three gray straight lines; the dot-dashed line is the slope ~ -1.7 predicted by Equation (3.11), the dotted line represents the observed steep slope (~ -2.6) in the inter-arm regions, whereas the dashed line shows the observed shallow slope in the arm regions. The slope of the GMCMF is initially between -1.7 and -2.6 but becomes steepened and the total mass in the system keeps growing so that this does not reach any steady state (*c.f.*, Figure 4.3). The kink in the massive-end at 40 Myr indicates the onset for the CCC-dominant phase. After 40 Myr, CCC becomes dominant and massive GMCs $> 10^7 {\rm M}_\odot$ are continuously created, which is not consistent with observations, either. The steepened slope at the low-mass end appears due to overloading resurrection.

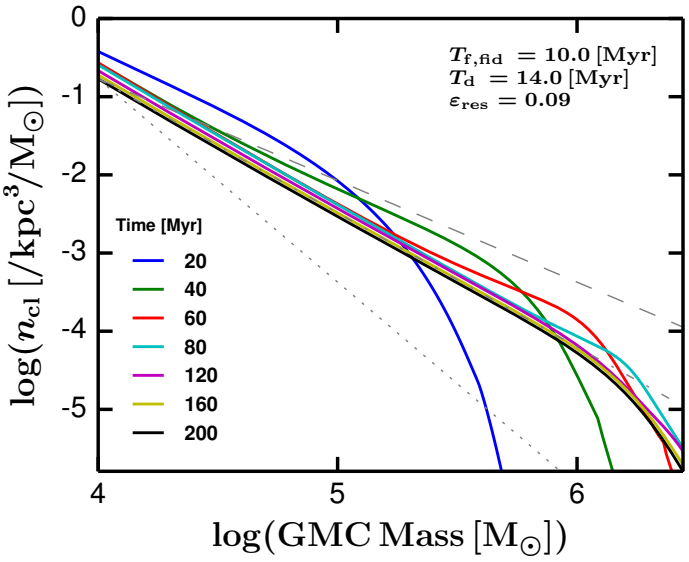

Figure 4.2: Case 6: Differential number density $n_{\rm cl}$ as a function of GMC mass including CCC with the fiducial timescales ($T_{\rm f,fid} = 10$Myr and $T_{\rm d} = 14$Myr) and with $\varepsilon_{\rm res} = 0.09$. The color corresponds to the time evolution. As a reference, we plot three gray straight lines; the dot-dashed line is the slope predicted by Equation (3.11), the dotted line represents the observed steep slope (~ -2.6) in the inter-arm regions, whereas the dashed line shows the observed shallow slope in the arm regions. The computed GMCMF successfully reproduces the fiducial slope ~ -1.7 predicted by Equation (3.11) and lands on a steady state as shown in Figure 4.3.

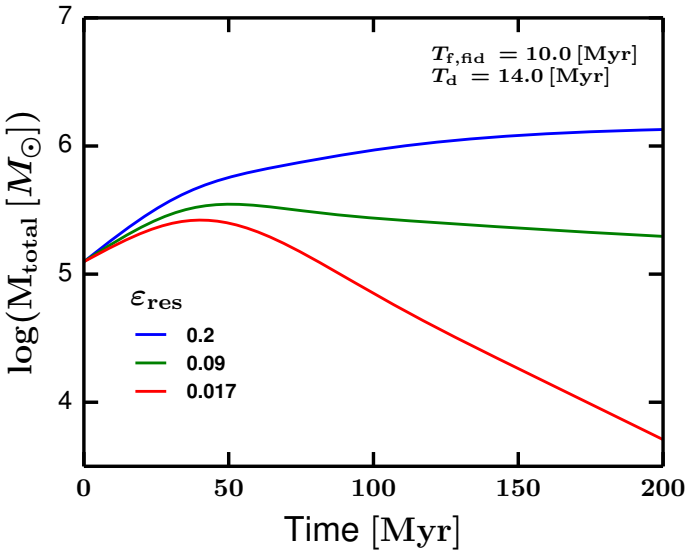

Figure 4.3: The total mass dependence on $\varepsilon_{\rm res}$ as a function of time with the fiducial setup ($T_{\rm f,fid} = 10$ Myr and $T_{\rm d} = 14$Myr). The different color represents the different $\varepsilon_{\rm res}$ from 0.0017 to 0.2. The GMCMF with $\varepsilon_{\rm res} = 0.09$ reaches a steady state after 130 Myr elapse. $\varepsilon_{\rm res} = 0.09$ reproduces the fiducial slope $-\alpha = -1.7$ as shown in Figure 4.2. Resurrecting more than $\varepsilon_{\rm res} = 0.09$ (*e.g.*, 0.2 in this figure) increase the total mass in the system and the GMCMF would not reach any steady state. Similarly, resurrecting less than $\varepsilon_{\rm res} = 0.09$ (*e.g.*, 0.0017 in this figure) eventually decrease the total mass in the system after 50 Myr. The steady resurrecting factor (~ 9 per cent) is predictable, which we will explain in Section 4.2.4.

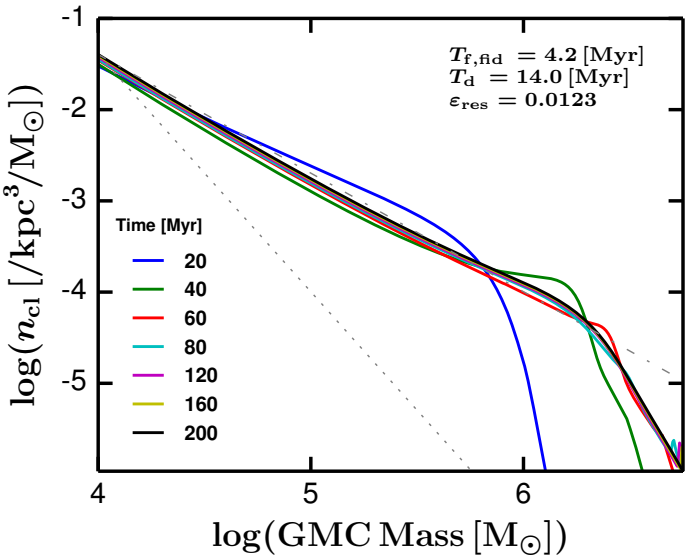

Figure 4.4: Case 7: Differential number density $n_{\rm cl}$ as a function of GMC mass including CCC with $T_{\rm f,fid} = 4.2$ Myr and $\varepsilon_{\rm res} = 0.0123$. The color corresponds to the time evolution. Note that the two colored lines (*i.e.*, the purple line for 120 Myr and the yellow line for 160 Myr) are overlapped by the black line for 200 Myr so that they are not visible on this plot. As a reference, we plot two gray straight lines; the dot-dashed line is the shallow slope (~ -1.3) observed in the arm regions, and the dotted line represents the steep slope (~ -2.6) observed in the inter-arm regions. The computed GMCMF successfully reproduces the shallow slope ~ -1.3 predicted by Equation (3.11) and reaches a steady state studied in Figure 4.5.

4.2.2 The Observed GMCMF Slopes in Arm Regions

We now focus on the shorter formation timescale $T_{\rm f,fid} = 4.2$ Myr (Case 7) to examine what $\varepsilon_{\rm res}$ would reproduce the slopes observed in arm regions. Figure 4.4 shows the GMCMF time evolution with $\varepsilon_{\rm res} = 0.0123$, which successfully reproduces the observed shallow slope ~ -1.3. Again, to check the steadiness, we compute the total mass in the system and Figure 4.5 shows the result with $\varepsilon_{\rm res}$ from 5.8×10^{-3} to 0.021. The figure also confirms that $\varepsilon_{\rm res} = 0.0123$ produces a steady state GMCMF. This factor 0.0123 indicates that almost 99 per cent of dispersed gas are accreting onto and fueling pre-existing GMCs due to the multiple episodes of compression and that only 1 per cent of dispersed gas are turned to form newer generation of GMCs. This extreme fraction is expected due to massive GMCs; massive GMCs have larger surface area than less massive GMCs and collect large amount of diffuse ISM gas to grow. Therefore, small $\varepsilon_{\rm res}$, or large $1-\varepsilon_{\rm res}$, is likely to be realized in arm regions, which have many massive GMCs. We will discuss the

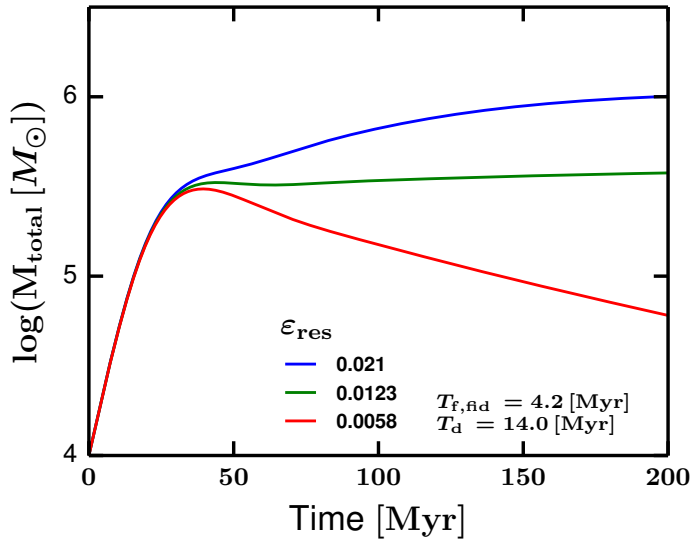

Figure 4.5: The total mass dependence on $\varepsilon_{\rm res}$ as a function of time with $T_{\rm f,fid} = 4.2$ Myr The different color represents the different $\varepsilon_{\rm res}$ from 5.8×10^{-3} to 0.021. The GMCMF with $\varepsilon_{\rm res} = 0.0123$ reaches a steady state, $M_{\rm total}$, which is $\sim 4 \times 10^5 {\rm M}_\odot$. $\varepsilon_{\rm res} = 0.0123$ reproduces the shallow slope $-\alpha = -1.3$ as shown in Figure 4.4. Resurrecting more than $\varepsilon_{\rm res} = 0.0123$ (*e.g.*, 0.021 in this figure) increase the total mass in the system. Similarly, resurrecting less than $\varepsilon_{\rm res} = 0.0123$ (*e.g.*, 5.8×10^{-3} in this figure) eventually decrease the total mass in the system after 60 Myr. The steady resurrecting factor (~ 1 per cent) is predictable, which we will explain in Section 4.2.4.

range of $\varepsilon_{\rm res}$ around 0.0123 that also keeps the GMCMF steady in Section 4.2.4.

4.2.3 The Observed GMCMF Slopes in Inter-Arm Regions

We now focus on the longer formation timescale $T_{\rm f,fid} = 22.4$ Myr (Case 8) to examine what $\varepsilon_{\rm res}$ would reproduce the slopes observed in inter-arm regions. Figure 4.6 shows the GMCMF time evolution with $\varepsilon_{\rm res} = 0.45$. This GMCMF has its slope ~ -2.4, shallower than the observed slope ~ -2.6 due to the coagulation by CCC, which is also observed in Figure 3.5. We compute the total mass in the system and Figure 4.7 shows the result with $\varepsilon_{\rm res}$ from 0.133 to 0.713. The figure confirms that $\varepsilon_{\rm res} = 0.45$ produces a steady state GMCMF. The initial condition is coincidently close enough to the steady state with $\varepsilon_{\rm res} = 0.45$ thus the GMCMF with $\varepsilon_{\rm res} = 0.45$ keep its total mass over the whole 200 Myr. This factor 0.45 indicates that about 55 per cent of dispersed gas are accreting onto and fueling pre-existing GMCs due to the multiple episodes of compression and that 45 per cent of dispersed gas are turned to form newer generation of GMCs. This is naturally expected because the inter-arm regions do not contain many massive GMCs that may collect diffuse ISM to grow. We will discuss the range of $\varepsilon_{\rm res}$ around 0.45 that also keeps the GMCMF steady in Section 4.2.4.

4.2.4 Analytical Estimation on the Resurrecting Factors

In this section, we derive an analytical estimation for the steady state $\varepsilon_{\rm res}$ with its possible variation as a function of the GMCMF slope to explain the reason why the values we choose for the resurrecting factor in Sections 4.2.2 and 4.2.3 can successfully reproduce the observed variation of the GMCMFs. Here, we assume that the GMCMF in a mass range from $m_{\rm min}$ to $m_{\rm max}$ has a steady power-law state $n_{\rm cl} = Am^{-\alpha}$, where A is a constant. We choose $m_{\rm min} = 10^4 {\rm M}_\odot$ in our calculation (see Appendix 6.3 for the choice of $m_{\rm min}$ value), whereas $m_{\rm max} \approx m_{\rm trunc}$ as shown in the figures from our calculation by now.

To derive $\varepsilon_{\rm res}$ in a steady state GMCMF, we multiply m by Equation (3.1) without the CCC term and modify the dispersal term into a form of $\partial/\partial m$:

$$\frac{\partial m n_{\rm cl}}{\partial t} + \frac{\partial}{\partial m} F(m) = 0\,. \tag{4.4}$$

Here,

$$F(m) = \frac{m^2 n_{\rm cl}}{T_{\rm f}(m)} - \int_{m_{\rm min}}^{m} \frac{m n_{\rm cl} {\rm d}m}{T_{\rm f}(m)} + \int_{m_{\rm min}}^{m} \frac{m n_{\rm cl} {\rm d}m}{T_{\rm d}}\,, \tag{4.5}$$

is the net mass flux at m across the mass coordinate. Because we consider a steady state GMCMF at $m \leq m_{\rm trunc}$, $T_{\rm f}$ will be treated as a constant in the following

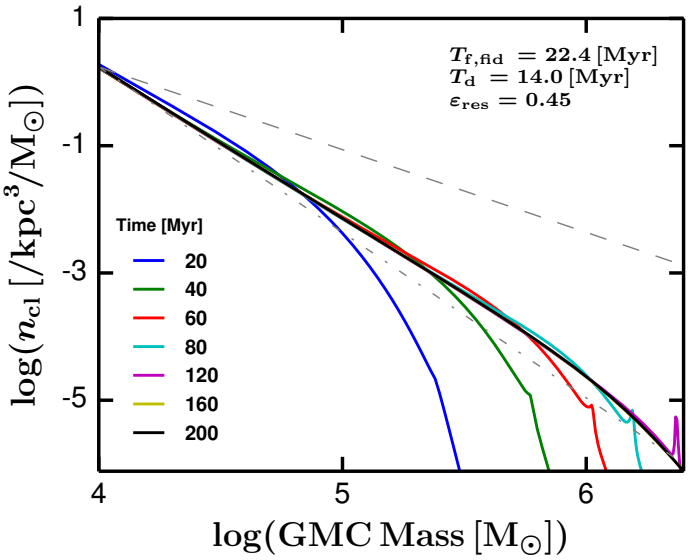

Figure 4.6: Case 8: Differential number density $n_{\rm cl}$ as a function of GMC mass including CCC with $T_{\rm f,fid} = 22.4$ Myr and $\varepsilon_{\rm res} = 0.45$. The color corresponds to the time evolution. Note that the yellow line for 160 Myr is overlapped by the black line for 200 Myr, thus it is not visible in this plot. As a reference, we plot two gray straight lines; the dot-dashed line is the steep slope (~ -2.6) observed in the inter-arm regions, and the dashed line represents the shallow slope (~ -1.3) observed in the arm regions. Although the computed GMCMF shows its slope ~ -2.4 slightly shallower than the observed value -2.6 due to the coagulation by CCC, this slope is basically predicted by Equation (3.11) and the GMCMF reaches a steady state studied in Figure 4.7.

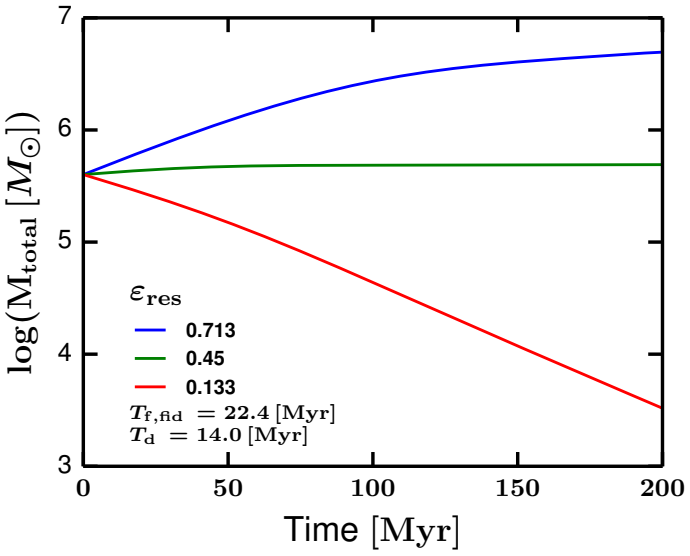

Figure 4.7: The total mass dependence on $\varepsilon_{\rm res}$ as a function of time with $T_{\rm f,fid} = 22.4$ Myr. The different color represents the different $\varepsilon_{\rm res}$ from 0.133 to 0.713. The GMCMF with $\varepsilon_{\rm res} = 0.45$ holds a steady state $M_{\rm total}$, which is $\sim 5 \times 10^5 {\rm M}_\odot$, and reproduces the steep slope $-\alpha = -2.6$ as shown in Figure 4.6. The steadiness of the GMCMF with $\varepsilon_{\rm res} = 0.45$ indicates that our initial condition setting only minimum-mass GMCs is close to the final steady state because smaller GMCs dominate the mass budget of the steepened GMCMF. Resurrecting more than $\varepsilon_{\rm res} = 0.45$ (*e.g.*, 0.713 in this figure) increase the total mass in the system. Similarly, resurrecting less than $\varepsilon_{\rm res} = 0.45$ (*e.g.*, 0.133 in this figure) decrease the total mass in the system. The steady resurrecting factor (~ 0.45 per cent) is predictable, which we will explain in Section 4.2.4.

analysis. Then $F(m)$ can be rewritten as:

$$F(m) = Am^{2-\alpha}\left(\frac{1}{T_{\rm f}} - \frac{1}{(2-\alpha)T_{\rm f}} + \frac{1}{(2-\alpha)T_{\rm d}}\right) + Am_{\rm min}^{2-\alpha}\left(\frac{1}{(2-\alpha)T_{\rm f}} - \frac{1}{(2-\alpha)T_{\rm d}}\right). \tag{4.6}$$

This mass flux is useful to evaluate the mass evolution in the system as we prove from now, and is also complementary with the original number density analysis because $\partial F(m)/\partial m = 0$ reproduces the steady state slope predicted in Equation (3.11):

$$\alpha = 1 + \frac{T_{\rm f}}{T_{\rm d}}\,. \tag{4.7}$$

We introduce four characteristic quantities that control $\varepsilon_{\rm res}$; the incoming flux at the minimum-mass end, $F_{\rm in}$, the outgoing flux at the high-mass end, $F_{\rm out}$, the total mass growth per unit time by all the pre-existing GMCs, $\dot{M}_{\rm grow}$, and the total dispersed mass generated per unit time from the system, $\dot{M}_{\rm disp}$. They are given as:

$$F_{\rm in} = F(m_{\rm min}) = m_{\rm min}^2 n_{\rm cl}/T_{\rm f}\,, \tag{4.8}$$

$$F_{\rm out} = m_{\rm max}^2 n_{\rm cl}/T_{\rm f}\,, \tag{4.9}$$

$$\dot{M}_{\rm grow} = \int_{m_{\rm min}}^{m_{\rm max}} (n_{\rm cl} m/T_{\rm f})\,{\rm d}m\,, \tag{4.10}$$

$$\dot{M}_{\rm disp} = \int_{m_{\rm min}}^{m_{\rm max}} (n_{\rm cl} m/T_{\rm d})\,{\rm d}m\,. \tag{4.11}$$

With these quantities, $F(m_{\rm max})$ corresponds to $F_{\rm out} - \dot{M}_{\rm grow} + \dot{M}_{\rm disp}$. In the steady state, $F(m)$ is independent of m. Thus $F(m_{\rm min}) = F(m) = F(m_{\rm max})$ and this can be rewritten as:

$$F_{\rm in} = F_{\rm out} - \dot{M}_{\rm grow} + \dot{M}_{\rm disp}\,. \tag{4.12}$$

For massive GMCs, the power-law relation $n = Am^{-\alpha}$ is broken: the treatment is valid if we take $m_{\rm max} \approx m_{\rm trunc}$. For $m \gtrsim m_{\rm max}$, $T_{\rm f}$ is rapidly increases with mass and the dispersal becomes more important than the growth so that GMCs with $m \gtrsim m_{\rm max}$ are eventually dispersed. Therefore, $F_{\rm out}$ is interpreted as the mass dispersing rate at $m \geq m_{\rm max}$ and the total dispersal rate of GMCs is given by $\dot{M}_{\rm disp} + F_{\rm out}$. On the other hand, $F_{\rm in}$ means the formation rate of minimum-mass GMCs. Therefore, the resurrecting factor is given by

$$\varepsilon_{\rm res} = \frac{F_{\rm in}}{F_{\rm out} + \dot{M}_{\rm disp}}\,. \tag{4.13}$$

We consider that the GMCMF from $m_{\rm min}$ to $m_{\rm max}$ becomes in a steady state when

Table 4.1: Estimated resurrecting factor as a function of growth timescale

	Estimated $\varepsilon_{\rm res}$		
$\log(m_{\rm max})$	$T_{\rm f,fid} = 4.2$	$T_{\rm f,fid} = 10$	$T_{\rm f,fid} = 22.4$
($M_\odot$)	(Myr)	(Myr)	(Myr)
6.5	0.0201	0.0798	0.383

Note. Predicted $\varepsilon_{\rm res,std}$ for three timescales: $T_{\rm f,fid} = 4.2, 10$, and 22.4 Myr based on Equation (4.14). All the cases have a constant $T_{\rm d} = 14$ Myr.

$\varepsilon_{\rm res} = \varepsilon_{\rm res,std}$. Combined with Equation (4.12), $\varepsilon_{\rm res,std}$ is given as:

$$\begin{aligned} &\varepsilon_{\rm res,std} \\ &= \frac{F_{\rm in}}{F_{\rm in} + \dot{M}_{\rm grow}} \\ &= \begin{cases} \left\{1 + \frac{1}{2-\alpha}\left[\left(\frac{m_{\rm max}}{m_{\rm min}}\right)^{2-\alpha} - 1\right]\right\}^{-1} & (\text{for } \alpha \neq 2)\,, \\ \left[1 + \ln(m_{\rm max}/m_{\rm min})\right]^{-1} & (\text{for } \alpha = 2)\,. \end{cases} \end{aligned} \tag{4.14}$$

Table 4.1 shows the $\varepsilon_{\rm res,std}$ computed by Equation (4.14). Here, as a representative case of $m_{\rm max} < m_{\rm trunc}$, we opt to use $m_{\rm max} = 10^{6.2} M_\odot$, which is also consistent with the truncated mass scale observed in our computed GMCMF (see also Fig. 4.8). Because $m_{\rm max} \gg m_{\rm min}$, Equation (4.14) can be simplified as

$$\varepsilon_{\rm res,std} = \begin{cases} (2-\alpha)\left(\frac{m_{\rm min}}{m_{\rm max}}\right)^{2-\alpha} & (\text{for } \alpha < 2)\,, \\ \left[\ln(m_{\rm max}/m_{\rm min})\right]^{-1} & (\text{for } \alpha = 2)\,, \\ \frac{\alpha-2}{\alpha-1} \quad (\text{for } \alpha > 2)\,. \end{cases} \tag{4.15}$$

Note that the accuracy of the approximation $m_{\rm max} < m_{\rm trunc}$ differs between cases, and thus the computed GMCMFs exhibit the resurrecting factors that slightly deviate by a factor $0.6 - 1.2$ from Equation (4.14) (*i.e.*, Table 4.1).

The range of the resurrecting factor

The integration of Equation (4.4) over m from $m_{\rm min}$ to $m_{\rm max}$ results in

$$\begin{aligned} \frac{dM_{\rm total}}{dt} &= F(m_{\rm min}) - F(m_{\rm max})\,, \\ &= F_{\rm in} - F_{\rm out} - \dot{M}_{\rm disp} + \dot{M}_{\rm grow}\,, \\ &= \left(1 - \frac{1}{\varepsilon_{\rm res}}\right) F_{\rm in} + \dot{M}_{\rm grow}\,. \end{aligned} \tag{4.16}$$

where $M_{\rm total}$ is the total mass of GMCs from $m_{\rm min}$ to $m_{\rm max}$:

$$M_{\rm total} = \int_{m_{\rm min}}^{m_{\rm max}} m n_{\rm cl} {\rm d}m\,, \tag{4.17}$$

In the steady state, $dM_{\rm total}/dt = 0$ and $\varepsilon_{\rm res} = \varepsilon_{\rm res,std}$. Therefore,

$$\dot{M}_{\rm grow} = -\left(1 - \frac{1}{\varepsilon_{\rm res,std}}\right) F_{\rm in}\,. \tag{4.18}$$

The variation of $\varepsilon_{\rm res}$ changes $n_{\rm cl}$ and hence $\dot{M}_{\rm grow}$. However for simplicity, we here ignore the dependence of $\dot{M}_{\rm grow}$ on $\varepsilon_{\rm res}$ by considering $\varepsilon_{\rm res} \sim \varepsilon_{\rm res,std}$. From Equations (4.16) and (4.18), we obtain

$$\frac{dM_{\rm total}}{dt} = \left(\frac{1}{\varepsilon_{\rm res,std}} - \frac{1}{\varepsilon_{\rm res}}\right) F_{\rm in}\,. \tag{4.19}$$

If the GMCMF is steady and the total mass in the system $M_{\rm total}$ does not increase/reduce by factor β within a certain timescale $T_{\rm steady}$,

$$\left|\frac{\beta M_{\rm total}}{\dot{M}_{\rm total}}\right| \gtrsim T_{\rm steady}\,. \tag{4.20}$$

Combining with Equation (4.18), the range of $\varepsilon_{\rm res}$ that leads to steady state becomes:

$$\left(1 - \frac{\varepsilon_{\rm res,std}}{\varepsilon_{\rm res,std} + a}\right) \lesssim \frac{\varepsilon_{\rm res}}{\varepsilon_{\rm res,std}} \lesssim \left(1 + \frac{\varepsilon_{\rm res,std}}{a - \varepsilon_{\rm res,std}}\right)\,, \tag{4.21}$$

where $a = F_{\rm in} T_{\rm steady}/(M_{\rm total}\beta)$.

Figure 4.8 shows the $\varepsilon_{\rm res,std}$ and $\varepsilon_{\rm res}$ variation based on Equations (4.14) and (4.21) with $m_{\rm max} = 10^{6.2}{\rm M}_\odot$. Here, we assume that the GMCMF can be steady and localized within the half galactic rotation (in a case of two spiral arms in a galactic disk) so that $T_{\rm steady} = 100$ Myr and opt to use $\beta = 0.5$. The figure shows that $\varepsilon_{\rm res}$ increase with α. This trend is naturally expected because the inter-arm regions have less number of massive GMCs that can sweep up dispersed gas compared with the arm regions and dispersed gas easily produce minimum-mass GMCs when they experience multiple episodes of compression.

On the one hand, overwhelming resurrection more than the maximum $\varepsilon_{\rm res}$ increase the number density of GMCs, which ends up with the CCC-dominated regime after the long time elapse. On the other hand, the GMC number density decreases so that the GMCMF decays with resurrecting factor less than the minimum $\varepsilon_{\rm res}$.

Unseen gas

Up until now, we have shown that $\varepsilon_{\rm res}$ between $\mathcal{O}(0.01)$ to $\mathcal{O}(0.1)$ reproduces the observed GMCMF slope. The estimated face values themselves are important, but moreover, our results strongly suggest that understanding the fate of dispersed gas is inevitable to study the gas resurrecting processes in the ISM. The gas phases that are not well observed yet (*e.g.*, CO-dark H_2 gas (Hosokawa & Inutsuka 2006a; Tang et al. 2016; Xu et al. 2016) and optically thick HI gas (Fukui et al. 2015a))

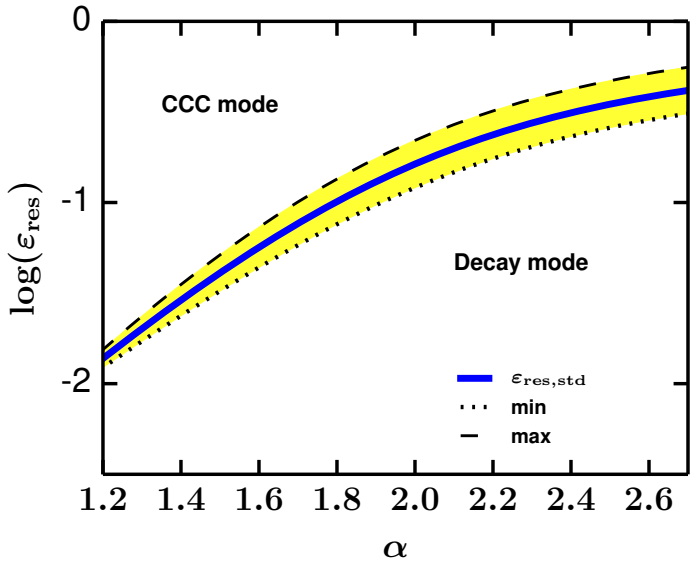

Figure 4.8: The range of the resurrecting factor, $\varepsilon_{\rm res}$, that sustain a steady GMCMF as a function of the GMCMF slope $-\alpha$ (*i.e.*, $n_{\rm cl}(m) \propto m^{-\alpha}$). The thick solid blue line shows the estimated $\varepsilon_{\rm res,std}$ based on Equation (4.14). The dotted and dashed lines correspond to minimum and maximum of $\varepsilon_{\rm res}$ evaluated from Equation (4.21) with $\beta = 0.5$, $T_{\rm steady} = 100$ Myr, and $m_{\rm max} = 10^{6.2}{\rm M}_{\odot}$. $\varepsilon_{\rm res}$ increases with α and saturates when α becomes large (*i.e.*, when the GMCMF has a steep slope) as expected from Equation (4.15). The variation of $\varepsilon_{\rm res}$ at a given α is less than one order of magnitude for all the α range. The GMCMFs with shallow slopes typically have $\varepsilon_{\rm res} = \mathcal{O}(10^{-2})$ whereas $\mathcal{O}(10^{-1})$ for steep slopes, which indicates that dispersed gas contributes more to the formation of newer generation GMC in inter-arm regions. The overloading resurrection more than maximum $\varepsilon_{\rm res}$ leads to the CCC-dominated regime. On the other hand, the GMCMF decays with the resurrection less than the minimum $\varepsilon_{\rm res}$.

also come into play as well as usual CO-bright molecular gas. Three dimensional detailed magnetohydrodynamics simulation, for example, is required to understand the evolution of those unseen gas phases and to test whether it reproduces $\varepsilon_{\rm res}$ that we predict here.

Note that, the amount of CO-dark gas generated by GMC dispersal depends on metallicity, which can be estimated as:

$$M_{\rm CO-dark} = 4\pi R_{\rm HII}^2 \, N_{\rm H}(A_{\rm V}) \, 1.4 m_{\rm H} \, . \tag{4.22}$$

Here, $M_{\rm CO-dark}$ is the generated mass of CO-dark gas, $R_{\rm HII}$ is the radius of individual HII regions, $N_{\rm H}(A_{\rm V})$ is the column density in a layer between the hydrogen ionization front and CO dissociation front as a function of the corresponding visual extinction $A_{\rm V}$ in that layer, and $m_{\rm H}$ is the mass of single hydrogen atom. The column density is observationally (mostly in X-rays) given as:

$$N_{\rm H}(A_{\rm V}) \simeq 2 \times 10^{21} \times A_{\rm V} \, . \tag{4.23}$$

(see Predehl & Schmitt 1995; Zhu et al. 2017). The self-shielding of hydrogen molecules requires $A_{\rm V} \sim 0.25$ whereas dust-shielding of CO molecules requires $A_{\rm V} \sim 2$ (Draine & Bertoldi 1996; Lee et al. 1996; Glover & Mac Low 2011)[2]. Therefore, lower-metallicity environment produces more CO-dark gas because the lengthscale corresponding to $A_{\rm V} \sim 2$ becomes longer with lower metallicity. If we consider a condition where (albeit this is unlikely in the real ISM),

4.3 Discussion: CCC Frequency and Its Impact

In this section, we briefly discuss CCC frequency and connection to star formation on galactic scales. Other caveats and possible modifications in our formulation will be covered later in Chapter 6 in detail.

Our results by now indicate that CCC is limited only at the massive-end and does not alter the GMCMF time evolution significantly. This seems contrary to the CCC importance suggested by galactic simulations and observations, but this is still consistent. The collision timescale typically varies from 1 to 100 Myr (see Figure 3.3), which is consistent with global galactic simulations (*c.f.*, 25 Myr by Tasker & Tan (2009), 8 - 28 Myr by Dobbs et al. (2015)). Figure 3.3 shows that GMCs $> 10^6 {\rm M}_\odot$ experience CCC much more frequently than GMCs $< 10^5 {\rm M}_\odot$ as expected by the kernel function (Equation (3.6)). The lack of star cluster formation during CCC in our calculation by now generates many massive GMCs at the massive-end (*c.f.*, Tasker & Tan 2009). However, we expect that such drastic star

[2]The bond dissociation energy for CO molecules is 11.1 eV (Pauling & Sheehan 1949; Brackett 1956) whereas that for hydrogen molecules is 4.5 eV (Kołos & Wolniewicz 1965; Liu et al. 2009). Note that CO molecules in the ISM are not abundant enough to be self-shielded thus require dust-shielding; the typical ratio of CO molecules to hydrogen molecules is the order of 10^{-6} in the ISM (*e.g.*, Burgh et al. 2007; Sheffer et al. 2008) and 10^{-4} in dark clouds (*e.g.*, Young & Scoville 1991) See also Glover & Clark (2015) for simulations of low-metallicity environments.

cluster formation take place only when larger GMCs collide each other (Fukui et al. 2014), which may affect the massive-end but not the slope. Therefore, our results indicate that inclusion of star cluster formation still does not impact the GMCMF slope significantly. We will prove this speculation by modeling CCC-driven star formation in Chapter 5.

Chapter 5

CCC-Driven Star Formation[1]

5.1 Two GMC Populations: reformulation including star formation induced by cloud-cloud collisions

In our previous time evolution equation introduced in equation (3.1), we do not implement any rapid star formation triggered by CCC. However, observations of compact star cluster forming sites (*e.g.* Torii et al. 2011; Kudryavtseva et al. 2012; Torii et al. 2015; Fukui et al. 2016, 2017c; Kohno et al. 2017) indicate that GMCs are likely to form stars effectively (within a short timescale $\lesssim 1$ Myr) after GMCs experience CCC, because of drastic compression of WNM and high accretion rate by enhanced sound velocity (*c.f.*, Inoue et al. 2017). Increasing number of CCC-candidate clouds reported from radio observations (*e.g.* Fukui et al. 2014, 2016) and the indication of frequent CCC events in galactic disk simulations (*e.g.*, Tasker & Tan 2009; Dobbs et al. 2015) suggest the importance in the investigation of the impact of CCC-driven star formation onto GMCMF evolution and its relative contribution to star formation rate (SFR) for the entire galactic disks.

Before calculating the SFR, we first introduce a revised version of time evolution equation for GMCMF, by specifying the evolution of GMCs that are undergoing the feedback from CCC-driven star cluster formation. To do this, we subdivide GMC populations into two: the differential number density of GMCs of mass m without experiencing CCC, $n_{\rm acc,cl}(m)$, and the one with CCC experience, $n_{\rm col,cl}(m)$. Hereafter, we call the GMC populations in $n_{\rm acc,cl}(m)$ as "normal" GMCs and the ones in $n_{\rm col,cl}(m)$ as "CCC" GMCs. The total differential number density of GMCs with mass m, $n_{\rm cl}(m)$ is given as

$$n_{\rm cl}(m) = n_{\rm acc,cl}(m) + n_{\rm col,cl}(m)\,. \tag{5.1}$$

The basic evolution follows the same equation as equation (4.3), but only CCC GMCs would have a shorter timescale for $T_{\rm d}$. Thus the revised evolution equation

[1] *The contents of this chapter are partially based upon the articles Kobayashi et al. (2017b) and Kobayashi et al. (2017a).*

becomes

$$\begin{aligned}
&\frac{\partial\left(n_{\rm acc,cl}+n_{\rm col,cl}\right)}{\partial t}+\frac{\partial}{\partial m}\left(\left(n_{\rm acc,cl}+n_{\rm col,cl}\right)\frac{m}{T_{\rm f}}\right)\\
=\;&-\frac{n_{\rm acc,cl}}{T_{\rm d}}-\frac{n_{\rm col,cl}}{T_{\rm d,col}}\\
&+\frac{1}{2}\int_0^\infty\int_0^\infty K(m_1,m_2)\\
&\quad\times\left(n_{\rm acc,cl,1}+n_{\rm col,cl,1}\right)\left(n_{\rm acc,cl,2}+n_{\rm col,cl,2}\right)\\
&\quad\times\delta(m-m_1-m_2){\rm d}m_1{\rm d}m_2\\
&-\int_0^\infty K(m,m_2)\\
&\quad\times\left(n_{\rm acc,cl}+n_{\rm col,cl}\right)\left(n_{\rm acc,cl,2}+n_{\rm col,cl,2}\right){\rm d}m_2\\
&+\frac{1}{m}\left.\frac{\partial\left(n_{\rm cl}m\right)}{\partial t}\right|_{\rm res}. \qquad (5.2)
\end{aligned}$$

The subscripts 1 and 2 represent the mass bins m_1 and m_2 (*e.g.*, $n_{\rm acc,cl,1}=n_{\rm acc,cl}(m_1)$).

This equation can be separated into two equations in which we calculate the time-evolution of $n_{\rm acc,cl}(m)$ and $n_{\rm col,cl}(m)$ respectively. For normal GMCs,

$$\begin{aligned}
&\frac{\partial n_{\rm acc,cl}}{\partial t}+\frac{\partial}{\partial m}\left(m\frac{n_{\rm acc,cl}}{T_{\rm f}}\right)\\
=\;&-\frac{n_{\rm acc,cl}}{T_{\rm d}}\\
&-\frac{n_{\rm acc,cl}}{n_{\rm cl}}\int_0^\infty K(m,m_2)\\
&\quad\times\left(n_{\rm acc,cl}+n_{\rm col,cl}\right)\left(n_{\rm acc,cl,2}+n_{\rm col,cl,2}\right){\rm d}m_2\\
&+\frac{1}{m}\left.\frac{\partial\left(n_{\rm cl}m\right)}{\partial t}\right|_{\rm res}, \qquad (5.3)
\end{aligned}$$

and for CCC GMCs,

$$\begin{aligned}
&\frac{\partial n_{\rm col,cl}}{\partial t}+\frac{\partial}{\partial m}\left(m\frac{n_{\rm col,cl}}{T_{\rm f}}\right)\\
=\;&-\frac{n_{\rm col,cl}}{T_{\rm d,col}}\\
&+\frac{1}{2}\int_0^\infty\int_0^\infty K(m_1,m_2)\\
&\quad\times\left(n_{\rm acc,cl,1}+n_{\rm col,cl,1}\right)\left(n_{\rm acc,cl,2}+n_{\rm col,cl,2}\right)\\
&\quad\times\delta(m-m_1-m_2){\rm d}m_1{\rm d}m_2\\
&-\frac{n_{\rm col,cl}}{n_{\rm cl}}\int_0^\infty K(m,m_2)\\
&\quad\times\left(n_{\rm acc,cl}+n_{\rm col,cl}\right)\left(n_{\rm acc,cl,2}+n_{\rm col,cl,2}\right){\rm d}m_2\,. \qquad (5.4)
\end{aligned}$$

We give the ample descriptions on each term in the following subsections.

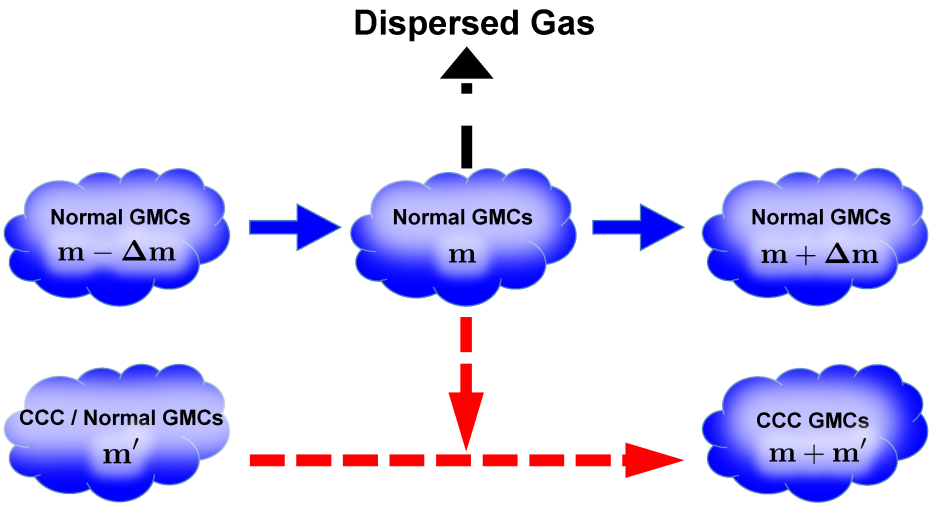

Figure 5.1: Flowchart 1 describing the mass-growth, self-dispersal, and CCC of normal GMCs with mass m. The solid blue lines correspond to the mass-growth due to multiple episodes of supersonic compressions. Given a mass bin width Δm in calculation, the multiple compressions grow GMCs from mass $m - \Delta m$ through m to $m + \Delta m$. The red dashed lines show the CCC process. When normal GMCs with mass m collide with GMCs with mass m' (either in normal or CCC populations), they coagulate together to create bigger GMCs with mass $m + m'$, which join CCC populations but not normal populations. The black dot-dashed lines are GMC self-dispersal.

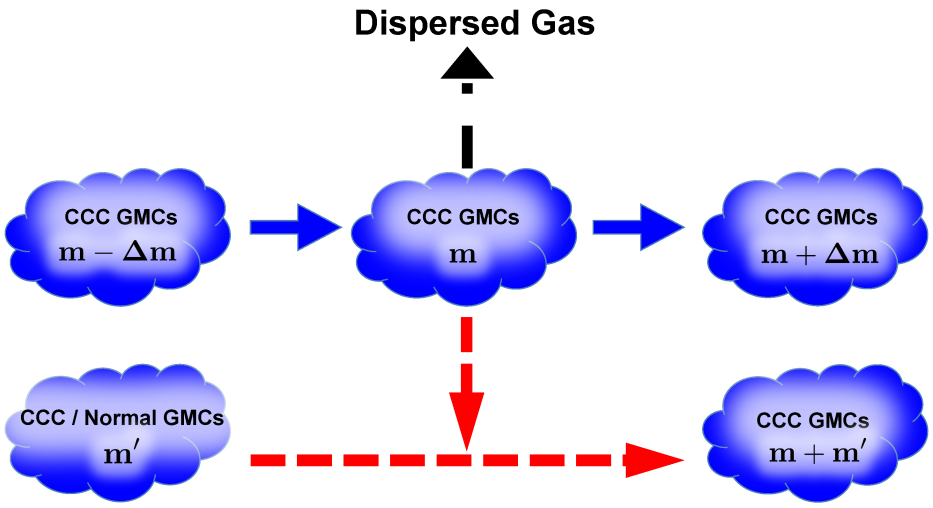

Figure 5.2: Flowchart 2 describing the mass-growth, self-dispersal, and CCC of CCC GMCs with mass m. The solid blue lines correspond to the mass-growth due to multiple episodes of supersonic compressions. Given a mass bin width Δm in calculation, the multiple compressions grow GMCs from mass $m-\Delta m$ through m to $m+\Delta m$. Here, we assume that CCC GMCs remain in CCC populations through this mass-growth because they are undergoing stellar feedback triggered by CCC, which separates normal and CCC populations. The red dashed lines show the CCC process. When CCC GMCs with mass m collide with GMCs with mass m' (either in normal or CCC populations), they coagulate together to create bigger GMCs with mass $m+m'$, which join CCC populations but not normal populations. The black dot-dashed lines are GMC self-dispersal, which have a shorter characteristic dispersal timescale compared with the one in normal populations as discussed in subsection 5.1.2.

5.1.1 Self-Growth Term

The second terms in equations (5.3) and (5.4) correspond to GMC mass-growth due to multiple episodes of supersonic compression. We assume that both normal population $n_{\rm acc,cl}(m)$ and CCC population $n_{\rm col,cl}(m)$ have the same $T_{\rm f}$ because the mass-growth driven by the phase transition dynamics presumably does not distinguish whether or not GMCs experience CCC. Therefore, the mass-growth rate for both populations can be characterized as $m/T_{\rm f}$ (see section 3.1.1 for the justification how $m/T_{\rm f}$ can be the mass-growth rate under the multiple episodes of supersonic compressions). A schematic flowchart of this mass-growth is shown as blue solid lines in figures 5.1 and 5.2.

5.1.2 Dispersal Term

The first terms on the right hand side of equations (5.3) and (5.4) represent GMC self-dispersal due to stellar feedback by massive stars born within GMCs. Simulations of colliding GMCs (Inoue & Fukui 2013; Takahira et al. 2014; Inoue et al. 2017) suggest triggering core formation in the shock-compressed layer. Especially, Inoue & Fukui (2013) and Inoue et al. (2017) indicate that the effective sound speed and resultant effective Jeans mass increase in the layer so that CCC enables rapid massive star formation. In addition, observations suggest that GMCs undergoing CCC may form stars within a very short timescale $\lesssim 1$ Myr (*c.f.* Kudryavtseva et al. 2012; Fukui et al. 2016). We therefore assume that, with a shorter star formation timescale $T_* = 1$ Myr, CCC GMCs have their dispersal timescale $T_{\rm d,col} = T_* + T_{\rm dest} = 5$ Myr. A schematic flowchart of these dispersal processes is shown as black dot-dashed lines in figures 5.1 and 5.2.

From the observational viewpoint, the stellar initial mass function (IMF) might be a top-heavy in cluster forming regions (*e.g.*, NGC6334: Muñoz et al. (2007), NGC3603:Harayama et al. (2008)). Magnetohydrodynamics simulations also demonstrate such top-heavy trend in CCC sites (at least before cores grow by mass accretion; *e.g.*, Inoue & Fukui (2013)). However for simplicity, we assume Salpeter IMF on the entire cloud scales even for GMCs undergoing or having undergone CCC. We opt to employ the same $T_{\rm dest} = 4$ Myr for both normal and CCC GMCs assuming that both GMC populations have the same dispersal efficiency with Salpeter IMF, whereas the star formation timescale T_* alone is shorter for CCC populations.

5.1.3 Cloud-Cloud Collision Terms

The second term on the right hand side of equation (5.3) and the last two terms in equation (5.4) correspond to CCC process. Equation (5.3) has only one term because CCC process decreases but never increase the normal GMC populations. Similarly to our previous analyses in the previous chapters, we assume that CCC would work as a coagulation process so that colliding GMCs essentially form a larger GMC. Thus, the last term in equation (5.3) represents the formation of CCC

GMCs with mass $m + m_2$ through the CCC between GMCs with mass m and m_2. Similarly, the first CCC term in equation (5.4) represents the formation of CCC GMCs with mass m through the CCC between GMCs with mass m_1 and m_2. Also, the second CCC term in equation (5.4) represents the formation of CCC GMCs with mass $m + m_2$ through the CCC between GMCs with mass m and m_2. In this formulation, we assume a perfect inelastic collision for the CCC, as we did in our previous formulation shown in Equation (3.1).

We classify the resultant massive GMCs as CCC populations. This treatment restricts ourselves to assuming that rapid star formation is always invoked once GMCs experience CCC no matter what combination of GMC collide (*i.e.*, collisions between normal populations, CCC populations, or normal and CCC populations). In this manner, GMCs become quickly dispersed once they experience CCC with a shorter dispersal timescale $T_{\rm d,col}$ compared with normal GMCs. A schematic flow of this CCC process is shown as red dashed lines in figures 5.1 and 5.2.

Note that the CCC-driven star formation and subsequent stellar feedback in our calculation does not create any smaller GMCs and thus CCC GMCs simply disperse at a given rate of $1/T_{\rm d,col}$. The creation of such smaller GMCs by stellar feedback would impact the power-law slope in the low-mass regime, which needs to be investigated further in the future.

5.1.4 Gas Resurrection

As defined in the previous chapter, the gas resurrection produces and replenishes minimum-mass GMC populations. In this study, minimum-mass GMCs have only normal population but not CCC population because our CCC implementation does not produce any smaller mass clouds. Therefore, the gas resurrection term appears only in equation (5.3) but not in equation (5.4). This gas resurrection rate is calculated by equation (4.1). The mass production rate of dispersed gas, $\dot{\rho}_{\rm total,disp}$, should be computed from both normal and CCC GMC populations thus is computed as

$$\dot{\rho}_{\rm total,disp} = \int \frac{m n_{\rm acc,cl}}{T_{\rm d}} {\rm d}m + \int \frac{m n_{\rm col,cl}}{T_{\rm d,col}} {\rm d}m \,. \tag{5.5}$$

We estimate that the steady state resurrecting factor for a typical galactic disk is about $\varepsilon_{\rm res} = 0.15$ (*i.e.*, 15 per cent gas resurrection (Kobayashi et al. 2017b)). We solve equation (5.2) simultaneously with equation (4.1) to calculate the gas resurrection.

5.2 Results

5.2.1 Slope of Giant Molecular Cloud Mass Function

We perform time integration of equation (5.2) coupled with equation (4.1). Figure 5.3 shows the resultant time evolution of GMCMF. We opt to employ our fidu-

cial parameters (*i.e.*, $T_{\rm f,fid} = 10$ Myr, $T_{\rm d} = 14$ Myr, $T_{\rm d,col} = 5$ Myr, $\varepsilon_{\rm res} = 0.15$). The figure includes a reference dot-dashed line showing the steady state power-law slope characterized by equation (3.11). GMCMF in the mass range $m \lesssim 10^{5.5}{\rm M}_\odot$ shows a single power-law slope close to this steady state solution. Compared with Figure 4.2 in the previous section where we calculated essentially the same condition but without CCC-driven star formation, the number of massive GMCs $\gtrsim 10^6{\rm M}_\odot$ shown in figure 5.3 decreases due to star formation driven by CCC and subsequent stellar feedback. Figure 5.3 also suggests that the power-law slope in the mass range $m \lesssim 10^{5,5}{\rm M}_\odot$ is still preserved over the GMCMF evolution even with CCC-driven star formation. Therefore, our result indicates that CCC impacts only the massive-end of GMCMF.

5.2.2 Star Formation Efficiency and Star Formation Rate

To determine the relative contributions of normal and CCC GMCs onto star formation on galactic scales, we need to calculate SFR in each population. In this study, we opt to employ a given star formation efficiency (SFE) averaged over all GMC populations to calculate SFR coarse-grained on galactic scale.

Hereafter, we define SFE, $\varepsilon_{\rm SFE}$, as the final mass fraction that goes into stars from a parental GMC at the time when the entire GMC becomes completely dispersed. Cumulative SFR can be evaluated as the product of SFE and the dispersal term in equation (5.2):

$$\begin{aligned} {\rm SFR}(>m) &= \varepsilon_{\rm SFE} \\ &\times \left(\int_m^\infty \frac{m n_{\rm acc,cl}}{T_{\rm d}}\, {\rm d}m + \int_m^\infty \frac{m n_{\rm col,cl}}{T_{\rm d,col}}\, {\rm d}m \right) . \end{aligned} \tag{5.6}$$

The first term corresponds to star formation due to normal GMC populations whereas the second term represents star formation originated in CCC GMC populations. For simplicity, we assume that the star formation timescale differs between two populations as included in $T_{\rm d}$ and $T_{\rm d,col}$ but the resultant SFE is the same for both populations as $\varepsilon_{\rm SFE}$.

Given a $n_{\rm cl}$ and $\varepsilon_{\rm SFE}$, one can calculate cumulative SFR with this equation. On one hand, we evaluate $n_{\rm cl}$ directly from the calculated GMCMF. On the other hand, we need to model $\varepsilon_{\rm SFE}$. In principle, individual GMCs can have different SFE. Observationally, SFE averaged over a galactic disk is equal to a few per cent (Zuckerman & Evans 1974). In this study, we employ a fixed efficiency 1 per cent as an ensemble-averaged SFE for simplicity. This 1 per cent can be obtained as follows. Given the Salpeter IMF, one massive star $\gtrsim 20{\rm M}_\odot$ can be born out of $1000{\rm M}_\odot$ star cluster. Such single massive star may disperse its parental cloud up to $10^5{\rm M}_\odot$ according to a detail line-radiation magnetohydrodynamics simulations (Hosokawa & Inutsuka 2006b; Inutsuka et al. 2015). This suggests that SFE is 1 per cent on average (1000 ${\rm M}_\odot$ star out of $10^5{\rm M}_\odot$ GMC). This efficiency is essentially

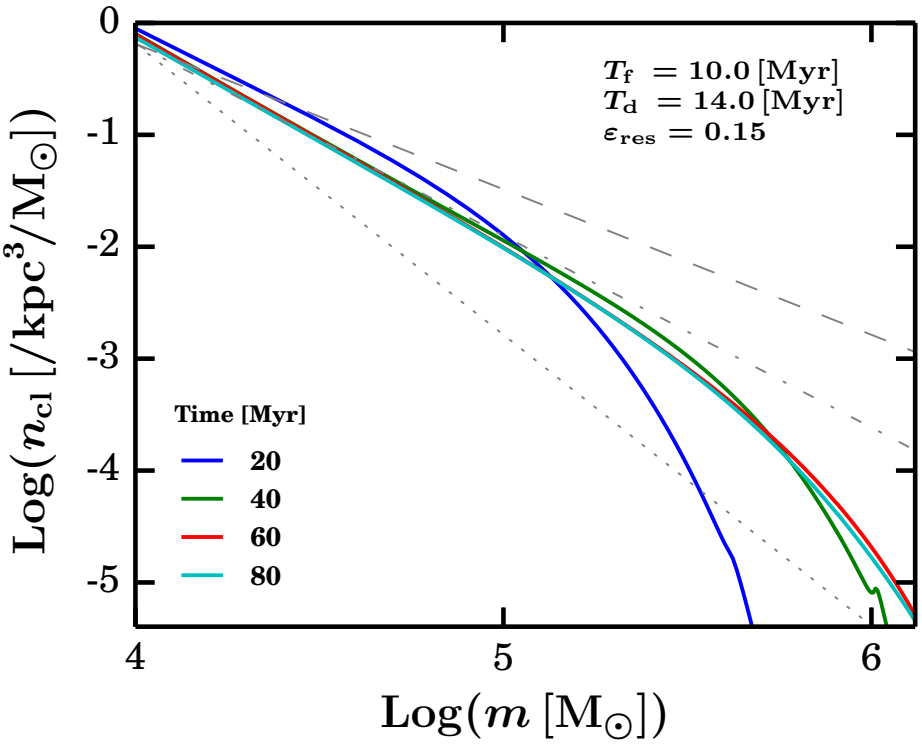

Figure 5.3: Differential number density $n_{\rm cl}$ as a function of GMC mass, with $T_{\rm f,fid} = 10$ Myr, $T_{\rm d} = 14$ Myr, $T_{\rm d,col} = 5$ Myr, $\varepsilon_{\rm res} = 0.15$. The color corresponds to time evolution. As a reference, we plot three thin gray lines; the dot-dashed line represents the steady state power-law slope $-1 - T_{\rm f}/T_{\rm d} \sim -1.7$, the dashed line corresponds to the observed shallow slope in arm regions of Galaxy M51, and the dotted line corresponds to the observed steep slope in inter-arm regions of Galaxy M51. The calculated GMCMF shows a power-law slope $\lesssim 10^{5.5}{\rm M}_\odot$ close to the steady state slope indicated by equation (3.11).

constant with GMC mass because massive GMCs $> 10^5 \mathrm{M}_\odot$ create more massive stars and more dispersal. Therefore, we employ $\varepsilon_{\mathrm{SFE}} = 0.01$ as our fiducial value.

Note that, this mass-independent SFE is not applicable to the low-mass GMCs $\lesssim 10^5 \mathrm{M}_\odot$ because their molecular gas mass is insufficient to produce a massive star that can blow out the entire parental GMC unless the stellar IMF in such low-mass GMCs prefer top-heavy IMF than Salpeter IMF. We are planning to investigate this effect in the future. Also note that we use T_{d} and $T_{\mathrm{d,col}}$ but neither T_* nor T_{dest} in equation (5.6) because of our definition of SFE.

Figure 5.4 shows the time evolution of cumulative SFR as a function of GMC mass in solid lines. This shows that the cumulative SFR becomes $\mathcal{O}(10^5)\mathrm{M}_\odot$ kpc^{-3} Myr^{-1}, which corresponds to the typical SFR of a few solar mass per year over a galactic disk (*e.g.*, the Milky Way galaxy by Spitzer data Robitaille & Whitney (2010)). In figure 5.4, we also plot the CCC-driven cumulative SFR in dotted lines, which is a fraction of total cumulative SFR. This suggests that most of the CCC-driven SFR comes from GMCs with mass $\gtrsim 10^{5.5}\mathrm{M}_\odot$, where the GMCMF slope is significantly deviated from the steady state power-law slope. In addition, the $\mathrm{SFR}(> 10^4\mathrm{M}_\odot)$ indicates that the CCC-driven SFR may amount to a few 10 per cent (at most half) of the total SFR on galactic disk. Our calculated CCC-driven SFR is likely to be overestimated and may correspond to an upper limit because our formulation allows all colliding GMCs to coagulate together even when only their peripheries touch each other. This overestimation is also due to assumed star formation efficiency in CCC GMCs (see subsection 5.3.1).

As star formation goes, the GMC mass gradually accumulate into stars. Our time-evolution equation (equation (5.2)) does not explicitly track such mass transformation. Although this is a very gradual process compared with other processes (mass-growth, dispersal, and CCC), the such mass becomes $\sim 10^8\mathrm{M}_\odot$ accumulated over an entire galactic disk, if we integrate the evolution equation more than 100 Myr with a given SFR about a few solar mass per year. This may amount to at least a few per cent of the total molecular gas budget in a single galaxy. Therefore, to extend the current semi-analytical formulation to galaxy evolution over cosmological timescale, mass transformation into stars needs to be formulated. We reserve this long-term evolution for future work. In this case, we also must take into account the gas inflow from halos down to galactic disks, which needs to be conducted together with cosmological large-scale structures.

5.2.3 Cloud-Cloud Collision Frequency as a Function of GMC Mass

In this subsection, we quantify the CCC frequency as a function of GMC mass. We can define two different timescales that characterize CCC process: "number collision timescale" and "mass collision timescale".

Based on the collision term in equation (5.2), the total number of collisions that a single GMC with mass m experiences per unit time is given as the following

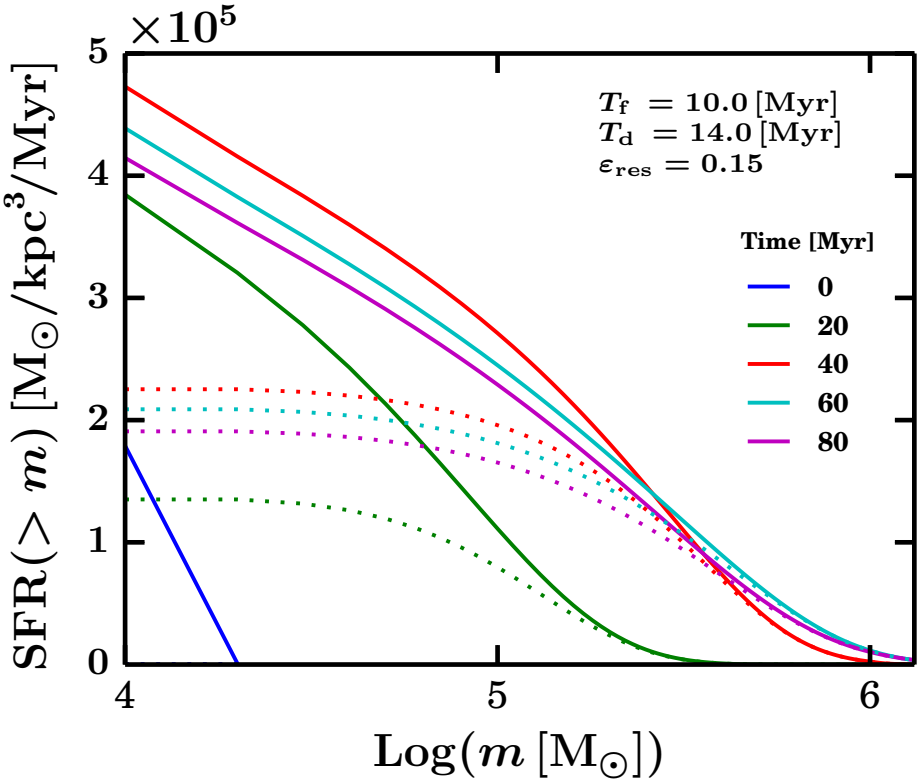

Figure 5.4: Cumulative star formation rate $\mathrm{SFR}(> m)$ as a function of GMC mass. The color corresponds to time evolution. The solid lines represent the overall cumulative SFR originating from normal and CCC GMCs, whereas the dotted lines show the cumulative SFR originated only in CCC GMCs. The vertical axis is in the unit of $\mathrm{M}_\odot\,\mathrm{kpc}^{-3}\,\mathrm{Myr}^{-1}$, thus total SFR on a galactic disk whose volume is similar to that of the Milky Way galaxy (*e.g.*, 10 kpc $\times$ 10 kpc $\times$ 100 pc) is a few solar mass per year in the range plotted here. This is a good agreement with observed typical SFR in the Milky Way and nearby galaxies.

integration:

$$\begin{aligned} & \int K(m, m_2) n_{\rm cl,2} {\rm d}m_2 \\ = & \int K(m, m_2) n_{\rm cl,2} m_2 {\rm d} \ln m_2 \, . \end{aligned} \tag{5.7}$$

Therefore, the CCC event rate between a single GMC with mass m and GMCs with m_2 with a given differential number density $n_{\rm cl,2}$ per unit logarithmic mass interval $\Delta \ln m_2$ is

$$K(m, m_2) n_{\rm cl,2} m_2 \, . \tag{5.8}$$

One can evaluate the typical collision timescale for a single GMC with mass m colliding with a GMC with mass m_2 as

$$T_{\rm col,num}(m, m_2) = \frac{1}{K(m, m_2) n_{\rm cl,2} m_2} \, . \tag{5.9}$$

Let us call this timescale $T_{\rm col,num}$ as "number collision timescale" because this is an e-folding timescale for the number of GMCs with mass m. Similarly, the total mass-gain (*i.e.*, mass-growth) of a single GMC with mass m due to CCC is given as the following integration:

$$\begin{aligned} & \int K(m, m_2) n_{\rm cl,2} m_2 {\rm d}m_2 \\ = & \int K(m, m_2) n_{\rm cl,2} m_2 m_2 {\rm d} \ln m_2 \, . \end{aligned} \tag{5.10}$$

Therefore, we can also define another typical timescale, over which a GMC with mass m grows in mass due to CCC with GMCs of mass m_2 per unit logarithmic mass interval $\Delta \ln m_2$ as:

$$T_{\rm col,mass}(m, m_2) = \frac{m}{K(m, m_2) n_{\rm cl,2} m_2 m_2} \, . \tag{5.11}$$

Let us name this timescale $T_{\rm col,mass}$ as "mass collision timescale" because this is an e-folding timescale for the total mass of GMCs with mass m. The CCC frequency for a given GMC population with mass m is therefore characterized as a function of m_2 by $T_{\rm col,num}(m, m_2)$ and $T_{\rm col,mass}(m, m_2)$.

Note that our formulation treats the CCC between GMCs with mass m and m_2 as a coagulation resulting into a GMC with mass $m+m_2$. Therefore, $T_{\rm col,mass}(m, m_2)$ in the regime of $m \gg m_2$ represents the mass-growth timescale of GMCs with mass m, which corresponds to the time evolution of GMCMF around mass m. However in the regime of $m \ll m_2$, the collisional outcome with mass $m + m_2$ is significantly larger than a GMC with mass m, thus $T_{\rm col,mass}(m, m_2)$ does not necessarily represent the time evolution of GMCMFs. For example, a CCC between GMCs with mass $10^4 {\rm M}_\odot$ and $10^6 {\rm M}_\odot$ forms a GMC with mass $1.01 \times 10^6 {\rm M}_\odot$. For

the GMC with mass $10^4 \mathrm{M}_\odot$, this coagulation effectively looks like rapid mass-growth. However, in terms of the GMCMF time evolution, this appears as the gradual mass-growth of GMCs at mass $10^6 \mathrm{M}_\odot$. It is thus more useful to compare $T_{\mathrm{col,mass}}(m, m_2)$ only in the regime of $m \geq m_2$ with other timescales (*e.g.*, T_{f} and T_{d}) when we discuss the time evolution of GMCMFs.

Number Collision Timescale

The left panel in figure 5.5 shows $T_{\mathrm{col,num}}$ as a function of mass pair in one CCC event. Based on its definition in equation (5.9), $T_{\mathrm{col,num}}(m, m_2)$ represents the e-folding timescale for a single GMC with mass m due to the collisions with GMCs with mass m_2. Thus the physical meaning of $T_{\mathrm{col,num}}(m, m_2)$ is different from that of $T_{\mathrm{col,num}}(m_2, m)$. Indeed, figure 5.5 shows such asymmetry between m and m_2. Note that, $T_{\mathrm{col,num}}(m, m_2)$ and $T_{\mathrm{col,num}}(m_2, m)$ differ from the total collisional event rate between m and m_2, which is symmetric between m and m_2. We discuss the total collisional event rate in section 5.2.3.

The figure indicates that massive GMCs (*i.e.*, larger mass range in the horizontal axis) have higher opportunity to collide with smaller clouds than with massive clouds because the number density of smaller clouds is larger than that of massive clouds. Due to the same reason, smaller GMCs (*i.e.*, smaller mass range in the horizontal axis) also have higher opportunity to collide with smaller clouds than with massive clouds. Such intuitive understanding can be analytically confirmed by equation (5.9) as follows. In $m \gg m_2$ regime, $T_{\mathrm{col,num}}$ can be written as:

$$T_{\mathrm{col,num}}(m, m_2) \propto \frac{1}{m m_2^{1-\alpha}} \,. \tag{5.12}$$

Therefore $T_{\mathrm{col,num}}$ becomes longer with m_2 as $T_{\mathrm{col,num}} \propto m_2^{0.7}$ given the typical GMCMF slope $-\alpha \sim -1.7$ as shown in figure 5.3. This corresponds to the increasing trend of $T_{\mathrm{col,num}}$ along the vertical axis at a given large mass in the horizontal mass coordinate in figure 5.5. Note that $T_{\mathrm{col,num}}(m, m_2)$ increases faster than $m_2^{0.7}$ in the range of $m_2 > 10^{5.5} \mathrm{M}_\odot$. In this regime, the GMCMF deviates from the power-law distribution assumed in equation 5.12. Thus, $T_{\mathrm{col,num}}(m, m_2)$ rapidly increases as $n_{\mathrm{cl},2}$ decreases with m_2. The resultant difference in $T_{\mathrm{col,num}}$ is two or more orders of magnitude (*e.g.*, between $T_{\mathrm{col,num}}(10^6 \mathrm{M}_\odot, 10^4 \mathrm{M}_\odot)$ and $T_{\mathrm{col,num}}(10^6 \mathrm{M}_\odot, 10^6 \mathrm{M}_\odot)$). On the other hand, in $m \lesssim m_2$ regime, $T_{\mathrm{col,num}}$ can be evaluated as:

$$T_{\mathrm{col,num}}(m, m_2) \propto \frac{1}{m_2^{2-\alpha}} \,. \tag{5.13}$$

Therefore $T_{\mathrm{col,num}}$ becomes shorter with m_2 as $T_{\mathrm{col,num}} \propto m_2^{-0.3}$ given the typical GMCMF slope $-\alpha \sim -1.7$ as shown in figure 5.3. This corresponds to the decreasing trend of $T_{\mathrm{col,num}}$ along the vertical axis at a given small mass in the horizontal mass coordinate in figure 5.5. However, its dependence on m_2 is limited to the power of $2 - \alpha = 0.3$ thus this trend is difficult to recognize in figure 5.3. In

addition, similar to equation (5.12), the power-law GMCMF assumption in equation (5.13) is invalid in the range of $m_2 > 10^{5.5}\mathrm{M}_\odot$. Thus $T_{\mathrm{col,num}}(m, m_2)$ increases rapidly as $n_{\mathrm{cl},2}$ decreases with m_2.

Note that the above discussion is based on GMCMF with $-\alpha \sim -1.7$ assuming that this represents overall averaged GMC population on a galactic disk. However, in case of inter-arm regions with $-\alpha < -2$ for example, $T_{\mathrm{col,num}}$ is always increasing function with m_2 because the number of large clouds is very few.

Mass Collision Timescale

As seen in section 5.2.3, $T_{\mathrm{col,num}}$ characterizes the frequency of individual CCC events that a single GMC with mass m experiences. However this does not always characterize impact on GMCMF evolution, because, for example, collision with small clouds may not largely contribute to mass-growth of massive clouds, which is not appreciable in GMCMF evolution. Therefore, we evaluate the mass-growth driven by CCC by calculating $T_{\mathrm{col,mass}}$, which gives the typical e-folding time in mass for a single GMC with mass m by CCC. The right panel in figure 5.5 shows $T_{\mathrm{col,mass}}$ as a function of GMC masses in a given GMC pair. This panel indicates that the mass-growth of massive clouds is still dominated by CCC with small to inter-mediate mass clouds. However, such CCC events increase only limited amount of mass so that $T_{\mathrm{col,mass}}$ has only up to one order of magnitude difference from that of CCCs between massive GMCs.

These trends can be analytically confirmed by equation (5.11) as follows, similar to the discussion for $T_{\mathrm{col,num}}$. In $m \gg m_2$ regime, $T_{\mathrm{col,mass}}$ can be written as:

$$T_{\mathrm{col,mass}}(m, m_2) \propto \frac{1}{m_2^{2-\alpha}} \,. \tag{5.14}$$

Therefore $T_{\mathrm{col,mass}}$ becomes shorter with m_2 as $T_{\mathrm{col,mass}} \propto m_2^{-0.3}$ given the typical GMCMF slope $-\alpha \sim -1.7$ as shown in figure 5.3. This corresponds to the decreasing trend of $T_{\mathrm{col,mass}}$ along the vertical axis at a given large mass in the horizontal mass coordinate in figure 5.5. Again, the rapid increment in $T_{\mathrm{col,mass}}$ in the range of $m_2 > 10^{5.5}\mathrm{M}_\odot$ corresponds to the deviation of the GMCMF from the power-law distribution in this mass range.

Similarly, in $m \lesssim m_2$ regime, $T_{\mathrm{col,mass}}$ can be evaluated as:

$$T_{\mathrm{col,mass}}(m, m_2) \propto \frac{m}{m_2^{3-\alpha}} \,. \tag{5.15}$$

Therefore $T_{\mathrm{col,mass}}$ becomes shorter with m_2 as $T_{\mathrm{col,mass}} \propto m_2^{-1.3}$ given the typical GMCMF slope $-\alpha \sim -1.7$ as shown in figure 5.3. This corresponds to the decreasing trend of $T_{\mathrm{col,mass}}$ along the vertical axis at a given small mass in the horizontal mass coordinate in figure 5.5. The slight increment in $T_{\mathrm{col,mass}}$ in the range of $m_2 > 10^{5.5}\mathrm{M}_\odot$ corresponds to the deviation of the GMCMF from the power-law distribution in this mass range.

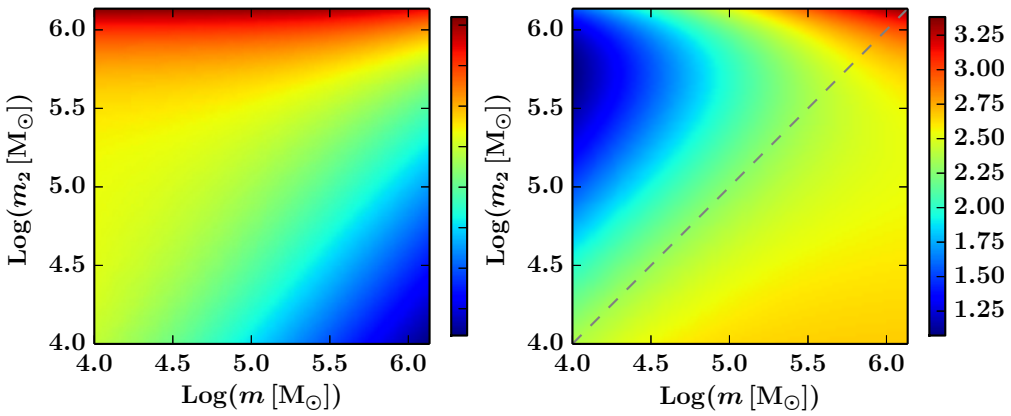

Figure 5.5: Left: The typical "number collision timescale" $T_{\rm col,num}(m, m_2)$ as a function of GMC mass combination involved in a CCC at 60 Myr. The horizontal axis corresponds to m and the vertical axis corresponds to m_2. The color scale corresponds to $\log_{10}(T_{\rm col,num}[{\rm Myr}])$. Right: The typical "mass collision timescale" $T_{\rm col,mass}(m, m_2)$ as a function of GMC mass combination involved in a CCC at 60 Myr. The horizontal axis corresponds to m and the vertical axis corresponds to m_2. The color scale corresponds to $\log_{10}(T_{\rm col,mass}[{\rm Myr}])$. The thin gray dashed line divides the panel into two regimes: $m > m_2$ (lower-right) and $m < m_2$ (upper-left).

Note that, as we have already discussed in the paragraph following equation (5.11), only the right-lower half of this panel (*i.e.*, $m \geq m_2$ regime) can be directly compared with other timescales governing the GMCMF evolution (*e.g.*, $T_{\rm f}$ and $T_{\rm d}$). In this regime, the typical $T_{\rm col,mass}$ has the order of 100 Myr, which is still longer than $T_{\rm d}$ or $T_{\rm d,col}$. Therefore, the massive-end of GMCMF does not show significant growth after 60 Myr.

Observability

In this sub-subsection, we explore simple estimation of CCC observability in galactic disks. The observability of CCC between GMCs with mass m and m_2, $f_{\rm obs}(m, m_2)$, can be characterized by multiplying its frequency and number density of GMCs:

$$f_{\rm obs}(m, m_2) = \frac{\Delta n(m)}{T_{\rm col,num}(m, m_2)}\,. \tag{5.16}$$

The number density $\Delta n(m)$ can be estimated from $n_{\rm cl}$ calculated in our GMCMF time evolution as:

$$\Delta n(m) \;=\; \int_m^{m+\Delta m} n_{\rm cl}\,{\rm d}m$$

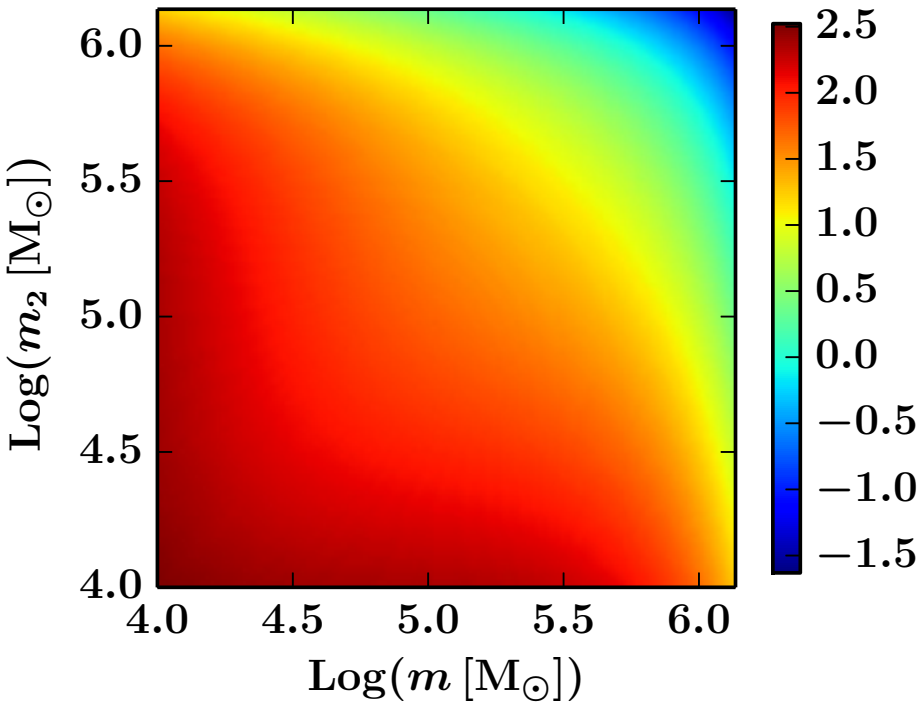

Figure 5.6: The expected number of CCC events observed in a galactic disk as a function of GMC mass pairs (*i.e.*, $N_{\rm obs}$ defined by equation (5.20)). Here we opt to employ $\Delta T_{\rm obs} = 1{\rm Myr}$ and $V_{\rm survey} = 10{\rm kpc}^3$ by assuming an ideal condition where we can observe all the GMCs across the entire galactic disk. The color scale is in the $\log_{10}$ scale. This figure indicates that most of the observationally accessible CCC events occur between GMCs with mass $\lesssim 10^{5.5}{\rm M}_\odot$, whereas the CCC between massive GMCs, which presumably gives significant impact on CCC-driven star formation, may not be observed.

$$= \int_{\ln m}^{\ln(m+\Delta m)} n_{\rm cl} m \, {\rm d} \ln m \, . \tag{5.17}$$

This integration width Δm is in principle determined by the capability of individual observations. Instead of specifying any capability, we here employ the number density per unit logarithmic mass interval $\Delta \ln m = \ln(m + \Delta m) - \ln m = 1$ for simplicity, thus

$$\Delta n(m) = n_{\rm cl} m \, . \tag{5.18}$$

This choice of $\Delta n(m)$ is consistent with the fact that we employ unit logarithmic mass interval $\Delta \ln m$ in equation (5.11) to define $T_{\rm col,num}$. This definition makes the observability $f_{\rm obs}(m, m_2)$ symmetric between m and m_2 as:

$$f_{\rm obs}(m, m_2) = K(m, m_2) n_{\rm cl,2} m_2 n_{\rm cl} m \, . \tag{5.19}$$

Such symmetry must exist because, unlike $T_{\rm col,num}$, the number of total collisional events itself cannot distinguish between m and m_2.

One can estimate the number of events expected to be observed within a galactic disk by multiplying $f_{\rm obs}$, the duration over which observation can identify colliding GMCs as a CCC event, $\Delta T_{\rm CCC}$, and the survey volume $V_{\rm survey}$:

$$N_{\rm obs}(m, m_2) = f_{\rm obs}(m, m_2) \Delta T_{\rm CCC} V_{\rm survey} \, . \tag{5.20}$$

As a demonstration, we make a simple prediction for future surveys under an ideal condition that we resolve and identify all the GMC populations across an entire galactic disk. Figure 5.6 shows the resultant $N_{\rm obs}$ where we assume $\Delta T_{\rm CCC} \sim 1{\rm Myr}$ and $V_{\rm survey} \sim 10{\rm kpc}^3$, which corresponds to the total volume of Milky Way galactic thin disk in which GMCs most likely reside. Our result suggests that we may observe over 100 events of CCC between $10^4 {\rm M}_\odot$. Indeed, most of the observed CCC candidates to date involve $\mathcal{O}(10^4){\rm M}_\odot$ GMCs (*e.g.*, Fukui et al. 2016). On the other hand, our result also indicates that it is less likely to observe the CCC events between GMCs with mass $> 10^{5.5}{\rm M}_\odot$ that play a dominant role in CCC-driven SFR. Therefore, we have to remind ourselves that it is not straightforward to claim that CCC-driven star formation is important for galactic star formation based only on the already observed CCC candidates by low-mass GMCs. Meanwhile, observations are also demanded to evaluate the stellar IMF at CCC sites.

Our optimistic assumption to observe an entire galactic disk requires the spatial resolution of a few arcseconds. For example, to resolve a GMC with its size of 1 pc at 20 kpc away from the Sun, the required resolution corresponds to

$$\frac{1[{\rm pc}]}{20\,{\rm kpc}} \times \frac{3600 \times 60 \times 60}{2\pi} \times \frac{1}{3} \simeq 3\,[{\rm arcseconds}] \, ,$$

provided that at least 3×3 pointing on the plane of the sky is necessary to identify two velocity components at CCC sites. ALMA may cover this spatial resolution thus the contamination of multiple clouds along the line-of-sight is more severe, especially if clouds are located at the opposite side of the galactic center (see Ikeda et al. (2007) for possible modification in cloud core mass function). Velocity difference is likely to be required to distinguish multiple clouds.

5.3 Discussion: Overestimation and Galactic Variation of CCC-Driven Star Formation Rate, and Lifetime/Age of GMCs

In this section, we first discuss possible overestimation in CCC-driven star formation rate. Then we propose new stringent definitions for the nomenclature "Lifetime" and "Age" of GMCs, which indicate a reason why the estimated GMC lifetimes in the literature significantly differ between articles by one to two orders of magnitude in Myr. Finally, we mention our pilot study of the variation of CCC-driven star formation rate as a function of galactic environment. Other detailed discussions, especially in our formulation, will be covered in Chapter 6.

5.3.1 Overestimation in Triggered Star Formation

As described in subsection 5.2.2, we assume that SFE in CCC sites is 1 per cent ($\varepsilon_{\rm SFE} = 0.01$) of the coagulated parental GMC mass. However, SFE could be simply limited by 1 per cent of the smaller GMC in a CCC pair. In case of a GMC pair with large mass difference, masses $10^4 {\rm M}_\odot$ and $10^6 {\rm M}_\odot$ for example, the resultant star cluster mass can be $\sim 10^2 {\rm M}_\odot = 1\%$ of $10^4 {\rm M}_\odot$, whereas our calculation estimates this as $\sim 10^4 {\rm M}_\odot = 1\%$ of $10^6 {\rm M}_\odot$. Therefore, in a CCC pair with large mass difference, our SFE becomes close to 100 per cent out of smaller GMCs.

Radio observations of CCC sites (*e.g.*, Fukui et al. 2016) suggest that at least 1 per cent of the smaller GMC mass in a given GMC pair turns into massive stars $> 20 {\rm M}_\odot$ and they could form as many massive stars equally as low-mass stars. Detailed magnetohydrodynamics simulations (*c.f.* Inoue et al. 2017) indicates that molecular cloud cores may have a flat IMF, although with poor statistics due to small number of samples. Only if stellar population follows Salpeter IMF even in CCC sites, then the number of simultaneously-formed low-mass stars $< 20 {\rm M}_\odot$ is larger than that of massive stars thus the total stellar mass can be comparable to colliding GMC mass, *i.e.*, up to 100 per cent SFE of colliding GMC mass.

Therefore, if actual CCC sites preferentially form massive stars, our calculated SFR triggered by CCC could be overestimated by a factor from a few to ten. This overestimation impacts the total SFR shown in figure 5.4 because CCC takes place most frequently between massive GMCs and small GMCs (see figure 5.5).

Coupled with possible overestimation in the CCC rate due to the perfect-inelastic assumption (see subsection 3.1.3), we interpret our calculated SFR driven by CCC as an upper limit.

5.3.2 Lifetime and Age of GMCs

The lifetime and age of GMCs are another two important quantities to understand star formation and star cluster formation along with galaxy evolution (*e.g.*, multiplicity of stellar ages in individual star clusters, migration history of our solar

system, evaporation timescale of protoplanetary disks in different galactic environment(see *e.g.*, Haisch et al. 2001; Meyer et al. 2007; Yasui et al. 2010), and so on). We here distinguish "lifetime" and "age"of GMCs; we define lifetime as the duration time for a GMC to its complete dispersal once star formation starts to take place, whereas age as the overall duration from GMC formation to its complete dispersal.

On one hand, the typical lifetime in our calculation corresponds to $T_{\rm d} = 14$ Myr. Some observations indicate such short lifetime (20–30 Myr) inferred from GMC classification in Large Magellanic Cloud (Kawamura et al. 2009) and an upper limit (30 Myr) estimated by GMC number counts in inter-arm regions in Galaxy M51 (Meidt et al. 2015). On the other hand, we have a delta function like mass distribution as the initial condition of our calculation where the minimum-mass GMCs alone exist. This enables us to highlight how fast GMCs can grow. To grow in mass, GMCs have to survive stellar feedback whose rate is determined by $T_{\rm d}$ (*i.e.*, more massive GMCs have older ages). Therefore, the age is in general longer than the lifetime. Figure 5.3 suggests that the GMC age is $\gtrsim 40(80)$ Myr, which GMCs require to grow from the minimum-mass $10^4{\rm M}_\odot$ to $\gtrsim 10^6(10^7){\rm M}_\odot$. Such longevity is indicated by observations within the Milky Way galaxy (*e.g.*, Barnes et al. 2011, 2016 and Barnes et al 2017, ApJ, submitted; *c.f.*, Kauffmann et al. 2013) and in nearby galaxies (*e.g.*, Koda et al. 2009).

By this analysis, we presume that observed short lifetimes are likely "lifetime" determined by GMC dispersal rate, whereas observed long lifetimes mostly correspond to "age" rather than lifetime.

5.3.3 Variation of CCC-driven Star Formation in Different Environment on Galactic Disks

In this thesis, we calculate and show CCC-driven SFR with a set of typical galactic disk parameters. Our next subject is to compare CCC-driven SFRs between arm and inter-arm regions. Intuitively, high CCC-driven SFR is expected in arm regions because the mass budget in arm regions is dominated by massive GMCs. However, mass-growth by multiple episodes of compression is also fast in arm regions (*i.e.*, short $T_{\rm f}$) to quickly create large amount of normal GMC populations. Thus, it is not obvious whether or not the "fraction" of CCC-driven SFR out of total SFR is high in arm regions, and vice versa for inter-arm regions. Indeed, our pilot calculations indicate that CCC-driven SFR covers 30–50 per cent of star formation in arm regions and 20–40 per cent in inter-arm regions. Time evolution of GMCMF and subsequent CCC-driven SFR have to be investigated further along with the migration of GMC groups between different regions (*e.g.*, arm to inter-arm and back into arm). This involves time evolution in parameters (especially $T_{\rm f}$, $T_{\rm d}$, $\varepsilon_{\rm res}$) and is left for future studies.

5.3.4 CCC-driven Power-law Slope

In this subsection, we are going to investigate whether or not the cascade collisional coagulation alone can create a steady state GMCMF similar to the ones that we have investigated by now. Let us calculate the mass flux as a function of GMC mass m. Suppose that the CCC kernel function has its mass dependence as $K \propto m^p$ and the resultant differential number density has a spectra $n \propto m^{-\alpha}$, the mass flux F due to the cascade collisional coagulation becomes (*c.f.*, Kwan 1979; Kobayashi & Tanaka 2010):

$$F \propto m^3 n^2 K \propto m^{-2\alpha+p+3} \,. \tag{5.21}$$

In a steady state, F is constant across the whole mass range (*i.e.*$F \propto m^0$), therefore

$$p = 2\alpha - 3 \,. \tag{5.22}$$

If the mass dependence of the kernel function has a variation with $p \in [-0.4, 2.2]$ the observed slopes can be reproduced, which typically varies $-\alpha = -1.3 - -2.6$. Thus, the regions where the GMC number density is large (*e.g.*, the Galactic Center) may form this type of CCC-driven GMCMF (*c.f.*, Tsuboi et al. 2015). However, the collision alone reduce the number of minimum-mass GMCs quickly and also create infinitely massive GMCs. Therefore, we still need some proper prescription for the creation process at the low-mass end and the dispersal process at the high-mass end. Note that, the GMCMF may have the same slope when collision is not cascade but always occurs only with the minimum-mass bin. This could occur, for example, in a system where somehow the minimum-mass GMC populations outnumbers other intermediate-mass GMCs. This is left for future studies.

Chapter 6

Discussion[1]

In this chapter, we first list and discuss various effects that may possibly modify our formulation, about which we are indeed asked frequently along our studies. Then we also explore the importance how to choose initial conditions and minimum-mass of GMCs. Finally we briefly mention non-disk regions (*e.g.*, galactic centers, dwarf galaxies, elliptical galaxies, and high-redshift galaxies), where our parameters may change from galactic disk regions we assume in this thesis.

6.1 Possible Improvements: Variation in the collision rate

In the following subsections, we examine a variety of effects that modify the time evolution of the GMCMF; (i) Variation in the cross section, (ii) Variation in the relative velocities, (iii) Assumed volume of the system, (iv) Initial conditions, (v) The choice for the minimum-mass GMC, (vi) self-gravity, and (vii) non-disk environment. The first three effects ((i) - (iii)) increase and decrease the rate for collisional coagulation. The setup variations fit into (iv) - (vii).

In Section 3.1.3, we introduced the CCC kernel function, which has a correction factor $c_{\rm col}$. This $c_{\rm col}$ involves various effects; four main effects can be the geometrical structure, the gravitational focusing, the column density of GMCs, and the relative velocity variation. We will briefly evaluate these effects to verify that $c_{\rm col}$ has an order unity and $c_{\rm col} = 1$ is enough approximation. In addition, we will note that the collision rate also depends on assumed volume in which the calculated GMC systems reside.

6.1.1 Geometrical Structure

To evaluate geometrical effect, let us ignore the thickness of GMCs for simplicity, which makes $c_{\rm col}$ a factor larger. We also assume that GMCs always coagulate even when their peripheries alone touch each other.

[1] *The contents of this chapter are partially based upon the articles Kobayashi et al. (2017b) and Kobayashi et al. (2017a).*

Given that GMCs have a uniform column density $\Sigma_{\rm mol}$, the cross section for face-on collisional coagulation between GMCs whose masses are m_1 and m_2 ($m_1 \geq m_2$), $\sigma_{\rm col\,peri\,1,2}$, is described as:

$$\begin{aligned}\sigma_{\rm col\,peri\,1,2} &= \pi\left(R_1+R_2\right)^2 \\ &= \pi\left(\sqrt{\frac{m_1}{\pi\Sigma_{\rm mol}}}+\sqrt{\frac{m_2}{\pi\Sigma_{\rm mol}}}\right)^2 \\ &= \frac{\left(\sqrt{m_1}+\sqrt{m_2}\right)^2}{\Sigma_{\rm mol}}\,,\end{aligned} \tag{6.1}$$

where R_1 and R_2 are the radii of GMCs with masses m_1 and m_2 respectively (see the left panel of Figure 6.1 for the schematic configuration). In this case, the correction factor becomes:

$$c_{\rm col} = \frac{\sigma_{\rm col\,peri\,1,2}}{\sigma_{\rm col\,1,2}} = 1+\frac{2\sqrt{m_1}\sqrt{m_2}}{m_1+m_2}\,. \tag{6.2}$$

The second term gives the deviation from the unity and thus $c_{\rm col}$ has its maximum value 2 when $m_1 = m_2$. In reality, GMCs are less likely to coagulate together when their peripheries alone touch each other so that Equation (6.2) overestimates the collision frequency and $c_{\rm col}$ should be smaller by some factor. Therefore, we can assume $c_{\rm col} = 1$ for simplicity.

The edge-on collision can be similarly evaluated. Provided that GMCs collide with an angle θ, the cross section becomes $2R_1 \times 2R_2 \times \sin\theta$ (see the right panel of Figure 6.1). $\sigma_{\rm col\,peri\,1,2}$ can be obtained by averaging this cross section over θ:

$$\begin{aligned}\sigma_{\rm col\,peri\,1,2} &= \frac{\int_0^\pi 2R_1 2R_2\sin\theta}{\pi} \\ &= \frac{8}{\pi}R_1R_2 \\ &= \frac{8}{\pi^2\Sigma_{\rm mol}}\sqrt{m_1m_2}\,.\end{aligned} \tag{6.3}$$

Therefore, the correction factor becomes:

$$c_{\rm col} = \frac{8}{\pi^2}\frac{\sqrt{m_1m_2}}{m_1+m_2}\,, \tag{6.4}$$

whose maximum is 0.57 when $m_1 = m_2$. Therefore, edge-on collision is less frequent than our fiducial cross section in Equation (3.6). Less frequent collision may impact on the shape of the massive end of the GMCMF. However, the slope calculated with $c_{\rm col} = 1$, which is already overestimated compared with this type of edge-on collisions, is not affected by CCC as shown in the figures presented in this thesis (*e.g.*, Figure 3.1). Therefore, for simplicity we can assume $c_{\rm col} = 1$ even for the edge-on collision if we restrict ourselves to the slope of the GMCMF.

One caveat here is that we focus only on the collision in face-on and edge-on. The other orientations leads to the cross section smaller than the configuration we

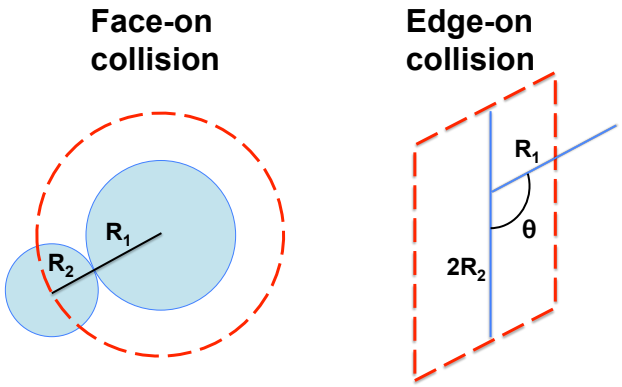

Figure 6.1: Schematic figure describing the geometrical configuration during cloud-cloud collisions (left: face-on collision; right: edge-on collision). GMCs have mass m_1 and m_2, radii R_1 and R_2 respectively. The red dashed area corresponds to the collisional cross section $\sigma_{\mathrm{col\,peri\,1,2}}$.

analyze here and would not greatly modify our GMCMF calculation results. Thus, we ignore such orientations for simplicity and left them for other works. Further investigation, especially three-dimensional hydrodynamics simulation, is needed.

6.1.2 Gravitational Focusing Factor

During a close-by encounter, two GMCs experience gravitational attraction toward each other (*i.e.*gravitational focusing effect), which effectively enlarges the cross section so that the rate for collisional coagulation increases. To evaluate the gravitational focusing effect, let us consider an example where a GMC whose mass and radius are m_2 and r_2 initially flies at a speed v_i with an impact parameter b with respect to another GMC with mass m_1 and radius r_1. Combining the angular momentum conservation and energy conservation, one can derive the ratio of the effective cross section b^2 against the area $(r_1 + r_2)^2$ as:

$$\begin{aligned} \frac{b^2}{(r_1+r_2)^2} &= 1 + \Theta \\ &= 1 + \frac{v_\mathrm{esc}^2}{v_\mathrm{i}^2} \\ &= 1 + \frac{2\mathrm{G}(m_1+m_2)}{(r_1+r_2)v_\mathrm{i}^2}\,, \end{aligned} \tag{6.5}$$

where $v_{\rm esc}$ is the escape velocity when the GMC peripheries touch each other. Θ is so called gravitational focusing factor, which characterize the relative increment of cross section due to gravitational attraction.

The condition where the gravitational focusing effect outnumbers the cross section would be $\Theta \gtrsim 1$. This condition with our ordinal assumption that GMCs have constant column density Σ and $v_{\rm i} = 10\,{\rm km\,s^{-1}}$ leads to:

$$\begin{aligned} &\frac{m_1+m_2}{r_1+r_2} \gtrsim 1.16\times10^4\,{\rm M_\odot\,pc^{-1}} \\ &\Rightarrow \frac{m_1+m_2}{\sqrt{m_1}+\sqrt{m_2}} \gtrsim \frac{1.16\times10^4\,{\rm M_\odot\,pc^{-1}}}{\sqrt{\pi\Sigma}}\,. \end{aligned} \tag{6.6}$$

The left hand side of Equation (6.6) has its minimum when $m_2 = 0.17m_1$ and maximum when $m_2 = m_1$. The most conservative estimation can be obtained by employing the maximum case $m_2 = m_1$, which results in $m_1 \gtrsim 5\times10^6{\rm M_\odot}$. This lower boundary may increase by another factor 3 to 5 because other collisions with $m_2 < m_1$ generally exist and also $v_{\rm esc} \gtrsim \mathcal{O}(10)v_{\rm i}$ is required for CCC to overwhelm GMC self-growth/dispersal. Therefore, we can conclude that the gravitational focusing effect may be involved only in the mass range beyond $10^7{\rm M_\odot}$. As shown in Sections 3.2 and after that, all the GMCMFs have already exhibited their well-defined slope below $10^7{\rm M_\odot}$ thus treating the correction factor $c_{\rm col} = 1$ is an enough approximation to compute the GMCMF slope correctly.

Note that our fiducial cross section is given as the sum of geometrical cross sections (*i.e.*$\pi r_1^2 + \pi r_2^2$) rather than $\pi(r_1+r_2)^2$ that we studied here. However, the former is smaller than the latter by only a factor one to two, thus the criterion $m_1 \gtrsim 5\times10^6{\rm M_\odot}$ remains valid in our setup. Overall, the gravitational focusing effect can increase the cross section by some factors but we can still assume $c_{\rm col} = 1$ for the mass range defining the GMCMF slope.

6.1.3 Column Density of GMCs

Latest observations suggest that GMC mean column density could have its peak at $(2-6)\times10^{21}\,{\rm cm^{-2}}$ (*e.g.*, Auriga-California: Harvey et al. (2013), Cygnus X: Schneider et al. (2016), etc.; see also Egusa et al. (2018) as a study of external galaxies.). This corresponds to visual extinction of a few, which is able to protect CO molecules from far-ultraviolet photons so that GMCs can be probed by CO line observations[2]. Our fiducial column density is $\Sigma_{\rm mol} = 10^{22}\,{\rm cm^{-2}}$, a factor few denser than the density suggested by the latest observations. Therefore, the assumed CCC rate may be biased lower by a factor few.

We would like to remind the readers that the column density we study here has to be the typical value averaged out in the entire volume of individual GMCs, namely ^{12}CO(1-0) bright volume, because we conduct statistical analyses by formulating the evolution equations for GMCs as a group, but not substructures within

[2] see Section 4.2.4 for details of self/dust-shielding of hydrogen and CO molecules.

individual GMCs. Most of the GMCs' volume is probably covered by such ^{12}CO(1-0) bright part, thus, in above discussion, we refer the readers to the peak value of observed probability distribution functions of GMC column density. It is beyond our current scope, but it is left for future studies to consistently combine the time evolution of GMCs that we study here and the time evolution of substructures within individual GMCs; *e.g.*, possible filaments and molecular cloud cores appeared as the high-density power-law tail with $10^{23}\,\mathrm{cm}^{-2}$ in the column density probability distribution functions, especially traced by molecular lines whose critical densities are higher than ^{12}CO(1-0) (*e.g.*, 13CO(1-0), HCO^+, HCN, N_2H^+ *etc.*). See also for section 8.2 for motivations to investigate such high-density structures in the future.

6.1.4 Relative Velocity

The relative velocity between clouds is another component that may vary the collisional kernel. Because our model assumes that GMCs are swept up by expanding shells (*e.g.* HII regions and supernova remnants), we expect that the relative velocity between GMCs is comparable to a typical shock expanding speed driven by the ionization-dissociation front (Hosokawa & Inutsuka 2006a) and does not have any strong mass dependence. Even a simple setup can derive this estimation; the Rankine-Hugoniot relation (see Landau & Lifshitz 1959 and Section 7.2), for example, predicts that the velocity change across the shock front is described as $v_2 = v_1 \times \{(\gamma-1)\mathcal{M}_1^2+2\} \times ((\gamma+1)\mathcal{M}_1^2)^{-1}$, where v_1 and v_2 are the fluid speed in the pre-shock and post-shock regions respectively, $\mathcal{M}_1$ is the Mach number in the pre-shock region, and γ is the polytropic index for the fluid. With a strong shock $\mathcal{M} \gg 1$, the cooling time can be longer than the dynamical time for the shock passing through a GMC, which leads to $\gamma > 1$ rather than $\gamma = 1$ even for a molecular cloud. Then the velocity change becomes $v_2 = \mathcal{O}(0.1)\, v_1$ thus GMCs in the post-shock regions may have a relative velocity $\mathcal{O}(0.1) \times 10\,\mathrm{km\,s^{-1}}$. Semi-analytic studies also demonstrate that that a molecular cloud moves slowly than the shock itself (Iwasaki et al. 2011a,b), thus the GMC's relative velocity would be somewhat smaller than $10\,\mathrm{km\,s^{-1}}$. Indeed, observations show that the mean intercloud dispersion in the Galaxy is a few $\mathrm{km\,s^{-1}}$ (Stark & Brand 1989; Stark & Lee 2005, 2006). Therefore, we opt to use $V_{\mathrm{rel},0} = 10\,\mathrm{km\,s^{-1}}$ irrespective of GMC mass, which may reduce c_{col} by a factor of a few. This compensates the increasing trend discussed in the previous sections so that c_{col} remains the order of unity. If the intercloud velocity dispersion in galactic disks is really driven-by expanding shells, then this value has to be universal because the shock expanding speed ($\sim$ the sound speed of medium within expanding shell) is mostly 10 km s^{-1} (10^4 K) due to Lyα cooling, which should be universally determined by electroweak interaction.

Note that the shear motion in galactic disk would not outnumber the velocity dispersion produced by shocks. For example, let us consider two clouds that are at a distance R from a galactic center and have a separation of d. If the speed of the galactic rotation is V_{rot}, then the shear speed can be estimated about $\sim V_{\mathrm{rot}} d R^{-1}$.

With $V_{\rm rot} = 200\,{\rm km\,s^{-1}}$, $d = 100\,{\rm pc}$, and $R = 8{\rm kpc}$ (*e.g.*, solar neighbors), the shear speed becomes $2.5\,{\rm km\,s^{-1}}$. At the galactic centers with smaller R, the shear motion definitely contributes more to the GMC relative velocity, but the significance is not obvious because GMCs are closer each other than disk regions so that may have smaller d. Because we now focus on disk regions, the shear motion does not alter the relative velocity appreciably in the conditions we present in the current thesis.

Also note that gravitational scattering is probably not the main factor controlling the relative velocity of GMCs. Because GMCs are collisional system, the two-body gravitational scattering may lead to equipartition among GMCs thus the resultant relative velocity is supposed to have some GMC mass dependence of $V_{\rm rel} \propto m^{0.5}$. Observationally, GMCs range over two to three orders of magnitude in mass (or even more if we consider smaller clouds observed only in the Milky Way). However, the cloud-to-cloud velocity dispersion has limited variation with a factor less than two(Stark & Brand 1989; Stark & Lee 2005, 2006). Therefore, we deduce that the relative velocity is set by multiple episodes of supersonic shocks and thus opt to use $V_{\rm rel,0} = 10$ km s^{-1} in this thesis.

6.1.5 Area for One-Zone

Our time-evolution equation is essentially one-zone and calculates the differential number density of GMC populations $n_{\rm cl}$, which therefore does not require any specified three-dimensional configuration for concerned volume in which calculated GMCMFs exist under CCC-absent cases. Nevertheless, one can still estimate calculated volume that is self-consistent within our modeling. For example, GMCs can travel roughly $1\,{\rm kpc}$ in 100 Myr with a proper velocity of $10\,{\rm km\,s^{-1}}$. Therefore, our calculated GMCMF up to 100 Myr should correspond to ensemble population of GMCs in a cylinder with a surface area of $1\,{\rm kpc}^2$ and with a depth of 100 pc given that a galactic thin disk has a scale height 100 pc in which GMCs populates (*e.g.*, Dame et al. 1987). It is less likely to have GMC collisions beyond this cylinder. However, to enable comparisons with observations, we assume that the area is bigger than $1\,{\rm kpc}^2$ by referring to the observed area covered by subdivided regions (*e.g.*, PAWS Colombo et al. (2014a): from $7.54\,{\rm kpc}^2$ in arm regions to $19.99\,{\rm kpc}^2$ in inter-arm regions), because GMCs are statistically able to collide each other even if they are apart more than 1 kpc in each subdivided area. In our calculation, this overestimated area overestimate the cumulative number of massive-end GMCs so that we invoke collisions with GMCs whose cumulative number is less than 1. In this article, we aim at demonstrating our modeling for a typical region in a galactic disk so that we opt to employ a cylinder with $10{\rm kpc}^2$ area and with 100 pc depth.

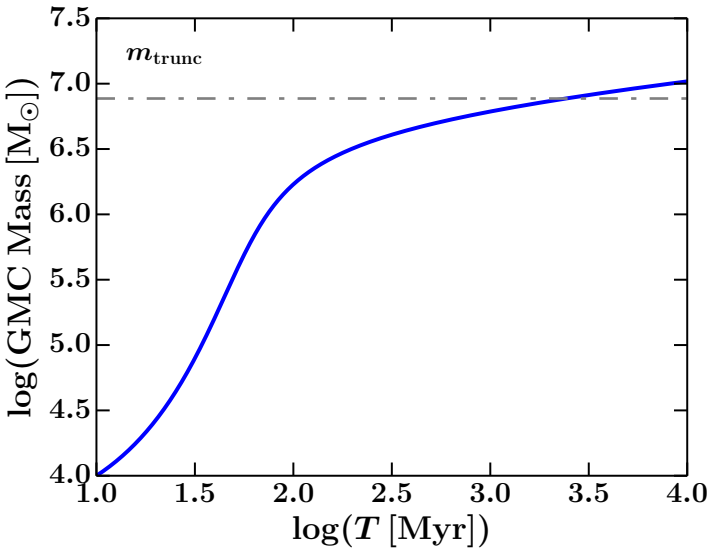

Figure 6.2: $T(m) = \int T_{\rm f}(m)/m \, {\rm d}m$ with $T_{\rm f,fid} = 10$ Myr, which gives the typical self-growth timescales for GMCs that have not undergone CCC. A horizontal dash-dot line indicates $m_{\rm trunc}$. As expected from the exponential growth picture in Section 3.1.1, $T(m)$ logarithmically grows until GMCs acquire $m_{\rm trunc}/\gamma \sim 10^6 {\rm M}_\odot$ up to which $T_{\rm f}$ is almost constant (*i.e.*, $T_{\rm f,fid}$). $T(m)$ rapidly increase beyond $m_{\rm trunc}/\gamma$ due to the $T_{\rm f}$ dependence on m (see Equation (3.4)).

6.1.6 Background

In this thesis, we assume that the background reservoir is always plenty enough to sustain the steady state of GMCMF. However, it is known in the Milky Way and nearby galaxies that the gas distribution (especially atom-to-molecular ratio) varies with the galactocentric radii (*c.f.*, Nakanishi & Sofue 2016). Therefore, it is desired to investigate the background gas evolution coupled with galactic environment. We will propose such analysis in global galactic-scale simulations in Chapter 7.

6.2 Initial Conditions

In general, the GMCMF time evolution may depend on the initial condition. To test the importance of the initial condition, we compute the time that is required for minimum-mass GMCs to grow to mass m by HI cloud accretion as:

$$T(m) = \int_{m_{\rm min}}^{m} [T_{\rm f}(m)/m] \, {\rm d}m \, . \tag{6.7}$$

This integration originates from our substitution $({\rm d}m/{\rm d}t)_{\rm self} = m/T_{\rm f}(m)$ in Section 3.1.1. Equation (6.7) suggests that GMCs grow exponentially in $m < m_{\rm trunc}$.

We take the integration in Equation (6.7) and Figure 6.2 shows the result as a function of GMC mass. Note that, here, we include the $T_{\rm f}$ dependence on GMC mass (see Equation (3.4)). Therefore, the computed time exhibits a rapid increase at the massive end in Figure 6.2.

As shown in Figure 6.2, minimum-mass GMCs reach $10^6 {\rm M}_\odot$ within 100 Myrs. Therefore, initial conditions for our calculation is erased typically less than one rotation of galactic disk and we expect that the observed GMCMF would not be affected significantly by the initial conditions. In case the initial condition is not influential in the resultant GMCMF, then formulation that depends on the initial condition (*e.g.*, cosmological Press-Schechter formalism: Press & Schechter 1974) may not describe well the time evolution of the GMCMF.

Note that the GMCMF evolution can be modified in earlier stage if with the initial condition where very massive GMCs dominate the total mass of the system. However, based on the multiphase magnetohydrodynamics simulations (*e.g.* Inoue & Inutsuka 2008), multiple successive compression should first create smaller GMCs and cultivate them to massive ones, rather than produce very massive ones directly from WNM. Therefore, we opt to preset only minimum-mass GMCs at the beginning of our calculation. (See also the next section for how to determine the minimum mass).

6.3 The Choice for the Minimum-Mass GMC

The concept of minimum-mass ($m_{\rm min}$) GMC is necessary to compute the GMCMF numerically. However, it is not obvious what value should be used as the "minimum" mass. Thus, to estimate this minimum value, let us consider a large hydrogen cloud. Given the mean number density in this cloud is $\sim 10^2\,{\rm cm}^{-3}$ and the visual extinction is 1 or larger due to the dust shielding to form molecular hydrogen (*i.e.*the total hydrogen column density $2\times10^{21}\,{\rm cm}^{-2}$ (Bohlin et al. 1978; Rachford et al. 2009; Draine 2011)), the typical length for this type of hydrogen cloud is expected about $2\times10^{21}/10^2 = 2\times10^{19}{\rm cm}$. If we assume that the cloud has this length stretched at all the solid angles, then the total hydrogen mass in this cloud is given as:

$$\begin{aligned} &\frac{4}{3}\pi\left(2\times10^{19}\right)^3\times10^2\times2\mu m_{\rm H} \\ &\simeq 2.6\times10^4{\rm M}_\odot\,. \end{aligned} \tag{6.8}$$

As another estimation, let us also consider virialization of molecular cloud. The virial parameter, α, which represents the ratio of thermal energy against self-gravitational energy, can be written as $\alpha = 5\delta v^2 R/(GM)$, where δv^2 is the velocity dispersion of the cloud, R and M is its radius and mass, respectively. If the cloud is a uniform sphere, then $M = 4/3\pi R^3\rho \simeq 4/3\pi R^3 2.7 m_{\rm p}$, where $m_{\rm p}$ is the proton mass. The column density of the cloud, N, can be roughly evaluated as $N \simeq 2R\rho/(2.7m_{\rm p})$. Thus combination of these equations gives M as a function

of R and δv as

$$M = \left(\frac{2}{3}\,\pi\,R_0^2\,2.7\,N\right)^{\frac{\gamma+1}{\gamma-1}} \left(\frac{m_{\rm p}\,\alpha\,G}{5\,\delta v_0^2\,R_0}\right)^{\frac{2}{\gamma-1}} m_{\rm p}\,, \tag{6.9}$$

where $\delta v = \delta v_0 (R/R_0)^\gamma$. Typical observed parameters (*e.g.*, $R_0 = 1$ pc, $\delta v_0 = 1$ km s^{-1}, $N = 10^{22}$ cm^{-2}, $\gamma = 0.5$, with a conservative approximation of the virialization $\alpha = 1$ (Heyer & Brunt 2004)) give $M \simeq 1.8 \times 10^4 {\rm M}_\odot$.

ISM simulations (*e.g.*, Inoue & Inutsuka 2012) also indicate that $10^4{\rm M}_\odot$ is a typical minimum GMC created after 10 Myr. The minimum limit $\gtrsim 10^4{\rm M}_\odot$ is consistent with the value observationally used (see Williams et al. 2000) as the definition of GMCs. Thus we opt to use $10^4{\rm M}_\odot$ as the minimum-mass for GMCs.

However, the estimation by Equation (6.8) evaluates the minimum amount of total hydrogen but not molecular hydrogen alone. Therefore, in a static case where, for example, diffuse HI gas extend around dense H_2 gas, the mass of dense H_2 gas can be half or less than Equation (6.8) prediction. Under a dynamical situation, turbulence stirs HI and H_2 gas to break up H_2 cloud into smaller H_2 clouds whose mass can be smaller than that estimated by Equation (6.8). Moreover, if molecular gas self-shielding alone is effective when the dust is poor, the required total hydrogen column density can be smaller by a few orders of magnitude. Thus, even though we cannot specify the exact number, it maybe optimal to set somewhat smaller value than shown in Equation (6.8) as the minimum-mass of GMCs. We will investigate the minimum-mass choice further in our forthcoming paper, combining with the effect CO-dark H_2 gas and the $T_{\rm d}$ variation in low-mass less star-forming GMCs.

Note that, if the highest-density (star forming) H_2 regions have a filamentary structure (*c.f.* André et al. 2010; Molinari et al. 2010; Arzoumanian et al. 2011; Hill et al. 2011; Könyves et al. 2015), it is not obvious whether HI gas sufficiently extend around those H_2 regions to sustain the column density condition ($2 \times 10^{21}\,{\rm cm}^{-2}$). This needs to be studied further and left for future works.

6.4 Importance of Self-Gravity

For the formation of GMCs, we consider multiple episodes of supersonic compression due to massive stars and supernovae. One may question whether or not self-gravity is important on pc-scale in a context of GMC formation. To test this, let us consider an idealistic case where free-fall collapse of the ISM occurs. If there is mixture of WNM and CNM with its density of 10 particles cm^{-3} and its temperature of 100 K, the free-fall time of this gas cloud can be estimated as:

$$\tau_{\rm freefall} = \sqrt{\frac{3\pi}{32{\rm G}\rho}}\,, \tag{6.10}$$

where G is the gravitational constant and ρ is mass density. The resultant timescale is about 50 Myr, which is factor longer than $T_{\rm f}$. Therefore, multiple compressional

event leads to faster GMC formation than self-gravity of the ISM by themselves. This is an order of magnitude estimation thus both timescales can be comparable in some conditions (*e.g.*, initially with somewhat high density), but it is less likely that self-gravity overrides multiple compressional process. Moreover, if you calculate the corresponding Jeans length and Jeans mass:

$$\lambda_{\rm Jeans} = C_{\rm s}\tau_{\rm freefall}\,, \quad M_{\rm Jeans} = \frac{4}{3}\pi\lambda_{\rm Jeans}^3\rho\,, \tag{6.11}$$

where $C_{\rm s}$ is the sound speed (~ 1 km s^{-1} for 100 K), one can find that $\lambda_{\rm Jeans} \simeq 50$ pc and $M_{\rm Jeans} \simeq 10^5 {\rm M}_\odot$. Therefore, self-gravity alone creates relatively large GMCs, and cannot provide small GMCs $\simeq 10^4 {\rm M}_\odot$ (or even smaller as observed in the Milky Way galaxy). To reproduce observed profiles of GMCMF by self-gravity, it requires some aid by feedback to disrupt large GMCs into smaller clouds constantly. Instead, in our model, we can create both small and large GMCs by accumulating mass through thermal instability and, which naturally reproduce observed GMCMFs as we have shown by now. Therefore, we admit that we may need to reconsider of self-gravity effect for massive GMCs, but we assume that this effect is sub-dominant.

6.5 Non-Disk Environment: Galactic Centers, Dwarf/Elliptical Galaxies, and High-Redshift Galaxies

Observationally, both the number density and cloud-to-cloud velocity dispersion of GMCs increase towards galactic centers (*e.g.*, Central Molecular Zone in the case of the Milky Way galaxy: Morris & Serabyn (1996)). Therefore, the CCC rate is also enhanced at galactic centers. Investigation in further inner region of galactic disks needs to take into account such variation. However in this study, we restrict ourselves to a disk region, for example the solar circle in the case of the Milky Way galaxy. Also, super star cluster formation sites show high relative velocities 10 - 20 km s^{-1} (*e.g.*, Furukawa et al. 2009; Ohama et al. 2010; Fukui et al. 2014, 2016), where super star cluster is defined as star clusters having 10 - 20 O stars. Such possibility that massive star formation is enhanced as a function of relative velocity between GMCs also has to be investigated, but we focus on a simple question how much star formation can be induced by CCC at a given star formation efficiency in this study. Note that, at galactic centers, the magnetic field strength was reported to be very large (*e.g.*, a few milli-Gauss), at least, locally. This stronger fields presumably modifies self-growth timescale $T_{\rm f}$ as well.

In non-disk small galaxies or some specific volume in galactic disks, molecular cloud formation and subsequent star cluster formation can be triggered by large-scale colliding HI flow (*e.g.*, Fukui et al. 2017e: inflow from Small Magellanic Cloud onto Large Magellanic Cloud). Also, as introduced in Chapter 1, GMCMF started to be observed in elliptical galaxies and high-redshift galaxies as well albeit still limited number of samples (*e.g.*, Utomo et al. 2015; Tosaki et al. 2016). These

environment are beyond our scope in the current thesis but needs to be investigated in the future.

Chapter 7

Towards A Galactic View: Supernova Remnant Expansion and Effective Equation of State in the Multiphase Interstellar Medium

In this chapter, we investigate the validity of the assumption in $T_{\rm f}$ estimation in our current studies. As a pilot study of such an investigation, we perform hydrodynamics simulations, with which our current sutdies can be extended and connected to future galacitc-scale studies.

7.1 The Evolution of Supernova Remnants

As we already introduced in section 2.2.3, we assume that shock propagation driven by expanding HII regions and supernova remnants initiates the phase transition from WNM to CNM and molecular gas. The evaluation of typical $T_{\rm f}$ is based on an assumption that the typical expansion rate of a single supernova remnant is typically up to 100 pc at 1 Myr after its explosion (see sections 2.2.3 and 3.2.3). Therefore, our estimation of $T_{\rm f}$ and following explanation of GMCMF variation could be invalid if the actual expansion rate in the real ISM is significantly different from this value.

The expansion of individual supernova remnants is studied in detail mostly in one-dimension both analytically and by simulations (*e.g.*, various ambient ISM conditions (Thornton et al. 1998) and the effect of magnetic fields (Slavin & Cox 1992)). They indeed suggest that the typical shock-front radius is $80 - 100$ pc at 1 Myr. However, most of these studies employ a uniform density in the surrounding ISM and cover the cooling process in relatively hot regime (*e.g.*, cooling function

in hot HII regions of > 1500 K (Dalgarno & McCray 1972) and soft X-ray spectrum with the electron temperature of $> 1.6 \times 10^5$ K (Raymond & Smith 1977)). Recently, Kim et al. (2017) perform a series of more detailed simulations in three-dimension that investigate supernova remnant expansions in the multiphase ISM. Their simulations with the spatial resolution of 1.5 pc cover the time evolution up to 0.3 Myr after the supernova explosion, showing that shock propagation is suppressed if the shock encounters some dense part (*i.e.*, CNM and molecular gas) of the ambient ISM and the porosity of the remnants emerge. Nevertheless, the shock-front already reached 50 pc by the time of 0.3 Myr thus the remnant size could become 100 pc by 1 Myr.

To extend these studies and confirm the estimation of "100 pc at 1 Myr", two important aspects are spatial resolution and dimensionality as well as cooling process in low temperature regime. CNM and molecular gas formation in the post-shock region induce significant gas contraction in the post-shock layer; for example, the conversion from WNM to CNM results in the contraction of the order of two in volume, which may suppress the shock-front propagation. Therefore to precisely determine the shock-propagation speed, it is ideal to resolve the scale of thermal instability (see also Katz (1992) over-cooling problem in insufficient resolution regime). Also, dimensionality could alter the shock propagation because dense gas is allowed to move in the post-shock layer after its formation in three-dimensional case whereas one-dimensional setup essentially keep piling up dense gas.

To investigate the possible modification in the shock propagation depending on cooling, resolution, and dimensionality in supernova remnants, we decided to perform hydrodynamics simulations of colliding HI flow. From section 7.2, we introduce our simulation setups and analysis methods, and present simulated results in section 7.3. Base on these simulation results, we finally address our prospective studies of galaxy evolution in section 7.4.

7.2 Colliding HI Flow: Effective Equation of State and Shock Propagation Speed

To conduct simulations tracing shock propagation, we opt to perform colliding HI flow simulations. In reality, single shock front propagates in the ISM thus we do not necessarily have to test colliding flows. However, this colliding condition enables us to confine the shock-compressed layer at the center of our simulation box, thus it is easy to identify and track the shock propagation[1]. Therefore, for simplicity due to this technical reason, we decided to perform colliding HI flow simulations.

Colliding HI flow is widely simulated in the context of CNM and molecular gas formation in the ISM through thermal instability (*e.g.*, Inoue & Inutsuka (2008); see also section 2.2.2). In this setup, two shock fronts emerge at the intersection of

[1]This is the reason why many of the multiphase ISM simulation studies in the literature choose colliding HI flow instead of moving their simulation box to track a single shock propagation.

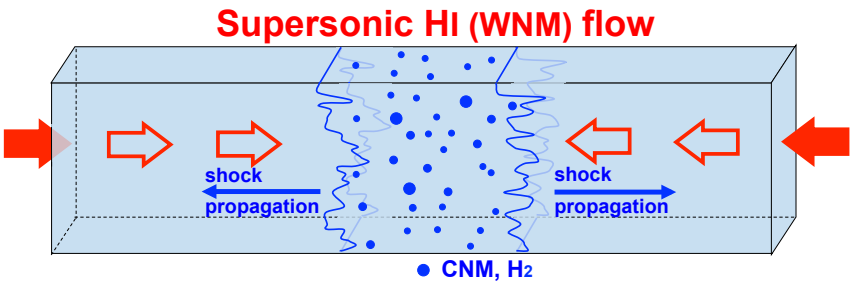

Figure 7.1: The schematic figure describing the concept and setup of colliding HI flow simulations. Supersonic WNM flow keeps being injected toward the center of the simulation box. The shock-compressed layer emerge at the box center, in which dense CNM and molecular gas form through thermal instability. The shock front gradually expand outwards with time due to the mass accretion from WNM flow into the shock-compressed layer.

injected flow and the shock-compressed layer. Within the shock-compressed layer, CNM and molecular gas form by thermal instability. The shock front positions move to the pre-shock regions because the mass within the shock-compressed layer increase with time due to the mass accretion from the flows. Therefore in principle, such shock propagation is analogous to the expansion of supernova remnants where the shock front sweeps the ambient ISM and turbulent multiphase ISM form behind the shock. Figure 7.1 shows the concept and setup of colliding HI flow simulations.

This analysis enables us not only to measure the shock propagation but also to explore the physical properties within the shock-compressed layer (*e.g.*, density, velocity dispersion, and volume filling factor). Combination of these properties with measured shock propagation speed leads us to formulate an effective equation of state for the multiphase ISM (*i.e.*, an effective equation of state of one fluid that represents the multiphase ISM). Therefore, before looking into the details of our simulations, in section 7.2.1, we first describe our method of constructing the effective equation of state, which is essentially based on the shock-jump conditions for supersonic shocks. Then we present our results of colliding HI flow simulations. Finally we measure the shock propagation speed and evaluate the effective equation of state.

7.2.1 Shock Jump Condition in the Multiphase ISM

Shock jump conditions are the conditions that have to be satisfied across the shock front in supersonic shocks. These are obtained by discretizing the conservation

laws of mass, momentum, and energy:

$$\nabla \cdot (\rho \mathbf{v}) = 0\,, \quad \frac{\partial \pi_{ik}}{\partial x_k} = 0\,, \quad \nabla \cdot \left[\rho \mathbf{v} \left(\frac{1}{2}v^2 + h + \phi\right)\right] = 0\,. \tag{7.1}$$

Here, x_k is spatial derivative, h is enthalpy, ϕ is potential, and π_{ik} is given as $\pi_{ik} = p\delta_{ik} + \rho v_i v_k$ where δ_{ik} Is Kronecker delta. The discretized version of these equations are written as:

$$\rho_1 v_1 = \rho_2 v_2\,, \quad \frac{1}{2}v_1^2 + h_1 = \frac{1}{2}v_2^2 + h_2\,, \quad \frac{1}{2}v_1^2 + \frac{\gamma}{\gamma-1}\frac{p_1}{\rho_1} = \frac{1}{2}v_2^2 + \frac{\gamma}{\gamma-1}\frac{p_2}{\rho_2}\,. \tag{7.2}$$

Here, the subscriptions indicate that physical values in the pre-shock region (1) and the post-shock region (2), and we ignore the variation of the potential ϕ by assuming that the thickness of the shock front is small compared with the system size (for example, it is a few mean free-path if determined by molecular viscosity). This set of equations are called the Rankine-Hugoniot relation (see Landau & Lifshitz 1959). The combination of the first and third equations gives an relation that connects the ratio of physical quantities and Mach number of flow:

$$\frac{\rho_2}{\rho_1} = \frac{(\gamma+1)\mathcal{M}_1^2}{(\gamma-1)\mathcal{M}_1^2 + 2}\,. \tag{7.3}$$

Here, $\mathcal{M}_1$ is the Mach number of incident supersonic flow (*i.e.*, the Mach number in the pre-shock region defined as $v_1/C_{\mathrm{s},1}$ where $C_{\mathrm{s},1}$ is the sound speed in the pre-shock region.)[2]

In case of one fluid, ρ and γ appeared in Equation 7.3 correspond to the density and the specific heat[3] of that concerned fluid. However, in case of multiphase fluid, ρ and γ should represent the mean value in the pre-shock and the post-shock regions. In principle, such effective γ for multiphase ISM can be determined by measuring the shock wave propagation speed and mean density of the pre-shock and the post-shock regions, which we use to evaluate $\mathcal{M}_1$ and ρ_2/ρ_1 in Equation 7.3.

7.2.2 Scheme and Setup of Colliding HI Flow

Our simulation code is essentially based on the magnetohydrodynamics code developed in Inoue & Inutsuka (2008). Hydrodynamics equations are solved by the second-order Godunov scheme (van Leer 1979), which employs the Riemann solver (see also Sano et al. (1999)). The time-independency in the Riemann Problem solutions enables this scheme to be second-order even with only one time-integration at each timestep.

[2]These are the conditions for normal shock waves. See Landau & Lifshitz (1959) for the corresponding equations of oblique shock waves, which have a dependence of $\sin^2\alpha$ where α is the angle between the incident supersonic flow and the shock front.

[3]This is specific heat because of ideal gas assumption that we already used in Equation 7.2.

For the hydrodynamics part, we solve the following equation:

$$\partial_t \vec{U}(t,x) + \partial_x \vec{F}_x = \partial_x \vec{Q}_x + \vec{S}(t,x)\,. \tag{7.4}$$

Here $\vec{U}$ is given as

$$\vec{U} = (\rho, \rho v_x, \rho v_y, \rho v_z, e)\,, \tag{7.5}$$
$$\tag{7.6}$$

where ρ is the mass density per volume, v_x, v_y, and v_z are the fluid velocity in x, y, and z directions, respectively, and e is the total energy per volume:

$$e = \frac{p}{\gamma - 1} + \frac{\rho(v_x^2 + v_y^2 + v_z^2)}{2}\,. \tag{7.7}$$

Here, p is the thermal pressure, and γ is the specific heat[4]. $\vec{F}$ is given as

$$\vec{F}_x = \begin{pmatrix} \rho v_x \\ \rho v_x^2 + p \\ \rho v_y v_x \\ \rho v_z v_x \\ (\rho e + p) v_x \end{pmatrix}\,. \tag{7.8}$$

The heat flux $\vec{Q}$ is given as

$$\vec{Q}_x = \begin{pmatrix} 0 \\ 0 \\ 0 \\ 0 \\ \kappa(T)\,\partial_x T \end{pmatrix}\,. \tag{7.9}$$

Here κ is the thermal conductivity, T is the fluid temperature. For the thermal conductivity, we consider the H + H collision from Parker (1953) ($\kappa(T) = 2.5 \times 10^3\, T^{0.5}$ erg cm^{-1} s^{-1} K^{-1}). The cooling and heating processes appear as a source term $\vec{S}$:

$$\vec{S}(t,x) = \begin{pmatrix} 0 \\ 0 \\ 0 \\ 0 \\ -\rho\mathcal{L} \end{pmatrix}\,. \tag{7.10}$$

Here, $\mathcal{L}$ is the heating and cooling rate per mass and we employ the fitting formula of $\mathcal{L}$ from Koyama & Inutsuka (2002) (see in Chapter C.2). Instead of employing the direct Eulerian scheme, we solve these equations in Lagrangian coordinates and remap the physical quantities onto the Eulerian coordinates (van Leer 1979).

[4]Note that this is not the effective γ of the multiphase ISM that we aim at measuring.

We prepare a simulation box, each side of which has 20 pc, 10 pc, and 10 pc in x, y, z directions respectively (Cartesian coordinates), and inject supersonic HI flows along x direction from both boundaries at the end of x coordinate. We perform 256 $\times$ 128 $\times$ 128 mesh simulations, whose spatial resolution is 0.08 pc accordingly. Table 7.1 summarizes the properties of injected supersonic flows and the modifications in the cooling and heating functions. As our fiducial test (Case 1), we employ a typical WNM property with its density of 0.57 particles cm^{-3} and its pressure of $3.5 \times 10^3 k_{\rm B}$. We opt to employ the mean molecular weight as 1.27 assuming that hydrogen (including their ions) compose 91 per cent of the fluid and helium (including their ions) compose the rest 9 per cent. The corresponding cooling time is

$$\tau_{\rm cool} = \frac{k_{\rm B} T}{n\Lambda} \simeq 5.31 \times 10^{13}\,{\rm s} = 1.68\,{\rm Myr}\,, \tag{7.11}$$

and the corresponding cooling length is

$$l_{\rm a} = C_{\rm s}\tau_{\rm cool} \simeq 2.51 \times 10^{17}\,{\rm cm} = 0.833\,{\rm pc}\,. \tag{7.12}$$

As the initial condition, we set the uniform flow in both left-half and right-half regions of our simulation box as tabulated in Table 7.1. The HI flows have opposite signs so that they start to collide each other at the center of our simulation box right after the simulation starts. The contact position of two fluids with opposite velocities is initially perturbed to shorten the duration for developing turbulence in the shock-compressed layer. We opt to perturb the contact position that has Kolmogorov-like spectrum (Kolmogorov 1941) as:

$$\delta x = \sum_{k_y\,k_z}^{k_{y,\rm max}=10\,k_{z,\rm max}=10} P(k_y, k_z)\sin(k_y y + k_z z + \alpha_{k_y,k_z})\,, \tag{7.13}$$

$$P(k_y, k_z) = A(k_y, k_z)\,|k|^{-11/6}\,. \tag{7.14}$$

Here, δx is the deviation from the simulation box center, $k_{y,\rm max}$ and $k_{z,\rm max}$ are the maximum number of modes applied, α_{k_y,k_z} is a random phase, and $P(k_y, k_z)$ is the power-spectrum of this perturbation. We choose the amplitude $A(k_y, k_z)$ that sets the variance of this perturbation normalized as 1 per cent of the entire simulation box size in x-direction. Figure 7.2 shows one of such initial conditions in the velocity field.

Once the simulation stars, two shock fronts emerge at the box center and propagate in time toward the both sides of our simulation box (*i.e.*, mass keep accumulating in the shock-compressed layer because we keep injecting supersonic flows along x axis from the plane at x = 0 and 20 pc). We identify the shock fronts as a temperature jump. Note that we do not apply any forcing for inducing turbulence so that the turbulence developed in the shock-compressed layer is purely translational motion of cold gas generated by thermal instability.

We present the results in the next section and the obtained physical quantities at the time of 3 Myr are all summarized in Table 7.2.

Table 7.1: Studied conditions for colliding HI flow simulations

Cases	Parameters					
	Density $(\rho/m_{\rm n})$ (particles cm^{-3})	Pressure $(p/k_{\rm B})$ (K cm^{-3})	Temeperature (Kelvin)	$\tau_{\rm cool}$ (Myr)	Cooling Factor	Conduction
0	0.570	3.500×10^3	6140	-	no	no
1	0.570	3.500×10^3	6140	1.684	1	yes
2	0.100	7.531×10^2	7531	1.558	1	yes
3	1.050	4.687×10^3	4472	1.014	1	yes
4	0.570	3.500×10^3	6140	2.018	0.5	yes
5	0.570	3.500×10^3	6140	3.174	0.1	yes
6(1D)	0.570	3.500×10^3	6140	1.684	1	yes

Note. Seven cases that we study in this chapter. The first four parameters represent the properties of the WNM that we inject from both boundaries of our simulation box. Density is the volume number density where ρ is mass density and $m_{\rm n}$ is the mass of individual particles. Pressure is written in the unit divided by the Boltzmann Constant $k_{\rm B}$. Temperature is the corresponding temperature. Flow speed is the injected speed at the boundaries. $\tau_{\rm cool}$ is the corresponding typical cooling time in each setup calculated by Equation 1.10. Cooling Factor indicates the factors we apply to the fitting cooling function from Koyama & Inutsuka (2002). Conduction shows whether we include $H + H$ thermal conduction (yes) or not (no). Case 0 represents adiabatic colliding flow thus we mark $-$ for $\tau_{\rm cool}$, no for Cooling Factor, and no for Conduction. Throughout these simulations, we employ the box size of 20 pc $\times$ 10 pc $\times$ 10 pc in x, y, z directions respectively. Note that Case 6 employs the same condition from Case 1 but the calculation performs only in the x-direction, thus is essentially restricted to a one-dimensional evolution.

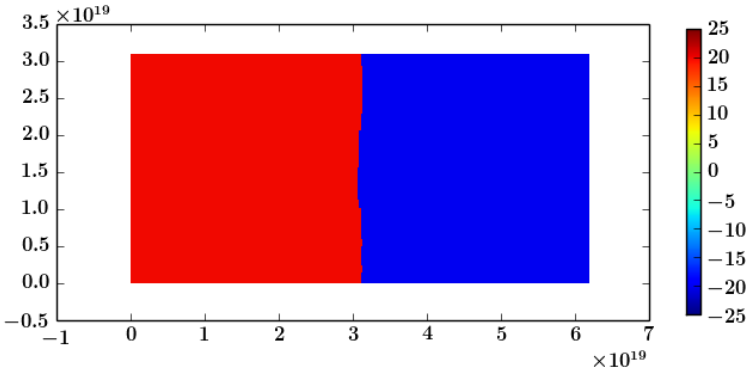

Figure 7.2: The initial velocity field of Case 0. The color corresponds to the velocity of fluid in the unit of km s^{-1}. The tick labels correspond to the physical scale of our simulation box in the unit of cm. The contact position of two fluids is perturbed as introduced in Equation 7.14.

7.3 Results

7.3.1 The Effect of Heating, Cooling, and Thermal Conduction

First, as a test calculation to check the simulation code feasibility, we perform a simulation of adiabatic fluid where we ignore the cooling, heating, and thermal conductivity (Case 0). Figure 7.3 shows three snapshots from the time evolution of density in the xy plane. The fluid is adiabatically heated up and two shock fronts propagate outwards. There is no thermal instability in this case due to no cooling, thus the shock-compressed layer is quiet and stratified structure grows as the shock fronts propagate. Indeed, the measured shock propagation speed of 9 km s^{-1} is maximum among the ones we calculate in this chapter. The velocity dispersion within the shock-compressed layer is also only 1 km s^{-1}. We calculate the effective polytropic index based on Equation 7.3 then obtain 1.656. This value is close to the polytropic index of $5/3$ (*i.e.*, mono atomic index) that we impose on the fluid, which proves our calculation feasibility and also the technique of Equation 7.3.

Next, we perform our fiducial calculation as Case 1. Here we calculate the cooling, heating, and thermal conduction. Figure 7.4 shows the calculated density evolution. Compared with previous adiabatic calculation, the mean density of the ISM within the shock-compressed layer is enhanced due to cooling and turbulence emerges. The accreting mass is accumulated into those cold high density blobs and thus the shock propagation slows down. We search the shock front along x-axis at each given pair of y and z coordinates and calculate their average. The calculated shock-front propagation as a function of time is shown in Figure 7.5. We fit these data points by a linear function of time, which is also shown in Figure 7.5. The measured propagation speed is about 1.2 km s^{-1}, retarded by a factor of seven compared with the adiabatic case. Thus in colliding HI flow, highly turbulent mul-

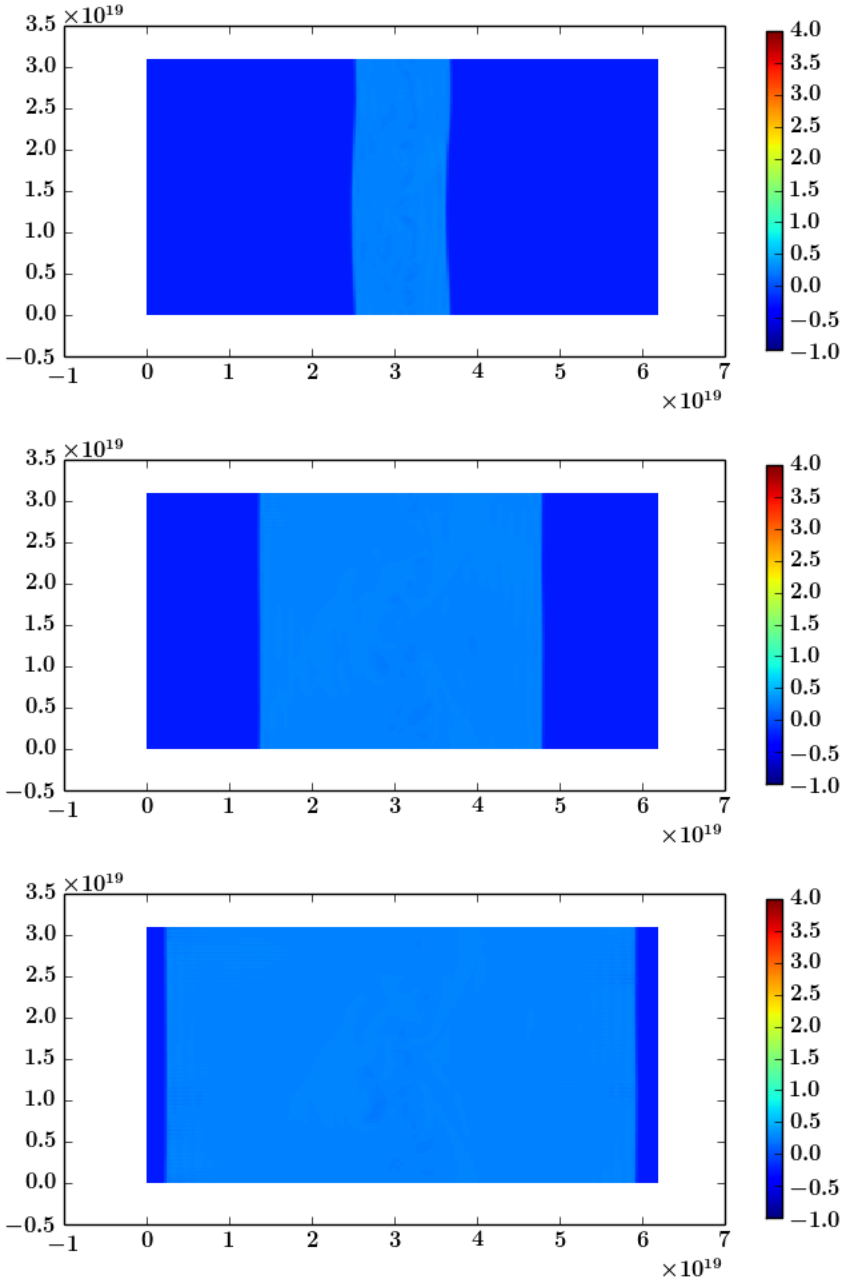

Figure 7.3: Case 0: time evolution of adiabatic fluid. The panels show the density map at 0.2 Myr, 0.6 Myr, and 1.0 Myr from the top to the bottom. The color corresponds to the logarithm of the number density in the unit of cm^{-3}. The tick labels correspond to the physical scale of our simulation box in the unit of cm. The shock propagates outwards smoothly.

tiphase ISM is confined in the shock-compressed layer and this region does not drastically expand. The measured effective polytropic index is almost unity and its reason can be understood by the combination of the mass budget and the volume filling factor in the shock-compressed layer (see the three following paragraphs).

We calculate the mass in the shock-compressed layer and Figure 7.6 shows the obtained cumulative mass distribution whose number density is higher at a given density. In addition, we calculate the volume filling factor in the layer as a function of number density and the result is shown in Figure 7.7. In these analysis, we divide the rane of number density from 0.1 cm^{-3} to 1000 cm^{-3} into 20 bins. These results suggest that fluid with density of > 10 (> 100) cm^{-3} accounts for more than 85 (27) per cent of the mass in the shock-compressed layer, whereas the volume is dominated by fluid with density of 1-10 cm^{-3}. This trend is hold throughout our calculation (*i.e.*, until 10 Myr) once the time exceeds one cooling-time. Therefore, the mass and volume in the effective equation of state can be represented by the total mass in $>$ 10 cm^{-3} regime and the total volume in $<$ 10 cm^{-3} regime, respectively.

Figure 7.8 shows the pressure and density of the cells in the shock-compressed layer. We extract only 4000 cells as the representatives of all the cells in the layer. The distribution of the cells on this figure indicates that, the density of the injected WNM is first enhanced to ~ 1 cm^{-3} almost adiabatically, then they move to higher density regimes due to cooling. Most of the mass is going to be embedded in highest-density cells as Figure 7.6 shows. However, the volume of the layer is dominated by low-density cells (see Figure 7.7), thus most of the cells appear in the low-density regime on Figure 7.8. These cells populate close to the isothermal line extended from the injected WNM condition, which results in the effective polytropic index of almost unity.

We also measure the volume-weighted velocity dispersion within the shock-compressed layer and the result is shown in Figure 7.9. The result shows that the velocity dispersion does not significantly vary between densities less than one-order of magnitude. Almost constant velocity dispersion $\simeq 1$ km s^{-1} for > 10 cm^{-3} indicates that the kinetic energy density is almost proportional to the mass density. This constancy is compatible with an observed density-independent Larson's law in the Milky Way molecular cloud (*e.g.*, L1551 (Yoshida et al. 2010)), but its origin is still an open question. Note that, the combination of Figures 7.7 and 7.9 indicates that the overall turbulent energy of dense cold clumps is comparable to that of diffuse warm gas.

7.3.2 Various Conditions

The initial condition we employ in Case 1 is WNM at thermally equilibrium state of 0.57 particles cm^{-3}. However in reality, the ISM have fluctuations. To simulate such conditions, we perform two additional simulations with lower number density (Case 2: 0.1 particles cm^{-3}) and higher number density (Case 3: 1.0 particles cm^{-3}). Figures 7.10 and 7.11 show the results respectively. Comparison between

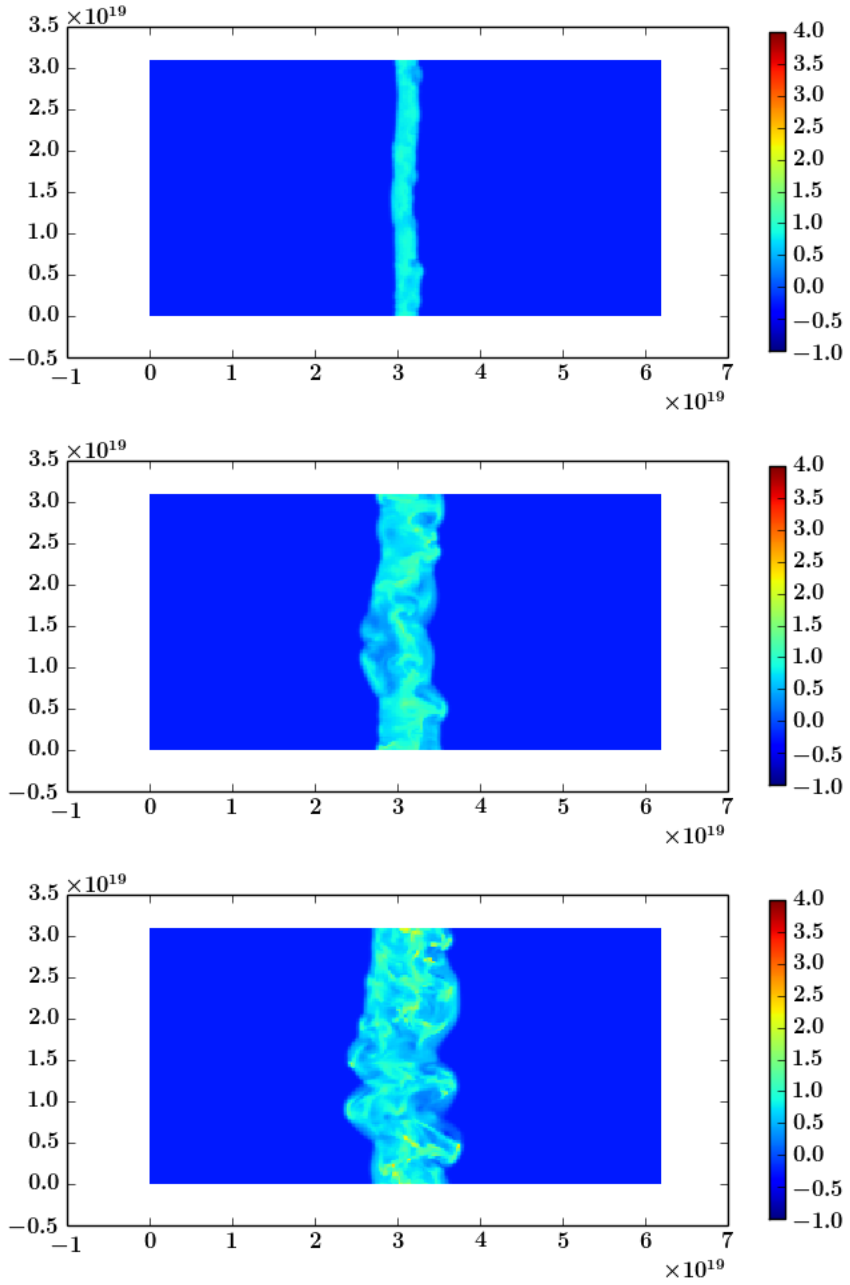

Figure 7.4: Case 1: time evolution of colliding HI flow. The panels show the density map at 0.2 Myr, 0.6 Myr, and 1.0 Myr from the top to the bottom. The color corresponds to the logarithm of the number density in the unit of cm^{-3}. The tick labels correspond to the physical scale of our simulation box in the unit of cm. The shock-compressed layer is formed at the center, within which turbulent multiphase ISM form.

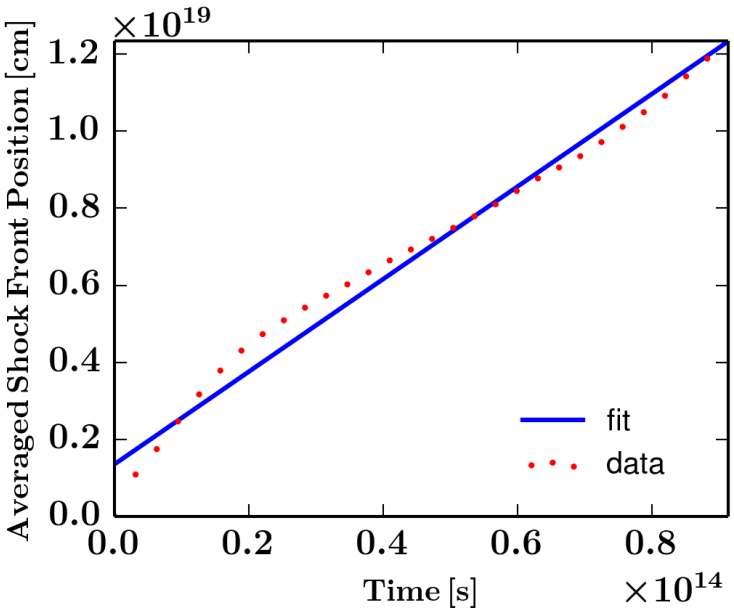

Figure 7.5: The measured shock propagation in Case 1. The horizontal axis shows the elapsed time (in the unit of second) since the collision of colliding flows starts. The vertical axis corresponds to the position (in the unit of centimeter) from the simulation box center where the flows collide. The red scatter points represent the measured shock front position and the blue solid line indicate the fitted shock front position as a function of time. Here, "averaged" means the position averaged over the entire shock front positions. The fitted linear function suggests that the propagation speed is 1.2 km s^{-1}. Note that the width of the shock-compressed layer in the density map is double from the shock front position shown in this figure because there are two shocks propagating to the left and the right in x direction.

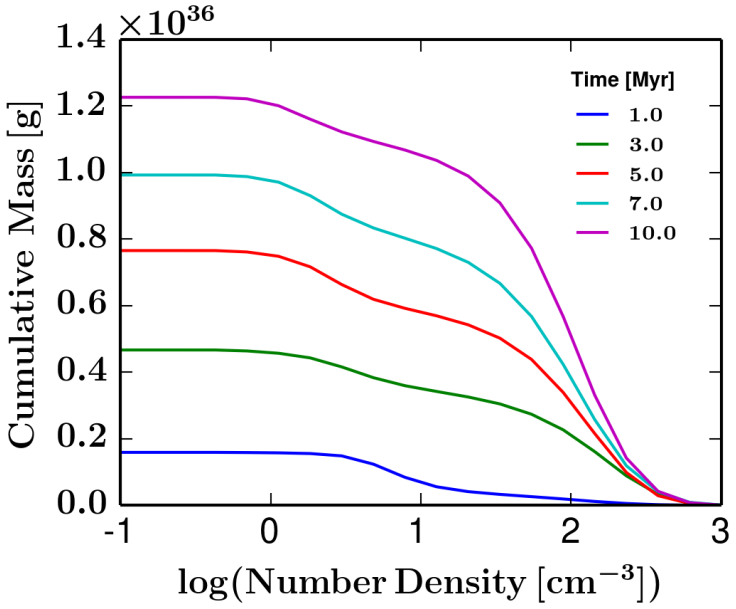

Figure 7.6: The cumulative mass in the shock-compressed layer as a function of number density. The horizontal axis shows the number density (in the unit of per cubic centimeter). The vertical axis is the cumulative mass (in the unit of gram) whose number density is higher at a given horizontal axis, thus the value at the left vertical axis corresponds to the total mass carried by fluid whose number density is > 0.1 cm^{-3}. The color scheme represents the time evolution. The region with $> 10(100)$ cm^{-3} accounts for the 85 (27) per cent of the mass in the shock-compressed layer. The total mass injected into the shock-compressed layer due to colliding HI flow by the time of 10 Myr can be estimated as 2×10 pc $\times 10$ pc $\times$ 20 km s^{-1} $\times$ 10 Myr $\times$ 0.57 cm^{-3} $\times$ 1.27 $\times$ 1.67 $\times$ 10^{-24} g $\simeq 1.5 \times 10^{36}$ g, which matches well with the 10 Myr line shown in the figure. Here the first 2 indicates the two shock fronts, and 1.27 is the mean molecular weight.

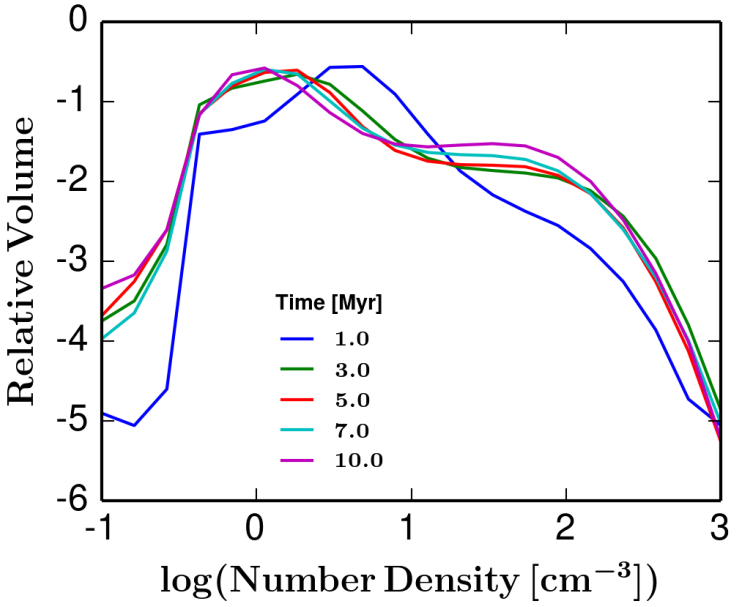

Figure 7.7: The volume filling factor in the shock-compressed layer as a function of number density. The horizontal axis shows the number density (in the unit of per cubic centimeter). The vertical axis is the volume filling factor with respect to the total volume of the shock-compressed layer. The color scheme represents the time evolution. After the one cooling time ($\sim$ 1 Myr), most of the volume is occupied by fluid with density of 1 - 10 cm^{-3} and also partially by the fluid with density of 10 - 100 cm^{-3}.

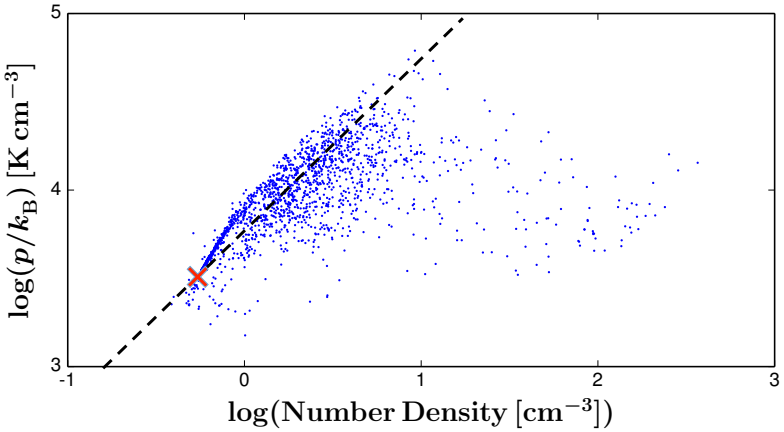

Figure 7.8: The density-pressure diagram in the shock-compressed layer at 3 Myr. The horizontal axis shows the number density (in the unit of per cubic centimeter). The vertical axis is the pressure divided by the Boltzmann constant. The red cross mark indicates the density and pressure of the injected WNM. The black dashed line corresponds to the isothermal line. Individual data points correspond to individual cells in the shock-compressed layer.

these two cases suggest that initially high-density medium reach thermally unstable phase due to shock compression faster than initially low-density medium, and form CNM and turbulent structure in the shock-compressed layer. Table 7.2 summarizes this trend. However, the measured effective polytropic index does not significantly vary from the fiducial calculation. This indicates that we could use single polytropic index in many cases for galactic-scale simulations even when the thermal and dynamical state of the multiphase ISM below simulation resolution.

The calculations shown by now assume conditions of the present-day ISM. For example, the heating and cooling rate assumes the solar metallicity and a typical size distribution for dust particles, called the MRN size distribution (Mathis et al. 1977). To deduce hints for time evolution of the ISM over cosmological timescales, we decided to investigate the metallicity dependence by simply multiplying some factors both to heating and cooling rate (see also Inoue & Omukai (2015)). We opt to multiply a same factor both on cooling and heating rate by assuming that lower-metallicity region have less star forming activity so that stellar radiation field is also weak. Note that, Ly_α cooling is presumably independent from metallicity, thus only the second term in Equation C.3 and Equation C.4 are modified in this analysis. As Case 3, we multiply 0.5 so that the amount of dust and also radiation field is reduced by this factor. Similarly, we multiply 0.1 in Case 4.

Figures 7.12 and 7.13 show the results and Table 7.2 summarizes the measured physical quantities. The trend can be intuitively understood that multiplying smaller factor kills thermal instability more, which reduces turbulence and the volume of high-density regions. Again, the results indicate that we may employ unity

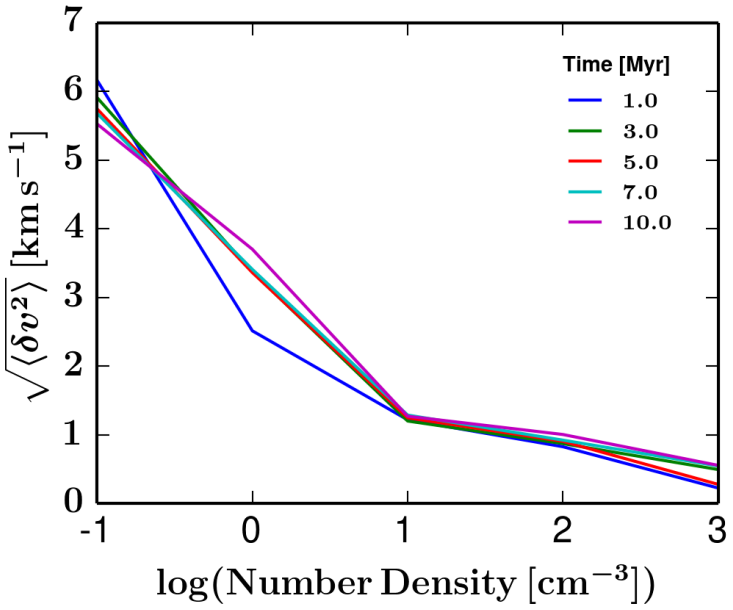

Figure 7.9: The three-dimensional velocity dispersion in the shock-compressed layer as a function of number density. The horizontal axis shows the number density (in the unit of per cubic centimeter). The vertical axis corresponds to the three-dimensional velocity dispersion (in the unit of km s^{-1}). The color scheme represents the time evolution. After the one cooling time ($\sim$ 1 Myr), most of the volume is occupied by fluid with density of 1 - 10 cm^{-3} and also partially by the fluid with density of 10 - 100 cm^{-3}.

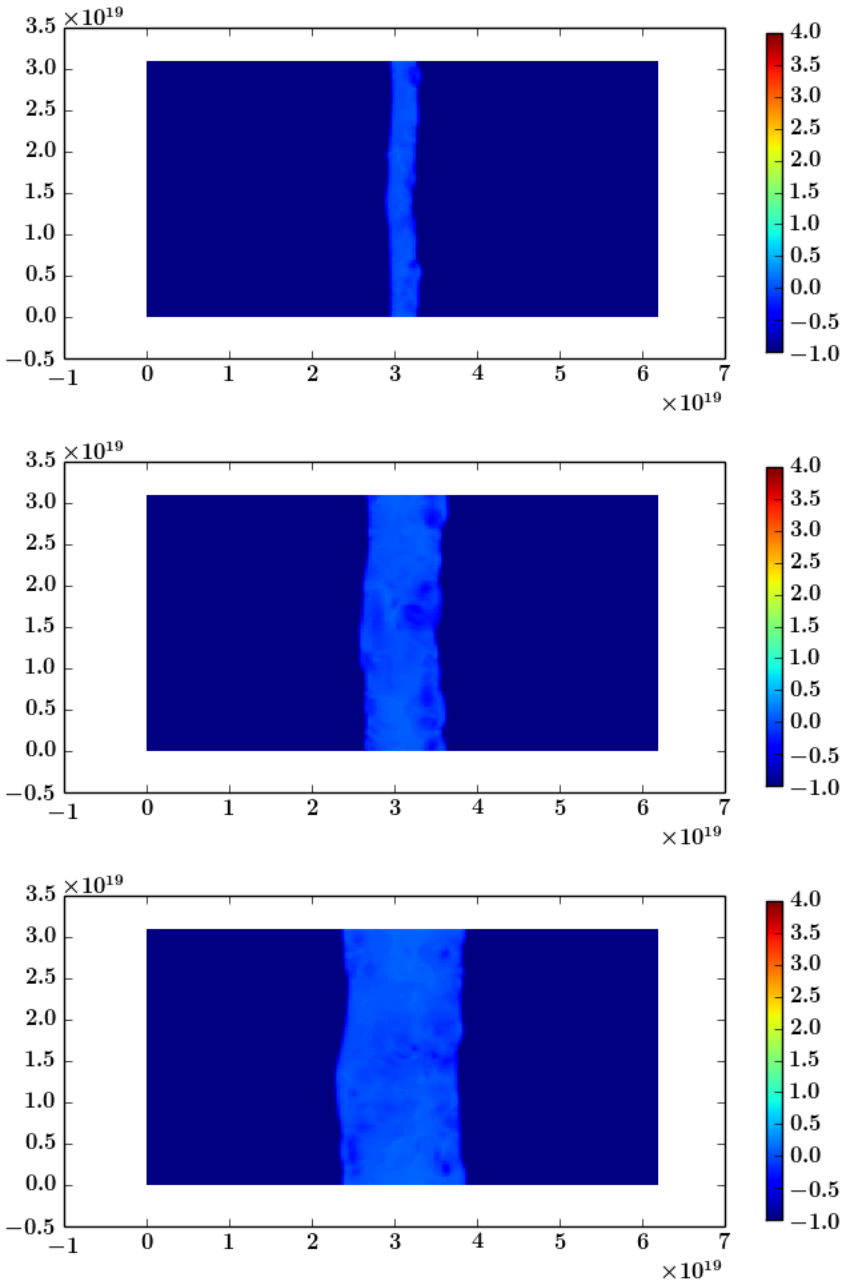

Figure 7.10: Case 2: time evolution of colliding HI flow with assumed high density. The panels show the density map at 0.2 Myr, 0.6 Myr, and 1.0 Myr from the top to the bottom. The color corresponds to the logarithm of the number density in the unit of cm^{-3}. The tick labels correspond to the physical scale of our simulation box in the unit of cm.

Table 7.2: Physical properties of simulated HI flow

Cases	Parameters			
	Shock Propagation Speed (km s^{-1})	Effective Polytropic Index	$\sqrt{\langle \delta v^2 \rangle}$ (km s^{-1})	Mass over 10 cm^{-3} ($M_\odot$)
0	9.061	1.656	1.092	-
1	1.201	0.959	3.905	1.808×10^2
2	1.888	0.970	1.231	-
3	2.111	1.083	4.501	5.344×10^2
4	1.416	0.979	4.631	1.759×10^2
5	1.684	0.991	1.444	1.189×10^2

Note. Obtained properties of colliding HI flow at the time of 3 Myr. Shock Propagation Speed is measured as the propagation speed of temparature jump. Effective Polytropic Index is calculated based on Equation 7.3. $\sqrt{\langle \delta v^2 \rangle}$ is the ensemble averaged velocity dispersion in the overall shock-compressed layer. Mass over 10 cm^{-3} is the total mass (in the unit of $M_\odot$) summed over the cells whose volume number density is > 10 cm^{-3}, "$-$" mark indicates that no cell exceeds 10 cm^{-3} by the final time of the calculation domain. Note that, although we show the time evolution until 10 Myr in Case 1 (*e.g.*, Figures 7.4, 7.5, 7.6, 7.7, and 7.9, we analyze our simulations until 3 Myr for the listed quantities in this table, to eliminate the effect of unrealistic disturbances appearing in the shock fronts (see 7.3.4).

as the effective polytropic index. However, detail setups (*e.g.*, metal species, dust evolution *etc.*) have to be considered further in the future.

7.3.3 Dimensionality

All the calculations shown by now are three-dimensional thus the motions of dense cold gas are highly turbulent in the shock-compressed layer. In this section, as Case 6, we perform the same simulation in Case 1 but instead calculate one-dimensional simulation, by solving only x-direction in Equation 7.4. The result is shown in Figure 7.14. The shock-compressed layer initially grows but gradually shrinks due to cooling. The fluid evolution is confined in the x-direction and thus the formed cold dense gas cannot induce turbulent motion. The resultant shock-compressed layer becomes a thin layer whose number density is essentially determined by the ram pressure of the incident colliding flow.

The ram pressure is evaluated as:

$$\begin{aligned} P_{\rm thermal,fin} &= P_{\rm thermal,int} + \rho_{\rm int} v_{\rm int}^2 \,, \\ &\simeq 3.86 \times 10^4 k_{\rm B} \,, \end{aligned} \tag{7.15}$$

where the subscripts $\rm fin$ denote the values expected in the shock-compressed layer and $\rm int$ represents the conditions in the incident colliding HI flow. Therefore,

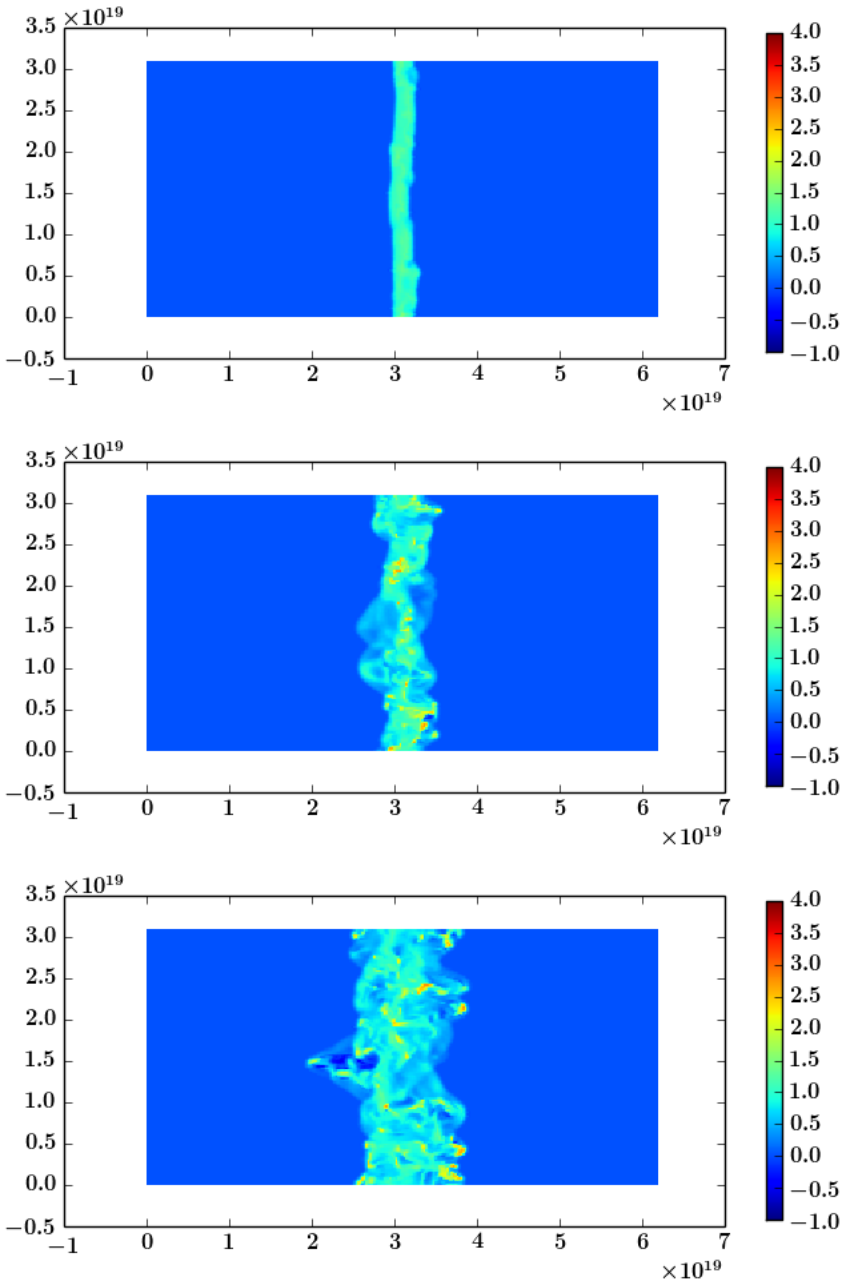

Figure 7.11: Case 3: time evolution of colliding HI flow with assumed high density. The panels show the density map at 0.2 Myr, 0.6 Myr, and 1.0 Myr from the top to the bottom. The color corresponds to the logarithm of the number density in the unit of cm^{-3}. The tick labels correspond to the physical scale of our simulation box in the unit of cm.

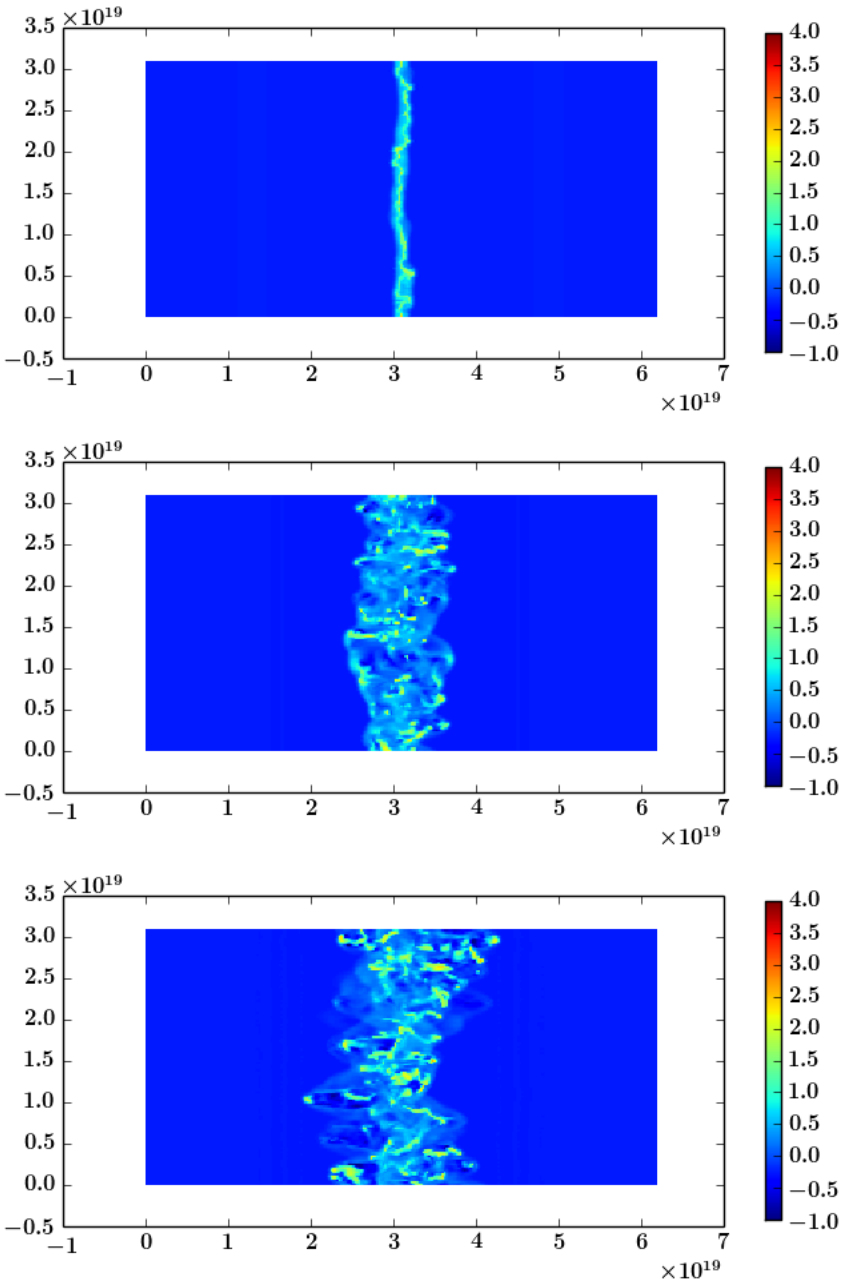

Figure 7.12: Case 4: time evolution of colliding HI flow with assumed low metallicity. The panels show the density map at 0.2 Myr, 0.6 Myr, and 1.0 Myr from the top to the bottom. The color corresponds to the logarithm of the number density in the unit of cm^{-3}. The tick labels correspond to the physical scale of our simulation box in the unit of cm.

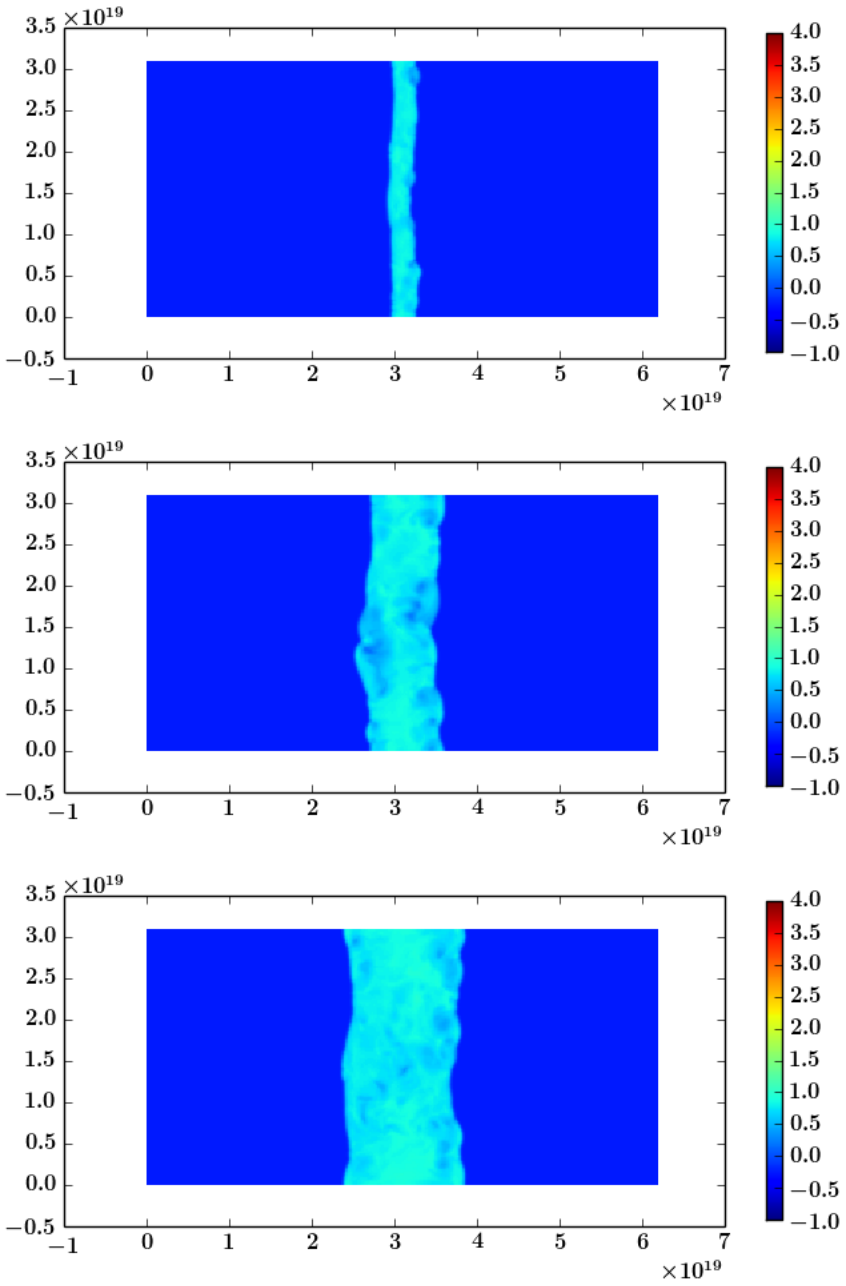

Figure 7.13: Case 5: time evolution of colliding HI flow with assumed low metallicity. The panels show the density map at 0.2 Myr, 0.6 Myr, and 1.0 Myr from the top to the bottom. The color corresponds to the logarithm of the number density in the unit of cm^{-3}. The tick labels correspond to the physical scale of our simulation box in the unit of cm.

once the shock-compressed layer reaches one phase medium in thermal equilibrium state, then the expected number density and temperature are 2000 cm^{-3} and 20 K. Due to this high compression ratio, the shock-compressed layer, the shock front slowly propagates with this density and temperature within the layer. The propagation speed, $v_{\mathrm{shock,prop}}$, can be evaluated by equating the mass gain in the layer and the mass inflow from the incident colliding flow:

$$\begin{aligned} 2000\,\mathrm{cm}^{-3} \times v_{\mathrm{shock,prop}} &= 0.57\,\mathrm{cm}^{-3} \times 20\,\mathrm{km\,s}^{-1}\,, \\ \Rightarrow v_{\mathrm{shock,prop}} &\simeq 5.7 \times 10^{-3}\mathrm{km\,s}^{-1}\,. \end{aligned} \tag{7.16}$$

Note that, the shock propagation discussed here corresponds to the growth in the thickness of the HI shell formed on the surface of expanding bubbles. The actual shock propagation speed in the ISM is the sum of this propagation speed and the incident HI flow speed. Therefore, the three dimension (Case 1) indicates 22 km s^{-1} whereas one dimension (Case 6) indicates 20 km s^{-1}. Therefore, the dimensionality alters the shock propagation speed at most 10 per cent.

7.3.4 Summary of Multi-Phase ISM Simulation

We perform hydrodynamics simulations of colliding HI flow to measure the effective Polytropic index and the shock propagation speed. Our simulated conditions correspond to an adiabatic case, and six cases with cooling, heating, and thermal conduction, two of which are fiducial (one-dimensional and three-dimensional calculations), two are for testing possible density fluctuation in the ISM, and the rest two are for testing low-metallicity environment. Our results indicate that, although the effective polytropic index of the multiphase ISM can be set as unity in most cases, the turbulence energy density and the accumulated amount of high-density gas may have factor of two to four difference depending on the properties of colliding HI flows (*e.g.*, density, metallicity, and so on). In addition, we find that the dimensionality does not significantly alter the shock-propagation speed (only up to 10 per cent). Therefore, one-dimensional evaluation is still valid for estimating the expansion rate of bubbles in the multiphase ISM driven by supernovae and massive stars, and the corresponding interval timescale of repeated supersonic shock passage in the ISM. We reserve further parameter surveys to summarize this trend for our future investigations.

Note that, dense clumps formed behind one shock front may pass through the shock-compressed layer and penetrate the other shock front on the other side. The shock fronts start to be significantly disturbed and many dense cold clumps are observed traveling away from shock fronts at later stages. For example in our fiducial calculation Case 1, such disturbances appear at about 5 Myr. This phenomenon is physically correct in our setup but simply due to our choice of colliding HI flow condition. In most cases in reality, however, only single shock propagates in the ISM. The penetration of dense cold clumps thorough shock fronts is less likely to take place. Therefore, our future task is to perform a single shock front propagation

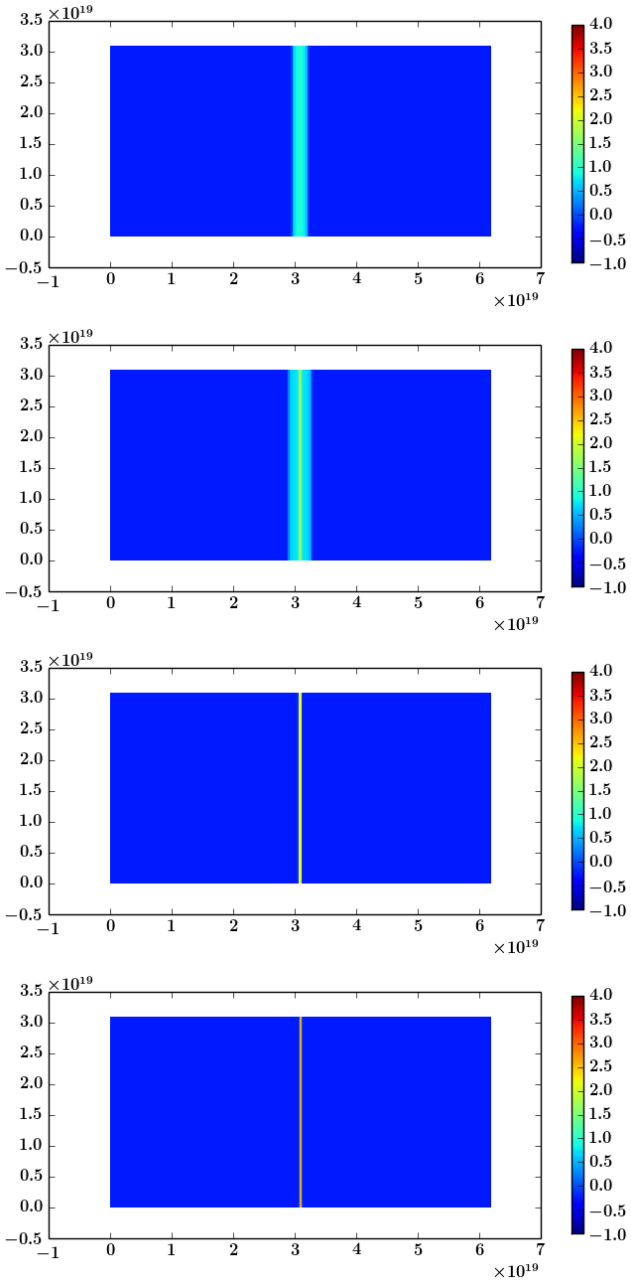

Figure 7.14: Case 6: time evolution of colliding HI flow. Panels show the density map at 0.2 Myr, 0.6 Myr, 1.0 Myr, and 1.5 Myr from the top to the bottom. The color corresponds to the logarithm of the number density in the unit of cm^{-3}. The tick labels correspond to the physical scale of our simulation box in the unit of cm. The shock-compressed layer is formed at the center, which initially grows and later shrinks due to cooling. The pressure and the density in the shock-compressed layer essentially reach the level expected from the ram pressure of the incident colliding flow.

(such as Koyama & Inutsuka 2002) to investigate more stable long-term evolution of shock wave propagation in the multiphase ISM. In addition, such dense clumps are expected to be trapped in (or restored into) the shock-compressed layer by gravity in reality. Implementation of self-gravity is thus our another future work.

Spatial resolution and magnetic fields are other improvements expected in our studies. Our current simulations have a spatial resolution of 0.08 pc, which is almost comparable to the cooling length of CNM (see section 1.4.4). Therefore, we barely resolve the thermal instability in the most densest part of the shock-compressed layer (*e.g.*, > 100 cm^{-3}). Also, previous studies of magnetohydrodynamics simulations indicate that the magnetic fields of a few micro Gauss in the ambient ISM may alter the shape/porosity of supernova remnants, in particular in its late phase (*e.g.*, snowplow phase; Slavin & Cox 1992; Hanayama & Tomisaka 2006). Thus, as a future study, we are planning to perform simulations again with finer spatial resolutions and with magnetic fields.

7.4 Implication for Galactic-Scale Simulation

By chapter 6, we present our time evolution model for GMCMFs on 100-pc scales. This semi-analytical model opens up windows for large parameter surveys to investigate observational features and relations in wide variety of galactic environment that past, ongoing, and upcoming observations can reach, for example, Kennicutt-Schmidt law (Kennicutt 1998; Gao & Solomon 2004).

In our current GMCMF model, we opt to conduct our investigations with the parameters basically constant (*e.g.*, $T_{\rm f}$, $T_{\rm d}$, $\varepsilon_{\rm res}$, $\varepsilon_{\rm SFE}$ *etc.*). This is based on an assumption that the GMCMF evolution is relatively fast (see Section 6.2) so that GMCMFs are likely shaped in a given local environment. However in general, GMC groups migrate within galactic disks, from arms to inter-arms and back into arms for example. The parameters in our model, especially $T_{\rm f}$, $T_{\rm d}$, and $\varepsilon_{\rm res}$, could be environment-dependent in more general studies. Therefore, we have to introduce formulations that make the parameters evolve by themselves in time.

Such modifications within semi-analytical formulation restrict ourselves to conducting simple extensions from our current studies in a given galactic environment. Ideally, such an ISM evolution has to be coupled with galaxy evolution consistently. One method to achieve this aspiration is performing galactic-scale simulations by employing our semi-analytical models as a subgrid model. Figure 7.15 describes our plan of galactic simulations by using Smoothed Particle Hydrodynamics (SPH) method (Lucy 1977; Gingold & Monaghan 1977; Inutsuka 2002; Sugiura & Inutsuka 2016). Meanwhile the entire disk of a galaxy is represented by group of SPH particles, individual SPH particles solve the time evolution of the multiphase ISM based on our GMCMF model.

Measured physical properties of the multiphase ISM in section 7.3 are necessary for describing the state of individual SPH particles, with which the interaction between SPH particles are determined. From our analysis in section 7.3, the mass

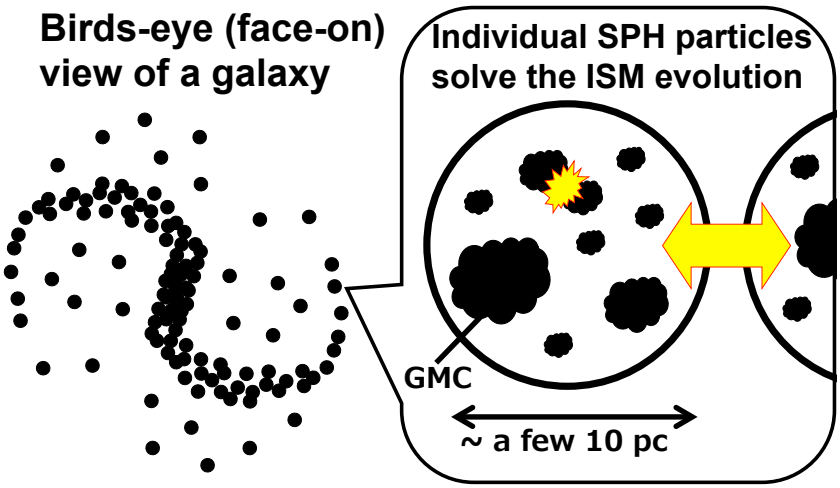

Figure 7.15: Schematic figure describing the procedure of our prospective SPH simulations. The left part of this figure shows that the entire galactic disk is simulated with SPH particles. The right part of this figure indicates that individual SPH particles calculate the time evolution of the multiphase ISM based on our GMCMF model. The yellow flashing icon in one SPH particle indicates CCC and the yellow two-headed allow represents interaction between SPH particles (*e.g.*, through gravity, pressure gradient, and so on). In this manner, galaxy evolution is expected to be consistently and simultaneously calculated along with GMC formation, evolution, dispersal and CCC on sub 100-pc scales.

and volume of individual particles are represented by the total mass of GMCs and the total volume of WNM, respectively, within the particles. The effective equation of state of each particle (*i.e.*, the multiphase ISM[5] coarse-grained over a few 10 pc) has its polytropic index as unity. We believe that this formulation indeed becomes essential not only in ISM studies but even for cosmological large-scale structure simulations where galaxies are prescribed by some subgrid method.

[5]Technically speaking, "multiphase" here has to include all the phases in the ISM, but in practice we mainly meant as WNM, CNM, and GMCs.

Chapter 8

Summary, Conclusions, and Future Prospects[1]

In this chapter, we first summarize this thesis followed with conclusions. At the end, we address future prospects, especially potential synergies with and suggestions to ongoing and future observations.

8.1 Summary and Conclusions

In this thesis, we have formulated a time evolution equation for giant molecular cloud (GMC) mass functions in multiphase interstellar medium (ISM) and largely explored their evolutions in various regions of galactic disks. By this, we aimed at connecting the cloud-scale physics to galaxy evolution. Our final formulation includes GMC formation and mass-growth due to multiple episodes of supersonic compression, GMC self-dispersal due to massive stars that are born within those GMCs, gas resurrection that replenishes the minimum-mass GMC populations, and rapid massive star formation and its feedback driven by cloud-cloud collision (CCC) events. Our formulation is based on the paradigm that GMCs are created from magnetized WNM in galactic disks through multiple episodes of compression and such compression is driven by the network of expanding HII regions and the late phase of supernova remnants. We performed integration of this time evolution equation to reproduce and explain the possible origin of the observed variation in the slope of the mass functions.

First, we formulated a time evolution equation including GMC formation, mass-growth, dispersal, and coagulation due to CCCs. We assume that dispersal is dominated by self-dispersal and is independent of parental GMC mass, and CCC works as an perfect inelastic coagulation. The integration of this time evolution equation gives GMCMF time evolution. Our results predict that GMC mass functions have a single power-law exponent in the mass range $< 10^{5.5}\mathrm{M}_{\odot}$ (where $\mathrm{M}_{\odot}$ represents

[1] *The contents of this chapter are partially based upon the articles Kobayashi et al. (2017b) and Kobayashi et al. (2017a).*

the solar mass), which is well characterized by GMC self-growth and dispersal timescales. In addition, our results suggest that the CCC effect is limited only in the massive-end of the mass function, therefore CCC is sub-dominant process shaping the GMCMF evolution, except for very crowded regions like galactic centers where GMC number density is higher than normal galactic disk regions.

Next, we identify a gas *resurrection* channel that allows the gas dispersed by massive stars to regenerate GMC populations or to accrete onto the pre-existing GMCs. To evaluate this, we introduce "gas resurrecting factor", which is a fraction of such resurrected gas out of total amount of dispersed gas. We explore, both in semi-analytical and numerically, what resurrecting factor has to be achieved to reproduce the observed profile of GMCMF. Our analysis indicates that almost all the dispersed gas in arm regions can be captured by pre-existing massive GMCs because of their large surface area, whereas nearly half of the dispersed gas in inter-arm regions is used for replenishing the minimum-mass GMC populations because inter-arm regions host less number of massive GMCs than arm regions. We find that there is a one-to-one relation between gas resurrecting factor and power-law slope of GMCMFs. Thus, our results suggest that measurement of the GMCMF slope provides a powerful method to constrain those GMC timescales and the gas resurrecting factor in various environment across galactic disks. Also, as a future investigation, detail simulations are desired to identify which phase of the ISM is important for this gas resurrection.

In addition, we introduced CCC-driven star formation terms in our time evolution equation. This formulation allows us to evaluate GMC rapid dispersal due to CCCs and compute star formation rate originated in CCCs. The time integration of the time evolution equation indicate that the stellar feedback triggered by cloud-cloud collisions modify only the massive end of GMC mass functions. Thus the mass functions still exhibit power-law slopes in the low-mass regime ($\lesssim 10^{5.5}\mathrm{M}_{\odot}$). Our results suggest that, although CCC events between smaller clouds outnumber the ones between massive GMCs, the amount of stars produced by CCC is mostly driven by massive GMCs $\gtrsim 10^{5.5}\mathrm{M}_{\odot}$. The resultant cumulative CCC-driven star formation may amount to a few 10 per cent (at most half) of the total star formation activity in the Milky Way and nearby galaxies. We also predict the observability for CCC sites and show that almost all of the CCC sites that observations possibly reach consist of less massive GMCs $\lesssim 10^{5.5}\mathrm{M}_{\odot}$, which have less impacts on the total CCC-driven star formation. Therefore, in addition to recent observational indication of CCCs between law-mass GMCs, it is still desired to conduct further observations to identify CCC sites due to massive GMCs and quantitatively evaluate CCC-driven star formation.

Finally, we have performed three-dimensional hydrodynamics simulations of colliding HI flow where multiphase turbulent ISM is developed within shock-compressed layer. We measured the shock propagation speed and the density jump by comparing the mean density in and out the layer. This analysis gives an effective equation of state for the multiphase ISM, which has an effective polytropic index close to unity. The shock-propagation speed differs only up to 10 per cent between

one-dimensional and higher-dimensional evaluations. We reserve detail analysis with higher spatial resolution and with magnetic fields for future studies.

Throughout this thesis, our prescription focuses on evolution over the last 1 Giga year in the history of the Universe. Beyond which, we has to incorporate various other detailed processes, such as time evolution of magnetic fields, gas accretion from large scale structure, galaxy mergers, metal enrichment process, and so on. Including all these processes into one prescription is still challenging. Nevertheless, the current study with the effective equation of state marks a first step to study galaxy evolution in which the evolution of multiphase ISM and star formation are consistently calculated.

8.2 Future Prospects

As introduce in Section 1.5, stars form at densest parts of GMCs. It is thus important to evaluate the dense gas mass fraction within GMCs, especially relative fractions such as mass in filaments out of GMCs, mass in molecular cloud cores out of filaments, mass that ables to form protostars out of currently visible molecular cloud cores, and so on. It becomes important to conduct both observational studies evaluating dense gas mass fraction in GMCs and theoretical studies determining how this fraction is governed (*c.f.*, Vázquez-Semadeni et al. (2011); *c.f.*, Morokuma-Matsui & Muraoka (2017) for galactic-scale studies). *Herschel* observations indicate that the fraction of filament mass out of GMCs can be limited to $\simeq 10$ per cent (*e.g.*, Könyves et al. 2010). They also indicate that only 15 per cent of the mass above $A_{\rm V} = 7$ is stored in prestellar cores. The mechanism that sets these fraction may be responsible for inefficient star formation in galactic disks, whose efficiency is more than 10 times lower than expected efficiency for free-fall ISM collapse. Also, CCC observations indicate that massive star formation takes place only in high column density regions in CCC sites (*e.g.*, $> 10^{23}$ cm^{-3} Furukawa et al. 2009; Ohama et al. 2010; Fukui et al. 2014, 2016). In our GMCMF model, we did not explicitly question the internal structure of GMCs except for the assumption employed to determine $T_{\rm f}$. We have to model the evolution of such internal structure to give more consistent star formation prescription. If filaments are ubiquitous in all GMCs, we have to understand not only its formation, but also mass-feeding onto this filaments to sustain star formation activity (Hennebelle & André 2013) and/or filament dispersal mechanism. We are part of B-fields In STar forming RegiOns (BISTRO) project in JCMT Telescope[2], which measures polarizations of magnetic fields funneling onto filaments, and hope that these measurements as well as other continuum surveys (*e.g.*, ArTEMIS[3]: André et al. (2016)) provide further insights into star formation.

Observational collaboration also has to be done. Atacama Large Millime-

[2] http://www.eaobservatory.org/jcmt/science/large-programs/gb_bfields/

[3] http://www.apex-telescope.org/instruments/pi/artemis/

ter/Submillimeter Array (ALMA; Beasley et al. (2006); *c.f.*, Iguchi et al. (2009)) is currently one of the largest radio interferometer over 0.3-3 mm wavelength range. ALMA started Large Programs from its Cycle 4, which accommodate projects whose observations require more than 50 hours in 12-m Array[4]. Indeed, there are proposals submitted to ALMA aiming at surveys of GMC mapping in nearby galaxies. One representative survey of such ALMA Large Program proposals is accepted in Cycle 5 to target at all the nearby massive disk galaxies whose stellar mass is greater than $10^{9.75}\mathrm{M}_{\odot}$ (ID:2017.1.00886.L[5]). Not only ALMA, but also JCMT observatory has its large project CHIMPS2[6], which is 404 hours observation in 13CO and C18O(J=3-2) towards inner parts of the Milky Way galaxy. Pilot survey (CHIMPS: Moore et al. (2015); Rigby et al. (2016)) already show its results, including a clump mass function followed with discussions of universality in core formation efficiency. Nobeyama 45 m telescope in National Astronomical Society of Japan also conduct its legacy surveys[7], all of which are related to star formation. Among them, COMING survey (Muraoka et al. 2016; Hatakeyama et al. 2017) as a complementary studies with ALMA is promising to provide important information of molecular gas distribution and its variation against atomic hydrogen, albeit relatively low-resolution that cannot spatially resolve individual GMCs. FUGIN project (Umemoto et al. 2017) also reveals many bubble structure in the galactic plane and report candidate CCC site. By performing galactic-scale SPH simulation, we aim at producing results compatible with these observations in the future.

[4]Cycle 5 Proposer's Guide: https://almascience.nao.ac.jp/documents-and-tools/cycle5/alma-proposers-guide

[5]https://almascience.nrao.edu/observing/highest-priority-projects

[6]http://www.eaobservatory.org/jcmt/science/large-programs/chimps2/

[7]http://www.nro.nao.ac.jp/~nro45mrt/html/prop/NP.html

Acknowledgment

I am greatly indebted to my supervisor Prof. Naoshi Sugiyama for guiding me over the last 5 years during my Ph.D. course. His extensive mentoring greatly helped my important decisions and supported my mentality. If he had not been as a professor in Nagoya University, I might have left this field already.

I am thankful to Shu-ichiro Inutsuka for educating me on a daily basis. He was always supportive on me to conduct this project in a way that his enthusiasm and our practical discussions enhanced my motivation.

I have the honor of collaborating with Yasuo Fukui; he kindly provides me a great opportunity to study molecular cloud properties in the Milky Way and nearby galaxies, which also gives me a chance to investigate cloud-cloud collision on galactic scales.

Hiroshi Kobayashi, Tsuyoshi Inoue, and Kenji Hasegawa patiently listen to me and always provided practical advice in every single step. I studied greatly from Takahiko Matsubara, Kiyotomo Ichiki, and Takeru Suzuki not only science but also virtue. I also appreciate Tsutomu Takeuchi for giving me this great opportunity to study at Nagoya University. Other members in the cosmology group at Nagoya University (Hiroyuki Tashiro, Atsushi J. Nishizawa, Yuko Urakwa, Sachiko Kuroyanagi, Atsushi T. Nishizawa, Daisuke Nitta, Naoya Kitajima, and Jean-Baptiste Durrive) educated me in detail based on their specialties. I obtained wide backgrounds from them during the last 5 years from small talks to scientific talks. I thank to other former members of astrophysics groups at Nagoya University: Yoshiki Matsuoka, Chiaki Hikage, Kenji Kadota, Toyokazu Sekiguchi, Maresuke Shiraishi, Yoshinori Satoh, Shogo Masaki, Yoshitaka Takeuchi, Takahiro Inagaki, Shohei Aoyama, Kohei Kumazaki, Hayato Shimabukuro, Daichi Kashino, Shohei Saga, Shinsuke Asaba, Katsuhiro Murata, Mai Fujiwara, Ryosuke Asano, Tomoko Suzuki, Hiroshi Kimura, Iwasaki Kazunari, Yusuke Tsukamoto, Takuma Matsumoto, Masahiro Ogihara, Hiroyuki Kurokawa, Satoko Sorahana, Jennifer Stone, Sanemichi Takahashi, Yuri Fuji, Roh SoonYoung, Yuki Tanaka, Tetsuya Kudoh, Minako Noguchi, Katarzyna Ewa Małek, and Aleksandra Alicja Solarz. I cannot thank enough my colleagues: Atsuko Kawakita, Koichiro Horiguchi, Ryota Okamoto, Mikito Yamamoto, Hoshino Hanako, Takanori Suzuki, Jun Nishizawa, Kei Koborinai, Hiroaki Kawahara, Yoshihiro Shigekami, Risa Sakakibara. I also thank all the other people with whom I interact in Nagoya University by now. They all stand by me always. I cannot adapt myself to Nagoya University environment

without their kind education.

It was very great to interacting with Keiichi Kodaira, Hiroshi Karoji, Philippe Andre, Patrick Hennebelle, Enrique Vazquez-Semadeni, and Yoshiaki Taniguchi. They encouraged me throughout this project.

Intensive discussion with Eve Ostriker, Jeremy Goodman, Chang-Goo Kim, Munan Gong, and James Stone greatly motivate me to consider connections from my studies to galactic-scale simulations and chemistry in star-forming regions. This experience became the important first step to plan my long-term research after the graduation. I appreciate Alexie Leauthaud, Surhud More, Clotilde Laigle, Henry McCracken, Jason Rhodes, and Robert Lupton for many practical discussions on my weak gravitational lensing analysis, data production, and English grammar collections. Their kind support educated me to acquire skills for scientific research. I thank Jin Koda, Kengo Tachihara, Hidetoshi Sano, Akihiko Hirota, Atsushi Nishimura, Dario Colombo, Veselina Kalinova, Jens Kauffmann, Thushara Pillai, Karl Menten, Eva Schinnerer, Sharon Meidt, Henrik Beuther, Juan Soler, Jouni Kainulainen, Dimitrios Gouliermis, Maria Jesus Jimenez, Takuma Kokusho, Kazushi Sakamoto, Patrick Koch, Ya-Wen Tang, Doris Arzoumanian, Jhon Silverman, Yusei Koyama, Masayuki Tanaka, Akio Inoue, Fumi Egusa, Kana Morokuma-Matsui, Kotaro Khono, Yoichi Tamura, Hiroyuki Nakanishi, Koichiro Nakanishi, and Misato Fukagawa for educating me with their observational backgrounds. I also appreciate Hosokawa Takashi, Kazunari Iwasaki, Masahiro Nagashima, Kohei Inayoshi, Martin Bureau, Ralph Schoenrich, Steven Longmore, Toby Moore, Jonathan Henshaw, Gary Fuller, Anthony Whitworth, Nicolas Peretto, Ana Duarte Cabral, Paul Clark, Cathie Clarke, Thomas Haworth, Chiaki Kobayashi, Hua-Bai Li, Kengo Tomida, Kentaro Nagamine, Jonathan Tan, Stefanie Walch, Daniel Seifried, Diederik Kruijssen, Melanie Chevance, Sarah Jeffreson, Daniel Haydon, Marta Reina-Campos, Ralf Klessen, Eric Pellegrini, Daniel Rahner, Bhaskar Agarwal, Ronald Taam, Hiroyuki Hirashita, Kouichi Hirotani, Huei-Ru Chen, Shih-Ping Lai, Tomotsugu Goto, and Sei-ichiro Watanabe for fruitful discussions. It was great memory to enoucrage each other: Yutaka Hirai, Tatsuya Matsumoto, Tomohiro Ono, Jiro Shimoda, and Kazuhiro Shima throughout our Ph.D. period.

The secretaries at Nagoya University (Hitomi Tanaka, Machiko Yoshida, and Kyoko Yamazaki) provided amazingly attentive and motherly care on me. I now would like to honor them as my *mother* in Nagoya. Moreover, jogging is central to making me healthy and powerful all the time. I thank those who join the jogging activity every week. I also thank Shogo Masaki, Akimasa Kataoka, Ryo Tazaki, Kohei Hattori, Kazunori Akiyama, Teppei Okumura, Miho Ishigaki, Shun Saitoh and Akira Konno for helping me during my job hunting.

The studies I present in the current thesis is supported by Grants-in-Aid from the Ministry of Education, Culture, Sports, Science, and Technology of Japan. This grants-in-Aid helped me to visit researchers all over the world to have fruitful discussions. Also, my hydrodynamics simulations and their analysis were carried out on Cray XC30 at Center for Computational Astrophysics, National Astronomical Observatory of Japan. These computational resources give me a great opportunity

to perform large simulations.

I appreciate the former president of Meiji University Hiromi Naya, for giving me an opportunity to study physics. I owe Tokuzo Shimada for starting my career in Meiji University. His passion initiated and strengthened my will to study astrophysics. I want to thank Tomohiko Kiyooka, Hifumi Hayashi, and Keita Hatooka and Keizo Yamawaki. They broaden my horizon to overseas. I thank all the other friends from Meiji University; some of them kindly keep in touch closely to date.

Education by Toshihiko Miyagawa gave me vast insights and various way of thinking. This principle underlies all the field of acadmic studies. Michael W. Maksimuk stimulated me a lot. Countless interaction with him forms the core of myself as a physicist. They are definitely the outstanding master and mentor in my life. I also thank many anonymous passengers next to me on airplanes while I was heading to conferences overseas during this project; they encouraged me greatly and kindly. I hope this thesis can reach them.

Living in this Universe is miracle. Studying Astrophysics and Cosmology is indescribable. I cannot imagine such a beautiful life without all the love from my parents. Without their understanding, my dream to go to graduate school and study Astrophysics and Cosmology in Nagoya would never come true. Their frequent messages from a non-physicist viewpoint offered perspectives to me. Their financial support is the strongest backbone that establishes my studying environment where I am always enthusiastic on physics. Lastly but most importantly, their occasional mental support made my hearts resuming its beat from time to time. I am proud of myself as a child of my parents, “Masato Kobayashi”.

Appendix A

Mass Functions

In this chapter, we quickly summarize nomenclature and notations we use in this thesis to evaluate mass functions. One can find that the power with respect to mass has information of the mass budget in a considered system.

The differential number density of GMCs with mass m is represented by $n_{\rm cl}$. Thus the cumulative number density of GMC groups with mass greater than m, $n(>m)$, is given as

$$n(>m) = \int_m^\infty n_{\rm cl}(m){\rm d}m\,, \tag{A.1}$$

and the total number of GMC groups within a given volume $N_{\rm tot}$ is given as

$$N_{\rm tot} = \oint \int_0^\infty n_{\rm cl}(m){\rm d}m\,{\rm d}V\,. \tag{A.2}$$

Similarly, the total mass density of GMC groups with mass greater than m, $\rho_{\rm GMC}$, is given as

$$\rho_{\rm GMC} = \int_0^\infty n_{\rm cl}(m)m{\rm d}m \tag{A.3}$$

$$= \int_1^\infty n_{\rm cl}(m)m^2{\rm d}\ln(m)\,. \tag{A.4}$$

Therefore, the mass density of GMC groups with mass m per unit logarithmic mass interval $\Delta \ln m$ can be evaluated as

$$n_{\rm cl}(m)m^2\,. \tag{A.5}$$

Given a GMCMF with its profile of $n_{\rm cl} \propto m^{-\alpha}$, Equation A.5 shows that $-\alpha+2 > 0$ (*i.e.*, $-\alpha > -2$) corresponds to the case where the mass budget in a considered system is dominated by massive GMCs, whereas $-\alpha + 2 < 0$ (*i.e.*, $-\alpha < -2$) corresponds to the case where the mass budget in a considered system is dominated by low-mass GMCs. PAWS results ($-\alpha > -2$ in arm regions and $-\alpha < -2$ in inter-arm regions; see Subsection 2.1.2) indicate that massive GMCs dominate the mass budget in arm regions and low-mass GMCs have larger amount of mass in inter-arm regions.

Appendix B

Comparison with The Conservation Law of Mass

In this chapter, we highlight the second term in our time evolution equation of GMCMFs, and make comparison between our formulation and ordinary mass conservation law in fluid dynamics. This comparison provides a better and more intuitive understanding that our formulation is based on the GMC number conservation but not mass conservation. During this chapter, we present one-dimensional formulation to make the comparison easy, but three-dimensional formulation is essentially the same.

B.1 Lagrangian View of GMC Mass-Growth

Our time evolution equation for GMC mass functions (Equation 5.2) is formulated based on the Eulerian perspective. In this section, we present its Lagrange perspective.

In the ordinary conservation law of mass in fluid dynamics, the Eulerian formulation and the Lagrangian formulation can be written as follows respectively:

$$\frac{\partial \rho}{\partial t} + \frac{\partial}{\partial x}(\rho v_x) = 0\,, \quad \frac{\mathrm{D}\rho}{\mathrm{D}t} + \rho \frac{\partial v_x}{\partial x} = 0\,. \tag{B.1}$$

Here v_x is the bulk velocity of fluid in x-direction. This indicates that the density ρ increases in the direction of $\partial v_x / \partial x < 0$.

Similarly, the second term in Equation 5.2 can be written both in Eulerian and Lagrangian forms as follows:

$$\frac{\partial n_{\mathrm{cl}}}{\partial t} + \frac{\partial}{\partial m}\left(n_{\mathrm{cl}} v_m\right) = 0\,, \quad \frac{\mathrm{D}n_{\mathrm{cl}}}{\mathrm{D}t} + n_{\mathrm{cl}} \frac{\partial n_{\mathrm{cl}}}{\partial m} = 0\,. \tag{B.2}$$

Here v_m means the speed of GMCs in mass space, which corresponds to the mass-growth rate. This indicates that the differential number density n_{cl} increases in the direction of $\partial v_m / \partial m < 0$. In other words, n_{cl} becomes larger in the direction

of populations growing in mass more slowly. Therefore, $n_{\rm cl}$ in our calculation is always larger for lower-mass GMCs due to our assumed mass-growth speed of $v_m = m/T_{\rm f}$.

B.2 Differences between Numbers and Mass

The mass-growth part of our time evolution equation (Equation B.2) is based on "number" conservation of GMCs (see Subsection 3.1.1). Let us multiply this equation by mass m to evaluate the evolution of GMC mass:

$$\frac{\partial m n_{\rm cl}}{\partial t} + m\frac{\partial}{\partial m}\left(n v_m\right) = 0 \tag{B.3}$$

$$\Rightarrow \frac{\partial m n_{\rm cl}}{\partial t} + \frac{\partial}{\partial m}\left(m n_{\rm cl} v_m\right) = n v_m \,. \tag{B.4}$$

The comparison with Equation B.1 shows that our formulation is based on the number conservation thus there is a source term appears on the right hand side in mass evolution equation (Equation B.4). This source term means that GMC populations at intermediate mass ranges grow in mass when they flow in mass space, with the growth-speed of individual GMCs characterized as v_m. Therefore, we here would like to emphasize again that our formulation is based on the number conservation but not mass conservation.

Appendix C

Micro Processes in Multiphase ISM

C.1 Cosmic Ray Ionization in GMCs

In diffuse ISM, ultraviolet photons can dissociate molecules. However, they cannot penetrate into deep inside GMCs because they are absorbed by dust particles or are consumed for dissociation of molecules at the surface of GMCs. Instead, cosmic rays, mostly protons of its energy 1-100 MeV, can propagate along magnetic field lines channeled in GMCs and ionize molecules. Therefore cosmic rays are important to evaluate the ionization degree in GMCs.

First, hydrogen molecules are disrupted due to collision with cosmic rays and produce H^+. Then, this H^+ interact with another hydrogen molecule to produce H_3^+ and H. On the other hand, H_3^+ is disrupted by CO molecules in GMCs and generate HCO^+ and hydrogen molecule. Then this HCO^+ can be converted to CO and H by collision with electrons. In the case of equilibrium state where hydrogen destruction and reproduction rates balance out each other, then the ionization degree can be estimated as:

$$\frac{n_{\rm electron}}{n_{H_2}} \sim 10^{-7}\sqrt{\frac{10^4\,{\rm cm}^{-3}}{n_{H_2}}}\,. \tag{C.1}$$

Therefore, the typical ionization degree in GMCs is 10^{-7}. Of course, this degree increases towards the surface of GMCs and reaches $\sim 10^{-4}$, assumed that the dissociation of carbons by ultraviolet photons is dominant process at the surface.

C.2 Heating and Cooling

The effect of heating and cooling alone in the typical ISM on the time evolution of fluid energy density can be evaluated as follows:

$$\rho \frac{\mathrm{d}u}{\mathrm{d}t} = \left(\frac{\rho}{m_{\mathrm{gas}}}\right)\Gamma - \left(\frac{\rho}{m_{\mathrm{gas}}}\right)^2 \Lambda \,. \tag{C.2}$$

Here, ρ is mass density, u denotes the internal energy per mass, m_{gas} is the mass of individual particle mass of given fluid, and Γ and Λ are heating rate and cooling rate respectively.

It is ideal to calculate heating and cooling process precisely, which has to involve detail chemical evolution in the ISM. Here, chemical evolution means time evolution of chemical species. However, individual chemical processes have various reaction rates, some of which is on a timescale of human beings. Therefore, it is difficult to perform detail chemical evolution coupled with fluids on parsec scales[1].

Instead of solving detailed heating and cooling processes directly, Koyama & Inutsuka (2002) propose an integrated formula based on detail line calculations from Koyama & Inutsuka (2000). Their formulation is given as a function of fluid temperature:

$$\frac{\Lambda(T)}{\Gamma} = 10^7 \exp\left(\frac{-118400}{T+1000}\right) + 1.4\times10^{-2}\sqrt{T}\exp\left(\frac{-92}{T}\right)\ \mathrm{cm}^3\,, \tag{C.3}$$

$$\Gamma = 2\times10^{-26}\,\mathrm{ergs\,s^{-1}}\,. \tag{C.4}$$

Here, they investigate photoelectric heating from small grains and polycyclic aromatic hydrocarbons, heating and ionization by cosmic rays and X-rays, heating by H2 formation and destruction, atomic line cooling from hydrogen Ly$_\alpha$, CII, OI, FeII, SiII, rovibrational line cooling from H_2 and CO, and atomic and molecular collisions with grains (see also Dalgarno & McCray (1972)). The first term in Equation C.3 is mostly determined by Ly$_\alpha$ cooling and the second term is governed by CII cooling. Note that the original formula written in Koyama & Inutsuka (2002) have two typographical errors (Vázquez-Semadeni et al. 2007).

[1] At least, there seems no study that solves detail chemical evolution by second-order in time.

Bibliography

Adams S. M., Kochanek C. S., Beacom J. F., Vagins M. R., Stanek K. Z., 2013, ApJ, 778, 164

Anathpindika S. V., 2010, MNRAS, 405, 1431

André P., Saraceno P., 2005, in Wilson A., ed., ESA Special Publication Vol. 577, ESA Special Publication. pp 179–184

André P., et al., 2010, A&A, 518, L102

André P., Men'shchikov A., Könyves V., Arzoumanian D., 2011, in Alves J., Elmegreen B. G., Girart J. M., Trimble V., eds, IAU Symposium Vol. 270, Computational Star Formation. pp 255–262, doi:10.1017/S1743921311000470

André P., et al., 2016, A&A, 592, A54

Arata S., Yajima H., Nagamine K., 2017, ArXiv e-prints,

Arraki K. S., Klypin A., More S., Trujillo-Gomez S., 2014, MNRAS, 438, 1466

Arzoumanian D., et al., 2011, A&A, 529, L6

Audit E., Hennebelle P., 2005, A&A, 433, 1

Audit E., Hennebelle P., 2008, in Pogorelov N. V., Audit E., Zank G. P., eds, Astronomical Society of the Pacific Conference Series Vol. 385, Numerical Modeling of Space Plasma Flows. p. 73

Baba J., Morokuma-Matsui K., Saitoh T. R., 2017, MNRAS, 464, 246

Balbus S. A., 1988, ApJ, 328, 395

Balbus S. A., 1995, ApJ, 453, 380

Barnabè M., Spiniello C., Koopmans L. V. E., Trager S. C., Czoske O., Treu T., 2013, MNRAS, 436, 253

Barnes P. J., et al., 2011, ApJS, 196, 12

Barnes P. J., Hernandez A. K., O'Dougherty S. N., Schap III W. J., Muller E., 2016, ApJ, 831, 67

Bastian N., Covey K. R., Meyer M. R., 2010, ARA&A, 48, 339

Battersby C., Ginsburg A., Bally J., Longmore S., Dunham M., Darling J., 2014, ApJ, 787, 113

Beasley A. J., Murowinski R., Tarenghi M., 2006, in Society of Photo-Optical Instrumentation Engineers (SPIE) Conference Series. p. 626702, doi:10.1117/12.671227

Beccari G., et al., 2017, A&A, 604, A22

Beck R., 2001, Space Sci. Rev., 99, 243

Beck R., 2004, in Alfaro E. J., Pérez E., Franco J., eds, Astrophysics and Space Science Library Vol. 315, How Does the Galaxy Work?. p. 277, doi:10.1007/1-4020-2620-X˙57

Beck R., 2007, A&A, 470, 539

Beck R., 2015, A&A, 578, A93

Behroozi P. S., Conroy C., Wechsler R. H., 2010, ApJ, 717, 379

Bernet M. L., Miniati F., Lilly S. J., Kronberg P. P., Dessauges-Zavadsky M., 2008, Nature, 454, 302

Bigiel F., Leroy A., Walter F., Brinks E., de Blok W. J. G., Madore B., Thornley M. D., 2008, AJ, 136, 2846

Bigiel F., et al., 2011, ApJ, 730, L13

Bihr S., et al., 2015, A&A, 580, A112

Blumenthal G. R., Faber S. M., Flores R., Primack J. R., 1986, ApJ, 301, 27

Bohlin R. C., Savage B. D., Drake J. F., 1978, ApJ, 224, 132

Bond J. R., Cole S., Efstathiou G., Kaiser N., 1991, ApJ, 379, 440

Brackett T. E., 1956, JCP, 24, 1103

Braine J., Rosolowsky E., Gratier P., Corbelli E., Schuster K., 2018, ArXiv e-prints,

Breitschwerdt D., Feige J., Schulreich M. M., Avillez M. A. D., Dettbarn C., Fuchs B., 2016, Nature, 532, 73

Bronfman L., Casassus S., May J., Nyman L.-Å., 2000, A&A, 358, 521

Burgh E. B., France K., McCandliss S. R., 2007, ApJ, 658, 446

Burkert A., Lin D. N. C., 2000, ApJ, 537, 270

Burton W. B., Gordon M. A., Bania T. M., Lockman F. J., 1975, ApJ, 202, 30

Carretta E., Bragaglia A., Gratton R. G., Recio-Blanco A., Lucatello S., D'Orazi V., Cassisi S., 2010, A&A, 516, A55

Chabrier G., 2003, PASP, 115, 763

Ciardullo R., Feldmeier J. J., Jacoby G. H., Kuzio de Naray R., Laychak M. B., Durrell P. R., 2002, ApJ, 577, 31

Colombo D., et al., 2014a, ApJ, 784, 3

Colombo D., et al., 2014b, ApJ, 784, 4

Conroy C., van Dokkum P. G., 2012, ApJ, 760, 71

Conroy C., Gunn J. E., White M., 2009, ApJ, 699, 486

Corder S., Sheth K., Scoville N. Z., Koda J., Vogel S. N., Ostriker E., 2008, ApJ, 689, 148

Courteau S., et al., 2014, Reviews of Modern Physics, 86, 47

Cowie L. L., 1980, ApJ, 236, 868

Crutcher R. M., 2012, ARA&A, 50, 29

D'Antona F., Caloi V., Mazzitelli I., 1997, ApJ, 477, 519

D'Antona F., Milone A. P., Tailo M., Ventura P., Vesperini E., di Criscienzo M., 2017, Nature Astronomy, 1, 0186

Daddi E., et al., 2007, ApJ, 670, 156

Dalgarno A., McCray R. A., 1972, ARA&A, 10, 375

Dame T. M., et al., 1987, ApJ, 322, 706

Dame T. M., Hartmann D., Thaddeus P., 2001, ApJ, 547, 792

Dawson J. R., McClure-Griffiths N. M., Kawamura A., Mizuno N., Onishi T., Mizuno A., Fukui Y., 2011a, ApJ, 728, 127

Dawson J. R., McClure-Griffiths N. M., Dickey J. M., Fukui Y., 2011b, ApJ, 741, 85

Dawson J. R., McClure-Griffiths N. M., Wong T., Dickey J. M., Hughes A., Fukui Y., Kawamura A., 2013, ApJ, 763, 56

Delgado-Serrano R., Hammer F., Yang Y. B., Puech M., Flores H., Rodrigues M., 2010, A&A, 509, A78

Dewangan L. K., 2017, ApJ, 837, 44

Dewangan L. K., Ojha D. K., Luna A., Anandarao B. G., Ninan J. P., Mallick K. K., Mayya Y. D., 2016, ApJ, 819, 66

Dobashi K., Matsumoto T., Shimoikura T., Saito H., Akisato K., Ohashi K., Nakagomi K., 2014, ApJ, 797, 58

Dobbs C. L., Pringle J. E., 2013, MNRAS, 432, 653

Dobbs C. L., Pringle J. E., Duarte-Cabral A., 2015, MNRAS, 446, 3608

Draine B. T., 1983, ApJ, 270, 519

Draine B. T., 2011, Physics of the Interstellar and Intergalactic Medium

Draine B. T., Bertoldi F., 1996, ApJ, 468, 269

Dressler A., 1980, ApJ, 236, 351

Dubinski J., Carlberg R. G., 1991, ApJ, 378, 496

Dutton A. A., et al., 2011, MNRAS, 416, 322

Egusa F., Kohno K., Sofue Y., Nakanishi H., Komugi S., 2009, ApJ, 697, 1870

Egusa F., Mentuch Cooper E., Koda J., Baba J., 2017, MNRAS, 465, 460

Egusa F., Hirota A., Baba J., Muraoka K., 2018, ArXiv e-prints,

Ehlerová S., Palouš J., 2016, A&A, 587, A5

Elbaz D., et al., 2007, A&A, 468, 33

Elmegreen D. M., Elmegreen B. G., Ravindranath S., Coe D. A., 2007, ApJ, 658, 763

Elphick C., Regev O., Spiegel E. A., 1991, MNRAS, 250, 617

Engargiola G., Plambeck R. L., Rosolowsky E., Blitz L., 2003, ApJS, 149, 343

Eufrasio R. T., et al., 2017, ApJ, 851, 10

Evans II N. J., Heiderman A., Vutisalchavakul N., 2014, ApJ, 782, 114

Field G. B., 1965, ApJ, 142, 531

Field G. B., Saslaw W. C., 1965, ApJ, 142, 568

Field G. B., Goldsmith D. W., Habing H. J., 1969, ApJ, 155, L149

Fletcher A., Beck R., Shukurov A., Berkhuijsen E. M., Horellou C., 2011, MNRAS, 412, 2396

Flores R. A., Primack J. R., 1994, ApJ, 427, L1

Förster Schreiber N. M., et al., 2009, ApJ, 706, 1364

Friedmann A., 1922, Zeitschrift fur Physik, 10, 377

Fujimoto Y., Tasker E. J., Wakayama M., Habe A., 2014, MNRAS, 439, 936

Fukui Y., et al., 1999, PASJ, 51, 745

Fukui Y., Mizuno N., Yamaguchi R., Mizuno A., Onishi T., 2001, PASJ, 53, L41

Fukui Y., et al., 2014, ApJ, 780, 36

Fukui Y., Torii K., Onishi T., Yamamoto H., Okamoto R., Hayakawa T., Tachihara K., Sano H., 2015a, ApJ, 798, 6

Fukui Y., et al., 2015b, ApJ, 807, L4

Fukui Y., et al., 2016, ApJ, 820, 26

Fukui Y., et al., 2017a, ArXiv e-prints,

Fukui Y., et al., 2017d, ArXiv e-prints,

Fukui Y., et al., 2017c, ArXiv e-prints,

Fukui Y., Hattori Y., Torii K., Ohama A., Nishimura A., Kohno M., Yamamoto H., Tachihara K., 2017b, ArXiv e-prints,

Fukui Y., Tsuge K., Sano H., Bekki K., Yozin C., Tachihara K., Inoue T., 2017e, PASJ, 69, L5

Fuller G. A., Myers P. C., 1992, ApJ, 384, 523

Furukawa N., Dawson J. R., Ohama A., Kawamura A., Mizuno N., Onishi T., Fukui Y., 2009, ApJ, 696, L115

Gao Y., Solomon P. M., 2004, ApJ, 606, 271

Gatto A., et al., 2017, MNRAS, 466, 1903

Genzel R., et al., 2008, ApJ, 687, 59

Gerola H., Seiden P. E., 1978, ApJ, 223, 129

Gingold R. A., Monaghan J. J., 1977, MNRAS, 181, 375

Girichidis P., et al., 2016, MNRAS, 456, 3432

Glover S. C. O., Clark P. C., 2015, ArXiv e-prints,

Glover S. C. O., Mac Low M.-M., 2011, MNRAS, 412, 337

Gnedin O. Y., Kravtsov A. V., Klypin A. A., Nagai D., 2004, ApJ, 616, 16

Gounelle M., Meibom A., Hennebelle P., Inutsuka S.-i., 2009, ApJ, 694, L1

Gratier P., et al., 2012, A&A, 542, A108

Griffin M. J., et al., 2010, A&A, 518, L3

Habe A., Ohta K., 1992, PASJ, 44, 203

Haisch Jr. K. E., Lada E. A., Lada C. J., 2001, ApJ, 553, L153

Hall J. S., 1949, Science, 109, 166

Hanayama H., Tomisaka K., 2006, ApJ, 641, 905

Harayama Y., Eisenhauer F., Martins F., 2008, ApJ, 675, 1319

Harikane Y., et al., 2016, ApJ, 821, 123

Harvey P. M., et al., 2013, ApJ, 764, 133

Hatakeyama T., et al., 2017, PASJ, 69, 67

Haworth T. J., et al., 2015a, MNRAS, 450, 10

Haworth T. J., Shima K., Tasker E. J., Fukui Y., Torii K., Dale J. E., Takahira K., Habe A., 2015b, MNRAS, 454, 1634

Hayashi K., et al., 2017, ArXiv e-prints,

Heiderman A., Evans II N. J., Allen L. E., Huard T., Heyer M., 2010, ApJ, 723, 1019

Heitsch F., Burkert A., Hartmann L. W., Slyz A. D., Devriendt J. E. G., 2005, ApJ, 633, L113

Heitsch F., Slyz A. D., Devriendt J. E. G., Hartmann L. W., Burkert A., 2006, ApJ, 648, 1052

Heitsch F., Stone J. M., Hartmann L. W., 2009, ApJ, 695, 248

Hennebelle P., André P., 2013, A&A, 560, A68

Hennebelle P., Audit E., 2007, A&A, 465, 431

Hennebelle P., Pérault M., 1999, A&A, 351, 309

Hennebelle P., Pérault M., 2000, A&A, 359, 1124

Hennebelle P., Audit E., Miville-Deschênes M.-A., 2007, A&A, 465, 445

Heyer M. H., Brunt C. M., 2004, ApJ, 615, L45

Heyer M., Dame T. M., 2015, ARA&A, 53, 583

Heyer M. H., Carpenter J. M., Snell R. L., 2001, ApJ, 551, 852

Hill T., et al., 2011, A&A, 533, A94

Hiltner W. A., 1949, ApJ, 109, 471

Hopkins A. M., Beacom J. F., 2006, ApJ, 651, 142

Hosokawa T., Inutsuka S.-i., 2006a, ApJ, 646, 240

Hosokawa T., Inutsuka S.-i., 2006b, ApJ, 648, L131

Hubble E. P., 1926, ApJ, 64, 321

Iguchi S., et al., 2009, PASJ, 61, 1

Ikeda N., Sunada K., Kitamura Y., 2007, ApJ, 665, 1194

Inoue T., Fukui Y., 2013, ApJ, 774, L31

Inoue T., Inutsuka S.-i., 2008, ApJ, 687, 303

Inoue T., Inutsuka S.-i., 2009, ApJ, 704, 161

Inoue T., Inutsuka S.-i., 2012, ApJ, 759, 35

Inoue T., Omukai K., 2015, ApJ, 805, 73

Inoue T., Hennebelle P., Fukui Y., Matsumoto T., Iwasaki K., Inutsuka S.-i., 2017, ArXiv e-prints,

Inutsuka S.-i., 2001, ApJ, 559, L149

Inutsuka S.-I., 2002, Journal of Computational Physics, 179, 238

Inutsuka S.-i., Inoue T., Iwasaki K., Hosokawa T., 2015, A&A, 580, A49

Iwasaki K., Inutsuka S.-i., Tsuribe T., 2011a, ApJ, 733, 16

Iwasaki K., Inutsuka S.-i., Tsuribe T., 2011b, ApJ, 733, 17

Jansson R., Farrar G. R., 2012, ApJ, 761, L11

Jenkins E. B., Tripp T. M., 2011, ApJ, 734, 65

Jennings Z. G., Williams B. F., Murphy J. W., Dalcanton J. J., Gilbert K. M., Dolphin A. E., Weisz D. R., Fouesneau M., 2014, ApJ, 795, 170

Kashino D., et al., 2013, ApJ, 777, L8

Katz N., 1992, ApJ, 391, 502

Kauffmann J., Pillai T., Goldsmith P. F., 2013, ApJ, 779, 185

Kawamura A., Onishi T., Yonekura Y., Dobashi K., Mizuno A., Ogawa H., Fukui Y., 1998, ApJS, 117, 387

Kawamura A., et al., 2009, ApJS, 184, 1

Kennicutt Jr. R. C., 1998, ApJ, 498, 541

Kennicutt R. C., Evans N. J., 2012, ARA&A, 50, 531

Kennicutt Jr. R. C., Edgar B. K., Hodge P. W., 1989, ApJ, 337, 761

Kim C.-G., Ostriker E. C., 2015a, ApJ, 802, 99

Kim C.-G., Ostriker E. C., 2015b, ApJ, 815, 67

Kim C.-G., Ostriker E. C., 2017, ApJ, 846, 133

Kim J.-G., Kim W.-T., Ostriker E. C., 2016, ApJ, 819, 137

Kim C.-G., Ostriker E. C., Raileanu R., 2017, ApJ, 834, 25

Kirsanova M. S., Salii S. V., Sobolev A. M., Olofsson A. O. H., Ladeyschikov D. A., Thomasson M., 2017, ArXiv e-prints,

Kobayashi H., Tanaka H., 2010, Icarus, 206, 735

Kobayashi M. I. N., Leauthaud A., More S., Okabe N., Laigle C., Rhodes J., Takeuchi T. T., 2015, MNRAS, 449, 2128

Kobayashi H., Tanaka H., Okuzumi S., 2016, ApJ, 817, 105

Kobayashi M. I. N., Kobayashi H., Inutsuka S.-i., Fukui Y., 2017a, ArXiv e-prints,

Kobayashi M. I. N., Inutsuka S.-i., Kobayashi H., Hasegawa K., 2017b, ApJ, 836, 175

Koda J., 2013, in Kawabe R., Kuno N., Yamamoto S., eds, Astronomical Society of the Pacific Conference Series Vol. 476, New Trends in Radio Astronomy in the ALMA Era: The 30th Anniversary of Nobeyama Radio Observatory. p. 49, arXiv:1305.4633

Koda J., et al., 2009, ApJ, 700, L132

Koda J., et al., 2011, ApJS, 193, 19

Koda J., et al., 2012, ApJ, 761, 41

Koda J., Scoville N., Heyer M., 2016, ApJ, 823, 76

Kohno M., et al., 2017, ArXiv e-prints,

Kokubo E., Ida S., 1996, Icarus, 123, 180

Kolmogorov A., 1941, Akademiia Nauk SSSR Doklady, 30, 301

Kołos W., Wolniewicz L., 1965, JCP, 43, 2429

Komugi S., Sofue Y., Nakanishi H., Onodera S., Egusa F., 2005, PASJ, 57, 733

Könyves V., et al., 2010, A&A, 518, L106

Könyves V., et al., 2015, A&A, 584, A91

Körtgen B., Banerjee R., 2015, MNRAS, 451, 3340

Koyama H., Inutsuka S.-I., 2000, ApJ, 532, 980

Koyama H., Inutsuka S.-i., 2002, ApJ, 564, L97

Koyama Y., et al., 2013, MNRAS, 434, 423

Koyama Y., Kodama T., Tadaki K.-i., Hayashi M., Tanaka I., Shimakawa R., 2014, ApJ, 789, 18

Koyama S., et al., 2017, ArXiv e-prints,

Kramer C., Stutzki J., Rohrig R., Corneliussen U., 1998, A&A, 329, 249

Kritsuk A. G., Norman M. L., 2002, ApJ, 569, L127

Kroupa P., 2001, MNRAS, 322, 231

Kruijssen J. M. D., Longmore S. N., 2014, MNRAS, 439, 3239

Kudoh T., Basu S., 2011, ApJ, 728, 123

Kudryavtseva N., et al., 2012, ApJ, 750, L44

Kwan J., 1979, ApJ, 229, 567

Kwan J., Valdes F., 1983, ApJ, 271, 604

Lacey C., Cole S., 1993, MNRAS, 262, 627

Lada C. J., Lombardi M., Alves J. F., 2010, ApJ, 724, 687

Lada C. J., Forbrich J., Lombardi M., Alves J. F., 2012, ApJ, 745, 190

Lada C. J., Lombardi M., Roman-Zuniga C., Forbrich J., Alves J. F., 2013, ApJ, 778, 133

Landau L. D., Lifshitz E. M., 1959, Fluid mechanics

Larson R. B., 1981, MNRAS, 194, 809

Leavitt H. S., 1908, Annals of Harvard College Observatory, 60, 87

Leavitt H. S., Pickering E. C., 1912, Harvard College Observatory Circular, 173, 1

Lee H.-H., Herbst E., Pineau des Forets G., Roueff E., Le Bourlot J., 1996, A&A, 311, 690

Lemaître G., 1927, Annales de la Société Scientifique de Bruxelles, 47, 49

Leroy A. K., et al., 2017, ArXiv e-prints,

Levinson F. H., Roberts Jr. W. W., 1981, ApJ, 245, 465

Li H.-b., Fang M., Henning T., Kainulainen J., 2013, MNRAS, 436, 3707

Lin C. C., Shu F. H., 1964, ApJ, 140, 646

Liu J., Salumbides E. J., Hollenstein U., Koelemeij J. C. J., Eikema K. S. E., Ubachs W., Merkt F., 2009, JCP, 130, 174306

Lucy L. B., 1977, AJ, 82, 1013

Macciò A. V., Paduroiu S., Anderhalden D., Schneider A., Moore B., 2012, MNRAS, 424, 1105

Madau P., Dickinson M., 2014, ARA&A, 52, 415

Malyshkin L., Goodman J., 2001, Icarus, 150, 314

Mashchenko S., Couchman H. M. P., Wadsley J., 2006, Nature, 442, 539

Mathis J. S., Rumpl W., Nordsieck K. H., 1977, ApJ, 217, 425

McKee C. F., Ostriker J. P., 1977, ApJ, 218, 148

Meidt S. E., et al., 2015, ApJ, 806, 72

Meyer M. R., Backman D. E., Weinberger A. J., Wyatt M. C., 2007, Protostars and Planets V, pp 573–588

Michikoshi S., Kokubo E., 2016a, ApJ, 821, 35

Michikoshi S., Kokubo E., 2016b, ApJ, 823, 121

Mizuno A., Fukui Y., 2004, in Clemens D., Shah R., Brainerd T., eds, Astronomical Society of the Pacific Conference Series Vol. 317, Milky Way Surveys: The Structure and Evolution of our Galaxy. p. 59

Möbius E., et al., 2009, Science, 326, 969

Molinari S., et al., 2010, A&A, 518, L100

Moore B., 1994, Nature, 370, 629

Moore T. J. T., et al., 2015, MNRAS, 453, 4264

Morokuma-Matsui K., Muraoka K., 2017, ApJ, 837, 137

Morris M., Serabyn E., 1996, ARA&A, 34, 645

Mouschovias T. C., 1974, ApJ, 192, 37

Mouschovias T. C., 1976, ApJ, 207, 141

Muñoz D. J., Mardones D., Garay G., Rebolledo D., Brooks K., Bontemps S., 2007, ApJ, 668, 906

Muraoka K., et al., 2016, PASJ, 68, 89

Murata K. L., et al., 2014, ApJ, 786, 15

Myers P. C., 1978, ApJ, 225, 380

Nagashima M., Koyama H., Inutsuka S.-i., 2005, MNRAS, 361, L25

Nagashima M., Inutsuka S.-i., Koyama H., 2006, ApJ, 652, L41

Nakamura F., Li Z.-Y., 2008, ApJ, 687, 354

Nakamura F., et al., 2012, ApJ, 746, 25

Nakamura F., et al., 2014, ApJ, 791, L23

Nakanishi H., Sofue Y., 2016, PASJ, 68, 5

Navarro J. F., Eke V. R., Frenk C. S., 1996a, MNRAS, 283, L72

Navarro J. F., Frenk C. S., White S. D. M., 1996b, ApJ, 462, 563

Navarro J. F., Frenk C. S., White S. D. M., 1997, ApJ, 490, 493

Nguyen-Luong Q., et al., 2016, ApJ, 833, 23

Nishimura A., et al., 2017b, ArXiv e-prints,

Nishimura A., et al., 2017a, ArXiv e-prints,

Noeske K. G., et al., 2007, ApJ, 660, L43

Ntormousi E., Dawson J. R., Hennebelle P., Fierlinger K., 2017, ArXiv e-prints,

Oey M. S., Clarke C. J., 1997, MNRAS, 289

Oey M. S., Smedley S. A., 1998, AJ, 116, 1263

Oey M. S., Watson A. M., Kern K., Walth G. L., 2005, AJ, 129, 393

Ohama A., et al., 2010, ApJ, 709, 975

Ohama A., et al., 2017a, ArXiv e-prints,

Ohama A., et al., 2017b, ArXiv e-prints,

Ohama A., et al., 2017c, ArXiv e-prints,

Onishi T., et al., 1999, PASJ, 51, 871

Onodera S., et al., 2010, ApJ, 722, L127

Ostriker J. P., Steinhardt P., 2003, Science, 300, 1909

Palla F., Stahler S. W., 2000, ApJ, 540, 255

Palmeirim P., et al., 2017, A&A, 605, A35

Parker E. N., 1953, ApJ, 117, 431

Parker E. N., 1966, ApJ, 145, 811

Pauling L., Sheehan W. F., 1949, Proceedings of the National Academy of Science, 35, 359

Peter A. H. G., Rocha M., Bullock J. S., Kaplinghat M., 2013, MNRAS, 430, 105

Peters T., et al., 2017, MNRAS, 466, 3293

Pettitt A. R., Tasker E. J., Wadsley J. W., Keller B. W., Benincasa S. M., 2017, MNRAS, 468, 4189

Pety J., et al., 2013, ApJ, 779, 43

Pilbratt G. L., et al., 2010, A&A, 518, L1

Planck Collaboration et al., 2014a, A&A, 571, A15

Planck Collaboration et al., 2014b, A&A, 571, A16

Poglitsch A., et al., 2010, A&A, 518, L2

Predehl P., Schmitt J. H. M. M., 1995, A&A, 293, 889

Press W. H., Schechter P., 1974, ApJ, 187, 425

Rachford B. L., et al., 2009, ApJS, 180, 125

Rahner D., Pellegrini E. W., Glover S. C. O., Klessen R. S., 2017, ArXiv e-prints,

Raymond J. C., Smith B. W., 1977, ApJS, 35, 419

Reina-Campos M., Kruijssen J. M. D., 2017, MNRAS, 469, 1282

Rice T. S., Goodman A. A., Bergin E. A., Beaumont C., Dame T. M., 2016, ApJ, 822, 52

Rigby A. J., et al., 2016, MNRAS, 456, 2885

Robitaille T. P., Whitney B. A., 2010, ApJ, 710, L11

Rodighiero G., et al., 2014, MNRAS, 443, 19

Rosenberg H., 1910, Astronomische Nachrichten, 186, 71

Rosolowsky E., Engargiola G., Plambeck R., Blitz L., 2003, ApJ, 599, 258

Rosolowsky E., Keto E., Matsushita S., Willner S. P., 2007, ApJ, 661, 830

Roy A., et al., 2015, A&A, 584, A111

Roychowdhury S., Huang M.-L., Kauffmann G., Wang J., Chengalur J. N., 2015, MNRAS, 449, 3700

Russell H. N., 1914, Popular Astronomy, 22, 275

Safronov V. S., 1972, Evolution of the protoplanetary cloud and formation of the earth and planets.

Saigo K., et al., 2017, ApJ, 835, 108

Salpeter E. E., 1955, ApJ, 121, 161

Sano T., Inutsuka S., Miyama S. M., 1999, in Miyama S. M., Tomisaka K., Hanawa T., eds, Astrophysics and Space Science Library Vol. 240, Numerical Astrophysics. p. 383, doi:10.1007/978-94-011-4780-4˙114

Sano H., et al., 2017b, ArXiv e-prints,

Sano H., et al., 2017a, ArXiv e-prints,

Scalo J. M., 1986, Fund. Cosmic Phys., 11, 1

Schinnerer E., et al., 2013, ApJ, 779, 42

Schinnerer E., et al., 2017, ArXiv e-prints (accepted to ApJ),

Schmidt M., 1959, ApJ, 129, 243

Schneider N., et al., 2016, A&A, 587, A74

Schruba A., et al., 2011, AJ, 142, 37

Schwarz J., McCray R., Stein R. F., 1972, ApJ, 175, 673

Scoville N. Z., Hersh K., 1979, ApJ, 229, 578

Scoville N. Z., Solomon P. M., 1975, ApJ, 199, L105

Scoville N., et al., 2007, ApJS, 172, 1

Seiden P. E., Gerola H., 1979, ApJ, 233, 56

Seiden P. E., Schulman L. S., Gerola H., 1979, ApJ, 232, 702

Seifried D., et al., 2017, MNRAS, 472, 4797

Sellwood J. A., McGaugh S. S., 2005, ApJ, 634, 70

Sheffer Y., Rogers M., Federman S. R., Abel N. P., Gredel R., Lambert D. L., Shaw G., 2008, ApJ, 687, 1075

Sheth R. K., Tormen G., 1999, MNRAS, 308, 119

Shimajiri Y., et al., 2017, A&A, 604, A74

Shu F. H., 1992, The physics of astrophysics. Volume II: Gas dynamics.

Slavin J. D., Cox D. P., 1992, ApJ, 392, 131

Smith R. J., Lucey J. R., Carter D., 2012, MNRAS, 426, 2994

Smoluchowski M. V., 1916, Zeitschrift fur Physik, 17, 557

Somerville R. S., Primack J. R., 1999, MNRAS, 310, 1087

Spergel D. N., Steinhardt P. J., 2000, Physical Review Letters, 84, 3760

Stark A. A., Brand J., 1989, ApJ, 339, 763

Stark A. A., Lee Y., 2005, ApJ, 619, L159

Stark A. A., Lee Y., 2006, ApJ, 641, L113

Sugiura K., Inutsuka S.-i., 2016, Journal of Computational Physics, 308, 171

Sunyaev R. A., Zeldovich Y. B., 1970, Ap&SS, 7, 3

Tacconi L. J., et al., 2010, Nature, 463, 781

Tachihara K., Mizuno A., Fukui Y., 2000, ApJ, 528, 817

Tachihara K., Saigo K., Higuchi A. E., Inoue T., Inutsuka S.-i., Hackstein M., Haas M., Mugrauer M., 2012, ApJ, 754, 95

Takahira K., Tasker E. J., Habe A., 2014, ApJ, 792, 63

Takeuchi T., et al., 2010, PASJ, 62, 557

Tan J. C., 2000, ApJ, 536, 173

Tang N., Li D., Heiles C., Wang S., Pan Z., Wang J.-J., 2016, A&A, 593, A42

Tasker E. J., Tan J. C., 2009, ApJ, 700, 358

Thompson M. A., Urquhart J. S., Moore T. J. T., Morgan L. K., 2012, MNRAS, 421, 408

Thornton K., Gaudlitz M., Janka H.-T., Steinmetz M., 1998, ApJ, 500, 95

Tomisaka K., 1984, PASJ, 36, 457

Tomisaka K., 1986, PASJ, 38, 95

Torii K., et al., 2011, ApJ, 738, 46

Torii K., et al., 2015, ApJ, 806, 7

Torii K., et al., 2017a, ArXiv e-prints,

Torii K., et al., 2017b, ApJ, 835, 142

Torii K., et al., 2017c, ApJ, 840, 111

Tosaki T., et al., 2016, ArXiv e-prints (in press at PASJ),

Trubnikov B. A., 1971, Soviet Physics Doklady, 16, 124

Tsuboi M., Miyazaki A., Uehara K., 2015, PASJ, 67, 90

Tsutsumi D., et al., 2017, ArXiv e-prints,

Tyson J. A., Kochanski G. P., Dell'Antonio I. P., 1998, ApJ, 498, L107

Umemoto T., et al., 2017, PASJ, 69, 78

Usero A., et al., 2015, AJ, 150, 115

Utomo D., Blitz L., Davis T., Rosolowsky E., Bureau M., Cappellari M., Sarzi M., 2015, ApJ, 803, 16

Valdivia V., Hennebelle P., Gérin M., Lesaffre P., 2016, A&A, 587, A76

Vázquez-Semadeni E., Ryu D., Passot T., González R. F., Gazol A., 2006, ApJ, 643, 245

Vázquez-Semadeni E., Gómez G. C., Jappsen A. K., Ballesteros-Paredes J., González R. F., Klessen R. S., 2007, ApJ, 657, 870

Vázquez-Semadeni E., Banerjee R., Gómez G. C., Hennebelle P., Duffin D., Klessen R. S., 2011, MNRAS, 414, 2511

Wada K., Baba J., Saitoh T. R., 2011, ApJ, 735, 1

Walborn N. R., Parker J. W., 1992, ApJ, 399, L87

Walch S., et al., 2015, MNRAS, 454, 238

Walder R., Folini D., 1998a, Ap&SS, 260, 215

Walder R., Folini D., 1998b, A&A, 330, L21

Wallner A., et al., 2016, Nature, 532, 69

Weinberg D. H., Bullock J. S., Governato F., Kuzio de Naray R., Peter A. H. G., 2013, ArXiv e-prints,

Wetherill G. W., Stewart G. R., 1989, Icarus, 77, 330

Williams J. P., McKee C. F., 1997, ApJ, 476, 166

Williams J. P., Blitz L., McKee C. F., 2000, Protostars and Planets IV, p. 97

Wilson R. W., Jefferts K. B., Penzias A. A., 1970, ApJ, 161, L43

Wolfire M. G., Hollenbach D., McKee C. F., Tielens A. G. G. M., Bakes E. L. O., 1995, ApJ, 443, 152

Wolfire M. G., McKee C. F., Hollenbach D., Tielens A. G. G. M., 2003, ApJ, 587, 278

Wu J., Evans II N. J., Gao Y., Solomon P. M., Shirley Y. L., Vanden Bout P. A., 2005, ApJ, 635, L173

Wu B., Van Loo S., Tan J. C., Bruderer S., 2015, ApJ, 811, 56

Xu D., Li D., Yue N., Goldsmith P. F., 2016, ApJ, 819, 22

Yasui C., Kobayashi N., Tokunaga A. T., Saito M., Tokoku C., 2010, ApJ, 723, L113

Yonekura Y., Dobashi K., Mizuno A., Ogawa H., Fukui Y., 1997, ApJS, 110, 21

Yoshida A., Kitamura Y., Shimajiri Y., Kawabe R., 2010, ApJ, 718, 1019

Young J. S., Scoville N. Z., 1991, ARA&A, 29, 581

Zahid H. J., Dima G. I., Kewley L. J., Erb D. K., Davé R., 2012, ApJ, 757, 54

Zavala J., Vogelsberger M., Walker M. G., 2013, MNRAS, 431, L20

Zel'Dovich Y. B., Pikel'Ner S. B., 1969, Soviet Journal of Experimental and Theoretical Physics, 29, 170

Zeldovich Y. B., Sunyaev R. A., 1969, Ap&SS, 4, 301

Zhu H., Tian W., Li A., Zhang M., 2017, MNRAS, 471, 3494

Zolotov A., et al., 2012, ApJ, 761, 71

Zuckerman B., Evans II N. J., 1974, ApJ, 192, L149

Zwicky F., 1937, ApJ, 86, 217

de Blok W. J. G., McGaugh S. S., Rubin V. C., 2001, AJ, 122, 2396

van Dokkum P. G., 2008, ApJ, 674, 29

van Dokkum P. G., Conroy C., 2010, Nature, 468, 940

van Leer B., 1979, Journal of Computational Physics, 32, 101